

Development of Satellite Remote Sensing Techniques for Quantifying Volcanic Ash  
Cloud Properties

By

Michael J. Pavolonis

A dissertation submitted in partial fulfillment of  
the requirements for the degree of

Doctor of Philosophy

(Atmospheric and Oceanic Sciences)

at the

UNIVERSITY OF WISCONSIN-MADISON

2014

Date of final oral examination: 5/6/2014

The dissertation is approved by the following members of the Final Oral Committee:

Steve A. Ackerman, Professor, Atmospheric and Oceanic Sciences

Ralf Bennartz, Professor, Atmospheric and Oceanic Sciences

Jon Martin, Professor, Atmospheric and Oceanic Sciences

Grant Petty, Professor, Atmospheric and Oceanic Sciences

Kurt Feigl, Professor, Geoscience

# **Development of Satellite Remote Sensing Techniques for Quantifying Volcanic Ash Cloud Properties**

Michael J. Pavolonis

Under the supervision of Professor Steve A. Ackerman

At the University of Wisconsin – Madison

## **Abstract**

Novel new approaches to automatically detect and characterize volcanic ash using satellite data are presented. The Spectrally Enhanced Cloud Objects (SECO) ash detection algorithm, combines radiative transfer theory, Bayesian methods, and image processing/computer vision concepts to identify volcanic ash clouds in satellite data with skill that is generally comparable to a human expert, especially with respect to false alarm rate. The SECO method is globally applicable and can be applied to virtually any low earth orbit or geostationary satellite sensor. The new ash detection approach was quantitatively proven to be significantly more skillful than traditional pixel based approaches, including the commonly used “split-window” technique. The performance of the SECO approach is extremely promising and well suited for a variety of new and improved applications. A new approach to retrieve volcanic ash cloud properties from infrared satellite measurements was also developed. The algorithm utilizes an optimal estimation framework to retrieve ash cloud height, mass loading, and effective particle

radius. Optimal estimation allows uncertainties in the measurements and forward model to be taken into account and uncertainty estimates for each of the retrieved parameters to be determined. Background atmospheric water vapor, surface temperature, and surface emissivity are explicitly accounted for on a pixel-by-pixel basis, so the algorithm is globally applicable. In addition, the ash cloud retrieval algorithm is unique because it allows the cloud temperature/height to be a free parameter.

Volcanic ash clouds are a major aviation hazard. Fine-grained ash from explosive eruptions can be transported long distances (>1000 km) from the source volcano by atmospheric winds, severely disrupting aviation operations. Volcanic ash clouds are complex and the background environment in which they reside can be as well. Thus, sophisticated satellite remote sensing techniques for extracting ash cloud properties are needed to increase the timeliness and accuracy of volcanic ash advisories and forecasts. As demonstrated using the 2008 eruption of Kasatochi volcano in Alaska, the new theoretical ash remote sensing framework is well suited for advanced applications such as automated volcanic ash cloud alerting and constraining model forecasts of volcanic ash dispersion and removal.

## Acknowledgements

I would like to thank Jeff Key, Ingrid Guch, and Al Powell of the National Oceanic and Atmospheric Administration (NOAA) Center for Satellite Applications and Research (STAR) for being supportive of this endeavor. They allowed me to balance professional and educational responsibilities in a manner that made completion of this degree possible.

The Cooperative Institute for Meteorological Satellite Studies (CIMSS) at the University of Wisconsin is a world-class research institute. I am exceptionally fortunate to work with so many great scientists at CIMSS. I am grateful to Justin Sieglaff and John Cintineo for their critical support in managing the large volumes of satellite data utilized during the research process and for carefully reviewing this dissertation. Shane Hubbard provided much needed support and encouragement during the “home stretch” of writing this thesis. I am also grateful to Andy Heidinger for our fantastic discussions on radiative transfer and retrieval theory. So much of my understanding of these concepts is a result of our discussions.

Steve Ackerman’s advice and guidance throughout the research process is greatly appreciated. Steve’s energy and enthusiasm is contagious. I thank committee members Ralf Bennartz, Kurt Feigl, Jon Martin, and Grant Petty for carefully reviewing this dissertation and providing so many great suggestions.

On March 24, 2012 we welcomed our daughter Ella to the world. Ella, thank you for providing countless reminders of what is really important in life. Finally, this dissertation would not be possible without the support of my wife, Melanie. Her unwavering support, encouragement, and guidance on the many occasions that I felt lost

will never be forgotten. She is the glue that keeps everything together, always sacrificing for the benefit of our family.

This research was supported by grants from the next generation Geostationary Operational Environmental Satellite (GOES-R) Algorithm Working Group (AWG) and Risk Reduction programs.

## Table of Contents

<b>Abstract</b> .....	<b>i</b>
<b>Acknowledgements</b> .....	<b>iii</b>
<b>Table of Contents</b> .....	<b>v</b>
<b>List of Tables</b> .....	<b>viii</b>
<b>List of Figures</b> .....	<b>xi</b>
<b>1. Introduction</b> .....	<b>1</b>
<b>2. Background and Motivation</b> .....	<b>4</b>
<b>3. Infrared Radiation and Cloud Microphysics</b> .....	<b>18</b>
<b>3.1. Introduction</b> .....	<b>18</b>
<b>3.2. Physical Basis of Cloud Composition Information</b> .....	<b>19</b>
<b>3.3. The Beta Method</b> .....	<b>21</b>
<b>3.4. Cloud Composition Differences in <math>\beta</math>-space</b> .....	<b>27</b>
<b>3.5. Estimating the Clear Sky Radiance and Transmittance</b> .....	<b>29</b>
<b>3.6. Sensitivity of Beta to Cloud Vertical Structure</b> .....	<b>31</b>
<b>3.7. Alternative Cloud Vertical Structure Assumptions</b> .....	<b>43</b>
<b>3.8. Summary</b> .....	<b>48</b>
<b>4. Multispectral Analysis of Volcanic Ash and Dust</b> .....	<b>50</b>
<b>4.1. Introduction</b> .....	<b>50</b>
<b>4.2. Satellite Measurements</b> .....	<b>51</b>
<b>4.3. Definition of Volcanic Ash and Dust Clouds</b> .....	<b>54</b>
<b>4.4. SECO Algorithm – Multispectral Analysis</b> .....	<b>64</b>
<b>4.5. Analysis of Volcanic Ash/Dust Probabilities</b> .....	<b>95</b>

4.6. Summary .....	111
5. Retrieval of Volcanic Ash and Dust Cloud Properties.....	113
5.1. Introduction .....	113
5.2. Infrared Measurements .....	114
5.3. Infrared Radiative Transfer Theory .....	116
5.4. Retrieval Forward Model.....	118
5.5. Optimal Estimation Retrieval Method.....	119
5.6. Microphysical Models .....	125
5.7. Results and Error Analysis.....	131
5.8. Summary .....	156
6. Volcanic Ash Cloud Objects.....	159
6.1. Introduction .....	159
6.2. Review of Multispectral Parameters .....	161
6.3. Review of Ash/Dust Cloud Property Retrieval.....	163
6.4. Cloud Object Analysis .....	164
6.5. Case Studies .....	183
6.6. Global Analysis.....	194
6.7. Summary .....	203
7. Analysis of Ash Cloud Properties .....	205
7.1. 2008 Eruption of Kasatochi, Alaska .....	205
7.2. Excursion: Analysis of Ash Cloud Geometric Thickness .....	235
8. Summary and Conclusions.....	237
Appendix A: Derivation of the all-sky infrared radiative transfer equation.....	244

<b>Appendix B: Derivation of analytical of Jacobians listed in Table 3.1.....</b>	<b>246</b>
<b>Appendix C: Description of Volcanic Ash and Dust Detection Training Data .....</b>	<b>254</b>
<b>Appendix D: Cloud Property Retrieval Kernel Matrix.....</b>	<b>260</b>
<b>Appendix E: Cloud Object Membership Criteria.....</b>	<b>262</b>
<b>References .....</b>	<b>265</b>

## List of Tables

Table 3.1: Symbols and definitions of the brightness temperature difference (BTD) and effective absorption optical depth ratio ( $\beta_{\text{tot}}$ ) Jacobians. The effective absorption optical depth ratio was calculated assuming that the effective cloud temperature is equal to the tropopause temperature. The denominator (numerator) wavelength in the beta ratio is denoted by $\lambda_D$ ( $\lambda_N$ ). The BTD is defined as $\lambda_D - \lambda_N$ .....	32
Table 3.2: A description of the parameters used in various radiative transfer model simulations of a maritime tropical and Sahara Desert scene.....	37
Table 4.1: Possible spectral channel combinations that can be used in the ash/dust detection algorithm are shown as a function of satellite imaging sensor spectral capabilities (relevant to ash and dust detection). Tier I sensors offer the most channels of relevance to the ash/dust detection algorithm presented in this dissertation and Tier III sensors offer the least. Sun glint is assumed to be present over water surfaces if the glint angle is less than $40^\circ$ . Stray light is assumed to be present if the solar zenith angle exceeds $90^\circ$ and the measured $0.65 \mu\text{m}$ counts is greater than a sensor dependent threshold. Please see Table 4.2 for a list of sensor acronyms. ....	52
Table 4.2: The satellite imaging radiometers of greatest relevance to the ash/dust detection algorithm described in this dissertation is listed below. Each sensor may be present on multiple spacecraft with different orbital parameters. ....	53
Table 4.3: The recipe used to create the 12-11, 11-3.9, $11 \mu\text{m}$ false color (or Red-Green-Blue) image is shown. Each parameter is linearly scaled to the value range given in the third and fourth columns of the table. ....	56
Table 4.4: The recipe used to create the 12-11, 11-8.5, $11 \mu\text{m}$ false color (or Red-Green-Blue) image is shown. Each parameter is linearly scaled to the value range given in the third and fourth columns of the table. ....	59

- Table 4.5: The top most portion of the table lists the individual radiative parameters utilized to construct SECO algorithm classifiers, along with the corresponding histogram binning scheme used to estimate the classifier PDFs. The multivariate classifier arrays (using the radiative parameter ID's shown in the top part of the table) are listed in the second part of the table as a function of satellite sensor and the conditions required for utilization. Sun glint is assumed to be present over water surfaces if the glint angle is less than  $40^\circ$ . Stray light is assumed to be present if the solar zenith angle exceeds  $90^\circ$  and the measured  $0.65 \mu\text{m}$  counts is greater than a sensor dependent threshold. .... 85
- Table 5.1: First guess values and associated uncertainties of each retrieved parameter.  $\theta_{\text{sat}}$  is the satellite zenith angle. If an upper level  $\text{SO}_2$  signal is present (see Chapter 3),  $T_{\text{eff}}(2)$  is utilized, otherwise  $T_{\text{eff}}(1)$  is used. .... 123
- Table 5.2: Instrument and forward model errors for each observation used in the retrieval. .... 125
- Table 6.1: The top most portion of the table lists the individual radiative parameters utilized to construct cloud object classifiers, along with the corresponding histogram-binning scheme used to estimate the classifier PDFs. The multivariate classifier variables (using the radiative parameter IDs shown in the top part of the table) are listed in the second part of the table as a function of satellite sensor and the conditions required for utilization. Sun glint is assumed to be present over water surfaces if the glint angle is less than  $40^\circ$ . Stray light is assumed to be present if the solar zenith angle exceeds  $90^\circ$  and the measured  $0.65 \mu\text{m}$  counts is greater than a sensor dependent threshold. Please see Table 4.2 for a list of sensor acronyms. .. 173
- Table 6.2: The radiative parameters that define an 8-element state vector, where each element is discretized using the associated histogram-binning scheme, are shown. .... 178
- Table 6.3: Each row in the table represents a set of cloud object selection criteria. During the cloud object selection process the “greater than” operator is applied to all criteria

except “Max Size” and “Cloud Flag.” The “less than or equal to” operator is applied to “Max Size” and the “greater than or equal to” operator is applied to “Cloud Flag.” If any single set of selection criteria is met, the cloud object is selected. The center of the cloud object must be within 50/10/5 km of a volcano in order to use the criteria listed below the V50/V10/V5 headers. .... 182

## List of Figures

- Figure 2.1: Major commercial flight routes (blue), historically active volcanoes (red), and the area of responsibility of each Volcanic Ash Advisory Center (VAAC) are overlaid on a global map. Source: ICAO ..... 6
- Figure 2.2: Graphic illustration of the Volcanic Explosivity Index (VEI). A red sphere representing the highest VEI category, 8, is not shown for clarity. Source: USGS... 8
- Figure 2.3: Radiative transfer model calculations of the 11  $\mu\text{m}$  brightness temperature and the 11-12  $\mu\text{m}$  “split-window” brightness temperature difference for a variety of cloud compositions with a volcanic ash component ranging from 0 to 100%. Each point on a given curve represents a different 0.55  $\mu\text{m}$  cloud optical depth. Adapted from Pavolonis et al. [2006]. ..... 11
- Figure 2.4: The frequency of occurrence [%] of 11-12  $\mu\text{m}$  “split-window” brightness temperature differences  $< -0.2$  K on April 4, 2003. No known volcanic ash clouds were present at the time of this image. Adapted from Pavolonis et al. [2006]. ..... 12
- Figure 3.1: The imaginary index of refraction for liquid water (solid), ice (dotted), andesite (dashed), and kaolinite (dash-dot) is shown as a function of wavelength. . 20
- Figure 3.2: Spectra of effective absorption optical depth ratios calculated from simulated high spectral resolution radiances in the 8 – 14  $\mu\text{m}$  range are shown in gray (with thinner line style) for an upper tropospheric ice cloud (composed of plates) with an optical depth of 0.5 at a wavelength of 10  $\mu\text{m}$ . An analogous spectrum of scaled extinction coefficients is also shown in black (with thick line style). Each panel represents a different effective particle radius. .... 26
- Figure 3.3: The 12/11  $\mu\text{m}$  scaled extinction ratio ( $\beta(12\mu\text{m}, 11\mu\text{m})$ ) is shown as a function of the 8.5/11  $\mu\text{m}$  scaled extinction ratio ( $\beta(8.5\mu\text{m}, 11\mu\text{m})$ ) for liquid water spheres (red), various ice crystal habits (blue), andesite spheres (brown), and kaolinite spheres (green). The ice crystal habits shown are plates, aggregates, bullet rosettes,

droxtals, hollow columns, solid columns, and spheroids. A range of particle sizes is shown for each composition. For liquid water (ice), the effective particle radius was varied from 5 to 30 (54)  $\mu\text{m}$ . The 5 and 15  $\mu\text{m}$  values of liquid water effective radius are labeled. The andesite and kaolinite effective particle radius was varied from 1 to 12  $\mu\text{m}$ . The large and small particle ends of each curve are labeled. The  $\beta$ -ratios were derived from the single scatter properties. The area shaded in light gray represents the envelope where volcanic ash and dust rock types not explicitly represented on this figure typically lie. .... 28

Figure 3.4: Surface temperature in K (Panel A), total precipitable water in cm (Panel B), 8.5- $\mu\text{m}$  surface emissivity (Panel C), and 11- $\mu\text{m}$  surface emissivity (Panel D) are shown mapped to a full disk viewed by a geostationary radiometer. The surface temperature and precipitable water are taken from a 12 hour Global Forecast System (GFS) forecast valid at 13:45 UTC on August 2, 2006. The surface emissivity is a monthly mean taken from the Seebor database. The white triangles indicate locations where Jacobians of the infrared radiative transfer equation were evaluated using these and other inputs from the GFS. .... 34

Figure 3.5: Evaluation of 8.5 – 11  $\mu\text{m}$  brightness temperature difference Jacobians (right hand side of figure) and 8.5- $\mu\text{m}$ /11- $\mu\text{m}$  effective absorption optical depth ratio Jacobians, calculated assuming an effective cloud temperature equal to the tropopause temperature (left hand side of figure), for a maritime tropical location. For each dependent variable, the partial derivative with respect to cloud microphysics (CM), cloud effective temperature (CT), 11- $\mu\text{m}$  cloud emissivity (CE), surface temperature (ST), total 11- $\mu\text{m}$  clear sky atmospheric transmittance (GT (mag)), the spectral variation of the clear sky atmospheric transmittance (GT (var)), the 11- $\mu\text{m}$  surface emissivity (SE (mag)), and the spectral variation of the surface emissivity (SE (var)) was evaluated as a function of the 11- $\mu\text{m}$  cloud emissivity. All Jacobians were scaled to a 1% change in the dependent variable and then normalized by the respective CM Jacobian. Blue (red) colors indicate that the magnitude of the Jacobian is less (greater) than the magnitude of the CM Jacobian. Three different

types of clouds were considered: an ice cloud in the upper troposphere (but significantly lower than the tropopause) (top row), a volcanic ash cloud in the middle troposphere (middle row), and a liquid water cloud in the lower troposphere (bottom row)..... 38

Figure 3.6: Same as Figure 3.5 except the 11 – 12- $\mu\text{m}$  brightness temperature difference and the 12- $\mu\text{m}$ /11- $\mu\text{m}$  effective absorption optical depth ratio were considered..... 39

Figure 3.7: Same as Figure 3.5, except the Jacobians were evaluated for a scene located over the Sahara Desert..... 42

Figure 3.8: Same as Figure 3.7, except the 11 – 12- $\mu\text{m}$  brightness temperature difference and the 12- $\mu\text{m}$ /11- $\mu\text{m}$  effective absorption optical depth ratio were considered..... 43

Figure 3.9: Calculations showing the 12- $\mu\text{m}$ /11- $\mu\text{m}$  (top) and 8.5- $\mu\text{m}$ /11- $\mu\text{m}$  (bottom) effective absorption optical depth ratio ( $\beta$ ) derived assuming a cloud vertical level that gives an 11- $\mu\text{m}$  cloud emissivity equal to 0.99 (performed regardless of the true cloud emissivity). Each  $\beta$  is expressed as a function of the true 11- $\mu\text{m}$  cloud emissivity for an upper tropospheric ice cloud (dashed line) and a lower tropospheric liquid water cloud (solid line). The range of values expected based on the single scatter properties are given by the dotted line. These calculations were performed for a maritime tropical location..... 45

Figure 3.10: Same as Figure 3.9 except for a location over the Sahara Desert was considered..... 46

Figure 4.1: A false color Terra MODIS image centered on the Aleutian Islands (Alaska) on February 19, 2001 at 23:10 UTC is shown. The 12 - 11  $\mu\text{m}$  brightness temperature difference (BTD) is displayed on the red color gun, the 11 – 3.75  $\mu\text{m}$  BTD is displayed on the green color gun, and the 11  $\mu\text{m}$  brightness temperature is displayed in the blue color gun. The scaling ranges used to make the image are shown in Table 4.3. The white annotations are used to highlight some important features. The volcanic ash cloud was produced by an eruption of Mount Cleveland,

Alaska. In the annotations, “meteo cloud” refers to liquid water or ice clouds generated by typical meteorological processes. This MODIS image was taken from the sunlit portion of the orbit..... 57

Figure 4.2: Same as Figure 4.1 except the Terra MODIS image is valid at February 20, 2001 at 08:45 UTC. The inset shows the zoomed in view of the volcanic cloud produced by an eruption of Mount Cleveland. This MODIS image was taken at night..... 58

Figure 4.3: A false color Terra MODIS image centered on the Aleutian Islands (Alaska) on February 19, 2001 at 23:10 UTC is shown. The  $12 - 11 \mu\text{m}$  brightness temperature difference (BTD) is displayed on the red color gun, the  $11 - 8.5 \mu\text{m}$  BTD is displayed on the green color gun, and the  $11 \mu\text{m}$  brightness temperature is displayed in the blue color gun. The scaling ranges used to make the image are shown in Table 4.4. The white annotations are used to highlight some important features. The volcanic ash and  $\text{SO}_2$  cloud was produced by an eruption of Mount Cleveland, Alaska. In the annotations, “meteo cloud” refers to liquid water or ice clouds generated by typical meteorological processes. This MODIS image was taken from the sunlit portion of the orbit. .... 60

Figure 4.4: Same as Figure 4.3 except the Terra MODIS image is valid at February 20, 2001 at 08:45 UTC. The inset shows the zoomed in view of the volcanic cloud produced by an eruption of Mount Cleveland. This MODIS image was taken at night..... 61

Figure 4.5: A “split-window” ( $11 - 12 \mu\text{m}$  brightness temperature difference) Terra MODIS image centered on the Aleutian Islands (Alaska) on February 19, 2001 at 23:10 UTC is shown. Yellow annotations are used to highlight certain key features including an ash cloud produced by an eruption of Mount Cleveland, Alaska. In the annotations, “meteo cloud” refers to liquid water or ice clouds generated by typical meteorological processes. This MODIS image was taken from the sunlit portion of the orbit. .... 63

Figure 4.6: Same as Figure 4.5 except the Terra MODIS image is valid at February 20, 2001 at 08:45 UTC. The inset shows the zoomed in view of the volcanic cloud produced by an eruption of Mount Cleveland. This MODIS image was taken at night..... 64

Figure 4.7: Images of the classifiers, used during typical sunlit conditions, by the Bayes approach that estimates the probability that a given satellite pixel contains volcanic ash and/or dust are shown. The parameters were computed for a Terra MODIS image from February 19, 2001 at 23:10 UTC. The approximate bounds of an ash cloud produced by an eruption of Mount Cleveland (Alaska) are overlaid on each image in white. A). Multispectral false color image. B).  $\beta_{\text{tot}}(12\mu\text{m}, 11\mu\text{m})$  overlaid on an 11  $\mu\text{m}$  brightness temperature (BT) image. C).  $\beta_{\text{opaque}}(12\mu\text{m}, 11\mu\text{m})$  overlaid on an 11  $\mu\text{m}$  BT image. D).  $\beta_{\text{tot}_{\sigma 8}}(12\mu\text{m}, 11\mu\text{m})$  overlaid on an 11  $\mu\text{m}$  BT image. E).  $\beta_{\text{tot}_{\sigma 7}}(12\mu\text{m}, 11\mu\text{m})$  overlaid on an 11  $\mu\text{m}$  BT image. F).  $\beta_{\text{tot}}(8.5\mu\text{m}, 11\mu\text{m})$  overlaid on an 11  $\mu\text{m}$  BT image. G).  $\beta_{\text{opaque}}(8.5\mu\text{m}, 11\mu\text{m})$  overlaid on an 11  $\mu\text{m}$  BT image. H).  $\beta_{\text{tot}}(7.3\mu\text{m}, 11\mu\text{m})$  overlaid on an 11  $\mu\text{m}$  BT image. I).  $\rho(3.9\mu\text{m}, 0.65\mu\text{m})$ . Only panels B through I are used as a classifier. Panel A is included to aid in scene interpretation. See text for additional details..... 70

Figure 4.8: Images of the classifiers, used at night, by the Bayes approach that estimates the probability that a given satellite pixel contains volcanic ash and/or dust are shown. The parameters were computed for a Terra MODIS image from February 20, 2001 at 08:45 UTC. The approximate bounds of an ash cloud produced by an eruption of Mount Cleveland (Alaska) are overlaid on each image in white. A). Multispectral false color image. B).  $\beta_{\text{tot}}(12\mu\text{m}, 11\mu\text{m})$  overlaid on an 11  $\mu\text{m}$  brightness temperature (BT) image. C).  $\beta_{\text{opaque}}(12\mu\text{m}, 11\mu\text{m})$  overlaid on an 11  $\mu\text{m}$  BT image. D).  $\beta_{\text{tot}_{\sigma 8}}(12\mu\text{m}, 11\mu\text{m})$  overlaid on an 11  $\mu\text{m}$  BT image. E).  $\beta_{\text{tot}_{\sigma 7}}(12\mu\text{m}, 11\mu\text{m})$  overlaid on an 11  $\mu\text{m}$  BT image. F).  $\beta_{\text{tot}}(8.5\mu\text{m}, 11\mu\text{m})$  overlaid on an 11  $\mu\text{m}$  BT image. G).  $\beta_{\text{opaque}}(8.5\mu\text{m}, 11\mu\text{m})$  overlaid on an 11  $\mu\text{m}$  BT image. H).  $\beta_{\text{tot}}(7.3\mu\text{m}, 11\mu\text{m})$  overlaid on an 11  $\mu\text{m}$  BT image. I).  $\epsilon_p(3.9\mu\text{m})$ . Only

panels B through I are used as a classifier. Panel A is included to aid in scene interpretation. See text for additional details. .... 71

Figure 4.9: The empirical relationship used to estimate the top of troposphere referenced 12/11  $\mu\text{m}$  effective absorption optical depth ratio [ $\beta_{\text{tot}}(12\mu\text{m}, 11\mu\text{m})$ ] from the clear minus observed 11 – 12  $\mu\text{m}$  brightness temperature difference (BTD) is shown. .... 80

Figure 4.10: A). Normalized distribution of the 11 – 12  $\mu\text{m}$  brightness temperature difference (BTD) of the data used to derive the ash/dust and the non-ash/dust class conditional probabilities, B). Same as panel A, except the distribution is not normalized and is shown using a log y-axis, C). Skill statistics of a simple threshold based 11 – 12  $\mu\text{m}$  BTD ash/dust detection approach, applied to the training data set, is plotted as a function of the chosen threshold (classify as ash/dust if 11-12  $\mu\text{m}$  BTD  $\leq$  threshold on x-axis). The probability of detection (red), false alarm rate (green), and critical success index (black) are shown. .... 83

Figure 4.11: The ratio of the ash/dust class conditional probability to the class conditional probability of all other features is shown as a function of various multivariate spectral classifiers for an open water surface. The cyan through red portion of the color scheme indicates that the class conditional probability of ash/dust is greater than the class conditional probability of all non-ash/dust features for that histogram bin. A).  $\beta_{\text{tot}}(12\mu\text{m}, 11\mu\text{m})$  vs.  $\rho(3.9\mu\text{m}, 0.65\mu\text{m})$  (daytime classifier), B).  $\beta_{\text{opaque}}(12\mu\text{m}, 11\mu\text{m})$  vs.  $\rho(3.9\mu\text{m}, 0.65\mu\text{m})$  (daytime classifier), C).  $\beta_{\text{tot}_{\sigma 8}}(12\mu\text{m}, 11\mu\text{m})$  vs.  $\rho(3.9\mu\text{m}, 0.65\mu\text{m})$  (daytime classifier), D).  $\beta_{\text{tot}_{\sigma 7}}(12\mu\text{m}, 11\mu\text{m})$  vs.  $\rho(3.9\mu\text{m}, 0.65\mu\text{m})$  (daytime classifier), E).  $\beta_{\text{tot}}(12\mu\text{m}, 11\mu\text{m})$  vs.  $\epsilon_p(3.9\mu\text{m})$  (nighttime classifier), F).  $\beta_{\text{opaque}}(12\mu\text{m}, 11\mu\text{m})$  vs.  $\epsilon_p(3.9\mu\text{m})$  (nighttime classifier), G).  $\beta_{\text{tot}_{\sigma 8}}(12\mu\text{m}, 11\mu\text{m})$  vs.  $\epsilon_p(3.9\mu\text{m})$  (nighttime classifier), H).  $\beta_{\text{tot}_{\sigma 7}}(12\mu\text{m}, 11\mu\text{m})$  vs.  $\epsilon_p(3.9\mu\text{m})$  (nighttime classifier), I).  $\beta_{\text{tot}}(12\mu\text{m}, 11\mu\text{m})$  vs.  $\beta_{\text{tot}}(8.5\mu\text{m}, 11\mu\text{m})$  (day and night classifier), J).  $\beta_{\text{opaque}}(12\mu\text{m}, 11\mu\text{m})$  vs.  $\beta_{\text{opaque}}(8.5\mu\text{m}, 11\mu\text{m})$  (day and night classifier), K).  $\beta_{\text{tot}}(12\mu\text{m}, 11\mu\text{m})$  vs.  $\beta_{\text{tot}}(7.3\mu\text{m}, 11\mu\text{m})$  (day and night classifier), L).  $\epsilon_{\text{tot}}(11\mu\text{m})$  vs.  $\beta_{\text{tot}}(12\mu\text{m}, 11\mu\text{m})$  (twilight classifier only), M).  $\epsilon_{\text{tot}}(11\mu\text{m})$  vs.  $\beta_{\text{opaque}}(12\mu\text{m}, 11\mu\text{m})$  (twilight classifier only), N).  $\epsilon_{\text{tot}}(11\mu\text{m})$  vs.  $\beta_{\text{tot}_{\sigma 8}}(12\mu\text{m}, 11\mu\text{m})$

(twilight classifier only), O).  $\epsilon_{\text{tot}}(11\mu\text{m})$  vs.  $\beta_{\text{tot}_{\sigma 7}}(12\mu\text{m}, 11\mu\text{m})$  (twilight classifier only). Panels A through K are valid for  $0.10 < \epsilon_{\text{tot}}(11\mu\text{m}) < 0.20$ . ..... 91

Figure 4.12: Same as Figure 4.11, except panels A through D are valid over all land surfaces excluding snow and ice and panel E through O are valid over all land surfaces including snow and ice. .... 92

Figure 4.13: Same as panels A through D in Figure 4.11 and Figure 4.12, except over snow and ice surfaces (including frozen water). .... 93

Figure 4.14: Analogous to Figure 4.11, Figure 4.12, and Figure 4.13 except the ash/dust to non-ash/dust conditional probability ratio for the BTD(11 – 12  $\mu\text{m}$ ) related classifiers are shown for a land surface with a clear sky 11  $\mu\text{m}$  brightness temperature  $> 270$  K. A). BTD(11 – 12  $\mu\text{m}$ ) vs.  $\rho(3.9\mu\text{m}, 0.65\mu\text{m})$  (daytime classifier), B). BTD(11 – 12  $\mu\text{m}$ ) vs.  $\epsilon_p(3.9\mu\text{m})$  (nighttime classifier), and C). BTD(11 – 12  $\mu\text{m}$ ) vs.  $\epsilon_{\text{tot}}(11\mu\text{m})$  (twilight classifier only). .... 94

Figure 4.15: The results of the Bayesian method are shown for a Terra MODIS image from February 19, 2001 at 23:10 UTC. A). 12-11  $\mu\text{m}$ , 11-8.5  $\mu\text{m}$ , and 11  $\mu\text{m}$  false color image. B). 12-11  $\mu\text{m}$ , 11-3.9  $\mu\text{m}$ , and 11  $\mu\text{m}$  false color image. C). 11  $\mu\text{m}$  image. D). Ash/dust probability image for 0.65, 3.9, 7.3, 8.5, 11, 12  $\mu\text{m}$  channel combination. E). Histogram of ash/dust probability inside (black) and outside (red) of manually analyzed ash/dust cloud. The panels in the third through fifth rows are analogous to the second row, except for the 0.65, 3.9, 8.5, 11, 12  $\mu\text{m}$ , 0.65, 3.9, 11, 12  $\mu\text{m}$ , and 11, 12  $\mu\text{m}$  channel combinations, respectively. The outer bounds of the manually defined ash/dust cloud are overlaid on each geo-referenced image. .... 99

Figure 4.16: Skill statistics of threshold based ash/dust detection, applied to several different metrics, are shown as a function of the selected threshold. The thresholds are relevant to the following metrics: 0.65, 3.9, 7.3, 8.5, 11, 12  $\mu\text{m}$  based probability (black), 0.65, 3.9, 8.5, 11, 12  $\mu\text{m}$  based probability (red), 0.65, 3.9, 11, 12  $\mu\text{m}$  based probability (blue), 11, 12  $\mu\text{m}$  based probability (green), and BTD(11-12  $\mu\text{m}$ ). The statistics are valid for a 5-minute MODIS granule with a starting time of February

19, 2001 at 23:10 UTC. The bottom x-axis is BTD(11-12 $\mu$ m) and the top x-axis is ash/dust probability. The critical success index (CSI) (A), probability of detection (B), and false alarm rate (C) are shown. The circles denote the threshold where the CSI is a maximum. .... 100

Figure 4.17: Same as Figure 4.15 except for a Terra MODIS image from February 20, 2001 at 08:45 UTC. Since this is a nighttime scene the 0.65  $\mu$ m channel is not utilized. .... 102

Figure 4.18: Same as Figure 4.16 except the statistics are valid for a 5 minute Terra MODIS granule with a starting time of February 20, 2001 at 08:45 UTC. .... 103

Figure 4.19: Same as Figure 4.15 except for an Aqua MODIS image from July 29, 2012 at 17:35 UTC. .... 106

Figure 4.20: Same as Figure 4.16 except the statistics are valid for a 5 minute Aqua MODIS granule with a starting time of July 29, 2012 at 17:35 UTC. .... 107

Figure 4.21: Same as Figure 4.15 except for a Terra MODIS image from January 24, 2014 at 03:55 UTC. Since this is a nighttime scene the 0.65  $\mu$ m channel is not utilized. .... 109

Figure 4.22: Same as Figure 4.16 except the statistics are valid for a 5 minute Terra MODIS granule with a starting time of January 24, 2014 at 03:55 UTC. .... 110

Figure 5.1: The black triangles show the 13.3/11  $\mu$ m scaled extinction ratio ( $\beta_{\text{theo}}(13.3/11 \mu\text{m})$ ) as a function of the 12/11  $\mu$ m scaled extinction ratio ( $\beta_{\text{theo}}(12/11 \mu\text{m})$ ) for 4 different rock types over a range of effective radii (1 – 15  $\mu$ m). A fourth order polynomial fit is shown in red. The numbers adjacent to the triangles indicate the effective radius in  $\mu$ m. Andesite, rhyolite, kaolinite, and gypsum are shown in panels a-d, respectively.  $\beta_{\text{theo}}(12/11 \mu\text{m})$  and  $\beta_{\text{theo}}(13.3/11 \mu\text{m})$  were derived from the single scatter properties as described in the text. .... 129

- Figure 5.2: The same as Figure 5.1 except the effective particle radius ( $r_{\text{eff}}$ ) is shown as a function of  $\beta_{\text{theo}}(12/11 \mu\text{m})$ . ..... 130
- Figure 5.3: The same as Figure 5.1 except the extinction cross section ( $\sigma_{\text{ext}}$ ) is shown as a function of  $\beta_{\text{theo}}(12/11 \mu\text{m})$ . ..... 131
- Figure 5.4: SEVIRI images from 0400 UTC on May 8, 2010. (a) Dust RGB image. (b) “Split-window” imagery. (c) 11  $\mu\text{m}$  imagery. (d) Retrieved effective cloud temperature. (e) Retrieved effective cloud emissivity. (f) Retrieved 12/11  $\mu\text{m}$  effective optical depth ratio. (g) Retrieved effective cloud temperature uncertainty ratio. (h) Retrieved effective cloud emissivity uncertainty ratio. (i) Retrieved 12/11  $\mu\text{m}$  effective optical depth ratio uncertainty ratio. The black solid line through the cloud represents a CALIPSO overpass. The andesite rock type was used to generate these results. .... 135
- Figure 5.5: SEVIRI images from 0400 UTC on May 8, 2010. (a-c) Retrieved effective cloud height as a function of rock type (andesite, rhyolite, and kaolinite, respectively). (d-f) Retrieved cloud mass loading as a function of rock type (andesite, rhyolite, and kaolinite, respectively). (g-i) Retrieved cloud effective radius as a function of rock type (andesite, rhyolite, and kaolinite, respectively). The black solid line through the cloud represents a CALIPSO overpass. .... 136
- Figure 5.6: A CALIOP 532 nm total attenuated backscatter cross-section from 04:01:59 UTC – 04:05:04 UTC on May 8, 2012. The cross section is shown with (bottom) and without (top) the retrieved SEVIRI cloud heights (as a function of the assumed rock type) overlaid. Magenta circles represent andesite. White circles denote rhyolite. Gray circles represent kaolinite. In both panels, the solid black line denotes the tropopause and the dashed black lines represent select atmospheric isotherms (in Kelvin). .... 137
- Figure 5.7: Same as Figure 5.4 except for the eastern Caribbean on 0530 UTC on February 12, 2010. The andesite rock type was used to generate these results. .... 140

- Figure 5.8: Same as Figure 5.5 except for the eastern Caribbean on 0530 UTC on February 12, 2010. .... 141
- Figure 5.9: Same as Figure 5.6 except for 05:34:04 UTC – 05:34:42 UTC on February 12, 2010..... 142
- Figure 5.10: Same as Figure 5.4 except for a dust outbreak near the west coast of Africa on 0245 UTC on June 22, 2007. The kaolinite rock type was used to generate these results. .... 145
- Figure 5.11: SEVIRI images near the west coast of Africa on 0245 UTC on June 22, 2007. (a-c) Retrieved effective cloud height as a function of rock type (kaolinite, gypsum, and andesite, respectively). (d-f) Retrieved cloud mass loading as a function of rock type (kaolinite, gypsum, and andesite, respectively). (g-i) Retrieved cloud effective radius as a function of rock type (kaolinite, gypsum, and andesite, respectively). The black solid line through the cloud represents a CALIPSO overpass. .... 146
- Figure 5.12: Same as Figure 5.6 except for 02:51:38 UTC – 02:53:40 UTC on June 22, 2007. Unlike Figure 5.6, magenta circles represent kaolinite, white circles denote gypsum and gray circles represent andesite. .... 147
- Figure 5.13: A comparison of SEVIRI ash cloud heights retrieved using the GOES-R approach and CALIOP measured cloud top heights is shown as a function of the nadir 11  $\mu\text{m}$  cloud emissivity derived from a combination of CALIOP and SEVIRI (first column) and the cloud geometric thickness given by CALIOP (second column). Each color represents a different 11- $\mu\text{m}$  cloud emissivity or cloud thickness bin. The results are also shown as a function of the rock type assumed by the retrieval (top=andesite, middle=rhyolite, bottom=kaolinite). The 1:1 line is shown in black. A total of 796 data points were used in this analysis. .... 152
- Figure 5.14: A comparison of SEVIRI ash cloud emissivity retrieved using the GOES-R approach and the 11  $\mu\text{m}$  cloud emissivity derived from a combination of CALIOP and SEVIRI are shown as a function of the CALIOP measured cloud top height (first column) and the cloud geometric thickness given by CALIOP (second column).

Each color represents a different cloud top height or cloud thickness bin. The results are also shown as a function of the rock type assumed by the retrieval (top=andesite, middle=rhyolite, bottom=kaolinite). The 1:1 line is shown in black. A total of 796 data points were used in this analysis..... 153

Figure 5.15: A comparison of SEVIRI ash 12/11  $\mu\text{m}$   $\beta$ -ratios retrieved using the GOES-R approach and the 12/11  $\mu\text{m}$   $\beta$ -ratios computed using a combination of CALIOP and SEVIRI is shown as a function of the cloud top height measured by CALIOP (first column) and the nadir 11  $\mu\text{m}$  cloud emissivity derived from a combination of CALIOP and SEVIRI (second column). Each color represents a different cloud top height or 11- $\mu\text{m}$  cloud emissivity bin. The results are also shown as a function of the rock type assumed by the retrieval (top=andesite, middle=rhyolite, bottom=kaolinite). The 1:1 line is shown in black. A total of 796 data points were used in this analysis..... 154

Figure 5.16: A comparison of SEVIRI ash mass loading retrieved using the GOES-R approach and the ash mass loading computed using a combination of CALIOP and SEVIRI is shown as a function of the cloud top height measured by CALIOP (first column) and the nadir 11  $\mu\text{m}$  cloud emissivity derived from a combination of CALIOP and SEVIRI (second column). Each color represents a different cloud top height or 11- $\mu\text{m}$  cloud emissivity bin. The results are also shown as a function of the rock type assumed by the retrieval (top=andesite, middle=rhyolite, bottom=kaolinite). The 1:1 line is shown in black. A total of 796 data points were used in this analysis..... 155

Figure 6.1: Images of the primary metrics utilized to construct cloud objects and apply a binary ash/dust classifier to each cloud object are shown. All parameters were derived from a Terra MODIS image from February 20, 2001 at 08:45 UTC. The approximate visual bounds of a volcanic ash cloud produced by an eruption of Mount Cleveland (Alaska) are overlaid on each image in white. A). 12-11 $\mu\text{m}$ , 11-8.5 $\mu\text{m}$ , and 11 $\mu\text{m}$  false color image. B). 12-11 $\mu\text{m}$ , 11-3.9 $\mu\text{m}$ , and 11 $\mu\text{m}$  false color image. C). Image of BTD(11-12 $\mu\text{m}$ ). D). Ash/dust pixel

probability image. E). Median ash/dust probability of pixels that compose each cloud object. F). The probability that the cloud object is part of a volcanic ash/dust cloud. G). The fraction of cloud object pixels that have a spectrally robust ash/dust signature using the most strict definition of spectral robustness. H). The fraction of cloud object pixels that have a spectrally robust ash/dust signature using the second most strict definition of spectral robustness. I). The fraction of cloud object pixels that have a spectrally robust ash/dust signature using the third strictest definition of spectral robustness. In Panels D-I the 11  $\mu\text{m}$  brightness temperature image is shown when the variable of interest is invalid. Two objects of interest are labeled “1” and “2” in Panel F. The 3.9, 7.3, 8.5, 11, and 12  $\mu\text{m}$  channels were used to generate these results. .... 168

Figure 6.2: The procedure used to determine the probability that a cloud object is part of a volcanic ash or dust cloud is illustrated. Each panel represents a different method for quantifying the spectral states within a cloud object (see panel titles for spectral state definition). The ten most common spectral states (for a given definition) within the cloud object labeled “1” in Figure 6.1F are denoted by the colored bars. The magnitude of the bar is representative of the area within the cloud object that exhibits a given spectral state (the area is shown on the y-axis on the left). The bar color represents the ratio of the ash/dust conditional probability to the non-ash/dust conditional probability, where the cyan to red color range indicates that the ash/dust conditional probability is greater than or equal to the non-ash/dust conditional probability. The specific parameters that define each spectral state are also labeled at the bottom of each bar. Finally, the box-and-whisker plot of the pixel ash/dust probability distribution within a given spectral state in the cloud object is overlaid in black and referenced to the y-axis on the right of each panel. The dotted and dashed horizontal gray lines indicate a pixel probability value of 1% and 50%, respectively. .... 175

Figure 6.3: Same as Figure 6.2, except for the cloud object labeled with a “2” in Figure 6.1F. Less than 10 spectral states were found in object “2,” regardless of the mechanism for defining spectral state. .... 176

Figure 6.4: The results of the SECO volcanic ash and dust detection algorithm are shown for a Terra MODIS image from February 20, 2001 at 08:45 UTC. A). 12-11  $\mu\text{m}$ , 11-8.5  $\mu\text{m}$ , and 11  $\mu\text{m}$  false color image. B). 12-11  $\mu\text{m}$ , 11-3.9  $\mu\text{m}$ , and 11  $\mu\text{m}$  false color image. C). Image of BTD(11-12 $\mu\text{m}$ ). D). Ash/dust pixel probability image for 0.65, 3.9, 7.3, 8.5, 11, 12  $\mu\text{m}$  channel combination. E). The SECO algorithm skill (blue bars) measured against manual analysis of multi-spectral imagery is expressed as the Critical Success Index (CSI), Probability of Detection (POD), and False Alarm Rate (FAR). The skill of the traditional “split-window” method using the BTD(11-12 $\mu\text{m}$ ) threshold that produces the greatest CSI for this particular scene is also shown (red bars). The panels in the third through fifth rows are analogous to the second row, except for the 3.9, 8.5, 11, 12  $\mu\text{m}$ , 3.9, 11, 12  $\mu\text{m}$ , and 11, 12  $\mu\text{m}$  channel combinations, respectively. The outer bounds of the manually defined ash/dust cloud are overlaid on each geo-referenced image..... 185

Figure 6.5: Same as Figure 6.1, except only the 11 and 12  $\mu\text{m}$  channels were used to generate these results..... 187

Figure 6.6: Same as Figure 6.4, except the results are shown for a sunlit (the 0.65  $\mu\text{m}$  channel is used) Terra MODIS image from February 19, 2001 at 23:10..... 189

Figure 6.7: Same as Figure 6.4, except the results are shown for a sunlit (the 0.65  $\mu\text{m}$  channel is used) Aqua MODIS image from July 29, 2012 at 17:35. .... 191

Figure 6.8: Same as Figure 6.4, except the results are shown for a Terra MODIS image from January 24, 2014 at 03:55..... 193

Figure 6.9: False color imagery constructed from the 12-11, 11-8.5, 11 $\mu\text{m}$  channel combination (top), 11-12 $\mu\text{m}$  “split-window” imagery (middle), and the results of the SECO ash/dust detection algorithm using the 0.65, 3.9, 7.3, 8.5, 11, and 12  $\mu\text{m}$  channel combination are shown for all Aqua MODIS ascending (afternoon) node overpasses on January 26, 2011. The SECO results are displayed by overlaying the pixel-level probability of ash/dust over the 11  $\mu\text{m}$  brightness temperature image in locations where the SECO algorithm detected ash or dust. .... 196

- Figure 6.10: Volcanic ash plumes produced by eruptions of Kizimen and Karymsky on the Kamchatka Peninsula (Russia), which were captured by Aqua MODIS on January 26, 2011 (02:05 UTC), are examined in greater detail. A). The 12-11, 11-8.5, 11 $\mu$ m false color image. B). The 12-11, 11-3.9, 11 $\mu$ m false color image. C). The 11-12 $\mu$ m “split-window” brightness temperature difference. D). The median cloud object probability from the 0.65, 3.9, 7.3, 8.5, 11, and 12  $\mu$ m implementation of the SECO algorithm overlaid on the corresponding 11  $\mu$ m brightness image..... 197
- Figure 6.11: Same as Figure 6.9 except for all descending (overnight) Aqua MODIS overpasses on January 26, 2011. .... 199
- Figure 6.12: Volcanic ash produced by a minor emission from Sakurajima and a more significant emission from Shinmoe-dake in Japan, which was captured by Aqua MODIS on January 26, 2011 (17:20 UTC), are examined in greater detail. A). The 12-11, 11-8.5, 11 $\mu$ m false color image. B). The 12-11, 11-3.9, 11 $\mu$ m false color image. C). The 11-12 $\mu$ m “split-window” brightness temperature difference. D). Volcanic ash detected by the 3.9, 7.3, 8.5, 11, and 12  $\mu$ m implementation of the SECO algorithm is denoted by valid values of pixel-level ash/dust probability in lieu of the 11  $\mu$ m brightness temperature value. .... 200
- Figure 6.13: Same as Figure 6.10, except for the January 26, 2011 15:35 UTC Aqua MODIS overpass. .... 201
- Figure 6.14: SECO and “split-window” algorithm performance statistics (CSI, POD, FAR) measured against manual analysis of multi-spectral imagery for an entire day of Aqua MODIS overpasses on January 26, 2011. Only MODIS granules that likely contain diffuse dust clouds with ill-defined edges are excluded. The SECO results, using the 0.65, 3.8, 7.3, 8.5, 11, and 12  $\mu$ m channel combination, are shown in blue and the “split-window” results obtained using the BTD(11-12 $\mu$ m) threshold that produced the greatest CSI for this particular day of data are shown in red. .... 202

Figure 7.1:Top: Map showing the location of Kasatochi Island (Source: AVO/ADGGS).  
Bottom: Aerial photo of Kasatochi Island on December 5, 2013 (Source: Richard Zimmer)..... 205

Figure 7.2:GOES-11 visible satellite images capturing the three explosive events during the August 7-8, 2008 eruption of Kasatochi. The cloud produced by Event 1 is shown at 23:30 UTC on 7 August (top left). The cloud produced by Event 2 is shown at 02:00 UTC and 02:30 UTC on 8 August (top right and bottom left, respectively). The cloud produced by Event 3 is shown at 05:00 UTC on 8 August. The clouds of interest are located in the center of each image. Source: CIMSS Satellite Blog..... 207

Figure 7.3:A comparison between the retrieved ash mass loading (top right) and the corresponding true color imagery (bottom) for a 9 August 2008 Aqua MODIS overpass (at 00:50 UTC) with Kasatochi volcanic ash is shown. Infrared-based false color imagery is also shown in the top left panel. The true color imagery was obtained from NASA. .... 210

Figure 7.4:Volcanic ash cloud properties as derived from an Aqua MODIS overpass on August 12, 2008 at 08:20 UTC. A false 12-11 $\mu$ m, 11-8.5 $\mu$ m, 11 $\mu$ m false color image (top left), ash cloud height (top right), ash effective particle radius (bottom left), and ash mass loading (bottom right) are shown. .... 212

Figure 7.5: Volcanic ash cloud properties as derived from an Aqua MODIS overpass on August 10, 2008 at 21:25 UTC. A false 12-11 $\mu$ m, 11-8.5 $\mu$ m, 11 $\mu$ m false color image (top left), ash cloud height (top right), ash effective particle radius (bottom left), and ash mass loading (bottom right) are shown. The approximate location of a 757 encounter with volcanic ash at 01:00 UTC on 11 August 2008 is denoted by the white square..... 214

Figure 7.6: HSRL aerosol backscatter cross section (top) and particulate circular depolarization ratio (bottom) from 0-12 UTC on 13 August 2008 in Madison, WI. Clouds produced by the eruption of Kasatochi volcano were definitively observed

- by the HSRL above 11 km ASL between 5-6 UTC and 7-8 UTC. The black region just after 9 UTC indicates missing data. ....217
- Figure 7.7: HSRL aerosol backscatter cross section (top) and particulate circular depolarization ratio (bottom) from August 15-31, 2008 in Madison, WI. Clouds produced by the eruption of Kasatochi volcano were definitively observed by the HSRL above 11 km ASL between August 15-19 and August 22-31.....219
- Figure 7.8: The CALIOP depolarization ratio from August 16, 2008 at 07:54-08:08 UTC (top) and August 28, 2008 at 08:18-08:31 UTC (bottom) is shown. Kasatochi clouds within 200 km of Madison, WI were sampled by CALIOP. In the top figure the Kasatochi cloud of interest is located above 11 km ASL and is centered on  $41.19^\circ$  latitude,  $-86.64^\circ$  longitude. In the bottom figure the Kasatochi cloud of interest is the sole identifiable feature above 17 km ASL.....221
- Figure 7.9: Composite maps of 12-11 $\mu$ m, 11-8.5  $\mu$ m, 11  $\mu$ m false color imagery (left column) and volcanic ash mass loading (right column) from three different Aqua MODIS overpasses. The 8 August 2008 AM overpasses (top), 8 August 2008 PM overpasses (middle), and 9 August AM overpasses (bottom) are shown. The ash mass loading is overlaid on 11  $\mu$ m brightness temperature imagery. ....225
- Figure 7.10: Composite maps of 12-11 $\mu$ m, 11-8.5  $\mu$ m, 11  $\mu$ m false color imagery (left column) and volcanic ash mass loading (right column) from three different Aqua MODIS overpasses. The 9 August 2008 PM overpasses (top), 10 August 2008 AM overpasses (middle), and 11 August AM overpasses (bottom) are shown. The ash mass loading is overlaid on 11  $\mu$ m brightness temperature imagery. ....226
- Figure 7.11: Same as Figure 7.9 except the retrieved ash cloud height is shown in the right column.....227
- Figure 7.12: Same as Figure 7.10 except the retrieved ash cloud height is shown in the right column. ....228

Figure 7.13: The total mass and area of airborne volcanic ash are shown as a function of the time since the third and final explosive event observed during the August 7-8, 2008 eruption of Kasatochi volcano. The total mass estimated using the methods described in this dissertation (black), the total mass reported by Corradini et al. [2010] (green), the total mass reported by Prata et al. [2010] (blue), and the total ash cloud area (red) are shown. .... 229

Figure 7.14: The 25<sup>th</sup> (red), 50<sup>th</sup> (black), and 75<sup>th</sup> (blue) percentiles of ash mass loading (top), effective particle radius (middle), and cloud top height (bottom) are shown as a function of time since the start of the third explosive event from the 2008 Eruption of Kasatochi. The interquartile range of cloud top height (brown) is also shown in the bottom panel. .... 233

Figure 7.15: The CALIOP-derived distribution of geometric ash cloud thickness is shown for Eyjafjallajökull observations (top) and observations of additional ash clouds produced by a variety of eruptions including Cordon Caulle (2011), Grimsvotn (2011), Kasatochi (2008), Okmok (2008), Soufriere Hills (2010), and Redoubt (2009) (bottom). The distribution shown in the top panel indicates that 75% of the ash layers sampled by CALIOP are less than 1 km thick. Similarly, the bottom panel distribution indicates that 73% of ash layers sampled are less than 1 km thick. The majority of the ash layers sampled were well dispersed from the volcano..... 236

## Chapter 1

### 1. Introduction

Volcanic eruptions are one of the most spectacular, but understandably most feared, natural phenomena; capable of altering global climate and producing an array of hazards that span many spatial and temporal scales. Eruption styles vary greatly, from effusion of lava (e.g. Kilauea in Hawaii) to highly explosive pyroclast<sup>1</sup> producing eruptions (e.g. 1980 Mount St. Helens). The hazards produced by a volcanic eruption and the instruments and methods used to observe an eruption largely depend on the eruption style and explosiveness. Explosive eruptions have the potential to produce far-reaching hazards.

Volcanic ash is a sub-class of pyroclasts that includes all volcanic rock fragments that are less than 2 mm in diameter. Fine-grained ash from explosive eruptions can be transported long distances (>1000 km) from the source volcano by atmospheric winds, creating a large-scale aviation hazard<sup>2</sup>. Given the large-scale nature of volcanic ash clouds, scientists primarily use satellites to track and study them. Non-satellite based observations of volcanic ash clouds are quite rare.

Volcanic ash clouds are complex and the background environment in which they reside can be as well. Thus, volcanic ash cloud remote sensing is a very challenging problem. Due to the challenging nature of the problem, scientists frequently employ several simplifying assumptions that limit the extent to which satellite measurements are utilized in furthering the understanding of volcanic ash clouds. For instance, the

---

<sup>1</sup> Volcanic rock and lava propelled into the air by eruptive forces, independent of size

<sup>2</sup> Flying through a volcanic ash cloud can cause severe damage to aircraft

atmosphere is often assumed to be void of constituents, such as water vapor and underlying liquid water or ice clouds, as they complicate the interpretation of the satellite measurements. In addition, quantitative information on the properties of thick vertical columns of volcanic ash, common in the early stages of an eruption, is scarce. Due to limitations of remote sensing techniques, satellites best observe volcanic ash clouds, in a quantitative manner, during the middle third of their observable residence time in the atmosphere. The observable residence time typically ranges from hours to about 10 days. As such, volcanic ash cloud properties are not well observed in many instances. More robust globally applicable satellite remote sensing algorithms are needed to address this observational gap.

In this dissertation, new globally applicable methods are developed to objectively identify volcanic ash and retrieve ash cloud properties from geostationary and low earth orbit meteorological satellites. In Chapter 2, the importance of improving the understanding of volcanic ash clouds is discussed and a review of various existing methods of observing volcanic ash clouds is given. At the end of Chapter 2, the objectives of this research effort are stated. A new framework for utilizing infrared measurements to infer cloud composition is presented in Chapter 3. Chapter 4 demonstrates that infrared observations, cast into the framework developed in Chapter 3, along with visible and near-infrared measurements are useful for determining the probability that volcanic ash is present in a given satellite pixel. In Chapter 5, a method for retrieving volcanic ash cloud properties (height, mass loading, and effective particle radius) from infrared measurements is presented. The volcanic ash probability results discussed in Chapter 4 are used to determine when the ash cloud property retrieval should

be performed. In Chapter 6, the results from Chapters 3-5 are used to develop a cloud object based approach to volcanic ash detection. Using the techniques described in Chapters 3-6, an analysis of volcanic ash cloud properties for a selected case is presented in Chapter 7. The final chapter of the dissertation (Chapter 8) contains a summary of the research methods and results, impacts, and the prospects for using the new approaches going forward.

## Chapter 2

### 2. Background and Motivation

Gaseous and particulate clouds produced by volcanic eruptions impact the Earth-Atmosphere system in several ways. For instance, a major volcanic eruption that injects sulfur gases into the stratosphere will cause the stratosphere to warm (while the surface cools) and enhance stratospheric ozone destruction in the months to years following the eruption [Robock 2000]. Further, the deposition of volcanic ash onto the ocean surface may play a significant but currently poorly understood role in the biogeochemical iron-cycle [Duggen et al. 2010]. Volcanic ash particles can also serve as cloud condensation and ice nuclei, and thus may naturally seed (or even over-seed) clouds [Durant et al. 2008]. Ash clouds from volcanic eruptions also pose a major risk to human health (e.g. Horwell and Baxter [2006]) and aviation [Casadevall 1994; Guffanti et al. 2010a]. While all of the impacts of volcanic clouds (climate, biogeochemical, weather modification, human health) are important, the primary motivation of the scientific research presented in this dissertation is to reduce the probability of catastrophic aircraft encounters with clouds that contain volcanic ash and enhance the economic resilience to aviation disruptions caused by volcanic eruptions.

Even though the aviation impacts of volcanic ash clouds have only recently gained widespread public attention due to the April/May 2010 eruption of Eyjafjallajökull in Iceland, airborne volcanic ash has been considered a major aviation hazard since 1982 when a British Airways Boeing 747 aircraft lost power to all four engines after flying into a volcanic ash cloud in Indonesia [Miller and Casadevall 2000]. A similar incident occurred in 1989 when KLM Flight-867 lost power to all four engines

after encountering an ash cloud outside of Anchorage, AK [Casadevall 1994]. Fortunately, the pilots of the British Airways and KLM flights narrowly avoided disaster after restarting some or all of the engines upon descending thousands of feet (without power) and out of the airspace heavily contaminated by volcanic ash. From 1959-2009 there have been 94 confirmed aircraft encounters with volcanic ash clouds, where 79 of those encounters resulted in airframe or engine damage and 9 of the encounters resulted in the loss of one or more engines in flight [Guffanti et al. 2010a]. Guffanti et al. [2010a] state that since 1976, when reporting of encounters became more common practice, an average of about 2 encounters per year have occurred. In addition, many of the reported encounters occurred more than 1000 km from the parent volcano. Even volcanic ash produced by relatively weak volcanic activity can pose a significant hazard to aviation if the volcano is located near an airport. For instance, aircraft descending into or climbing out of Kagoshima airport in Japan always need to be wary of low-level ash clouds from the nearby Sakurajima volcano [Onodera and Kamo 1994]. Volcanic ash clouds can damage aircraft in the following ways [ICAO 2007]:

- The melting temperature of volcanic ash ( $\sim 1100^{\circ}\text{C}$ ) is such that when ingested into jet engines it melts in the combustion chamber, cools down in the turbine, and deposits on the turbine vanes, which restricts the flow of high-pressure combustion gases. In the worst case scenario in-flight engine failure occurs.
- Volcanic ash is very abrasive and can sand blast cockpit windows, airframes, and flight surfaces. It can also erode the turbines.
- Volcanic ash can clog the pitot-static system, rendering airspeed measurements inaccurate.

- Ingestion of volcanic ash into air conditioning and cooling systems leads to contamination of the electrical and avionics units, fuel and hydraulic systems, and cargo-hold smoke detection systems.

The economic impacts of airborne volcanic ash are also significant. For instance, the April and May 2010 eruptions of Eyjafjallajökull [Gudmundsson et al. 2010] in Iceland had an unprecedented impact on aviation in the North Atlantic and Europe, causing over 100,000 flights, corresponding to about 50% of the world's air traffic, to be canceled; the economic impact of which is in the billions of dollars [Oxford Economics 2010]. High impact eruptions also occur in or near North American airspace. The eruption of Mount Redoubt, Alaska in March and April 2009 resulted in the cancellation of hundreds of passenger and cargo flights into and out of Anchorage [Tony Hall, National Weather Service, personal comm.]. The 2008 eruptions of Okmok and



*Figure 2.1: Major commercial flight routes (blue), historically active volcanoes (red), and the area of responsibility of each Volcanic Ash Advisory Center (VAAC) are overlaid on a global map. Source: ICAO*

Kasatochi in Alaska also significantly impacted United States airspace in the North Pacific [Guffanti et al., 2010b]. Accurate information on the location of volcanic ash in the atmosphere is critical for minimizing economic losses. On average, 50 – 60 volcanoes erupt per year (eruptions can last

anywhere from hours to years), 10 or more of which will produce a volcanic cloud that reaches jet aircraft cruising altitudes [ICAO, 2007]. Further, Figure 2.1 illustrates that global flight routes are often near volcanoes, making timely identification of dangerous ash clouds critical, especially given that volcanic ash clouds can reach jet aircraft cruising altitudes in as little as 5 minutes [ICAO 2007].

Volcanic cloud properties and the associated impacts on aviation largely depend on the attributes of the parent eruption and atmospheric conditions. Volcanic eruptions occur when magma in the Earth's crust ascends to the surface through fissures and cracks, exiting the sub-surface through vents. Magma is composed of silicate melt (silicon, oxygen, aluminum, sodium, potassium, calcium, magnesium, and iron), crystallized minerals, and volatiles ( $H_2O$ ,  $CO_2$ ,  $H_2S$ , and  $SO_2$ ) [Scaillet et al. 2013]. Explosive volcanic eruptions are often associated with highly silicic magmas, which have a greater viscosity than magmas with lower silicon content. The energy required to exsolve volatiles from high viscosity magmas prevents volatiles from boiling out of the molten rock in a gradual manner, allowing the vapor pressure of the volatile component of the magma to build until it exceeds the ambient pressure (assuming the high viscosity magma contains a sufficient amount of volatiles). The rapid decompression of volatile bubbles and gas expansion produces the energy required for an explosive volcanic eruption. Magma interactions with external sub-surface water sources and the attributes of the cracks and fissures, through which the magma is ascending, also influence the eruption characteristics. When an explosive eruption occurs, the silicate melt cools rapidly in the atmosphere forming volcanic glass, which fragments to form pyroclasts. Volcanic ash is

defined as pyroclasts with a diameter of 2 mm or less. A more detailed review of volcanic processes is given in Scaillet et al. [2013].

Vulcanologists assign a Volcanic Explosivity Index (VEI) to each volcanic eruption using very rough estimates of the total volume of erupted tephra (pyroclasts that

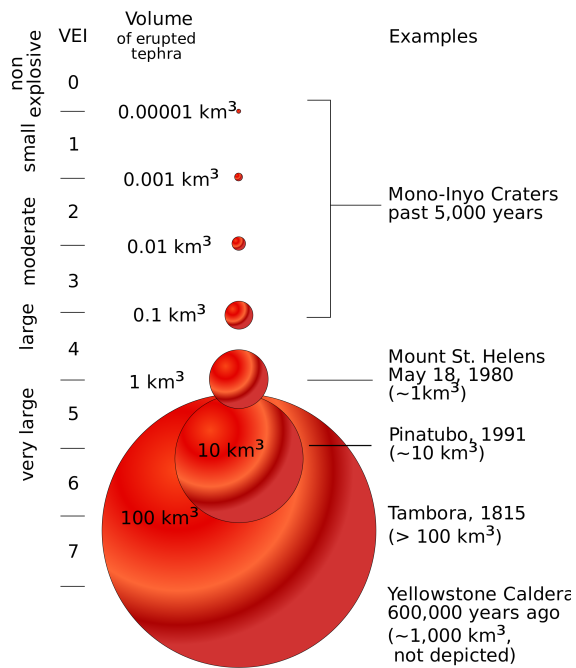


*Figure 2.2: Graphic illustration of the Volcanic Explosivity Index (VEI). A red sphere representing the highest VEI category, 8, is not shown for clarity. Source: USGS*

fall to the ground), the height of the eruptive column, and the duration of the explosive portion of the eruption [Newhall and Self 1982]. As shown in

Figure 2.2, the VEI of an eruption can range from 0 for effusive (non-explosive) lava producing eruptions such as Kilauea to 8 for “apocalyptic” eruptions such as a caldera forming eruption of Yellowstone [Simkin and Siebert 1994]. Eruptions

classified as VEI=2 or greater are considered explosive and as such produce volcanic clouds that are a concern to aviation [Simkin and Siebert 1994].

Clouds produced by volcanic eruptions are primarily composed of pyroclasts, volcanic gases, and, depending on the nature of the eruption and atmospheric conditions, liquid water and ice [Rose et al. 2000]. While larger pyroclasts fall out of the eruptive cloud rather quickly [Ernst et al. 1996], volcanic ash sized particles can remain suspended in the atmosphere much longer (days to weeks, with longer atmospheric

residence times possible) [Rose 1993]. The fate of ash in the atmosphere largely depends on the properties of the cloud (e.g. height, particle size distribution, and mass concentration) and atmospheric conditions (e.g. 3-dimensional fields of water - in all phases, temperature, horizontal wind, and vertical wind). Models that forecast volcanic ash dispersion and removal are prone to large errors [e.g. Schumann et al. 2011] and many questions regarding dispersion and removal processes remain [Rose and Durant 2011].

Scientists utilize a variety of measurement platforms to study volcanic ash clouds. For instance, ground-based radars provide useful information on the properties and dynamics within a thick eruptive column [Harris and Rose 1983; Lacasse et al. 2004; Tupper et al. 2005; Marzano et al. 2006a; Marzano et al. 2006b; Marzano et al. 2010; Schneider and Hoblitt, 2012]. Unfortunately, most volcanoes are well outside of radar coverage. Ground-based lidars [Pappalardo et al. 2004; Ansmann et al. 2010; Gasteiger et al. 2011] and sun photometers [Ansmann et al. 2010; Gasteiger et al. 2011] can also provide information on ash cloud properties in the rare event that an ash cloud is present within the field of view of these instruments. Infrared cameras have also been used to estimate ash cloud properties during a few dedicated field campaigns [Prata and Benardo 2009]. Due to the high impact nature of the 2010 eruption of Eyjafjallajökull, resources were provided to European research groups to deploy instrumented (non-jet) aircraft to take remote and in-situ measurements of ash cloud properties over Europe and the North Atlantic [Johnson et al. 2012; Marengo et al. 2011; Schumann et al. 2011; Bukowiecki et al. 2011; Newman et al. 2012; Turnbull et al. 2012]. In addition Hobbs et al. [1982] and Hobbs et al. [1991] collected airborne samples of volcanic ash clouds during the 1980

eruption of Mount St. Helens and the 1990 eruption of Redoubt in Alaska, respectively. Unfortunately, airborne measurements are expensive and risky, and hence rare. The primary tool utilized in both practical and research applications related to volcanic ash are satellites [Prata 2009]. The combination of the inability to predict when and where an eruption will occur, the remote location of many volcanoes, and the large horizontal dimension of dispersed ash clouds is why satellites are the primary tool for identifying, tracking, and studying volcanic ash clouds. In addition, approximately 90% of the world's volcanoes are not regularly monitored for activity [Ph. Bally Ed. 2012], therefore satellites often provide the only means to detect eruptive activity in a timely manner, which is critical for aviation.

Sawada [1987] was the first scientist to identify and track volcanic ash clouds in satellite imagery for a large number of cases in a systematic manner. Sawada's method, however, relied heavily on manual analysis of geostationary satellite imagery. Prior to Sawada [1987], the use of satellite data to study volcanic ash clouds was limited to a few case studies where it was used in a generally qualitative manner [Hanstrum and Watson 1983; Malingreau and Kaswanda 1986]. The first quantitative method for detecting volcanic ash from satellites was pioneered by Prata [1989a; 1989b]. Prata's method is known as the "reverse absorption" or "split-window" technique. In the "split-window" technique, bi-spectral measurements are used to exploit a composition dependent reversal in the sign of the slope of cloud absorptivity (or emissivity) between 10 and 12  $\mu\text{m}$  in the so-called "infrared atmospheric window," where water vapor absorption is less pronounced. The traditional "split-window" method consists of computing the difference in brightness temperature between measurements taken at approximately 11 and 12  $\mu\text{m}$

and applying a threshold. “Split-window” measurements are available on nearly every low earth orbit and geostationary meteorological satellite sensor.

Due to its silca ( $\text{SiO}_2$ ) content, volcanic ash typically absorbs, and hence emits, more radiation at  $11\ \mu\text{m}$  than  $12\ \mu\text{m}$ , resulting in a split-window brightness temperature

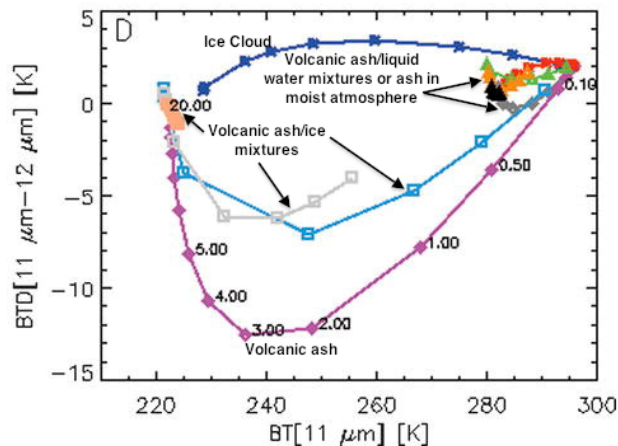


Figure 2.3: Radiative transfer model calculations of the  $11\ \mu\text{m}$  brightness temperature and the  $11\text{--}12\ \mu\text{m}$  “split-window” brightness temperature difference for a variety of cloud compositions with a volcanic ash component ranging from 0 to 100%. Each point on a given curve represents a different  $0.55\ \mu\text{m}$  cloud optical depth. Adapted from Pavolonis et al. [2006].

difference that is less than  $0\ \text{K}$  in the absence of competing absorption/emission/reflection effects at those wavelengths. Conversely, liquid water and ice clouds, generated by meteorological processes (meteorological clouds), typically have a “split-window” brightness temperature difference that is greater than  $0\ \text{K}$  because cloud absorption/emission is greater at  $12\ \mu\text{m}$  than  $11\ \mu\text{m}$ . Thus, a “split-window” threshold of about  $0\ \text{K}$  is

often used for ash/dust detection. Radiative transfer calculations illustrating the contrast between the “split-window” brightness temperature difference of volcanic ash clouds and other cloud types are shown in Figure 2.3.

Unfortunately, competing absorption/emission/reflection effects from atmospheric water vapor and hydrometeors, measurement errors, and other features exhibiting “reverse absorption” like signals limit the effectiveness of the “split-window” technique

for automated quantitative applications [e.g. Simpson et al. 2000; Prata et al. 2001; Tupper et al. 2004; Pavolonis et al. 2006]. Figure 2.3 demonstrates that volcanic ash clouds do not always exhibit a negative “split-window” brightness temperature difference in moist atmospheres or when mixed with hydrometeors. In addition, Figure 2.4 shows that, when viewed globally, the “split-window” brightness temperature difference is often observed to be negative for many other reasons besides the presence of volcanic ash. Ash clouds composed of large particles [Chapter 3 of this dissertation] and optically thick ash clouds [Pavolonis et al. 2006] can also deviate from the desired “split-window” behavior.

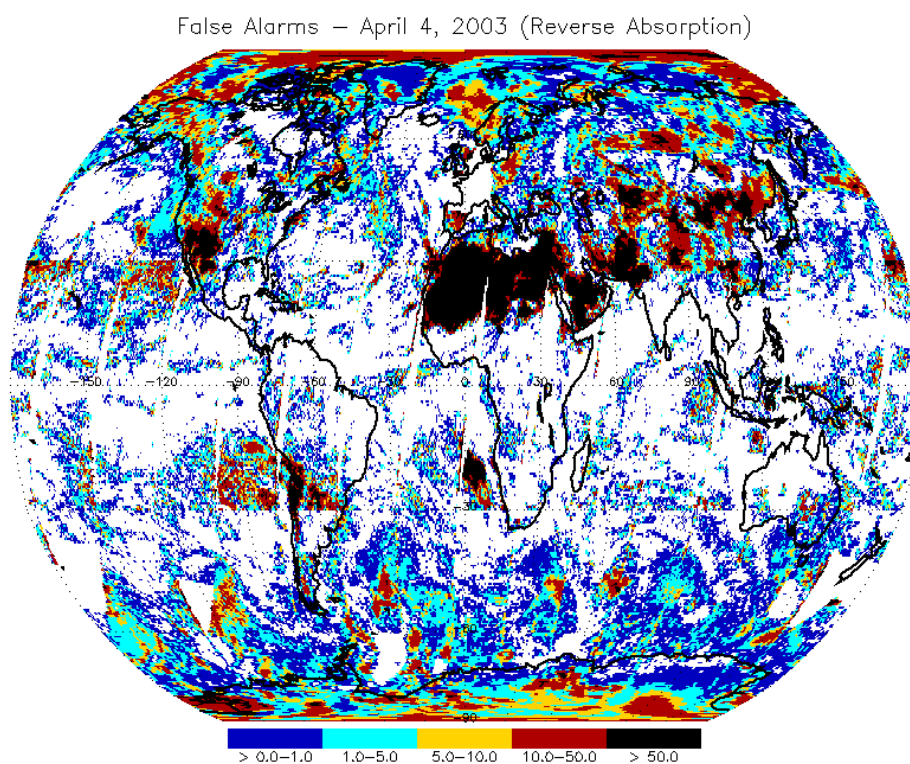


*Figure 2.4: The frequency of occurrence [%] of 11-12  $\mu\text{m}$  “split-window” brightness temperature differences  $< -0.2$  K on April 4, 2003. No known volcanic ash clouds were present at the time of this image. Adapted from Pavolonis et al. [2006].*

Efforts to improve upon the basic “split-window” approach, in a quantitative manner, include empirically correcting the 11 – 12  $\mu\text{m}$  brightness temperature difference

for atmospheric water vapor absorption [Yu et al. 2002; Corradini et al. 2008; Prata and Prata 2012], using the “split-window” method in conjunction with visible and near-infrared spectral channels [Prata and Grant 2001; Pergola et al. 2004; Pavolonis et al. 2006; Corradini et al. 2008], and the development of location specific thresholds [Pergola et al. 2004]. These efforts only produced modest improvements under certain conditions. High spectral resolution (termed “hyperspectral”) infrared measurements that are available on a few low earth orbit satellites have also been used to improve volcanic ash detection by utilizing many spectral channels in the 8-13  $\mu\text{m}$  wavelength range [Gangale et al. 2010; Clarisse et al. 2010a; Clarisse et al. 2013]. While hyperspectral infrared-based approaches do improve upon the traditional “split-window” technique, the coarse spatial resolution ( $> 10$  km) of hyperspectral sensors and the temporal sampling limitations of the few low earth orbit satellites with this measurement capability are limiting factors. Further, “split-window” limitations related to ash particle size and optical depth are not addressed by the hyperspectral approaches. In general, published satellite methodologies for detecting and tracking volcanic ash clouds have one or more of the following limitations.

1. The end results are qualitative and hence require manual interpretation and, as such, cannot be used in quantitative applications (e.g. [Hillger and Clark 2002a; Hillger and Clark 2002b; Ellrod et al. 2003; Miller 2003; Lensky and Rosenfeld 2008]).
2. The results depend strongly on solar zenith angle and/or the technique is only applicable over a subset of solar zenith angles (e.g. [Legrand et al. 2001; de Graaf et al. 2005; Pavolonis et al. 2006; Evan et al. 2006; Scollo et al. 2012]).

3. The technique can only be applied to a specific instrument or a small subset of instruments (e.g. [Liu et al. 2008; Clarisse et al. 2010a; DeSouza et al. 2010; Gangale et al. 2010; Winker et al. 2012; Clarisse et al. 2013]), and hence does not provide frequent (< 60 minutes) global coverage.
4. Finally, no published technique capable of providing frequent global coverage has been shown to be consistently skillful (very high probability of detection, very low false alarm rate) over a large range of cloud properties (cloud height/temperature/pressure, geometric thickness, composition, particle size, and cloud optical depth) and background states (surface emissivity, surface temperature, atmospheric temperature, and atmospheric composition).

Given the above limitations, existing satellite-based ash/dust detection techniques are not well suited for many important practical (operational) and research applications. For instance, Volcanic Ash Advisory Centers (VAACs), which are responsible for operationally issuing volcanic ash advisories to the aviation community, currently heavily rely on manual analysis of satellite imagery to track volcanic ash clouds. It is not feasible to routinely manually examine every satellite image for volcanic ash clouds, so some volcanic ash clouds go undetected for several hours [e.g. Pavolonis et al. 2006]. Thus, a reliable, fully automated, satellite-based volcanic ash detection system is needed to help improve the timeliness of volcanic ash advisories. The retrieval of important volcanic ash cloud properties such as cloud height, mass loading, particle size require *a priori* knowledge of the horizontal location of ash to constrain the inversion problem and prevent false alarms (pixels with valid retrieval results that are outside of the ash

cloud(s)) without significantly decreasing the probability of detection (e.g. [Prata and Prata 2012]; [Francis et al. 2012]; [Chapter 5 of this dissertation]). Current quantitative ash detection approaches are simply not skillful enough to utilize retrieved ash cloud properties to automatically and rigorously constrain model eruption source parameters [Mastin et al. 2009] or forward trajectory forecasts. Operational forecasters instead rely on manually initiated model simulations that utilize eruption source parameters that are prone to large errors, especially outside of the coverage of cloud or precipitation radars [Arason et al. 2011; Schneider and Hoblitt 2013].

Satellite derived ash cloud properties such as height, mass loading, and particle size are needed for near real-time characterization of volcanic ash hazards (e.g. VAACs are required to provide cloud height information in volcanic ash advisories). Spatially and temporally resolved ash cloud properties, as only satellite sensors can provide, are also needed to improve volcanic ash transport and dispersion models through improved understanding of ash cloud physics and data assimilation [Stohl et al. 2011; Schmehl et al. 2011; Denlinger et al. 2012; Bursik et al. 2012; Pouget et al. 2013]. Wen and Rose [1994] developed the first algorithm to retrieve volcanic ash cloud properties from satellite measurements. Their method utilized radiative transfer calculations and “split-window” measurements to retrieve the optical depth (at 11  $\mu\text{m}$ ) and effective particle radius [Hansen and Travis 1974] of volcanic ash when the “split-window” brightness temperature difference was less than 0 K. From the optical depth and effective particle radius, they estimated the mass loading (mass per unit area) of volcanic ash. To simplify this difficult problem, Wen and Rose assumed that the atmosphere was void of water vapor, the ash cloud and surface temperatures were spatially uniform, and the surface

behaved as a blackbody. Despite these assumptions, Wen and Rose demonstrated that useful ash cloud properties could be retrieved from “split-window” measurements.

Incremental improvements to the Wen and Rose method were made through empirical corrections for water vapor absorption [Yu et al. 2002; Corradini et al. 2008; Prata and Prata 2012] and refinement of retrieval inputs such as surface temperature and cloud temperature [Prata and Grant 2001; Corradini et al. 2008]. However, none of these methods explicitly account for atmospheric water vapor or allow surface temperature and emissivity to vary spatially. As well, it does not allow surface emissivity to deviate from blackbody behavior or allow the ash cloud temperature to be a free parameter in the retrieval. The approach described by Clarisse et al. [2010b] was the first to explicitly account for water vapor absorption and allow surface temperature to vary spatially, but cloud temperature was fixed in their retrieval. A retrieval methodology that explicitly accounts for background contributions (surface emission and background atmospheric gases) to the measured radiances and allows cloud temperature or height to be a free parameter in the retrieval is badly needed.

This study has five primary objectives, which will be addressed in sequential order since objectives 2-5 depend on all previous objectives. These objectives are to:

1. Increase the sensitivity of space-based infrared measurements to cloud microphysics by accounting for emission from the background clear sky atmosphere and the surface,
2. Use satellite measurements to estimate the probability that a given satellite pixel contains volcanic ash and quantitatively show that the probabilities provide a more robust framework for distinguishing volcanic ash from all other features, compared to the traditional “split-window” approach,

3. Develop and validate an algorithm that utilizes infrared satellite measurements to retrieve ash cloud height, mass loading, and effective particle radius while explicitly accounting for background contributions to the measured radiances,
4. Utilize results from the previous objectives to develop a cloud object based approach for detecting volcanic ash clouds and demonstrate that it exhibits greater skill than pixel based approaches, including the “split-window” approach,
5. Using the 2008 eruption of Kasatochi, demonstrate that the new satellite remote sensing techniques produce temporally and spatially resolved volcanic ash cloud properties that are consistent with basic physical expectations and compare the results to published results.

Finally, the research associated with objectives 1-4 was conducted within more general framework when possible. For instance, the theory and practical approach developed to achieve the first objective is applicable to all infrared relevant cloud types (e.g. liquid water, ice, dust, SO<sub>2</sub>), not just volcanic ash. In addition, the methods developed under objectives 2-4 can also be used to study clouds composed of desert dust, which has important weather and climate implications [e.g. Evan et al. 2011; Prospero and Lamb 2003; Wang et al. 2012; Jickells et al. 2005; Dunion and Velden 2004].

## Chapter 3

### 3. Infrared Radiation and Cloud Microphysics

#### 3.1. Introduction

Infrared measurements can be used to obtain quantitative information on cloud microphysics, including cloud composition and particle size, with the advantage that the measurements are independent of solar zenith angle. As such, infrared brightness temperatures (BTs) and brightness temperature differences (BTDs) have been used extensively in quantitative remote sensing applications for inferring cloud type (e.g. liquid water cloud, ice cloud, dust cloud, volcanic ash cloud, multilayered cloud) using both threshold and statistical methods (e.g. clustering, machine learning). For instance, Inoue [1985; 1987] used “split window” (11 – 12  $\mu\text{m}$ ) brightness temperature differences to identify cloud type. Strabala et al. [1994] and Baum et al. [2000] applied thresholds to 8.5 – 11  $\mu\text{m}$  and 11 – 12  $\mu\text{m}$  BTDs to help infer cloud phase. Pavolonis and Heidinger [2004] and Pavolonis et al. [2005] used a dynamic threshold technique to help infer cloud type, including multilayered cloud, from similar BTDs. Prata [1989a], and many others since, have used “split window” BTDs to detect volcanic ash and non-volcanic dust.

While all of the aforementioned brightness temperature difference methods have been applied with some success, it will be shown that, from a spectral point of view, the skill of BT/BTD approaches is fundamentally limited since the measured radiances are sensitive not only to cloud composition, but particle size, particle shape, optical depth, cloud height, surface emissivity, surface temperature, atmospheric gas concentrations, and atmospheric temperature as well. Depending on the situation, the background signal

(e.g. surface emissivity, surface temperature, atmospheric temperature, and atmospheric water vapor) can dominate the measured radiance. We will show that more advanced usage of measured infrared radiances can lead to significant increases in sensitivity to cloud microphysics, especially for optically thin clouds. In lieu of BTDs, a derived radiative parameter,  $\beta$ , which is directly related to particle size, habit, and composition, is utilized. The subsequent sections of this chapter will describe the physical basis of the new methodology for extracting cloud composition information from infrared radiances. In addition, the use of certain assumptions in constructing our new data space is motivated. In Chapter 4, actual measurements are used to help illustrate the value  $\beta$  compared to traditional BTDs for volcanic ash and dust detection. In this chapter, the term “cloud” will be used when referring to airborne particle distributions of any of the following compositions: liquid water, ice, volcanic ash, or non-volcanic dust.

### ***3.2. Physical Basis of Cloud Composition Information***

The spectral sensitivity to cloud composition is perhaps best understood by examining the imaginary index of refraction,  $m_i$ , as a function of wavelength. The imaginary index of refraction is often directly proportional to absorption/emission strength for a given particle composition, in that larger values are indicative of stronger absorption of radiation at a particular wavelength. However, absorption due to photon tunneling, which is proportional to the real index of refraction, can also contribute to the observed spectral absorption under certain circumstances [Mitchell 2000], but for simplicity, only absorption by the geometrical cross section, which is captured by the imaginary index of refraction, is discussed here. Figure 3.1 shows  $m_i$  for liquid water [Downing and Williams 1975], ice [Warren and Brandt 2008], volcanic rock (andesite)

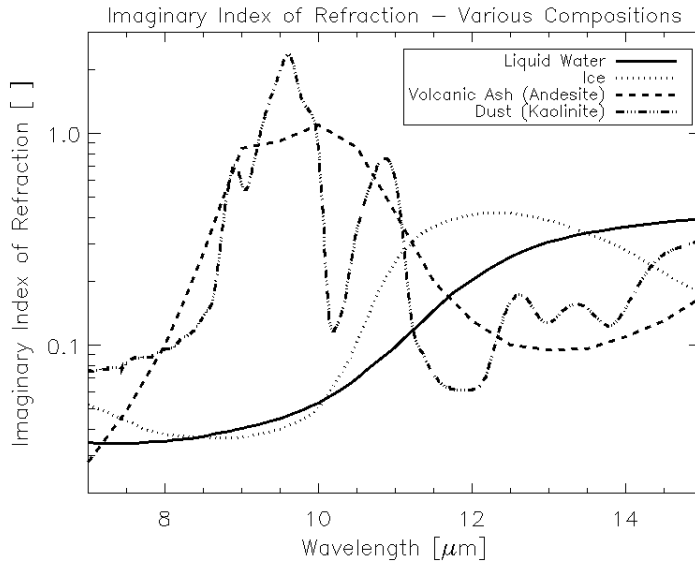


Figure 3.1: The imaginary index of refraction for liquid water (solid), ice (dotted), andesite (dashed), and kaolinite (dash-dot) is shown as a function of wavelength.

[Pollack et al. 1973], and non-volcanic dust (kaolinite) [Roush et al. 1991]. While the exact composition, and hence the  $m_i$ , of volcanic ash and dust vary depending on the source, andesite and kaolinite were chosen since both rocks exhibit the often exploited “reverse absorption” signature (e.g. Prata [1989a]). The “reverse absorption” signature is responsible for the sometimes-observed negative 11 – 12  $\mu\text{m}$  brightness temperature difference associated with volcanic ash and dust. Further, in this dissertation, the exact composition assumed for volcanic ash and dust is not critical since we are not attempting to identify specific types of rocks. We are, instead, interested in distinguishing between ice, liquid water, and dust/volcanic ash. Once a dust or volcanic ash cloud is detected, other methods can be used to determine more information about the rock type (e.g. Pavolonis et al. [2006]).

The  $m_i$  can be interpreted as follows. In Figure 3.1, one sees that around 8.5 - 10  $\mu\text{m}$  liquid water and ice absorb approximately equally, while near 11 – 13.5  $\mu\text{m}$  ice absorbs more strongly than water. Thus, all else being equal, the difference in measured radiation (or brightness temperature) between an 8.5  $\mu\text{m}$  channel and an 11  $\mu\text{m}$  channel

(or 12  $\mu\text{m}$  or 13.3  $\mu\text{m}$  channel) will be larger for an ice cloud compared to a liquid water cloud. The previous statement is only accurate if the liquid water and ice cloud have the same particle concentrations at the same vertical levels in the same atmosphere, and have the same particle size and shape distribution. That is what is meant by “all else being equal.” While Figure 3.1 is insightful, it can also be deceiving if not interpreted correctly. For example, it is possible that a liquid water cloud in a certain vertical layer with a certain particle distribution will look identical (in measurement space) to an ice cloud at the same vertical layer (in the same atmosphere), but with a different particle distribution. As another example, a scene with a liquid water cloud in one type of atmosphere (e.g. maritime tropical) may exhibit the same measured spectral radiance as a scene with an ice cloud in another type of atmosphere (e.g. continental mid-latitude). The same reasoning applies to differentiating between volcanic ash and liquid water/ice or non-volcanic dust and liquid water/ice.

To increase the sensitivity to cloud composition, the information contained in Figure 3.1 must be extracted from the measured radiances as best as possible. One way of doing this is to account for the background conditions (e.g. surface temperature, surface emissivity, atmospheric temperature, and atmospheric water vapor) of a given scene in an effort to isolate the cloud microphysical signal. This is difficult to accomplish with traditional BTs and BTDs. In the following section, we derive a data space that accounts for the background conditions.

### ***3.3. The Beta Method***

Assuming a satellite viewing perspective (e.g. upwelling radiation), a fully cloudy field of view, a non-scattering atmosphere (no molecular scattering), and a negligible

contribution from downwelling cloud emission or molecular emission that is reflected by the surface and transmitted to the top of troposphere (Zhang and Menzel [2002] showed that this term is very small at infrared wavelengths), the cloudy radiative transfer equation for a given infrared channel or wavelength can be written as in Equation ( 3.1) (e.g. Heidinger and Pavolonis [2009]).

$$R_{obs}(\lambda) = \varepsilon_{eff}(\lambda)R_{ac}(\lambda) + t_{ac}(\lambda)\varepsilon_{eff}(\lambda)B(\lambda, T_{eff}) + R_{clr}(\lambda)(1 - \varepsilon_{eff}(\lambda)) \quad (3.1)$$

In Equation ( 3.1), which is derived in Appendix A,  $\lambda$  is wavelength,  $R_{obs}$  is the observed radiance,  $R_{clr}$  is the clear sky radiance.  $R_{ac}$  and  $t_{ac}$  are the above cloud upwelling atmospheric radiance and transmittance, respectively.  $B$  is the Planck Function, and  $T_{eff}$  is the effective cloud temperature. The estimation of the clear sky radiance and transmittance will be explained later on in this section. The effective cloud emissivity [Cox 1976] is denoted by  $\varepsilon_{eff}$ . To avoid using additional symbols, the angular dependence is simply implied. Only fully cloudy fields of view are considered.

Equation ( 3.1) can readily be solved for the effective cloud emissivity as shown in ( 3.2).

$$\varepsilon_{eff}(\lambda) = \frac{R_{obs}(\lambda) - R_{clr}(\lambda)}{[B(\lambda, T_{eff})t_{ac}(\lambda) + R_{ac}(\lambda)] - R_{clr}(\lambda)} \quad (3.2)$$

In Equation ( 3.2), the term in brackets in the denominator is the blackbody cloud radiance that is transmitted to the top of atmosphere (TOA) plus the above cloud (ac) atmospheric radiance. This term is dependent upon the cloud vertical location. This dependence will be discussed in detail in later sections. It is worth noting that a two-layer cloud system, where the lower cloud layer is assumed to be opaque (e.g. a lower liquid water cloud layer) and the upper layer is allowed to be semi-transparent, can easily

be accommodated in Equation ( 3.2), if the clear sky radiance term is replaced with the upwelling top of atmosphere radiance from a black body cloud layer. Even if the vertical location of the lower cloud layer is chosen based on climatology, the estimate of cloud emissivity for the highest cloud layer can be improved for this type of multi-layered cloud system. For simplicity, we will only focus on single layer cloud systems in this chapter. Multi-layered cloud systems are addressed in Chapter 4.

The cloud microphysical signature cannot be captured with the effective cloud emissivity alone for a given spectral channel or wavelength. It is the spectral variation of the effective cloud emissivity that holds the cloud microphysical information. To harness this information, the effective cloud emissivity is used to calculate effective absorption optical depth ratios; otherwise known as  $\beta$ -ratios (see Inoue [1987]; Parol et al. [1991]; Giraud et al. [1997]; and Heidinger and Pavolonis [2009]). The  $\beta$ -ratio is computed from a spectral emissivity pair,  $\epsilon_{\text{eff}}(\lambda_1)$  and  $\epsilon_{\text{eff}}(\lambda_2)$ , as in Equation ( 3.3).

$$\beta_{\text{obs}} = \frac{\ln[1 - \epsilon_{\text{eff}}(\lambda_1)]}{\ln[1 - \epsilon_{\text{eff}}(\lambda_2)]} = \frac{\tau_{\text{abs, eff}}(\lambda_1)}{\tau_{\text{abs, eff}}(\lambda_2)} \quad (3.3)$$

Equation ( 3.3) can simply be interpreted as the ratio of effective absorption optical depth ( $\tau_{\text{abs, eff}}$ ) at two different wavelengths. The word “effective” is used since the cloud emissivity depends upon the effective cloud temperature. The effective cloud temperature is most often different from the thermodynamic cloud top temperature since the cloud emission originates from a layer in the cloud. The depth of this layer depends upon the cloud transmission profile, which is generally unknown. One must also consider that the effects of cloud scattering are implicit in the cloud emissivity calculation since the actual observed radiance will be influenced by cloud scattering to

some degree. In other words, no attempt is made to separate the effects of absorption and scattering. At wavelengths in the 10 to 13  $\mu\text{m}$  range, the effects of cloud scattering for upwelling radiation are quite small and usually negligible. But at infrared wavelengths in the 8 – 10  $\mu\text{m}$  range, the cloud reflectance can make a 1 – 3% contribution to the top of atmosphere radiance [Turner 2005]. Thus, it is best to think of satellite-derived effective cloud emissivity as a radiometric parameter, which, in most cases, is proportional to the fraction of radiation incident on the cloud base that is absorbed by the cloud. See Cox [1976] for an in depth explanation of effective cloud emissivity.

An appealing quality of  $\beta_{\text{obs}}$ , is that it can be interpreted in terms of the single scatter properties, which can be computed for a given cloud composition and particle distribution. Following Van de Hulst [1980] and Parol et al. [1991], a spectral ratio of scaled extinction coefficients can be calculated from the single scatter properties (single scatter albedo, asymmetry parameter, and extinction cross section), as follows.

$$\beta_{\text{theo}} = \frac{[1.0 - \omega(\lambda_1)g(\lambda_1)]\sigma_{\text{ext}}(\lambda_1)}{[1.0 - \omega(\lambda_2)g(\lambda_2)]\sigma_{\text{ext}}(\lambda_2)} \quad (3.4)$$

In Equation ( 3.4),  $\beta_{\text{theo}}$  is the spectral ratio of scaled extinction coefficients,  $\omega$  is the single scatter albedo,  $g$  is the asymmetry parameter, and  $\sigma_{\text{ext}}$  is the extinction cross section. At wavelengths in the 8 – 15  $\mu\text{m}$  range, where multiple scattering effects are small,  $\beta_{\text{theo}}$ , captures the essence of the cloudy radiative transfer such that

$$\beta_{\text{obs}} \approx \beta_{\text{theo}}. \quad (3.5)$$

Equation ( 3.4), which was first shown to be accurate for observation in the 10 – 12  $\mu\text{m}$  “window” by Parol et al. [1991], only depends upon the single scatter properties. It does not depend upon the observed radiances, cloud height, or cloud optical depth. To

illustrate that Equation ( 3.5) is a good approximation in the 8 – 14  $\mu\text{m}$  range, high spectral resolution ( $0.4\text{ cm}^{-1}$  resolution) radiative transfer simulations were performed using the Line-by-Line Radiative Transfer Model (LBLRTM; Clough and Iacono [1995]) to compute spectral gaseous optical depth profiles and a Discrete Ordinate Radiative Transfer (DISORT) method [Stamnes et al. 1988] to account for cloud scattering and absorption. These two radiative transfer tools were combined by Turner [2005] and termed LBLDIS for short. More details concerning LBLDIS can be found in Turner [2005]. LBLDIS was used to simulate an ice cloud (composed of plates) in the upper tropical troposphere. The single scatter properties for this type of cloud were taken from Yang et al. [2005]. The cloud optical depth was set to 0.5 at 10  $\mu\text{m}$  ( $1000\text{ cm}^{-1}$ ) and the effective particle radius was varied from 7 to 30  $\mu\text{m}$ . From the simulated radiances, a spectra of  $\beta_{\text{obs}}$  was calculated using Equations ( 3.2) and ( 3.3). The  $\beta_{\text{obs}}$  spectrum was constructed such that the wavenumber (or wavelength) in the denominator of Equation ( 3.3) was held constant and the wavenumber in the numerator was varied. An analogous  $\beta_{\text{theo}}$  spectrum was calculated using the single scatter properties as described by Equation ( 3.4). The goal here is to show that Equation ( 3.5) holds true over the 8 – 14  $\mu\text{m}$  range.

Figure 3.2 shows the  $\beta_{\text{obs}}$  and  $\beta_{\text{theo}}$  spectra for various effective particle radii. The results indicate that overall Equation ( 3.5) is a very good approximation, especially at wavelengths longer than 10  $\mu\text{m}$ . At wavelengths shorter than 10  $\mu\text{m}$ ,  $\beta_{\text{theo}}$  does not fit  $\beta_{\text{obs}}$  quite as well. The reasoning for this is as follows. For a given set of cloud microphysics, the amount of scattering will generally increase with decreasing wavelength, which likely imposes a small spectral dependence on the effective cloud temperature across this wavelength range, which was not accounted for here. For

simplicity, we will ignore this small spectral dependence in  $T_{\text{eff}}$ . This simplification does not have a large impact on the results, as we are more interested in the relative difference in  $\beta$  as a function of cloud composition, as opposed to the absolute accuracy of Equation (3.5).

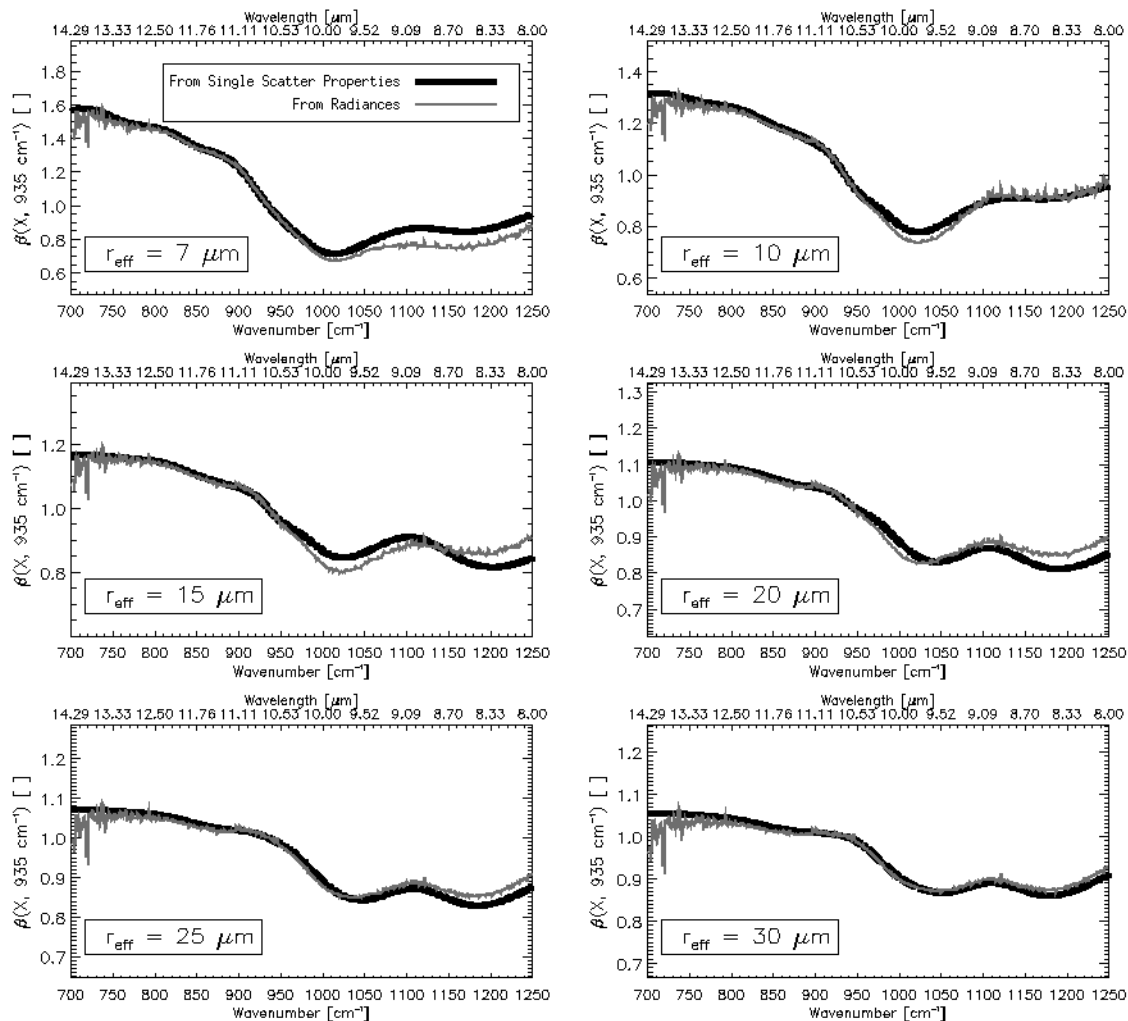


Figure 3.2: Spectra of effective absorption optical depth ratios calculated from simulated high spectral resolution radiances in the 8 – 14  $\mu\text{m}$  range are shown in gray (with thinner line style) for an upper tropospheric ice cloud (composed of plates) with an optical depth of 0.5 at a wavelength of 10  $\mu\text{m}$ . An analogous spectrum of scaled extinction coefficients is also shown in black (with thick line style). Each panel represents a different effective particle radius.

By using  $\beta$ -ratios as opposed to brightness temperature differences, we are not only accounting for the non-cloud contribution to the radiances, we are also providing a means to tie the observations back to theoretical size distributions. This framework clearly has practical and theoretical advantages over traditional brightness temperature differences. Parol et al. [1991] first showed that Equation ( 3.5) is a good approximation in the 10 – 12  $\mu\text{m}$  window. Since that time, faster computers and improvements in the efficiency and accuracy of clear sky radiative transfer modeling have allowed for more detailed exploration of the  $\beta$  data space and computation of  $\beta$ -ratios on a global scale.

### ***3.4. Cloud Composition Differences in $\beta$ -space***

Since the 8.5 – 11  $\mu\text{m}$  (hereafter, BTD(8.5 – 11 $\mu\text{m}$ )) and 11 – 12  $\mu\text{m}$  (hereafter, BTD(11 – 12 $\mu\text{m}$ )) BTDs are often used to determine cloud phase (e.g. [Strabala et al. 1994; Pavolonis et al. 2005]) and to detect volcanic ash and dust (e.g. [Pavolonis et al. 2006; Zhang et al. 2006; Prata 1989a]), these BTDs were selected for analysis. Analogously, the  $\beta_{\text{theo}}$  for the 8.5, 11 (hereafter,  $\beta(8.5\mu\text{m}, 11\mu\text{m})$ ) and 11, 12  $\mu\text{m}$  (hereafter,  $\beta(12\mu\text{m}, 11\mu\text{m})$ ) wavelengths were analyzed, where the 11  $\mu\text{m}$  emissivity is always placed in the denominator of Equation ( 3.4). Figure 3.3 shows the relationship between  $\beta(8.5\mu\text{m}, 11\mu\text{m})$  and  $\beta(12\mu\text{m}, 11\mu\text{m})$  as given by the single scatter properties (see Equation ( 3.4)) for various cloud compositions with a varying effective particle radius. The effective particle radius is defined as the ratio of the third to second moment of the size distribution [Hansen 1974]. With the exception of ice, all single scatter properties were calculated using Mie theory. The ice single scatter properties for seven different habits were taken from the Yang et al. [2005] database. Figure 3.3 indicates that the sensitivity to particle habit is small compared to the sensitivity to composition and

particle

size.

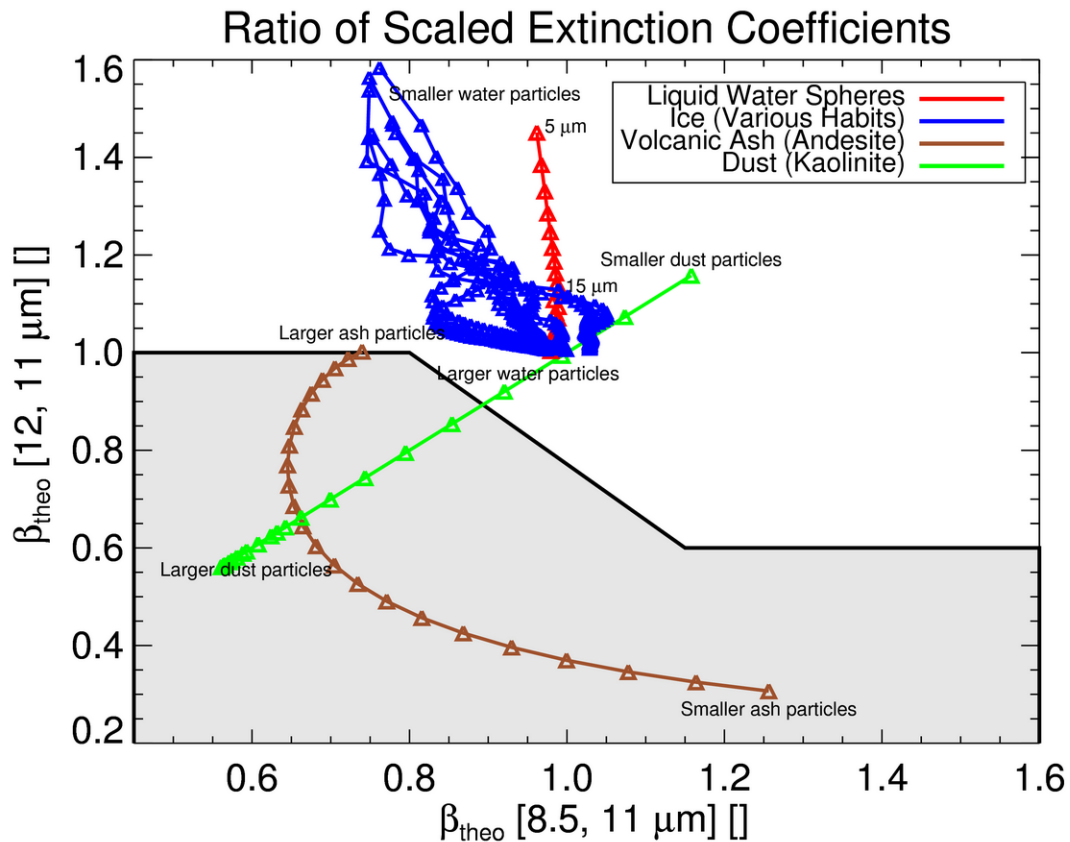


Figure 3.3: The 12/11  $\mu\text{m}$  scaled extinction ratio ( $\beta(12\mu\text{m}, 11\mu\text{m})$ ) is shown as a function of the 8.5/11  $\mu\text{m}$  scaled extinction ratio ( $\beta(8.5\mu\text{m}, 11\mu\text{m})$ ) for liquid water spheres (red), various ice crystal habits (blue), andesite spheres (brown), and kaolinite spheres (green). The ice crystal habits shown are plates, aggregates, bullet rosettes, droxtals, hollow columns, solid columns, and spheroids. A range of particle sizes is shown for each composition. For liquid water (ice), the effective particle radius was varied from 5 to 30 (54)  $\mu\text{m}$ . The 5 and 15  $\mu\text{m}$  values of liquid water effective radius are labeled. The andesite and kaolinite effective particle radius was varied from 1 to 12  $\mu\text{m}$ . The large and small particle ends of each curve are labeled. The  $\beta$ -ratios were derived from the single scatter properties. The area shaded in light gray represents the envelope where volcanic ash and dust rock types not explicitly represented on this figure typically lie.

Thus, variability in  $\beta$  due to ice crystal habit does not inhibit the determination of cloud composition, unless the liquid water effective radius is very large. In addition, one can see that most of the information on cloud thermodynamic phase is given by the difference in absorption between 8.5 and 11  $\mu\text{m}$ , while separating meteorological cloud from ash or

dust clouds is best performed using a tri-spectral technique. For ice and liquid water clouds, the difference in absorption at 11 and 12  $\mu\text{m}$  is mostly related to changes in particle size. This figure also indicates that separating dust from ash is difficult to do using just these particular spectral relationships. Unlike BTDs, these  $\beta_{\text{theo}}$  relationships are only a function of the cloud microphysical properties.

### ***3.5. Estimating the Clear Sky Radiance and Transmittance***

Since the calculation of effective cloud emissivity and hence  $\beta_{\text{obs}}$  depends on the clear sky radiance and transmittance profiles, our mechanism for estimating the clear sky terms in Equation ( 3.2) is described here. Clear sky transmittances and radiances are estimated using a fast clear sky radiative transfer model (RTM). These models, which are computationally efficient, will produce a clear sky transmittance/radiance profile and top-of-atmosphere radiances given an input temperature profile, water vapor profile, ozone profile, surface temperature, surface emissivity, and viewing angle. Currently, we use a regression-based model [Hannon et al. 1996]. The input data (with the exception of viewing angle and surface emissivity) comes from numerical weather prediction (NWP) models, such as the National Centers for Environmental Prediction (NCEP) Global Forecast System (GFS). NWP model data are convenient to use because of the constant spatial coverage. While the current NWP fields often have large errors in some fields, such as the surface temperature over land, they provide needed and useful information. Over the coming years, we expect the NWP fields to improve in accuracy and in spatial resolution, which should act to improve the clear sky radiance calculations. All of the NWP profile data are interpolated to 101 levels to improve the accuracy of the calculated transmittance profile, especially in regards to absorption channels (e.g. [Strow et al.

2003]). The spectrally resolved surface emissivity is taken from the global 5-km spatial resolution Seebor database [Seemann et al. 2008]. It is important to note that NWP data have been commonly used to drive the clear sky radiative transfer models used in infrared cloud retrievals. For example, the official Moderate Resolution Imaging Spectroradiometer (MODIS) cloud CO<sub>2</sub> slicing algorithm utilizes this same NWP-based approach to estimate the clear sky radiance [Menzel et al. 2008].

Since a more complete discussion regarding errors in the top-of-atmosphere clear sky radiance is given in Heidinger and Pavolonis [2009], only a brief summary is included here. For channels or wavelengths with weighting functions that peak at or near the surface (e.g. “window” channels), errors in the top-of-atmosphere clear sky brightness temperatures are generally less than 0.50 K for open-ocean. Over land, the GFS surface temperature error exhibits a diurnal cycle where the surface temperature is significantly underestimated during the day and slightly overestimated at night. Given the large uncertainties in surface temperature and uncertainties in surface emissivity, the top-of-atmosphere clear sky radiance calculation over land is prone to fairly large errors (up to 15 K over desert surfaces around local solar noon), although the impact of these errors is not always severe, depending on the cloud optical depth. In Chapter 4 and Chapter 6, it is shown that cloud composition information inferred using the  $\beta$  method is not significantly coupled to the NWP model, and fairly large errors in the clear sky radiance can be tolerated. Thus, assimilation of cloud composition information, extracted using the  $\beta$  method, into numerical models should not be prohibitive. Finally, it is important to note that the specific radiative transfer model and ancillary data (e.g. NWP, surface observations, independent remote sensing data, rawinsondes, etc...) used to generate the

clear sky radiances and transmittances does not significantly impact the results, so long as the estimates are reasonable. The physical concepts are not at all dependent on the clear sky radiative transfer scheme chosen.

### ***3.6. Sensitivity of Beta to Cloud Vertical Structure***

As shown earlier, the cloud emissivity is dependent on the vertical distribution of cloud particles between the upper and lower vertical boundaries. In the absence of high quality independent cloud vertical boundary information, such as from a lidar, the effective cloud temperature ( $T_{\text{eff}}$ ) is considered to be unknown. Previous studies have shown that infrared “window” channels are rather insensitive to the  $T_{\text{eff}}$  for semi-transparent clouds (e.g. [Heidinger and Pavolonis 2009]). Given this information, can one assume a constant  $T_{\text{eff}}$  and still effectively isolate the cloud microphysical signal using “window” channels? More specifically, since most clouds are at or below the tropopause, can we assume that  $T_{\text{eff}} = T_{\text{tropopause}}$ ?

To answer this question, we derived analytical expressions for various BTD and  $\beta_{\text{tot}}$  Jacobians, where  $\beta_{\text{tot}}$  is the  $\beta$  calculated using Equations ( 3.2) and ( 3.3) assuming that  $T_{\text{eff}} = T_{\text{tropopause}}$  (“tot” = top of troposphere). The purpose of this analysis is to determine the sensitivity of a given BTD and  $\beta_{\text{tot}}$  to: cloud microphysics (given by the true  $\beta$  taken from single scatter properties), the effective cloud temperature, the effective cloud emissivity, the surface temperature, the surface emissivity, and the atmospheric gaseous transmittance. The complete list of partial derivatives (Jacobians) is shown in Table 3.1. All of the analytical expressions, which are listed in Appendix B, were derived using Equations ( 3.1), ( 3.2), ( 3.3) and the Planck Function.

Table 3.1: Symbols and definitions of the brightness temperature difference (BTD) and effective absorption optical depth ratio ( $\beta_{\text{tot}}$ ) Jacobians. The effective absorption optical depth ratio was calculated assuming that the effective cloud temperature is equal to the tropopause temperature. The denominator (numerator) wavelength in the beta ratio is denoted by  $\lambda_D$  ( $\lambda_N$ ). The BTD is defined as  $\lambda_D - \lambda_N$ .

BTD Jacobian	$\beta$ Jacobian	Definition
$\partial\text{BTD}(\lambda_N, \lambda_D) / \partial\beta(\lambda_N, \lambda_D)$	$\partial\beta_{\text{tot}}(\lambda_N, \lambda_D) / \partial\beta(\lambda_N, \lambda_D)$	The partial derivative with respect to cloud microphysics given by spectral variation in cloud emissivity
$\partial\text{BTD}(\lambda_N, \lambda_D) / \partial T_{\text{eff}}$	$\partial\beta_{\text{tot}}(\lambda_N, \lambda_D) / \partial T_{\text{eff}}$	The partial derivative with respect to the effective cloud temperature
$\partial\text{BTD}(\lambda_N, \lambda_D) / \partial\epsilon_{\text{clid}}(\lambda_D)$	$\partial\beta_{\text{tot}}(\lambda_N, \lambda_D) / \partial\epsilon_{\text{clid}}(\lambda_D)$	The partial derivative with respect to the denominator ( $\lambda_D$ ) effective cloud emissivity
$\partial\text{BTD}(\lambda_N, \lambda_D) / \partial T_{\text{sfc}}$	$\partial\beta_{\text{tot}}(\lambda_N, \lambda_D) / \partial T_{\text{sfc}}$	The partial derivative with respect to the surface temperature.
$\partial\text{BTD}(\lambda_N, \lambda_D) / \partial t_{\text{atmos}}(\lambda_D)$	$\partial\beta_{\text{tot}}(\lambda_N, \lambda_D) / \partial t_{\text{atmos}}(\lambda_D)$	The partial derivative with respect to the denominator ( $\lambda_D$ ) clear sky atmospheric transmittance
$\partial\text{BTD}(\lambda_N, \lambda_D) / \partial\beta_{\text{atmos}}(\lambda_N, \lambda_D)$	$\partial\beta_{\text{tot}}(\lambda_N, \lambda_D) / \partial\beta_{\text{atmos}}(\lambda_N, \lambda_D)$	The partial derivative with respect to the spectral variation of clear sky atmospheric transmittance
$\partial\text{BTD}(\lambda_N, \lambda_D) / \partial\epsilon_{\text{sfc}}(\lambda_D)$	$\partial\beta_{\text{tot}}(\lambda_N, \lambda_D) / \partial\epsilon_{\text{sfc}}(\lambda_D)$	The partial derivative with respect to the denominator ( $\lambda_D$ ) surface emissivity
$\partial\text{BTD}(\lambda_N, \lambda_D) / \partial\beta_{\text{sfc}}(\lambda_N, \lambda_D)$	$\partial\beta_{\text{tot}}(\lambda_N, \lambda_D) / \partial\beta_{\text{sfc}}(\lambda_N, \lambda_D)$	The partial derivative with respect to the spectral variation of surface emissivity

Global Forecast Model (GFS) data were used to evaluate these analytical expressions for a variety of scenes. A description of the GFS can be found in Hamill et al. [2006]. We chose to simulate the 8.5, 11, and 12  $\mu\text{m}$  channels on the Spinning Enhanced Visible and Infrared Imager (SEVIRI). SEVIRI, which is in geostationary orbit, is a 12-channel imaging instrument with a spatial resolution of 3 km at nadir for the infrared channels. For more information on SEVIRI, see <http://www.eumetsat.int/>. We chose to simulate SEVIRI radiances primarily out of convenience since we are using it for other studies. The conclusions drawn from these analyses do not change if channels with a

similar central wavelength from another sensor are simulated. For reasons described in Section 3.4 the 8.5 – 11  $\mu\text{m}$  and 11 – 12  $\mu\text{m}$  BTDs and the  $\beta_{\text{tot}}$  for the 8.5, 11 and 11, 12  $\mu\text{m}$  channel pairs were analyzed, where the 11  $\mu\text{m}$  channel emissivity is always placed in the denominator of Equation ( 3.3). From here forward the BTDs and  $\beta_{\text{tot}}$  are referred to as BTD(8.5 – 11 $\mu\text{m}$ ), BTD(11 – 12 $\mu\text{m}$ ),  $\beta_{\text{tot}}$ (8.5 $\mu\text{m}$ , 11 $\mu\text{m}$ ), and  $\beta_{\text{tot}}$ (12 $\mu\text{m}$ , 11 $\mu\text{m}$ ), respectively.

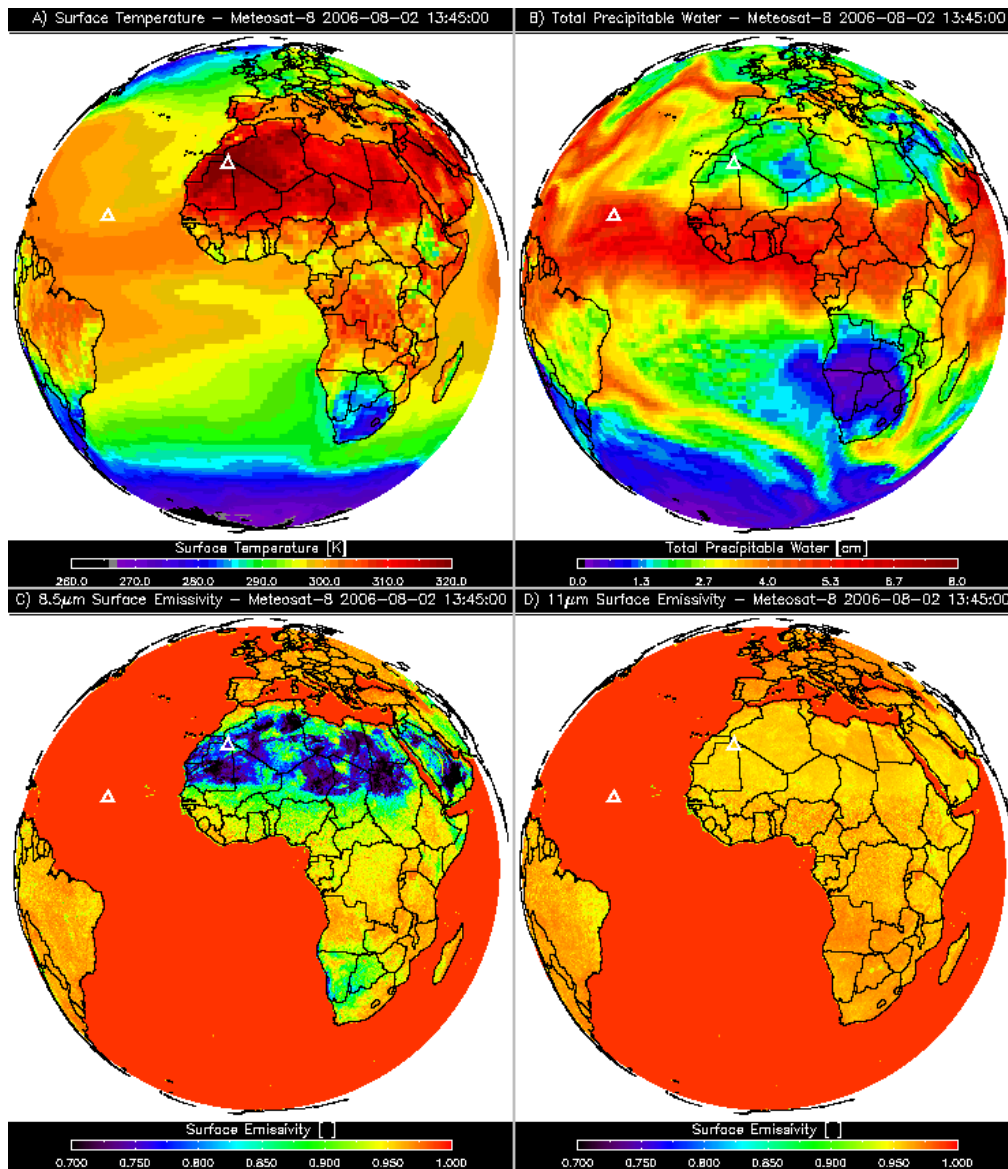


Figure 3.4: Surface temperature in K (Panel A), total precipitable water in cm (Panel B), 8.5- $\mu\text{m}$  surface emissivity (Panel C), and 11- $\mu\text{m}$  surface emissivity (Panel D) are shown mapped to a full disk viewed by a geostationary radiometer. The surface temperature and precipitable water are taken from a 12 hour Global Forecast System (GFS) forecast valid at 13:45 UTC on August 2, 2006. The surface emissivity is a monthly mean taken from the Seebor database. The white triangles indicate locations where Jacobians of the infrared radiative transfer equation were evaluated using these and other inputs from the GFS.

Figure 3.4 shows the GFS 12-hour forecast of surface temperature (Panel A) and total precipitable water (Panel B) over a spatial domain consistent with a SEVIRI full

disk for an arbitrarily chosen time (forecast valid on August 2, 2006 at 13:45 UTC). The August monthly mean 8.5  $\mu\text{m}$  and 11  $\mu\text{m}$  surface emissivity from the Seebor database are also shown in Panels C and D. The Jacobians were evaluated for several different locations in this spatial domain. Excluding bare land surfaces, the results vary only slightly. Thus, Jacobians for a maritime tropical location and a location in the Sahara Desert, denoted by the triangles on Figure 3.4, are shown here. For each scene, the 11  $\mu\text{m}$  cloud emissivity was varied from 0.01 to 0.99 and the location of the cloud in the vertical and the cloud composition were varied. The location of the cloud in the vertical was specified using a tropopause following pressure coordinate analogous to the terrain following sigma coordinates commonly employed by NWP models. A tropopause following coordinate system was chosen to account for the spatial variability of the tropopause height. The goal is to put the cloud in a vertical location such that the mass of air between the cloud top and the tropopause is roughly constant regardless of the height of the tropopause. The cloud pressure level is determined using the following expression.

$$P_{eff} = (P_{tropopause} - P_{surface})\sigma + P_{surface} \quad (3.6)$$

In Equation ( 3.6),  $P_{eff}$  is the cloud pressure used to determine the effective cloud temperature by matching  $P_{eff}$  to the corresponding temperature in the model profiles.  $P_{tropopause}$  is the pressure of the thermodynamically defined model tropopause.  $P_{surface}$  is the surface pressure and  $\sigma$  is the weighting factor that determines the vertical location of the cloud. In these sensitivity studies three different weighting factors ( $\sigma = 0.87$ ,  $\sigma = 0.63$ , and  $\sigma = 0.33$ ) were used. The 0.87 weighting factor results in a cloud located in the upper troposphere, which is about 75 - 120 hPa ( $\sim 3 - 5$  km) lower than the tropopause pressure. This is important since we are assuming a  $T_{eff}$  consistent with the tropopause

and we want to make sure that the true  $T_{\text{eff}}$  is significantly different than the one we assumed. The 0.63 and 0.33 weighting factors are consistent with the middle and lower troposphere, respectively.

Three different cloud compositions, ice, liquid water, and andesite (volcanic ash), were simulated. For ice, a true  $\beta$  value consistent with a plate habit and an effective particle radius of 20  $\mu\text{m}$ , based on the single scatter database of Yang et al. [2005] were used. The true  $\beta$  values for liquid water and volcanic ash were based upon single scatter properties generated using Mie theory assuming spherical particles. A  $\beta$  value consistent with an effective radius of 10  $\mu\text{m}$  was chosen for liquid water. For volcanic ash, a  $\beta$  value consistent with an effective radius of 2  $\mu\text{m}$  was chosen. All parameters used in these simulations are summarized in Table 3.2. For simplicity, only single layer clouds are considered in this analysis, even though both the BTD and  $\beta_{\text{tot}}$  will be sensitive to multiple cloud layers when the highest cloud layer is semi-transparent. In Chapter 4, real measurements are used to assess the impact of multilayered clouds on both the BTD and  $\beta_{\text{tot}}$ . The goal here is to provide theoretical insight into the sensitivity of the BTD and  $\beta_{\text{tot}}$  to cloud microphysics relative to other variables under straightforward conditions.

*Table 3.2: A description of the parameters used in various radiative transfer model simulations of a maritime tropical and Sahara Desert scene.*

Parameter	Maritime Tropical	Sahara Desert
Surface temperature	299 K	321.94 K
8.5 $\mu\text{m}$ surface emissivity	0.990	0.738
11 $\mu\text{m}$ surface emissivity	0.990	0.953
12 $\mu\text{m}$ surface emissivity	0.990	0.978
Total precipitable water	6.24 cm	1.85 cm
8.5 $\mu\text{m}$ clear atmospheric transmittance	0.433	0.784
11 $\mu\text{m}$ clear atmospheric transmittance	0.353	0.870
12 $\mu\text{m}$ clear atmospheric transmittance	0.209	0.800
Ice/ash/liquid water cloud $\sigma$	0.87/ 0.63/ 0.33	0.87/ 0.63/ 0.33
Ice/ash/liquid water cloud effective height	11.78/ 6.87/ 3.00 km	12.01/ 7.26/ 3.49 km
Ice/ash/liquid water cloud effective pressure	221.46/ 440.12/ 713.45 hPa	214.88/ 421.39/ 679.52 hPa
Ice/ash/liquid water cloud effective temperature	224.66/ 261.99/ 282.79 K	224.93/ 254.55/ 286.43 K
Ice/ash/liquid water cloud $\beta(8.5, 11 \mu\text{m})$	0.836/ 0.705/ 0.981	0.836/ 0.705/ 0.981
Ice/ash/liquid water cloud $\beta(12, 11 \mu\text{m})$	1.07/ 0.564/ 1.21	1.07/ 0.564/ 1.21
Ice/ash/liquid water cloud effective radius	20/ 2/ 10 $\mu\text{m}$	20/ 2/ 10 $\mu\text{m}$

In this analysis, all of the Jacobians were arbitrarily scaled to a 1% change (relative to the current value) in the independent variables to obtain consistent units for a given set of BTD or  $\beta_{\text{tot}}$  partial derivatives. This sort of scaling allows us to answer the following question. If each independent variable is perturbed by the same arbitrarily chosen amount, relative to the current value, while holding every other variable constant, which perturbation causes the greatest change in BTD or  $\beta_{\text{tot}}$ ?

### *3.6.1. Maritime Tropical Scene*

Sensitivity results for the 8.5, 11  $\mu\text{m}$  and the 11, 12  $\mu\text{m}$  channel combinations are shown for the maritime tropical scene in Figure 3.5 and Figure 3.6, respectively. The scaled  $\beta_{\text{tot}}$  Jacobians are displayed on the left hand side and the scaled BTD Jacobians on the right hand side. The top (middle, bottom) row in these multi-panel figures shows the sensitivity to the ice (volcanic ash, liquid water) cloud at the  $\sigma = 0.87$  ( $\sigma = 0.63$ ,  $\sigma = 0.33$ ) level. Because of the aforementioned scaling, the magnitude of a given Jacobian is arbitrary, thus it is the relative difference in magnitude between the Jacobians within each

separate panel of the figure that is significant. As such, the magnitude of each scaled Jacobian was normalized by the magnitude of the cloud microphysics Jacobian, where blue (red) colors indicate that the magnitude of the Jacobian was less (greater) than the magnitude of the cloud microphysics Jacobian.

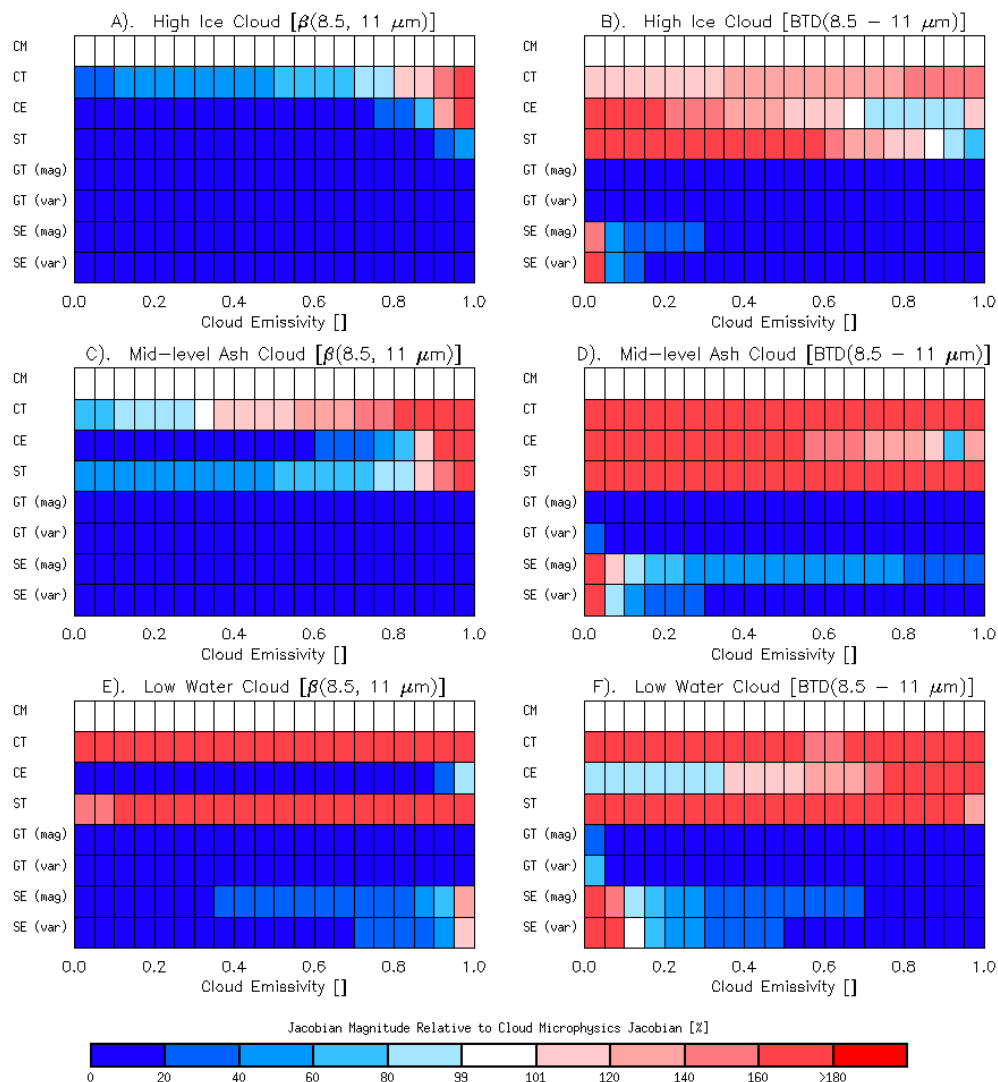


Figure 3.5: Evaluation of 8.5 – 11  $\mu\text{m}$  brightness temperature difference Jacobians (right hand side of figure) and 8.5- $\mu\text{m}$ /11- $\mu\text{m}$  effective absorption optical depth ratio Jacobians, calculated assuming an effective cloud temperature equal to the tropopause temperature (left hand side of figure), for a maritime tropical location. For each dependent variable, the partial derivative with respect to cloud microphysics (CM), cloud effective temperature (CT), 11- $\mu\text{m}$  cloud emissivity (CE), surface temperature (ST), total 11- $\mu\text{m}$  clear sky atmospheric transmittance (GT (mag)), the spectral variation of the clear sky

atmospheric transmittance ( $GT$  (var)), the 11- $\mu\text{m}$  surface emissivity ( $SE$  (mag)), and the spectral variation of the surface emissivity ( $SE$  (var)) was evaluated as a function of the 11- $\mu\text{m}$  cloud emissivity. All Jacobians were scaled to a 1% change in the dependent variable and then normalized by the respective CM Jacobian. Blue (red) colors indicate that the magnitude of the Jacobian is less (greater) than the magnitude of the CM Jacobian. Three different types of clouds were considered: an ice cloud in the upper troposphere (but significantly lower than the tropopause) (top row), a volcanic ash cloud in the middle troposphere (middle row), and a liquid water cloud in the lower troposphere (bottom row).

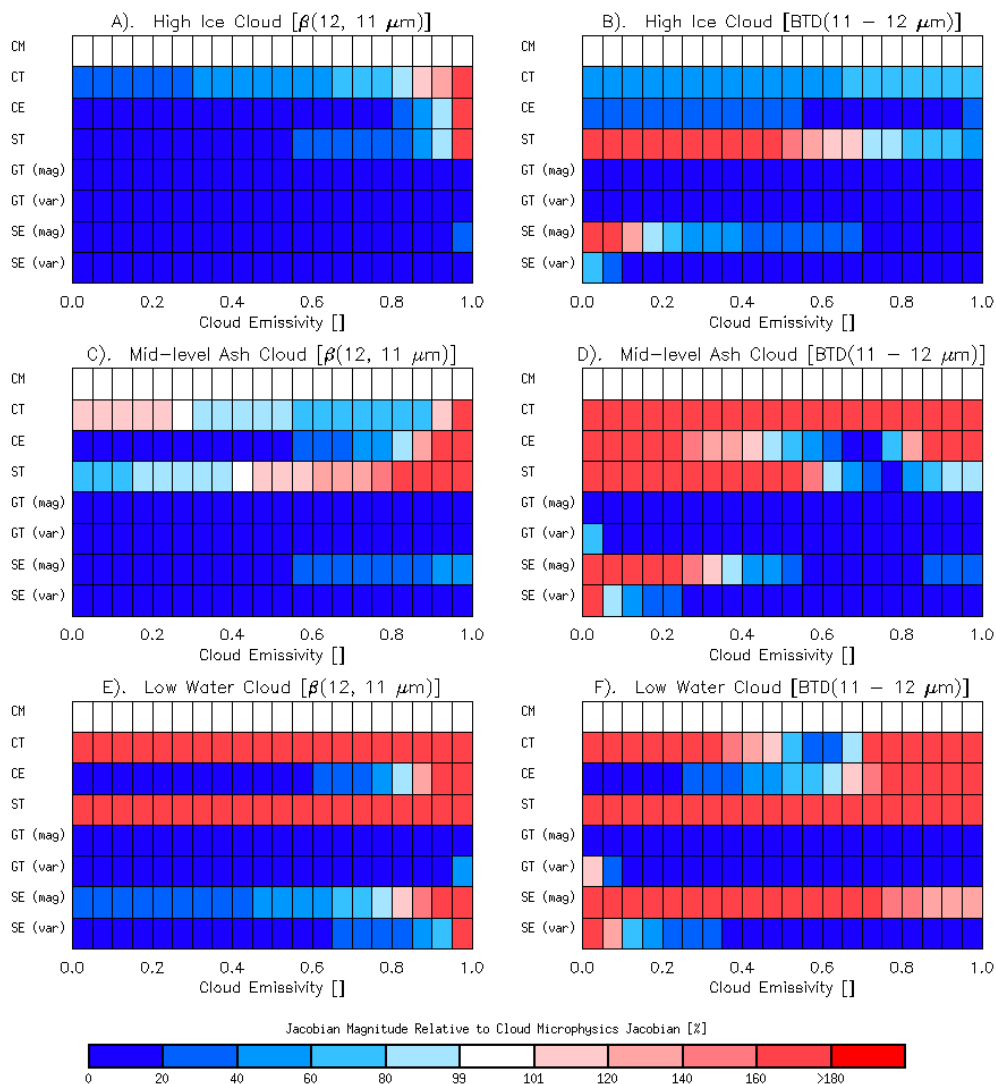


Figure 3.6: Same as Figure 3.5 except the 11 – 12- $\mu\text{m}$  brightness temperature difference and the 12- $\mu\text{m}$ /11- $\mu\text{m}$  effective absorption optical depth ratio were considered.

With regard to the ice cloud, which is located in the upper troposphere, about 4 km below the tropopause,  $\beta_{\text{tot}}$  is most sensitive to the cloud microphysics when the cloud emissivity is less than about 0.80 – 0.87 depending on which spectral channels are considered. As expected, at larger emissivities,  $\beta_{\text{tot}}$  gradually becomes most sensitive to the effective cloud temperature and the cloud emissivity. In contrast, the BTD for the 8.5, 11  $\mu\text{m}$  pair is never most sensitive to cloud microphysics, and the BTD for the 11, 12  $\mu\text{m}$  pair is only most sensitive to cloud microphysics at large emissivities. Note how the BTDs are very sensitive to surface temperature over most of the range of emissivities, while the sensitivity of  $\beta_{\text{tot}}$  to non-cloud variables is very small. While not shown, these general conclusions for an upper tropospheric cloud hold when other cloud compositions or ice crystal habits are considered.

The volcanic ash cloud at the  $\sigma = 0.63$  level, which is about 9 km below the tropopause, exhibits a reduced sensitivity to cloud microphysics compared to the ice cloud at the  $\sigma = 0.87$  level. Similar to the upper tropospheric ice cloud,  $\beta_{\text{tot}}$  is considerably more sensitive to cloud microphysics than the BTDs. The  $\beta_{\text{tot}}$  Jacobians indicates a slightly stronger sensitivity to non-cloud variables, especially the surface temperature. This is because of the larger difference between the assumed vertical cloud location and the true cloud location.

The liquid water cloud was placed about 13 km below the tropopause, in the lower troposphere at  $\sigma = 0.33$ . In this case, a very large error in the cloud vertical location resulted from our top of troposphere assumption, and as such,  $\beta_{\text{tot}}$  is most sensitive to the effective cloud temperature, not cloud microphysics. Despite this large

error in the vertical cloud location,  $\beta_{\text{tot}}$  is still noticeably more sensitive to cloud microphysics than the corresponding BTDs.

### 3.6.2. Sahara Desert Scene

Bare land surfaces such as those found in the Sahara Desert are characterized by lower infrared emissivities (relative to most other surfaces) with a large spectral variation in the 8.5 – 12  $\mu\text{m}$  window. Because of these features in the surface emissivity, it is well known that BTDs associated with semi-transparent clouds can be dominated by these surface signals (e.g. [Pavolonis et al. 2005]). Figure 3.7 and Figure 3.8 show that this is, in fact, the case for the 8.5, 11  $\mu\text{m}$  and the 11, 12  $\mu\text{m}$  channel pairs, respectively. The BTD(8.5 – 11 $\mu\text{m}$ ) (Figure 3.7) is very sensitive to surface emissivity over most of the range of cloud emissivities for each cloud type considered. Conversely,  $\beta_{\text{tot}}(8.5\mu\text{m}, 11\mu\text{m})$  is very sensitive to cloud microphysics for mid and high clouds over a large range of cloud emissivities. The  $\beta_{\text{tot}}(8.5\mu\text{m}, 11\mu\text{m})$  sensitivity results for the low liquid water cloud indicate that an accurate estimation of the cloud height is needed over low emissivity surfaces to better isolate the cloud microphysical signal. This is likely due to the reduced difference between the upwelling clear sky radiance and the cloudy sky radiance caused by the reduced surface emissivities. The BTD(8.5 – 11 $\mu\text{m}$ ) is also very insensitive to cloud microphysics under these same conditions. The difference in surface emissivity between the 11 and 12  $\mu\text{m}$  channels is not quite as large as for the 8.5 and 11  $\mu\text{m}$  channels and the magnitude of the 12  $\mu\text{m}$  surface emissivity is larger than the 8.5  $\mu\text{m}$  surface emissivity. Thus, the  $\beta_{\text{tot}}(12\mu\text{m}, 11\mu\text{m})$  for the mid-level ash cloud and the low-level liquid water cloud exhibits a much greater sensitivity to cloud microphysics than

$\beta_{\text{tot}}(8.5\mu\text{m}, 11\mu\text{m})$  under the same conditions. Overall,  $\beta_{\text{tot}}(12\mu\text{m}, 11\mu\text{m})$  is much more sensitive to cloud microphysics than BTD(11 – 12 $\mu\text{m}$ ).

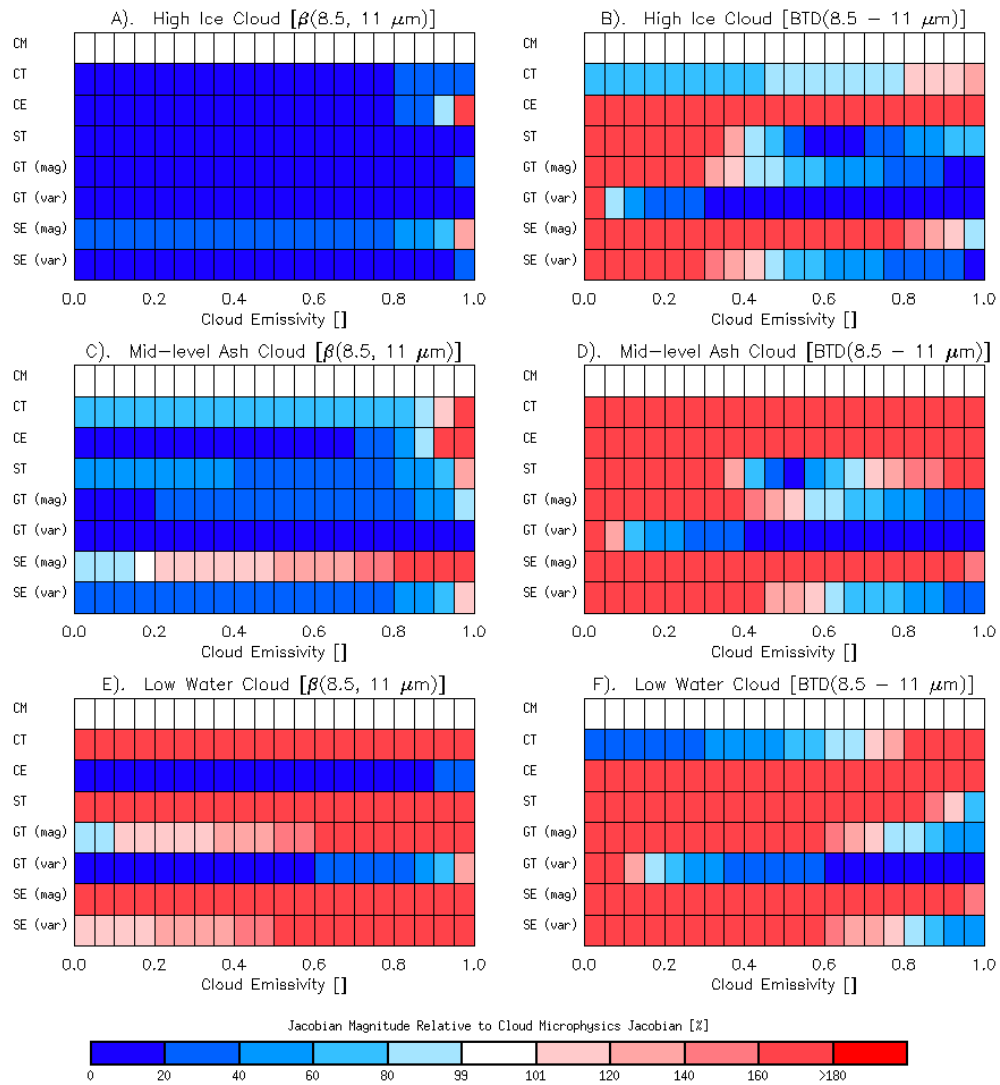


Figure 3.7: Same as Figure 3.5, except the Jacobians were evaluated for a scene located over the Sahara Desert.

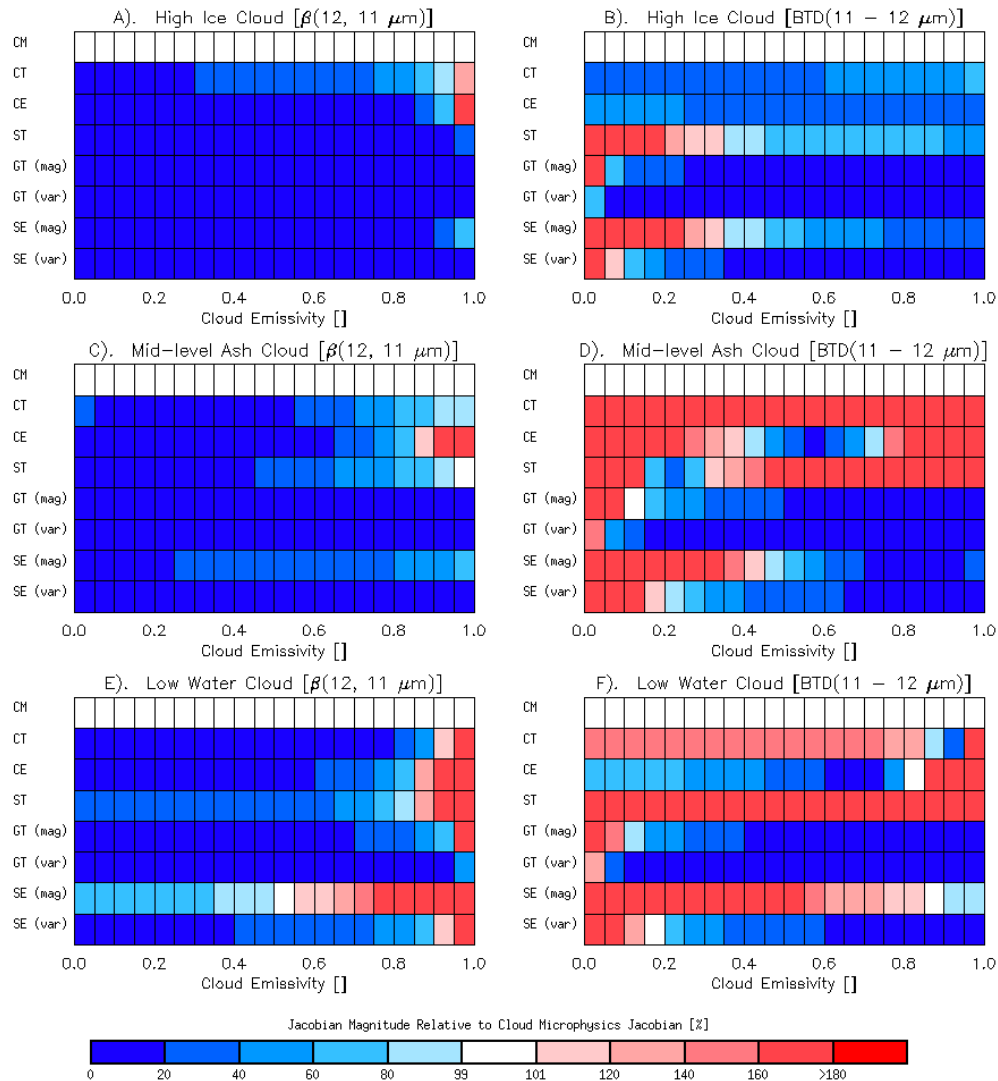


Figure 3.8: Same as Figure 3.7, except the 11 – 12- $\mu\text{m}$  brightness temperature difference and the 12- $\mu\text{m}$ /11- $\mu\text{m}$  effective absorption optical depth ratio were considered.

### 3.7. Alternative Cloud Vertical Structure Assumptions

While the results in the previous section indicate that the assumption of  $T_{\text{eff}} = T_{\text{tropopause}}$  used in constructing  $\beta_{\text{tot}}$  from combinations of the 8.5, 11, and 12  $\mu\text{m}$  channels is very effective, is it possible to improve upon this assumption under certain conditions? More specifically, can the microphysical sensitivity for mid and lower level clouds be improved if one has some *a priori* knowledge regarding the approximate cloud

emissivity? One method for determining if a cloud has a large cloud emissivity ( $\epsilon > 0.90$ ) is to calculate  $\beta_{\text{obs}}$  for a given channel pair choosing a cloud vertical level such that the 11  $\mu\text{m}$  emissivity is equal to 0.990. A value of 0.990 allows the other emissivity in the channel pair to have values greater than the 11  $\mu\text{m}$  emissivity, yet smaller than 1.0. In other words, using the 11  $\mu\text{m}$  channel as the first channel used in calculating  $\beta$ , the cloud emissivity of the second channel is determined using the vertical level that gives an 11  $\mu\text{m}$  cloud emissivity of 0.990. If the cloud actually has a large 11  $\mu\text{m}$  emissivity, then the  $\beta$  calculated using this assumption should fall well within the expected theoretical range given by the single scatter properties. If the cloud has an 11  $\mu\text{m}$  emissivity much smaller than 0.990, the  $\beta_{\text{obs}}$  should be greatly influenced by the spectral variability in surface emissivity and clear sky gaseous transmittance, and thus, may not fall within the expected theoretical range. The following analysis illustrates this point.

Figure 3.9 and Figure 3.10 show the  $\beta(12\mu\text{m}, 11\mu\text{m})$  and  $\beta(8.5\mu\text{m}, 11\mu\text{m})$  calculated under the assumption that 11  $\mu\text{m}$  cloud emissivity must be equal to 0.990 when the actual 11  $\mu\text{m}$  cloud emissivities were varied from 0.01 to 0.999. An ice cloud at the  $\sigma = 0.87$  level and a liquid water cloud at the  $\sigma = 0.33$  level were considered. The same maritime tropical (Figure 3.9) and Sahara Desert (Figure 3.10) conditions used in the Jacobian analysis presented in the previous sections were applied to generate these figures. The relevant parameters used in this analysis are shown in Table 3.2. The expected range of  $\beta(12\mu\text{m}, 11\mu\text{m})$  and  $\beta(8.5\mu\text{m}, 11\mu\text{m})$ , which are given by the single scatter property derived betas shown in Figure 3.3, are denoted by the dotted line in Figure 3.9 and Figure 3.10.

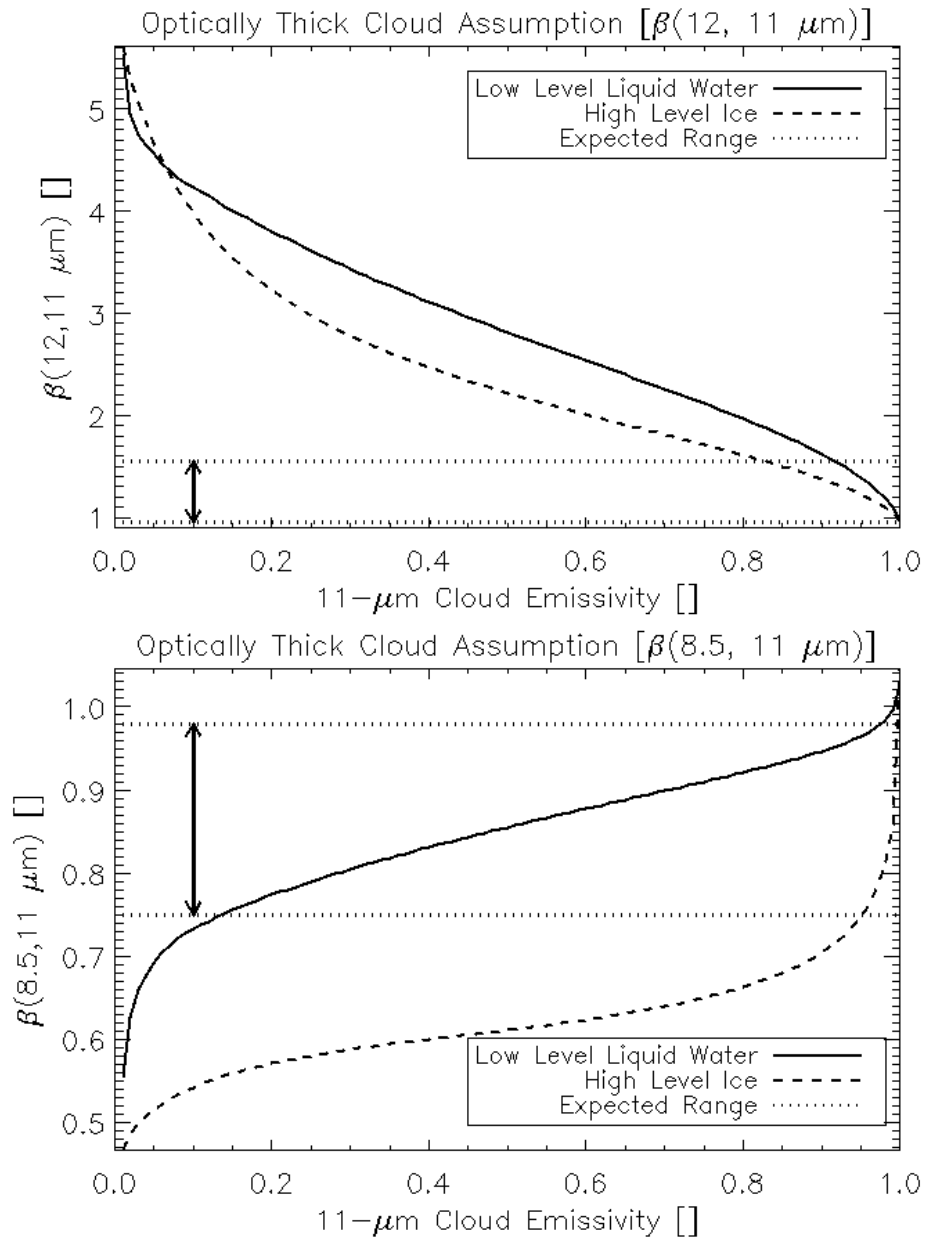


Figure 3.9: Calculations showing the 12- $\mu\text{m}/11\text{-}\mu\text{m}$  (top) and 8.5- $\mu\text{m}/11\text{-}\mu\text{m}$  (bottom) effective absorption optical depth ratio ( $\beta$ ) derived assuming a cloud vertical level that gives an 11- $\mu\text{m}$  cloud emissivity equal to 0.99 (performed regardless of the true cloud emissivity). Each  $\beta$  is expressed as a function of the true 11- $\mu\text{m}$  cloud emissivity for an upper tropospheric ice cloud (dashed line) and a lower tropospheric liquid water cloud (solid line). The range of values expected based on the single scatter properties are given by the dotted line. These calculations were performed for a maritime tropical location.

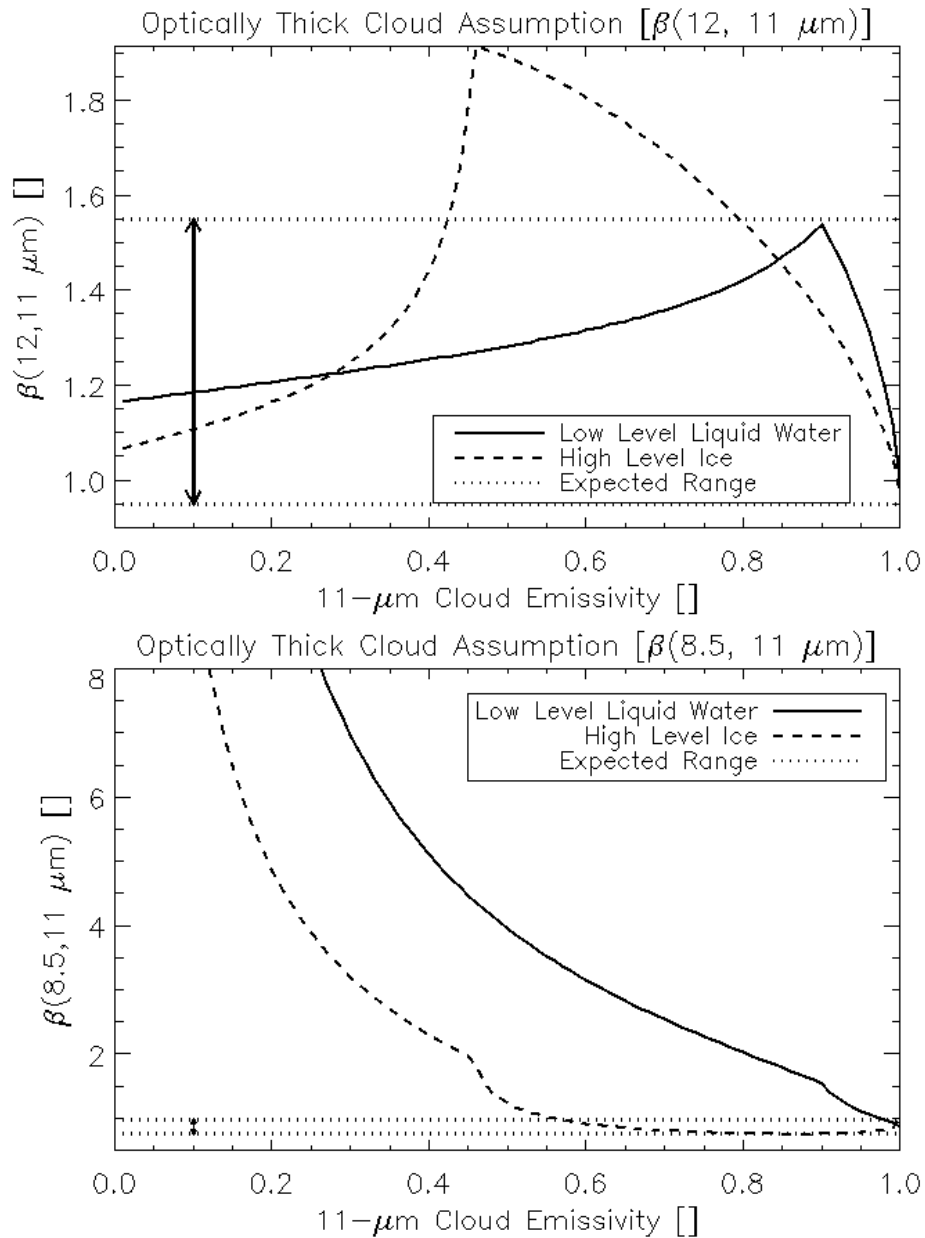


Figure 3.10: Same as Figure 3.9 except for a location over the Sahara Desert was considered.

Under the maritime tropical conditions listed in Table 3.2,  $\beta(12\mu\text{m}, 11\mu\text{m})$  is a very good indicator of whether a cloud has an  $11 \mu\text{m}$  emissivity  $> 0.90$  because unphysical values of  $\beta(12\mu\text{m}, 11\mu\text{m})$  are found over the low and middle ranges of  $11 \mu\text{m}$  cloud emissivity. It is important to note that we are not attempting to retrieve the actual

cloud emissivity, instead we are looking for a quick and effective way to determine which rough emissivity range (e.g. semi-transparent or near-opaque) the cloud falls into.  $\beta(12\mu\text{m}, 11\mu\text{m})$  owes its sensitivity to cloud opacity to the difference in atmospheric weighting functions between the two channels. Conversely,  $\beta(8.5\mu\text{m}, 11\mu\text{m})$  is not a very strong indicator of relative cloud opacity in this case because the difference in the 8.5 and 11  $\mu\text{m}$  clear sky atmospheric optical depth (0.84 and 1.04, respectively) is small compared to the difference in the 11 and 12  $\mu\text{m}$  clear sky optical depth (1.04 and 1.57, respectively). Differences in atmospheric optical depth are important, especially since the surface emissivity is spectrally constant in this case. The clear sky atmospheric optical depth (or alternatively, the atmospheric transmittance) impacts the difference between the black cloud radiance,  $B(\lambda, T_{\text{eff}})t_{\text{ac}}(\lambda) + R_{\text{ac}}(\lambda)$ , in Equation 2 and the clear sky radiance,  $R_{\text{clr}}(\lambda)$ . In other words, the upwelling top-of-atmosphere radiance from an elevated (e.g. above the surface) blackbody surface, and the atmosphere above ( $B(\lambda, T_{\text{eff}})t_{\text{ac}}(\lambda) + R_{\text{ac}}(\lambda)$ ), converges to the clear sky radiance ( $R_{\text{clr}}(\lambda)$ ) at a higher (colder in this case) atmospheric level for wavelengths that have a higher peaking atmospheric weighting function (or a surface emissivity that is significantly less than 1.0). The black cloud radiance is the only term in Equation ( 3.2) that is altered when a new cloud vertical level is considered. The maritime tropical results hold for most other conditions, but there are exceptions, as described below.

When the surface emissivity exhibits large spectral variations, such as over the Sahara Desert, the maritime tropical results are no longer valid. Figure 3.10 shows that  $\beta(8.5\mu\text{m}, 11\mu\text{m})$  can be used to identify the presence of opaque liquid water clouds over surfaces that have a small 8.5  $\mu\text{m}$  surface emissivity (0.738 in this case) relative to the

11 $\mu\text{m}$  surface emissivity (0.953 in this case). The smaller surface emissivity at 8.5  $\mu\text{m}$  leads to a much smaller difference between the 8.5  $\mu\text{m}$  black cloud radiance and the 8.5  $\mu\text{m}$  clear sky radiance in the denominator of Equation 2 relative to the same difference at 11  $\mu\text{m}$ .  $\beta(12\mu\text{m}, 11\mu\text{m})$  exhibits less sensitivity over the Sahara Desert for two reasons. The 11 and 12  $\mu\text{m}$  weighting functions differ less since the air mass is very dry. But, more importantly, the 12  $\mu\text{m}$  surface emissivity (0.978) is greater than the 11  $\mu\text{m}$  surface emissivity (0.953), which acts to reduce the impact of the spectral variation in clear sky atmospheric transmittance. Overall, these results indicate that it is possible to identify optically thick clouds using  $\beta$ . Given *a priori* knowledge of an opaque/near-opaque cloud, it may be possible to improve upon the  $T_{\text{eff}} = T_{\text{tropopause}}$  assumption by taking  $T_{\text{eff}}$  to be consistent with an optically thick cloud.

### 3.8. Summary

While the concept of effective absorption optical depth ratios ( $\beta$ ) has been around since at least the mid 1980's, this is the first study to explore the use of  $\beta$  for inferring cloud composition (ice, liquid water, ash, dust, etc...) in the absence of cloud vertical boundary information. The results showed that even in the absence of cloud vertical boundary information, one could significantly increase the sensitivity to cloud microphysics by converting the measured radiances to effective emissivity and constructing effective absorption optical depth ratios from a pair of spectral emissivities. The spectral pair(s) can be chosen to take advantage of differences in the spectral absorption for different compositions. The increase in sensitivity to cloud microphysics is relative to brightness temperature differences (BTDs) constructed from the same spectral pairs.

BTDs have been traditionally used to infer cloud composition. A detailed sensitivity analysis indicated that, for clouds with an 11  $\mu\text{m}$  emissivity less than about 0.85, commonly used BTDs constructed from 8.5, 11, and 12  $\mu\text{m}$  brightness temperatures are more sensitive to non-cloud variables, such as surface temperature, surface emissivity, and clear sky atmospheric transmittance, than cloud microphysics (which includes cloud composition). In contrast, betas constructed from the same spectral radiances showed a much greater sensitivity to cloud microphysics, despite the fact that a constant, and inaccurate, cloud level (taken to be the top of the troposphere) was assumed when calculating cloud emissivity. This result occurs because the spectral variation in radiance in the infrared “window” is largely insensitive to the cloud effective temperature. Additional analysis indicated that  $\beta$  could also be used to identify clouds that are optically thick (cloud emissivity  $> 0.9$ ). This knowledge can potentially be used to improve the sensitivity to cloud microphysics, and hence composition, for those same optically thick clouds. Another advantage of using  $\beta$  as opposed to BTDs is that  $\beta$  can be directly related to theoretical cloud particle distributions via the single scatter properties.

While the physical concepts described in this chapter apply to broadband and high spectral resolution (hyperspectral) infrared measurements, hyperspectral measurements offer a few clear advantages. Hyperspectral measurements provide more complete spectral coverage (e.g. there are generally fewer spectral gaps) and, hence, are a better source of microphysical information. The microphysical information is more robust because more of the detail contained in the index of refraction spectra can be resolved. The increased spectral sampling of hyperspectral measurements also allows one to smooth out noise associated with the measurements and/or the clear sky calculations.

## Chapter 4

### 4. Multispectral Analysis of Volcanic Ash and Dust

#### 4.1. Introduction

In an effort to address all of the aforementioned limitations (See Chapter 2) of previously published volcanic ash and dust detection methods, the Spectrally Enhanced Cloud Objects (SECO) technique has been developed. The SECO algorithm utilizes a combination of radiative transfer theory, a statistical model, and image processing techniques to identify volcanic ash and dust clouds in satellite imagery with skill comparable to that of a human expert. The fully automated SECO technique is globally applicable and can be adapted to a wide range of low earth orbit and geostationary satellite sensors. The SECO algorithm is designed to take full advantage of each sensor's volcanic ash/dust relevant capabilities. The SECO algorithm is described over the course of two chapters. This chapter will describe how the SECO algorithm utilizes advanced metrics to identify satellite pixels that potentially contain volcanic ash and/or dust with improved skill relative to the most utilized existing method. In Chapter 6, the cloud object based techniques that are applied to the results of the analysis, described in this chapter, will be discussed. In addition, Chapter 6 demonstrates that the end results of the complete SECO algorithm are comparable to manual analysis performed by human experts (especially in terms of false alarm rate). The SECO technique is the first fully automated algorithm, applicable to nearly any satellite sensor with infrared capabilities, which can be used in advanced real-time applications such as ash cloud alerting and ash/dust cloud dispersion forecasting. The SECO technique can also serve as a valuable research tool.

#### ***4.2. Satellite Measurements***

The SECO method is designed such that it can be applied to nearly any low earth orbit (LEO) or geostationary (GEO) imaging sensor, such that frequent global results can be obtained. The method can also be applied to sounding instruments, including hyperspectral infrared sounders, but this dissertation will focus on the higher spatial resolution (and higher temporal resolution in the case of GEO) measurements offered by imaging instruments. Spectral measurements centered near 0.65 (daytime only), 3.9, 7.3, 8.5, 11, and 12  $\mu\text{m}$  can be used by the SECO algorithm. The rationale for selecting these channels will be described in a later section. More specifically, the SECO algorithm can utilize any of the channel combinations shown in Table 4.1. For each channel combination the relevant sensors are also listed (Table 4.2 defines the sensor acronyms). The algorithm is designed to utilize the greatest number of spectral channels possible for a given sensor taking into account the quality of each spectral measurement on a pixel-by-pixel basis. While measurements that directly depend on solar zenith angle are utilized when possible, the SECO approach does not require sunlight to be present. The algorithm can operate solely with measurements that are not influenced by reflected sunlight.

Table 4.1: Possible spectral channel combinations that can be used in the ash/dust detection algorithm are shown as a function of satellite imaging sensor spectral capabilities (relevant to ash and dust detection). Tier I sensors offer the most channels of relevance to the ash/dust detection algorithm presented in this dissertation and Tier III sensors offer the least. Sun glint is assumed to be present over water surfaces if the glint angle is less than 40°. Stray light is assumed to be present if the solar zenith angle exceeds 90° and the measured 0.65 µm counts is greater than a sensor dependent threshold. Please see Table 4.2 for a list of sensor acronyms.

<b>Tier I Sensors:</b>		
MODIS MSG SEVIRI GOES-R ABI Himawari-8/9 AHI MTG FCI		
Approximate Central Wavelength	Sensor Channel Numbers	Conditions Required for Use*
0.65, 3.9, 7.3, 8.5, 11, 12 µm	1, 20, 28, 29, 31, 32 1, 4, 6, 7, 9, 10 2, 7, 10, 11, 14, 15 3, 7, 10, 11, 14, 15 3, 9, 11, 12, 14, 15	Solar zenith angle < 85° and no sun glint
3.9, 7.3, 8.5, 11, 12 µm	20, 28, 29, 31, 32 4, 6, 7, 9, 10 7, 10, 11, 14, 15 7, 10, 11, 14, 15 9, 11, 12, 14, 15	Solar zenith angle > 90° and no detectable stray light
7.3, 8.5, 11, 12 µm	28, 29, 31, 32 6, 7, 9, 10 10, 11, 14, 15 10, 11, 14, 15 11, 12, 14, 15	Only used if previous two channel combinations are not possible
8.5, 11, 12 µm	29, 31, 32 7, 9, 10 11, 14, 15 11, 14, 15 12, 14, 15	Only used if previous three channel combinations are not possible
11, 12 µm	31, 32 9, 10 14, 15 14, 15 14, 15	Only used if previous four channel combinations are not possible
<b>Tier II Sensors:</b>		
VIIRS		
Approximate Central Wavelength	Sensor Channel Numbers	Conditions Required for Use*
0.65, 3.9, 8.5, 11, 12 µm	M5, M12, M14, M15, M16	Solar zenith angle < 85° and no sun glint
3.9, 8.5, 11, 12 µm	M12, M14, M15, M16	Solar zenith angle > 90° and no detectable stray light
8.5, 11, 12 µm	M14, M15, M16	Only used if previous two channel combinations are not possible
11, 12 µm	M15, M16	Only used if previous three channel combinations are not possible
<b>Tier III Sensors:</b>		
AVHRR COMS-MI GOES Imager# MTSAT Imager		
Approximate Central Wavelength	Sensor Channel Numbers	Conditions Required for Use*
0.65, 3.9, 11, 12 µm	1, 3b, 4, 5 1, 2, 4, 5 1, 2, 4, 5 1, 5, 2, 3	Solar zenith angle < 85° and no sun glint
3.9, 11, 12 µm	3b, 4, 5 2, 4, 5 2, 4, 5 5, 2, 3	Solar zenith angle > 90° and no detectable stray light
11, 12 µm	4, 5 4, 5 4, 5 2, 3	Only used if previous two channel combinations are not possible

\*Each channel in a given spectral combination must also pass quality control. If one or more channels in a combination does not pass quality control the next best channel combination is attempted.

#The 12 µm channel is only available on the GOES-8, GOES-9, GOES-10, and GOES-11 spacecraft.

*Table 4.2: The satellite imaging radiometers of greatest relevance to the ash/dust detection algorithm described in this dissertation is listed below. Each sensor may be present on multiple spacecraft with different orbital parameters.*

<b>Sensor Acronym</b>	<b>Acronym Meaning</b>
AVHRR	Advanced Very High Resolution Radiometer
COMS MI	Communication, Ocean, and Meteorological Satellite (COMS) Meteorological Imager (MI)
GOES Imager	Geostationary Operational Environmental Satellite (GOES) Imager
GOES-R ABI*	Next Generation Geostationary Operational Environmental Satellite (GOES-R) Advanced Baseline Imager (ABI)
Himawari-8/9 AHI*	Himawari-8/9 Advanced Himawari Imager (AHI)
MODIS	MODerate Resolution Imaging Spectroradiometer
MTSAT Imager	Multifunctional Transport SATellites (MTSAT) Imager
MSG SEVIRI	Meteosat Second Generation (MSG) Spinning Enhanced Visible and Infrared Imager
MTG FCI*	Meteosat Third Generation (MTG) Flexible Combined Imager (FCI)
VIIRS	Visible Infrared Imaging Radiometer Suite

\*Capability will be launched and deployed in 2014 or later

The MODerate Resolution Imaging Spectroradiometer (MODIS), which has all the spectral channels (with a 1 km resolution at nadir) required to test each possible channel combination, is the primary instrument for developing and demonstrating the SECO approach. In Chapter 6, results from other sensors will also be briefly highlighted to help illustrate that the SECO approach is generic and robust enough to be applied to virtually any sensor (past, current, and future sensors included). The operational meteorological imaging sensor (as of early 2014) excluded from Table 4.1 and Table 4.2

is the Geostationary Operational Environmental Satellite (GOES) Imager on GOES-12 through GOES-15 [Schmit et al. 2001]. The 12- $\mu\text{m}$  channel on GOES-12 through GOES-15 was replaced by a 13.3  $\mu\text{m}$  channel, which, due to  $\text{CO}_2$  absorption, is more challenging to use for detecting volcanic ash and dust [Ellrod 2004]. We have developed the ability to utilize the 13.3- $\mu\text{m}$  channel in lieu of the 12  $\mu\text{m}$  channel, but this will not be discussed in this dissertation in order to focus on the more common case of the 12  $\mu\text{m}$  channel being available.

#### ***4.3. Definition of Volcanic Ash and Dust Clouds***

Prior to describing the SECO algorithm, we must first explain how we define volcanic ash and dust clouds. In this dissertation, volcanic ash and dust clouds are defined as a collection of satellite pixels that can be manually identified as ash or dust in well-scaled (visible, near-infrared, and infrared) *passive* satellite imagery by a human expert. Such a definition is quite reasonable given that automated algorithms can only detect volcanic ash or dust if a spatially and temporally (if applicable) coherent signature is present in the calibrated radiances for a given satellite sensor (e.g. the ash or dust cloud contributes to the measured spectral radiances more than noise). Thus, there are two general scenarios in which airborne ash or dust, if actually present, cannot be qualitatively (and hence quantitatively) detected using passive satellite data: 1). Overlapping cloud layers obscure the ash or dust cloud, 2). The mass loading of the ash is below detection limits for a given set of observing conditions and instrument capabilities. Prata and Prata [2012], Francis et al. [2012], and Pavolonis et al. [2013] showed that volcanic ash can generally be identified in passive satellite observations if it is the highest cloud layer and has a concentration with order of magnitude  $10^{-2}$   $\text{g/m}^2$  or greater.

Multispectral false color imagery sometimes referred to as Red-Green-Blue or RGB imagery is a proven tool used by human analysts, including operational forecasters, to manually identify volcanic ash and dust [Lensky and Rosenfeld 2008; Millington et al 2012]. Volcanic ash and dust relevant false color imagery is designed to maximize the color contrast between volcanic ash and dust and all other observable features (other cloud types and clear sky features) by exploiting the unique spectral variability of absorption and reflection exhibited by volcanic ash and dust relative to other cloud types and most surface features. More specifically, well-known absorption and reflection properties at wavelengths centered near 3.9, 8.5, 11, and 12  $\mu\text{m}$  are exploited [Prata and Grant 2001; Pavolonis et al. 2006; Lensky and Rosenfeld 2008; Pavolonis 2010; Francis et al. 2012; Pavolonis et al 2013]. From these spectral channels two false color images are generated as described next.

#### *4.3.1. Overview of 12-11, 11-3.9, 11 $\mu\text{m}$ RGB*

The first false color image is constructed by displaying the 12-11  $\mu\text{m}$  brightness temperature difference (BTD) on the red color gun, the 11-3.9  $\mu\text{m}$  BTD on the green color gun, and the 11  $\mu\text{m}$  brightness temperature (BT) on the blue color gun. Each parameter is linearly scaled and the default scaling range is given in Table 4.3. A different 11-3.9  $\mu\text{m}$  scaling range is used during the day (compared to night) to account for the influence of reflected sunlight at 3.9  $\mu\text{m}$ . The scaling range can be optionally modified to provide better contrast as needed on a case-by-case basis.

Table 4.3: The recipe used to create the 12-11, 11-3.9, 11  $\mu\text{m}$  false color (or Red-Green-Blue) image is shown. Each parameter is linearly scaled to the value range given in the third and fourth columns of the table.

Color Gun	Parameter	Default Scaling Min (K)	Default Scaling Max (K)
Red	12-11 $\mu\text{m}$ BTD*	-4.0	2.0
Green (day)	11-3.9 $\mu\text{m}$ BTD*	-60.0	0.0
Green (Night)	11-3.9 $\mu\text{m}$ BTD*	-30.0	5.0
Blue	11 $\mu\text{m}$ BT#	243.0	293.0

\*BTD = Brightness Temperature Difference

#BT = Brightness Temperature

An example daytime 12-11, 11-3.9, 11  $\mu\text{m}$  false color image is shown in Figure 4.1 (*Terra* MODIS – February 19, 2001 at 23:10 UTC), and a nighttime example is shown in Figure 4.2 (*Terra* MODIS – February 20, 2001 at 23:10 UTC). Annotations are used to highlight various features, including volcanic ash produced by an eruption of Cleveland volcano (Alaska), in Figure 4.1 and Figure 4.2. Generally well understood differences in spectral absorption and reflection combine to give volcanic ash and dust a distinct pink or reddish appearance in the 12-11, 11-3.9, 11  $\mu\text{m}$  RGB image [Lensky and Rosenfeld 2008]. In contrast, mid and high level meteorological clouds will have an appearance that is generally distinctively different from ash and dust primarily because of a much smaller contribution from the red color gun (see Figure 4.1 and Figure 4.2). While certain cloud (e.g. lower level liquid water clouds during the day) and surface features not related to volcanic ash or dust may also sometimes appear pink or red, the combination of the RGB color and spatial pattern recognition allow a human expert to identify volcanic ash and dust clouds that are not obscured by other clouds layers with very good skill. This is why Volcanic Ash Advisory Centers (VAACs) routinely utilize manual analysis of satellite imagery to define the horizontal location of ash clouds in

volcanic ash advisories. Refer to Pavolonis et al. [2006] for a detailed review of the absorption and scattering properties of clouds at 3.9, 11, and 12  $\mu\text{m}$ .

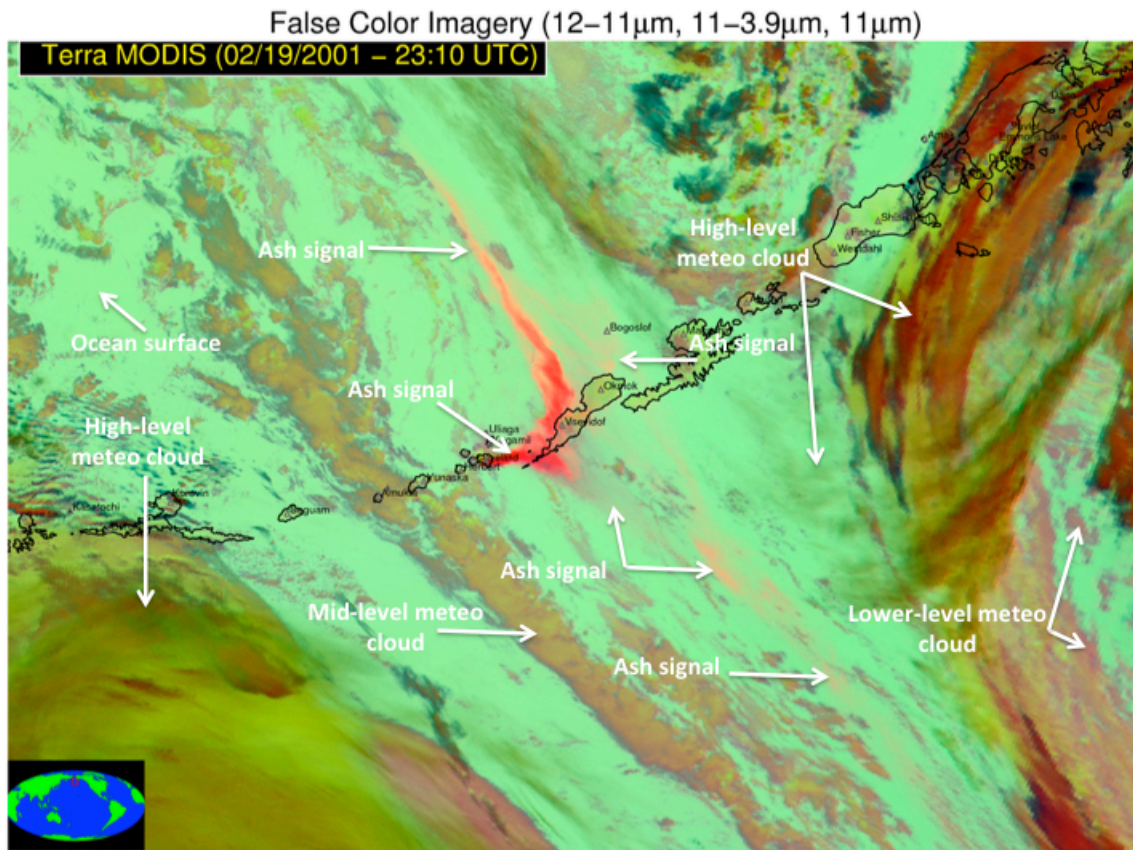
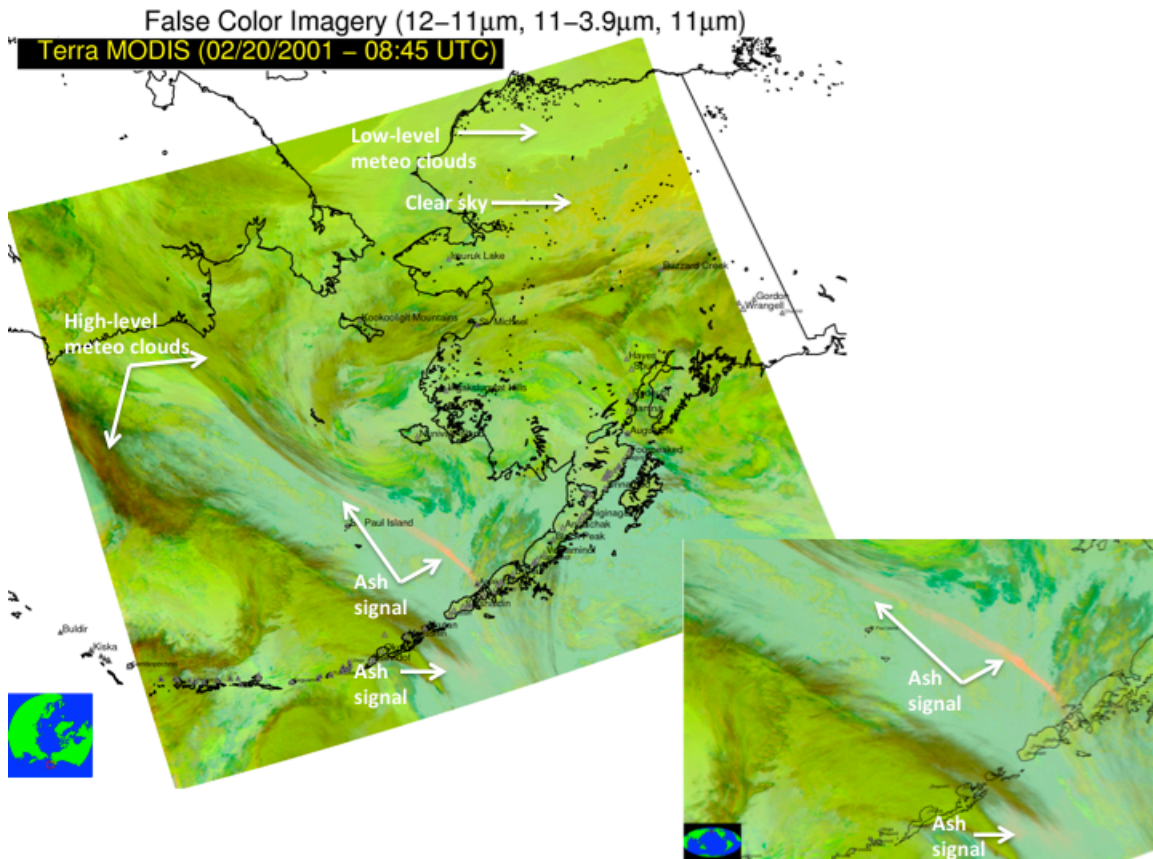


Figure 4.1: A false color Terra MODIS image centered on the Aleutian Islands (Alaska) on February 19, 2001 at 23:10 UTC is shown. The 12 - 11  $\mu\text{m}$  brightness temperature difference (BTD) is displayed on the red color gun, the 11 - 3.75  $\mu\text{m}$  BTD is displayed on the green color gun, and the 11  $\mu\text{m}$  brightness temperature is displayed in the blue color gun. The scaling ranges used to make the image are shown in Table 4.3. The white annotations are used to highlight some important features. The volcanic ash cloud was produced by an eruption of Mount Cleveland, Alaska. In the annotations, “meteo cloud” refers to liquid water or ice clouds generated by typical meteorological processes. This MODIS image was taken from the sunlit portion of the orbit.



*Figure 4.2: Same as Figure 4.1 except the Terra MODIS image is valid at February 20, 2001 at 08:45 UTC. The inset shows the zoomed in view of the volcanic cloud produced by an eruption of Mount Cleveland. This MODIS image was taken at night.*

#### 4.3.2. Overview 12-11, 11-8.5, 11 µm RGB

The second type of false color image is constructed in the same manner as the 12-11, 11-3.9, 11 µm RGB except the 8.5 µm channel is used in lieu of the 3.9 µm channel. Unlike the 12-11, 11-3.9, 11 µm RGB, the colors in the 12-11, 11-8.5, 11 µm RGB are influenced by SO<sub>2</sub> because several SO<sub>2</sub> absorption lines are located near 8.5 µm [e.g. Watson et al. 2004]. Each parameter is linearly scaled and the default scaling range is given in Table 4.4. The scaling range can be optionally modified to provide better contrast as needed on a case-by-case basis.

*Table 4.4: The recipe used to create the 12-11, 11-8.5, 11  $\mu\text{m}$  false color (or Red-Green-Blue) image is shown. Each parameter is linearly scaled to the value range given in the third and fourth columns of the table.*

<b>Color Gun</b>	<b>Parameter</b>	<b>Default Scaling Min (K)</b>	<b>Default Scaling Max (K)</b>
Red	12-11 $\mu\text{m}$ BTD*	-4.0	2.0
Green	11-8.5 $\mu\text{m}$ BTD*	-6.0	6.0
Blue	11 $\mu\text{m}$ BT#	243.0	293.0

\*BTD = Brightness Temperature Difference

#BT = Brightness Temperature

An annotated 12-11, 11-8.5, 11  $\mu\text{m}$  false color image, for the same scene depicted in Figure 4.1 (Figure 4.2), is shown in Figure 4.3 (Figure 4.4). When  $\text{SO}_2$  is not present, or is only present in very small amounts, most volcanic ash and dust clouds will take on a pink or reddish color, while liquid water clouds will have a beige to light yellow color and ice clouds will appear brownish or blackish [Lensky and Rosenfeld 2008]. See Chapter 3 for a review of cloud absorption and scattering properties in the 8 – 13  $\mu\text{m}$  spectral range. When  $\text{SO}_2$  is present in larger concentrations, the lack of  $\text{SO}_2$  absorption in the 11 and 12  $\mu\text{m}$  channels combined with the  $\text{SO}_2$  absorption in the 8.5  $\mu\text{m}$  channel causes ash clouds (the combination of ash and  $\text{SO}_2$  is far more common than the combination of dust and  $\text{SO}_2$ ) to be bright yellow in the RGB when  $\text{SO}_2$  is also present at the same vertical levels or above the ash in the same atmospheric column (see Cleveland volcano ash cloud in Figure 4.3 and Figure 4.4). While under clear sky conditions the spectral variability in the emissivity of land surfaces [Seemann et al. 2008] can produce similar colors in the 12-11, 11-8.5, 11  $\mu\text{m}$  RGB as ash and dust clouds, a human expert can generally use pattern recognition to differentiate between ash/dust and land surface features.

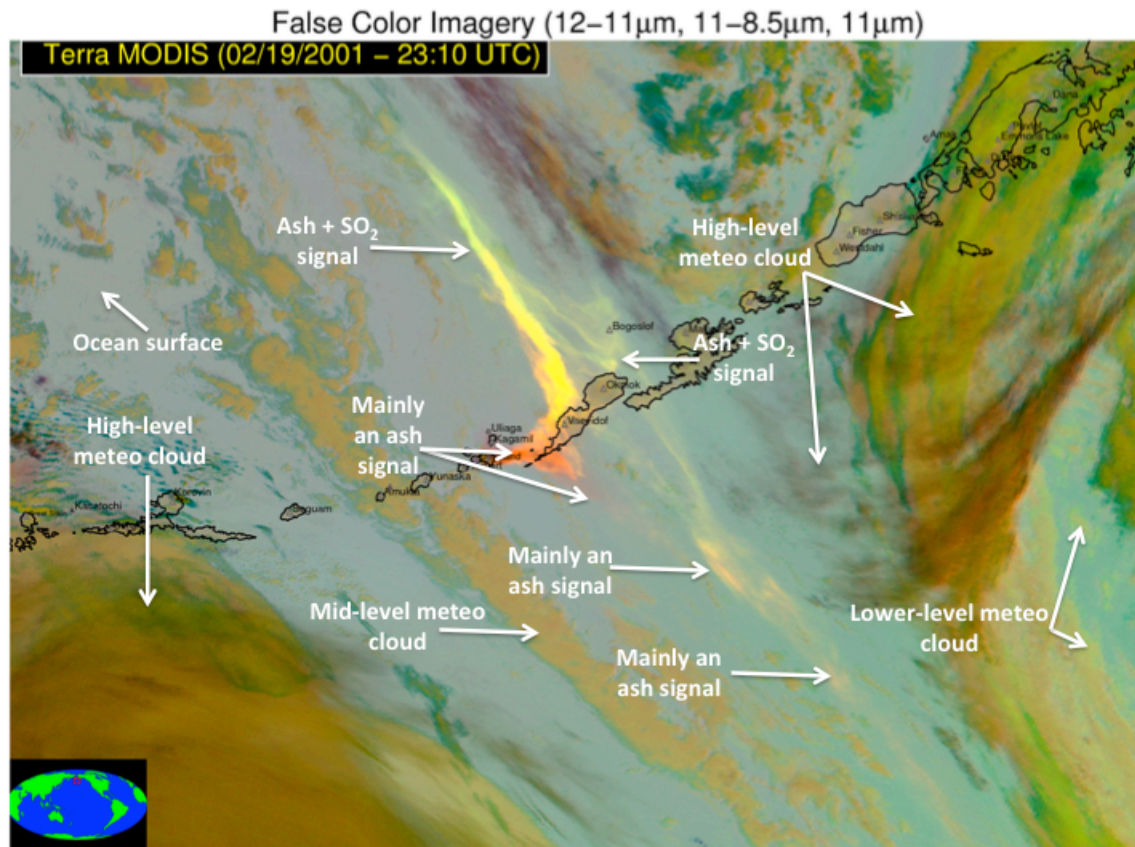


Figure 4.3: A false color Terra MODIS image centered on the Aleutian Islands (Alaska) on February 19, 2001 at 23:10 UTC is shown. The 12 - 11  $\mu$ m brightness temperature difference (BTD) is displayed on the red color gun, the 11 - 8.5  $\mu$ m BTD is displayed on the green color gun, and the 11  $\mu$ m brightness temperature is displayed in the blue color gun. The scaling ranges used to make the image are shown in Table 4.4. The white annotations are used to highlight some important features. The volcanic ash and SO<sub>2</sub> cloud was produced by an eruption of Mount Cleveland, Alaska. In the annotations, “meteo cloud” refers to liquid water or ice clouds generated by typical meteorological processes. This MODIS image was taken from the sunlit portion of the orbit.

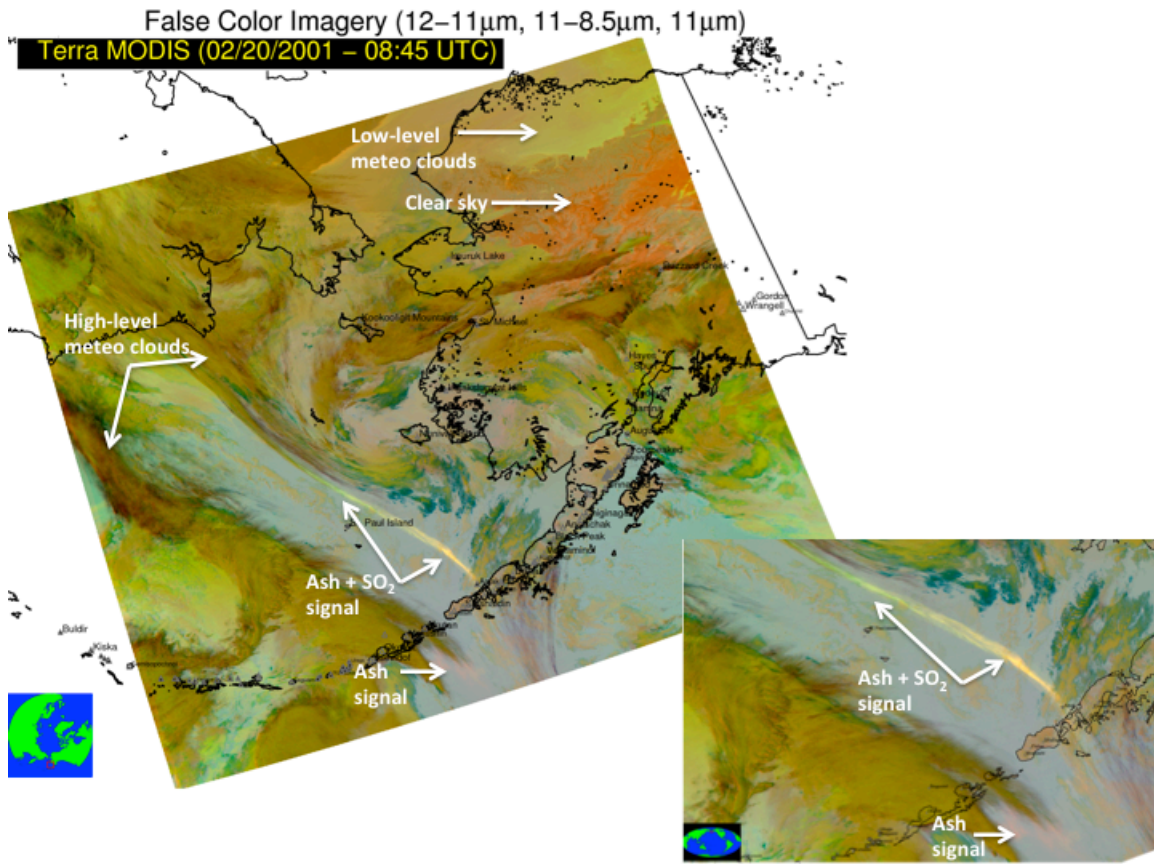


Figure 4.4: Same as Figure 4.3 except the Terra MODIS image is valid at February 20, 2001 at 08:45 UTC. The inset shows the zoomed in view of the volcanic cloud produced by an eruption of Mount Cleveland. This MODIS image was taken at night.

#### 4.3.3. Traditional “Split-window” Imagery

The oldest, and most common, method used to identify ash and dust clouds in passive satellite data is known as the “reverse absorption” or “split-window” technique [Prata 1989a; Prata 1989b]. The traditional “split-window” technique simply consists of calculating the 11 – 12  $\mu\text{m}$  BTD and applying a threshold. Volcanic ash and dust typically absorb more radiation at 11  $\mu\text{m}$  compared to 12  $\mu\text{m}$ , while the opposite is generally true for meteorological clouds. Thus, a threshold of about 0 K is often used to differentiate between ash/dust and other features. A “split-window” BTD image of the same scene depicted in Figure 4.1 and Figure 4.3 (Figure 4.2 and Figure 4.4) is shown in

Figure 4.5 (Figure 4.6). While the general presence of volcanic ash from the eruption of Cleveland volcano is obvious, there are several portions of the Cleveland volcanic clouds in Figure 4.5 and Figure 4.6 that have 11 – 12  $\mu\text{m}$  BTD values that are very similar to other non-volcanic cloud features, which limits the effectiveness of traditional “split-window” ash/dust detection in quantitative applications. When viewed globally, the ambiguity of the 11 – 12  $\mu\text{m}$  BTD is far more severe than what is shown in these two scenes from the Alaska region [Pavolonis et al. 2006]. Note how the spatial extent of the volcanic ash is generally easier to ascertain in the tri-spectral false color images, which, qualitatively, highlights the value of additional spectral information. Given that “split-window” based ash and dust detection techniques are still widely used in qualitative and quantitative applications, the performance of the SECO algorithm relative to the “split-window” approach will be discussed in this chapter and Chapter 6.

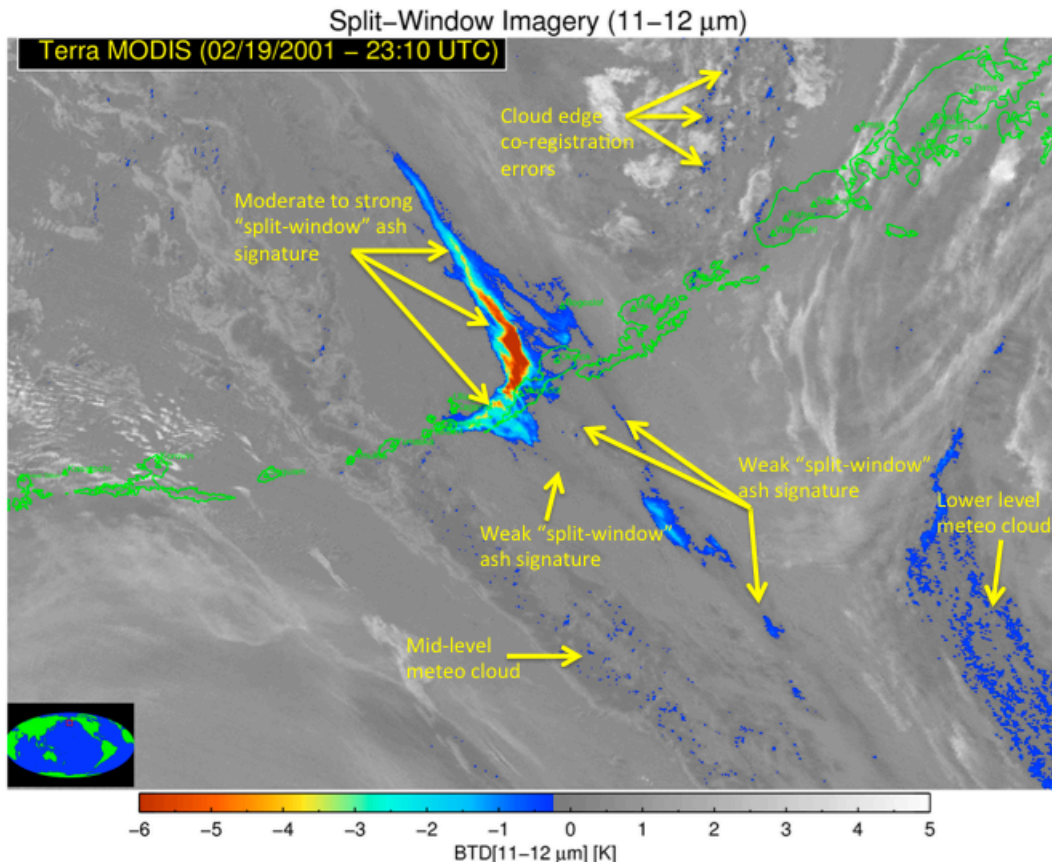


Figure 4.5: A “split-window” (11 – 12  $\mu\text{m}$  brightness temperature difference) Terra MODIS image centered on the Aleutian Islands (Alaska) on February 19, 2001 at 23:10 UTC is shown. Yellow annotations are used to highlight certain key features including an ash cloud produced by an eruption of Mount Cleveland, Alaska. In the annotations, “meteo cloud” refers to liquid water or ice clouds generated by typical meteorological processes. This MODIS image was taken from the sunlit portion of the orbit.

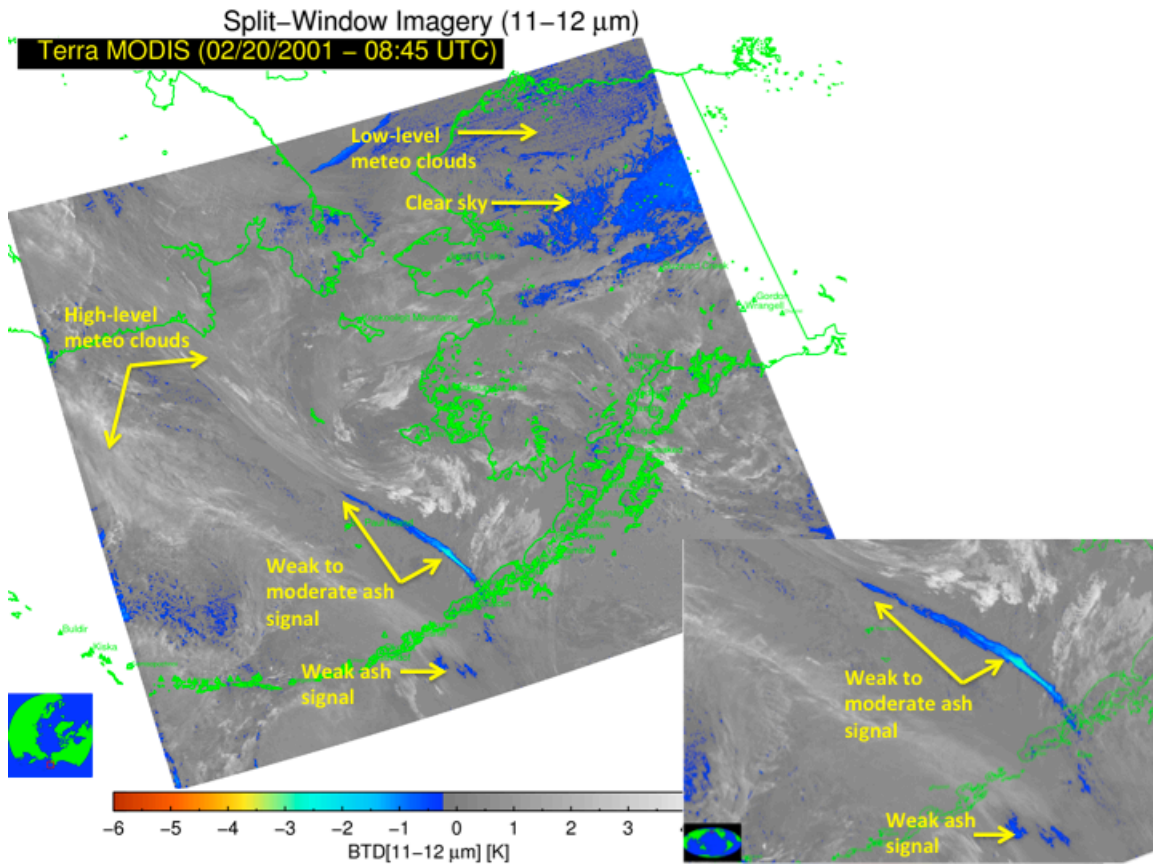


Figure 4.6: Same as Figure 4.5 except the Terra MODIS image is valid at February 20, 2001 at 08:45 UTC. The inset shows the zoomed in view of the volcanic cloud produced by an eruption of Mount Cleveland. This MODIS image was taken at night.

#### 4.4. SECO Algorithm – Multispectral Analysis

The SECO algorithm is comprised of four primary components. First, calibrated and navigated spectral measurements are converted to more robust spectral parameters when possible (e.g. increased sensitivity to cloud composition and decreased sensitivity to background conditions). Next, the spectrally robust metrics and a naïve Bayesian approach are used to estimate the probability that a given satellite pixel is part of an ash or dust cloud. In the third component of the SECO algorithm, spatially connected satellite pixels that exceed an ash/dust probability threshold are grouped into cloud objects and various statistical properties are computed for each cloud object. Finally, the

cloud object statistics are used to determine which objects are most likely ash/dust clouds. All pixels associated with objects determined to be volcanic ash or dust are classified as ash/dust and all other pixels are classified as a non-ash/dust feature. The first two components of the SECO algorithm (derivation of advanced metrics and estimation of ash/dust probability) are described in the following sections of this chapter, while the cloud object components are described in Chapter 6.

#### 4.4.1. Description of Spectral Metrics

Most of the infrared-based spectral metrics are based on the concepts described in Chapter 3. In lieu of infrared brightness temperatures and brightness temperature differences, which are very sensitive to background conditions (surface temperature, surface emissivity, atmospheric moisture and temperature), cloud emissivity and radiative parameters known as  $\beta$ -ratios are utilized. As demonstrated in Chapter 3, the effective cloud emissivity at a given infrared wavelength is computed as given in Equations ( 4.1) and ( 4.2).

$$\varepsilon_{eff}(\lambda) = \frac{R_{obs}(\lambda) - R_{clr}(\lambda)}{R_{cld}(\lambda) - R_{clr}(\lambda)} \quad (4.1)$$

$$R_{cld}(\lambda) = R_{ac}(\lambda) + B(\lambda, T_{eff})t_{ac}(\lambda) \quad (4.2)$$

In Equation ( 4.1), which is derived in Appendix A,  $\lambda$  is wavelength,  $R_{obs}$  is the observed radiance,  $R_{clr}$  is the clear sky radiance, and  $R_{cld}$  is the blackbody emission from the cloud that is transmitted to the top of the atmosphere. The effective cloud emissivity [Cox 1976] is denoted by  $\varepsilon_{eff}$ . The effects of cloud scattering are implicitly captured by the effective cloud emissivity (see Cox [1976]). In Equation ( 4.2),  $R_{ac}$  and  $t_{ac}$  are the above

cloud upwelling atmospheric radiance and transmittance, respectively.  $B$  is the Planck Function, and  $T_{\text{eff}}$  is the effective cloud temperature. The effective cloud temperature is most often different from the thermodynamic cloud top temperature since the emission of radiation originates from a layer in the cloud. The depth of this layer depends on the cloud extinction profile, which is generally unknown. The clear sky transmittance and radiance terms are determined using surface temperature, atmospheric temperature, water vapor, and ozone profiles from the Global Forecast Model (GFS) [Hamill et al. 2006], surface emissivity from the Seebor database [Seemann et al. 2008], the satellite zenith angle, and a regression based clear sky radiative transfer model [Hannon et al. 1996]. The procedure for determining the clear sky radiance and transmittance is the same as described in Heidinger and Pavolonis [2009] and Chapter 3.

The spectral variation of the effective cloud emissivity is directly related to cloud microphysical information (e.g. particle size, shape, composition, etc...). Effective optical depth ratios, otherwise known as  $\beta$ -ratios, have been previously used to extract cloud microphysical information from infrared measurements [Inoue 1985; Inoue 1987; Parol et al. 1991; Giraud et al. 1997; Heidinger and Pavolonis 2009; Chapter 3 of this dissertation]. For a given spectral pair of effective emissivity ( $\varepsilon_{\text{eff}}(\lambda_1)$  and  $\varepsilon_{\text{eff}}(\lambda_2)$ ) or effective absorption optical depth ( $\tau_{\text{abs,eff}}(\lambda_1)$  and  $\tau_{\text{abs,eff}}(\lambda_2)$ ), the effective absorption optical depth ratio,  $\beta(\lambda_1, \lambda_2)$ , can be computed using Equation ( 4.3).

$$\beta(\lambda_1, \lambda_2) = \frac{\ln[1 - \varepsilon_{\text{eff}}(\lambda_1)]}{\ln[1 - \varepsilon_{\text{eff}}(\lambda_2)]} = \frac{\tau_{\text{abs,eff}}(\lambda_1)}{\tau_{\text{abs,eff}}(\lambda_2)} \quad (4.3)$$

In order to compute  $\beta(\lambda_1, \lambda_2)$  for a given spectral pair, the location of the radiative center of the cloud, in the vertical, must be specified (see Equation ( 4.1) and ( 4.2)), but is

unknown since pixels that likely contain ash or dust must be identified prior to retrieving cloud properties such as  $T_{\text{eff}}$  (see Chapter 5). Thus, the “top of troposphere” and “opaque cloud” assumptions, described in detail in Chapter 3, are utilized. The “top of troposphere”  $\beta$ -ratio,  $\beta_{\text{tot}}(\lambda_1, \lambda_2)$ , is computed by assuming that the cloud radiative center is located at the top of the troposphere. The “opaque cloud”  $\beta$ -ratio,  $\beta_{\text{opaque}}(\lambda_1, \lambda_2)$ , is computed by assuming that the cloud radiative center is located at the highest level of the troposphere that results in  $\epsilon_{\text{eff}}(\lambda_1)$  or  $\epsilon_{\text{eff}}(\lambda_2)$  being equal to 0.98 (using Equation 1). As described in Chapter 3, the “tropopause” or “top of troposphere” assumption is very effective for determining the composition of semi-transparent clouds, while the “opaque cloud” assumption provides some additional skill, particularly when classifying optically thick clouds.  $\beta_{\text{tot}}(\lambda_1, \lambda_2)$  and  $\beta_{\text{opaque}}(\lambda_1, \lambda_2)$ , while very useful, do not account for underlying cloud layers. Semi-transparent ash and dust clouds will often reside above one or more meteorological cloud layers. In an attempt to roughly account for the influence of an underlying liquid water or ice cloud layer, a second and third set of “top of troposphere”  $\beta$ -ratios are computed (only for 11 and 12  $\mu\text{m}$  spectral pairing) by replacing  $R_{\text{clr}}(\lambda)$  in Equation ( 4.1) with the top of atmosphere radiance produced by a blackbody emitter located at the 0.8 and 0.7 sigma levels (a terrain following vertical coordinate), respectively. The pressure level ( $P$ ) associated with a given sigma ( $\sigma$ ) value is computed using Equation ( 4.4).

$$P = (P_{\text{surface}})\sigma \quad (4.4)$$

The 0.8 sigma level is used to approximate a low level (relative to the surface) underlying cloud layer, and  $\sigma = 0.7$  is used to approximate a mid level underlying cloud layer. The

second set of  $\beta$ -ratios are denoted by  $\beta_{\text{tot}_\sigma 8}(\lambda_1, \lambda_2)$ , and the third set are denoted by  $\beta_{\text{tot}_\sigma 7}(\lambda_1, \lambda_2)$ .

The choice of spectral channel pairings  $(\lambda_1, \lambda_2)$  used to construct  $\beta$ -ratios is designed to take advantage of absorption/scattering features that are generally unique to volcanic ash and/or dust clouds. As shown in Chapter 3, the combination of  $\beta(12\mu\text{m}, 11\mu\text{m})$  and  $\beta(8.5\mu\text{m}, 11\mu\text{m})$  is extremely useful for discriminating between volcanic ash/dust clouds and other cloud features. In the absence of large amounts of  $\text{SO}_2$ ,  $\beta(8.5\mu\text{m}, 11\mu\text{m})$  and, to a lesser extent,  $\beta(12\mu\text{m}, 11\mu\text{m})$  can individually take on similar values as meteorological clouds. The combination of  $\beta(12\mu\text{m}, 11\mu\text{m})$  and  $\beta(8.5\mu\text{m}, 11\mu\text{m})$ , however, is less likely to spectrally overlap with meteorological clouds (see Figure 3.3). When larger amounts ( $> 5$  Dobson Units) of  $\text{SO}_2$  are present, as is common in clouds produced by volcanic eruptions,  $\beta(8.5\mu\text{m}, 11\mu\text{m})$  takes on large values that are generally outside of the normal range for meteorological clouds, while  $\beta(12\mu\text{m}, 11\mu\text{m})$  is not impacted by  $\text{SO}_2$ . Thus, even if  $\text{SO}_2$  is present in or above the ash cloud, the combination  $\beta(12\mu\text{m}, 11\mu\text{m})$  and  $\beta(8.5\mu\text{m}, 11\mu\text{m})$  still exhibits behavior that is generally unique to volcanic ash clouds.

Figure 4.7 and Figure 4.8 show the  $\beta_{\text{tot}}(12\mu\text{m}, 11\mu\text{m})$ ,  $\beta_{\text{opaque}}(12\mu\text{m}, 11\mu\text{m})$ ,  $\beta_{\text{tot}_\sigma 8}(12\mu\text{m}, 11\mu\text{m})$ ,  $\beta_{\text{tot}_\sigma 7}(12\mu\text{m}, 11\mu\text{m})$ ,  $\beta_{\text{tot}}(8.5\mu\text{m}, 11\mu\text{m})$ , and  $\beta_{\text{opaque}}(8.5\mu\text{m}, 11\mu\text{m})$  parameters computed for the scenes introduced in Section 4.3. When  $\varepsilon(\lambda_1)$  and/or  $\varepsilon(\lambda_2)$  is less than zero, the 11  $\mu\text{m}$  brightness temperature is imaged in Figure 4.7 and Figure 4.8. Note how  $\beta_{\text{tot}}(8.5\mu\text{m}, 11\mu\text{m})$  (Panel F), and  $\beta_{\text{opaque}}(8.5\mu\text{m}, 11\mu\text{m})$  (Panel G) are much larger in regions with ash plus significant  $\text{SO}_2$  compared to ash regions that are not coupled with a significant  $\text{SO}_2$  spectral signature. The spatial variability of  $\beta_{\text{tot}}(12\mu\text{m},$

11 $\mu\text{m}$ ) (Panel B),  $\beta_{\text{opaque}}(12\mu\text{m}, 11\mu\text{m})$  (Panel C),  $\beta_{\text{tot}_{\sigma 8}}(12\mu\text{m}, 11\mu\text{m})$  (Panel D), and  $\beta_{\text{tot}_{\sigma 7}}(12\mu\text{m}, 11\mu\text{m})$  (Panel E) within the volcanic cloud can be generally attributed to varying cloud microphysical properties, especially the effective particle radius [Chapter 5 of this dissertation]. The  $\beta(12\mu\text{m}, 11\mu\text{m})$  parameters are not sensitive to  $\text{SO}_2$ . The majority of the volcanic ash in Figure 4.7 and Figure 4.8 does not overlap lower cloud layers so  $\beta_{\text{tot}_{\sigma 8}}(12\mu\text{m}, 11\mu\text{m})$  (Panel D) and  $\beta_{\text{tot}_{\sigma 7}}(12\mu\text{m}, 11\mu\text{m})$  (Panel E) most often do not have valid values. In regions where a valid multilayer version of  $\beta(12\mu\text{m}, 11\mu\text{m})$  cannot be computed the 11  $\mu\text{m}$  brightness temperature is displayed revealing that the majority of the ash cloud in both scenes is optically thin (very weak presentation in 11  $\mu\text{m}$  image).

The combination of  $\beta(12\mu\text{m}, 11\mu\text{m})$  and  $\beta(7.3\mu\text{m}, 11\mu\text{m})$  is also exploited as it aids in the detection of high-level volcanic ash and dust (dust, in large quantities, is less likely to be present at high levels than volcanic ash). The 7.3  $\mu\text{m}$  channel is centered on a fairly strong water vapor absorption feature, so the clear sky weighting function peaks in the mid to upper troposphere in all but the driest of atmospheres. Thus,  $\beta(7.3\mu\text{m}, 11\mu\text{m})$  is only useful when mid to high-level clouds is present. In the absence of  $\text{SO}_2$  (strong  $\text{SO}_2$  absorption features are captured by the 7.3  $\mu\text{m}$  channel), the increase in cloud absorption as a function of increasing wavelength between 7.3 and 11  $\mu\text{m}$  is much greater for volcanic ash and dust than liquid water or ice clouds, resulting in mid and high-level ash and dust clouds generally taking on smaller values of  $\beta(7.3\mu\text{m}, 11\mu\text{m})$  compared to meteorological clouds (see Figure 3.1). When mid to high-level  $\text{SO}_2$  is present,  $\beta(7.3\mu\text{m}, 11\mu\text{m})$  will be very large such that it is out of the normal range that encompasses meteorological clouds, making it particularly useful for volcanic ash detection.

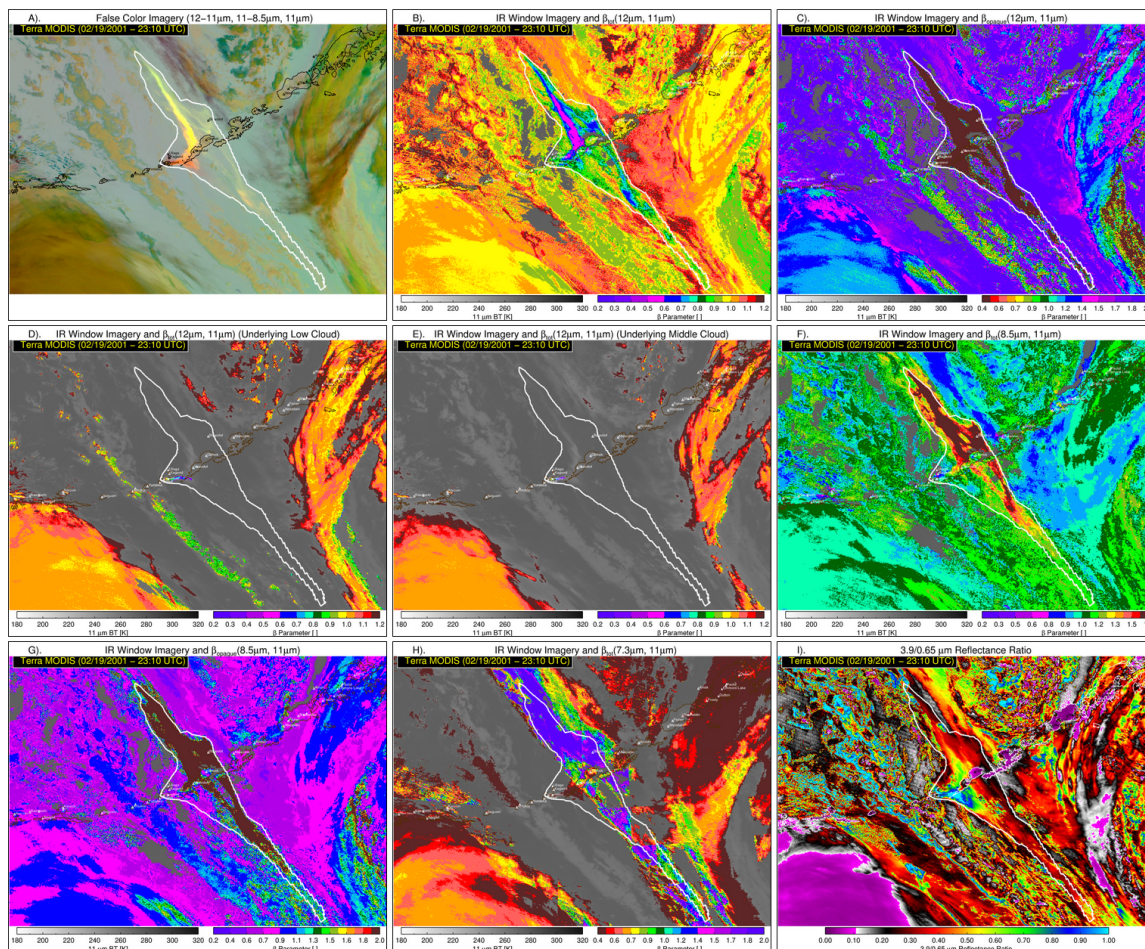


Figure 4.7: Images of the classifiers, used during typical sunlit conditions, by the Bayes approach that estimates the probability that a given satellite pixel contains volcanic ash and/or dust are shown. The parameters were computed for a Terra MODIS image from February 19, 2001 at 23:10 UTC. The approximate bounds of an ash cloud produced by an eruption of Mount Cleveland (Alaska) are overlaid on each image in white. A). Multispectral false color image. B).  $\beta_{tot}(12\mu m, 11\mu m)$  overlaid on an 11 μm brightness temperature (BT) image. C).  $\beta_{opaque}(12\mu m, 11\mu m)$  overlaid on an 11 μm BT image. D).  $\beta_{tot\_σ8}(12\mu m, 11\mu m)$  overlaid on an 11 μm BT image. E).  $\beta_{tot\_σ7}(12\mu m, 11\mu m)$  overlaid on an 11 μm BT image. F).  $\beta_{tot}(8.5\mu m, 11\mu m)$  overlaid on an 11 μm BT image. G).  $\beta_{opaque}(8.5\mu m, 11\mu m)$  overlaid on an 11 μm BT image. H).  $\beta_{tot}(7.3\mu m, 11\mu m)$  overlaid on an 11 μm BT image. I).  $\rho(3.9\mu m, 0.65\mu m)$ . Only panels B through I are used as a classifier. Panel A is included to aid in scene interpretation. See text for additional details.

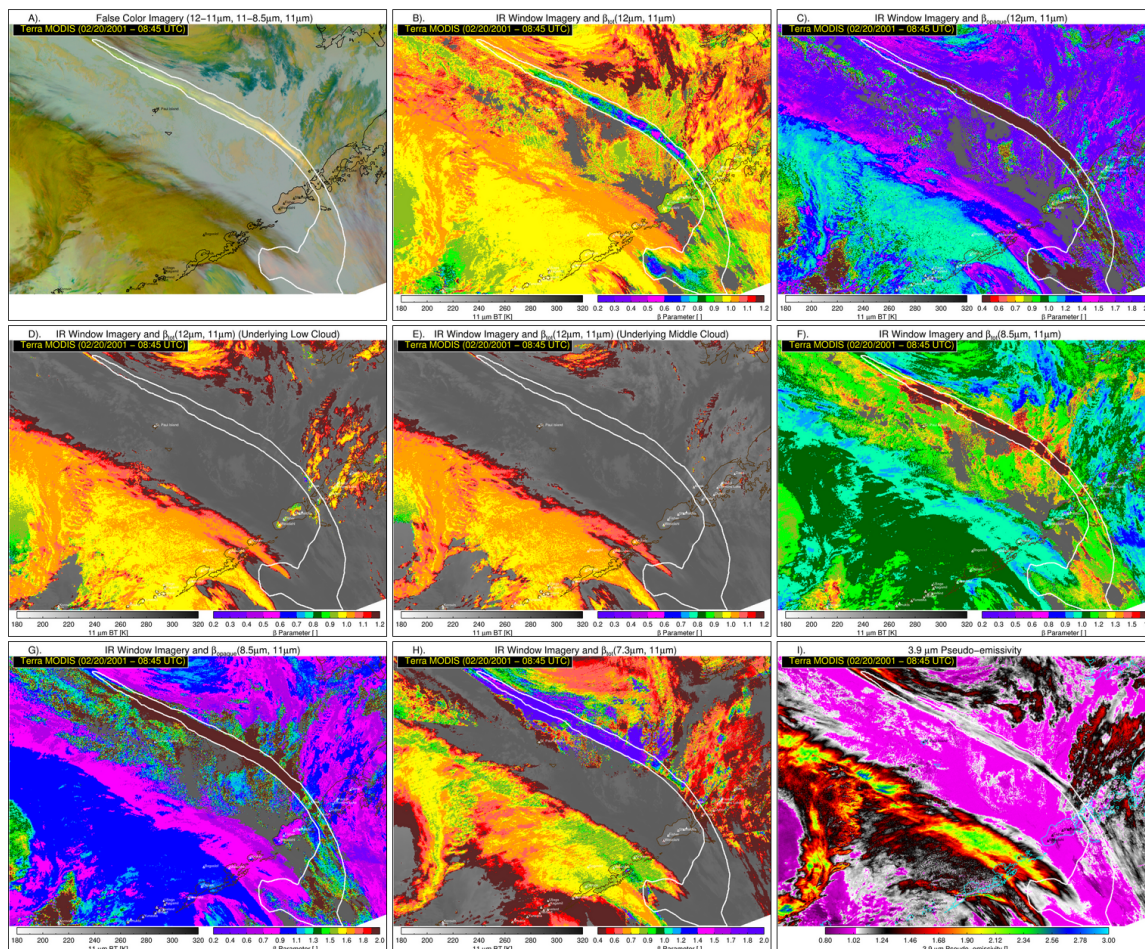


Figure 4.8: Images of the classifiers, used at night, by the Bayes approach that estimates the probability that a given satellite pixel contains volcanic ash and/or dust are shown. The parameters were computed for a Terra MODIS image from February 20, 2001 at 08:45 UTC. The approximate bounds of an ash cloud produced by an eruption of Mount Cleveland (Alaska) are overlaid on each image in white. A) Multispectral false color image. B)  $\beta_{tot}(12\mu\text{m}, 11\mu\text{m})$  overlaid on an 11  $\mu\text{m}$  brightness temperature (BT) image. C)  $\beta_{opaque}(12\mu\text{m}, 11\mu\text{m})$  overlaid on an 11  $\mu\text{m}$  BT image. D)  $\beta_{tot\_o8}(12\mu\text{m}, 11\mu\text{m})$  overlaid on an 11  $\mu\text{m}$  BT image. E)  $\beta_{tot\_o7}(12\mu\text{m}, 11\mu\text{m})$  overlaid on an 11  $\mu\text{m}$  BT image. F)  $\beta_{tot}(8.5\mu\text{m}, 11\mu\text{m})$  overlaid on an 11  $\mu\text{m}$  BT image. G)  $\beta_{opaque}(8.5\mu\text{m}, 11\mu\text{m})$  overlaid on an 11  $\mu\text{m}$  BT image. H)  $\beta_{tot}(7.3\mu\text{m}, 11\mu\text{m})$  overlaid on an 11  $\mu\text{m}$  BT image. I)  $\epsilon_p(3.9\mu\text{m})$ . Only panels B through I are used as a classifier. Panel A is included to aid in scene interpretation. See text for additional details.

It is important to note that  $\text{SO}_2$  absorption at 11 and 12  $\mu\text{m}$  is negligible, so a  $\beta(12\mu\text{m}, 11\mu\text{m})$  signal consistent with ash must always be present regardless of the influence of  $\text{SO}_2$  absorption, since  $\beta(7.3\mu\text{m}, 11\mu\text{m})$  and  $\beta(8.5\mu\text{m}, 11\mu\text{m})$  are always used

in tandem with  $\beta(12\mu\text{m}, 11\mu\text{m})$ . The  $\beta_{\text{tot}}(7.3\mu\text{m}, 11\mu\text{m})$  parameter is shown in Figure 4.7 and Figure 4.8 (Panel H). The  $\text{SO}_2$  sensitivity is clearly discernable by the large  $\beta_{\text{tot}}(7.3\mu\text{m}, 11\mu\text{m})$  values in regions where a strong  $\text{SO}_2$  spectral signature is present. The 12-11, 11-8.5, 11  $\mu\text{m}$  false color image from February 19, 2001 (23:10 UTC) (Figure 4.3 and Figure 4.7) indicates that the region of ash near Cleveland volcano does not have a strong  $\text{SO}_2$  spectral signature like many other portions of the ash cloud at this time. The lack of an obvious  $\text{SO}_2$  spectral signature in the 12-11, 11-8.5, 11  $\mu\text{m}$  false color image is supported by co-located  $\beta_{\text{tot}}(7.3\mu\text{m}, 11\mu\text{m})$  values that are small, as would be expected for volcanic ash in the absence of significant  $\text{SO}_2$ . At 08:45 UTC on February 20, 2001 (Figure 4.4 and Figure 4.8), there are portions of the ash cloud, mainly in the bottom right corner of the image, that do not have valid  $\beta_{\text{tot}}(7.3\mu\text{m}, 11\mu\text{m})$  values, probably because the ash is located at a much lower height than the peak of the 7.3  $\mu\text{m}$  clear sky weighting function.

Unfortunately, many satellite sensors do not have 7.3 and 8.5  $\mu\text{m}$  channels, but nearly every sensor allows the various forms of  $\beta(12\mu\text{m}, 11\mu\text{m})$  to be paired with near-infrared (day and night) and visible (daytime only) wavelength based spectral metrics. In the presence of sunlight (when the solar zenith angle  $< 85^\circ$  and the measurements are not influenced by sun glint over water), the ratio of the 3.9  $\mu\text{m}$  reflectance and the 0.65  $\mu\text{m}$  reflectance [ $\rho(3.9\mu\text{m}, 0.65\mu\text{m}) = r[3.9\mu\text{m}]/r[0.65\mu\text{m}]$ ] can be combined with “split-window” (11 and 12  $\mu\text{m}$ ) measurements to distinguish ash and dust clouds from other cloud types [Pavolonis et al., 2006]. Unlike meteorological clouds, the  $\rho(3.9\mu\text{m}, 0.65\mu\text{m})$  of volcanic ash and dust clouds tends to increase with decreasing  $\beta(12\mu\text{m}, 11\mu\text{m})$  for a given visible cloud optical depth and set of background conditions. The  $\rho(3.9\mu\text{m},$

0.65 $\mu\text{m}$ ) of volcanic ash and dust tends to be  $> 0.5$  when the visible cloud optical depth exceeds  $\sim 0.10$  [Pavolonis et al., 2006]. Meteorological clouds generally have a  $\rho(3.9\mu\text{m}, 0.65\mu\text{m}) < 0.5$ . The method for computing  $\rho(3.9\mu\text{m}, 0.65\mu\text{m})$  along with a more complete description of its utility for ash and dust detection is given in Pavolonis et al. [2006]. Figure 4.7 (Panel I) shows that  $\rho(3.9\mu\text{m}, 0.65\mu\text{m})$  within sections of the core of the ash cloud exceeds 0.50, while the  $\rho(3.9\mu\text{m}, 0.65\mu\text{m})$  of optically thick meteorological clouds (liquid or ice) is much smaller. However, the edge of meteorological clouds will also have large values of  $\rho(3.9\mu\text{m}, 0.65\mu\text{m})$ , but this effect is mitigated by pairing  $\rho(3.9\mu\text{m}, 0.65\mu\text{m})$  with  $\beta(12\mu\text{m}, 11\mu\text{m})$  in its various forms.

At solar zenith angles greater than  $90^\circ$ , and in the absence of stray light influences (significant sunlight impinging on the sensor when the solar zenith angle exceeds  $90^\circ$ ), the 3.9  $\mu\text{m}$  pseudo-emissivity [ $\varepsilon_p(3.9\mu\text{m})$ ] is used in conjunction with  $\beta(12\mu\text{m}, 11\mu\text{m})$  to help identify ash and dust clouds. The  $\varepsilon_p(3.9\mu\text{m})$  parameter is simply defined as the ratio of the measured 3.9- $\mu\text{m}$  radiance to the estimated 3.9- $\mu\text{m}$  blackbody radiance [ $\varepsilon_p(3.9\mu\text{m}) = R[3.9 \mu\text{m}]/R_{\text{bb}}[3.9\mu\text{m}]$ ]. As in Heidinger et al. [2012], the 3.9- $\mu\text{m}$ -blackbody radiance ( $R_{\text{bb}}[3.9\mu\text{m}]$ ) is estimated by the applying the Planck Function to the 3.9- $\mu\text{m}$  channel for a given sensor using the measured 11  $\mu\text{m}$  brightness temperature as the blackbody temperature. The  $\varepsilon_p(3.9\mu\text{m})$  parameter is very useful discriminating between semi-transparent clouds and low opaque clouds [Heidinger et al., 2012]. Typical behavior of the  $\beta(12\mu\text{m}, 11\mu\text{m})$  and  $\varepsilon_p(3.9\mu\text{m})$  pairing is as follows.

*Volcanic ash and dust clouds:  $\beta(12 \mu\text{m}, 11\mu\text{m}) < 1$  and  $\varepsilon_p(3.9\mu\text{m}) > 1$*

*Semi-transparent liquid water:  $\beta(12\mu\text{m}, 11\mu\text{m}) > 1$  and  $\varepsilon_p(3.9\mu\text{m}) > 1$*

*Most ice clouds:  $\beta(12\mu\text{m}, 11\mu\text{m}) > 1$  and  $\varepsilon_p(3.9\mu\text{m}) > 1$*

*Optically thick liquid water clouds:  $\beta(12\mu\text{m}, 11\mu\text{m}) < 1$  and  $\varepsilon_p(3.9\mu\text{m}) < 1$*

Figure 4.8 (Panel I) shows illustrates that  $\varepsilon_p(3.9\mu\text{m})$  of volcanic ash tends to be greater than the  $\varepsilon_p(3.9\mu\text{m})$  of clear sky or opaque low and mid level clouds. While in this particular case, the  $\varepsilon_p(3.9\mu\text{m})$  of semi-transparent ice clouds is large compared to volcanic ash, there are instances where the  $\varepsilon_p(3.9\mu\text{m})$  volcanic ash (or dust) and semi-transparent ice clouds can be comparable. On sensors that lack the 7.3 and 8.5  $\mu\text{m}$  channels,  $\beta(12\mu\text{m}, 11\mu\text{m})$  is not coupled with any other parameter in the day/night terminator region (solar zenith angle between 85-90°).

Each radiative parameter pairing is best used in conjunction with an indicator of how much the observed radiance deviates from the estimated clear sky radiance. As in Heidinger et al. [2012], the 11  $\mu\text{m}$  emissivity value a cloud would have if it were located at the top of the thermodynamically defined troposphere [ $\varepsilon_{\text{tot}}(11\mu\text{m})$ ] is used to quantify the confidence that a given signature is associated with a cloud and not a clear sky feature (e.g. the surface). As will be described in a later section, additional spatial analysis techniques are utilized to mitigate the impacts of errors in the clear sky radiance calculations. Clear sky radiance errors can be large [Heidinger and Pavolonis, 2009], particularly over land where the uncertainty in surface temperature and emissivity is significant.

#### *4.4.2. Naïve Bayesian Approach*

While the various metrics described in the previous section are useful for detecting volcanic ash and dust, the relationship between each spectral metric is quite complicated. In an effort to sufficiently capture the complicated relationships over a wide range of conditions and reduce the many pieces of spectral information into a single

objective metric, a Bayesian approach is utilized. Bayesian approaches have been successfully applied to several satellite-based classification problems [Uddstrom et al. 1999; Merchant et al. 2005; Heidinger et al. 2012; Kossin and Sitkowski 2009; Cintineo et al. 2014; Mackie and Watson 2014]. As discussed in Kossin and Sitkowski [2009] and Heidinger et al. [2012], the classical Bayesian approach is not practical when more than just a few features are used, as the size of the class conditional probability density functions can easily grow to an unmanageable size and become very difficult to sufficiently populate. Thus, in lieu of the classical implementation of the Bayesian approach [Uddstrom et al. 1999; Merchant et al. 2005], a Naïve Bayesian approach [Heidinger et al. 2012; Kossin and Sitkowski 2009; Cintineo et al. 2014] is used. The naïve Bayesian model is formulated by assuming that features ( $\mathbf{F}$ ) are independent within each class. The naïve Bayes classifier has been shown to perform quite well even when the features are clearly not independent [Domingos and Pazzani 1997; Hand and Yu 2001; Kossin and Sitkowski 2009; Heidinger et al. 2012; Cintineo et al. 2014]. Using the naïve Bayes formulation, the probability of ash or dust given an observed set of independent features ( $P(C_{yes}|\mathbf{F})$ ) is calculated using Equation ( 4.5) (the term,  $P(C_{yes}|\mathbf{F})$ , is also commonly referred to as the posterior probability).

$$P(C_{yes} | \mathbf{F}) = \frac{P(C_{yes}) \prod_{i=1}^N P(F_i | C_{yes})}{P(\mathbf{F})} \quad (4.5)$$

In Equation ( 4.5),  $P(C_{yes})$  is the prior probability that a given satellite pixel contains volcanic ash or dust without knowledge of  $\mathbf{F}$ ,  $P(F_i|C_{yes})$  is the estimated probability of observing a given feature ( $F_i$ ) when ash or dust are present (a total of  $N$  features are used),

and  $P(\mathbf{F})$  is the probability of a given set of features being observed and is computed using ( 4.6).

$$P(\mathbf{F}) = P(C_{yes}) \prod_{i=1}^N P(F_i | C_{yes}) + P(C_{no}) \prod_{i=1}^N P(F_i | C_{no}) \quad (4.6)$$

In Equation ( 4.6),  $P(C_{no})$  is the prior probability that a given satellite pixel does *not* contain volcanic ash or dust [e.g.  $P(C_{no}) = 1 - P(C_{yes})$ ] and  $P(F_i | C_{no})$  is the estimated probability of observing a given feature ( $F_i$ ) when ash or dust are *not* present.

The prior probability of ash/dust [ $P(C_{yes})$ ] is assumed to be 0.1%, which, while arbitrary and crude, this value roughly captures the fact that the global fractional coverage of ash or dust that *is detectable using passive satellite measurements* is generally small relative to all other observable cloud and surface features. In addition, the ash/dust conditional probability is often many orders of magnitude greater than the non-ash/dust conditional probability, rendering the impact of the prior probabilities minimal. Further, in our application, the posterior probability is largely used to determine cloud object membership (e.g. whether or not a given pixel should be used when constructing cloud objects) [Chapter 6 of this dissertation] and the use of constant prior probabilities ensures that it is purely the signature at a given time that influences cloud object membership for a given probability threshold, not the prior probabilities. Thus, we avoided using prior probabilities that depend on time and geographic location, but acknowledge that the climatological probability of ash/dust is likely several orders of magnitude greater near source regions than locations far removed from dust source regions or volcanoes that frequently produce ash clouds (e.g. Sakurajima, Japan).

The class conditional probability density functions (PDFs), the dimensions of which are subsequently described, are empirically constructed for each classifier ( $F_i$ ) from a large training data set. The “yes” class training data set consists of 344 5-minute MODIS granules (see Appendix C) with ash and/or dust clouds, the horizontal bounds of which were manually analyzed by a human expert using the same type of false color images described earlier and Region of Interest (ROI) software applications. Only situations where ash/dust clearly was the highest cloud layer were classified as ash/dust during the manual analysis process. In addition, cloud edges were drawn with an emphasis on avoiding false alarms (cross contamination) at the expense of excluding a small number of ash/dust pixels. The 344-ash/dust cases (305 ash scenes and 39 dust scenes) were selected so that a large number of background (surface and atmosphere) and ash/dust cloud states were sampled. For instance, low, mid, and high latitude eruptions of varying intensity (and varying  $\text{SO}_2$  emissions) were selected and an effort was made to ensure that a diverse set of underlying surfaces and clouds were sampled. MODIS scenes composed of re-suspended ash [e.g. Hadley et al. 2004] were also included. North American, African, Asian, and Australian dust clouds were sampled.

The training database for the “yes” class consists of about 6.5 million volcanic ash pixels and 3.7 million desert dust pixels, after applying several quality control measures and simple filters. The quality control measures and filters are described shortly. Even though the number of dust cloud pixels in the training data set is less than the number of ash cloud pixels, the method performs well when applied to dust clouds because ash and dust have similar spectral signatures in the broad to narrow band spectral channels that the SECO method utilizes, and the range of dust cloud property states is likely smaller

than the range of ash cloud property states because ash clouds are the result of complex, and highly variable, volcanological processes interacting with a wide range of complex and highly variable atmospheric processes.

A total of about 2.5 billion non-volcanic ash/dust pixels (after quality control and filtering), drawn from 2401 different 5-minute MODIS granules, were used to construct the training database for the “no” class. To avoid cross-contamination, the non-ash/dust training pixels were taken from MODIS granules that were independent of those used to construct the ash/dust component of the training. In fact, each of the 2401 5-minute MODIS granules used to build the “no” class training was deemed to be totally free of detectable ash or dust clouds through manual inspection of false color imagery. Global or near-global coverage was achieved for one day per month from November 2009 – October 2010 using both the *Terra* (mid-morning sun synchronous orbit) and *Aqua* (mid-afternoon sun synchronous orbit) satellites.

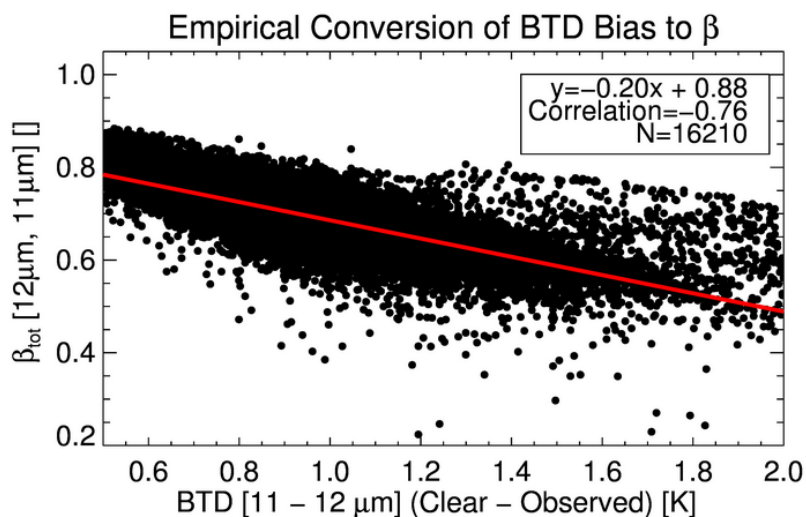
Despite the large size of the training data set, some portions of the various PDFs were not sampled. The un-sampled regions were consistent with physical expectations. Conditional probabilities cannot be equal to zero, so the observational count in every PDF bin was increased by a constant non-integer factor such that un-sampled PDF bins produce ash/dust and non-ash/dust conditional probabilities that are identical (the non-integer factor has no impact on the ratio between the “yes” and “no” class conditional probabilities in the bins that already contained observations). This simple step is needed to prevent arithmetic overflow and gracefully default to the prior probability in the rare event that the un-sampled portions of the PDF are observed when applied to satellite data

not included in the training data set. In the future, additional training cases can also be added should there be a need.

The non-volcanic ash/dust component of the training data will consist of clear and cloudy pixels, as no cloud mask was applied. The ash/dust training data may also contain a very small fraction of clear pixels due to smoothing of cloud edges as an unavoidable consequence of the manual analysis process. A cloud mask algorithm was not used to filter out clear pixels because all available algorithms classify volcanic ash and dust pixels as “clear” to varying degrees. All pixels, however, were required to have a  $\epsilon_{\text{tot}}(11\mu\text{m}) \geq 0.02$ , which ensures that pixels that have an observed 11  $\mu\text{m}$  radiance that deviates very little from the estimated 11  $\mu\text{m}$  clear sky radiance do not negatively influence the classifier training or the implementation of the SECO algorithm. This step eliminates many of the clear pixels without having to apply a separate cloud mask algorithm.

There are instances, however, where the  $\epsilon_{\text{tot}}(11\mu\text{m})$  of ash or dust clouds, that are identifiable in imagery, is less than 0.02 or even negative (the observed radiance is greater than the calculated clear sky radiance) due to errors in the clear sky radiance calculation or temperature inversion effects, especially over land surfaces. Errors in the NWP supplied surface temperature can be quite large [Heidinger and Pavolonis 2009] over land surfaces. When the surface temperature is underestimated, the clear sky radiance for a given surface-viewing channel (e.g. 11 and 12  $\mu\text{m}$ ) will also be underestimated, sometimes causing the observed radiance to be greater than the clear sky radiance, even under cloudy conditions. Errors in the surface temperature impact the calculation of the clear sky radiance at 11 and 12  $\mu\text{m}$  similarly enough that the bias

(calculated – observed) in the calculated clear sky 11 – 12  $\mu\text{m}$  BTD under observed clear sky conditions is much less than the clear sky brightness temperature bias in either channel alone. As such, the calculated clear sky minus the observed 11 – 12  $\mu\text{m}$  BTD (hereafter referred to as BTD\_Bias) can be empirically related to  $\beta_{\text{tot}}(12\mu\text{m}, 11\mu\text{m})$  for ash/dust clouds that have an observed 11  $\mu\text{m}$  radiance that does not strongly deviate from the clear sky radiance or in situations where the clear sky radiance is less than the observed radiance due to errors in the clear sky calculation and/or temperature inversion effects. The linear regression relationship shown in Figure 4.9 is used to “restore” potential volcanic ash and dust pixels that have a  $\varepsilon_{\text{tot}}(11\mu\text{m}) < 0.02$ , a



BTD\_Bias > 0.5 K,  
and an observed 11  
– 12  $\mu\text{m}$  BTD < 0 K.  
Francis et al. [2012]  
and Pavolonis et al.  
[2013] also utilized  
the BTD\_Bias to

Figure 4.9: The empirical relationship used to estimate the top of troposphere referenced 12/11  $\mu\text{m}$  effective absorption optical depth ratio  $[\beta_{\text{tot}}(12\mu\text{m}, 11\mu\text{m})]$  from the clear minus observed 11 – 12  $\mu\text{m}$  brightness temperature difference (BTD) is shown. aid in ash detection. A subset of the over land volcanic

ash/dust training data with  $0.02 < \varepsilon_{\text{tot}}(11\mu\text{m}) < 0.08$  were used to construct the relationship shown in Figure 4.9. The  $\varepsilon_{\text{tot}}(11\mu\text{m}) < 0.02$  screening rule and the empirical

conversion of  $BTD\_Bias$  to  $\beta_{tot}(12\mu m, 11\mu m)$  are also utilized during the practical implementation of the SECO algorithm.

Four simple filters are also applied to eliminate pixels from the “yes” and “no” training data that have a “split-window” signature that is strongly inconsistent with ash/dust, and is likely the result of the human expert’s inability to exactly define the edge of ash and dust clouds in imagery during the manual analysis process. The following filters are also applied during the practical implementation of the SECO algorithm.

1. All pixels with a  $\beta_{tot}(12\mu m, 11\mu m)$  value  $> 1.05$ , which is slightly greater than the upper theoretical limit for volcanic ash and dust [see Figure 3.3], are excluded from the “yes” and “no” training data.
2. All pixels must also have a 11 – 12  $\mu m$  BTD that is less than  $BTD\_MAX$  (see Equation ( 4.7) which corresponds to the 99<sup>th</sup> percentile value from the ash/dust training data set as a function of  $\varepsilon_{tot}(11\mu m)$ ). This filter function is designed to mitigate the impacts of possible errors associated with manually defining the edge of ash and dust clouds when  $\varepsilon_{tot}(11\mu m) \geq 0.5$ .

$$BTD\_MAX = \begin{cases} -1.19446\varepsilon_{tot}(11\mu m) + 1.14213, & 0.5 \leq \varepsilon_{tot}(11\mu m) \leq 1.0 \\ 1000.0, & \varepsilon_{tot}(11\mu m) < 0.5 \end{cases} \quad (4.7)$$

3. All pixels must also have a  $BTD\_Bias$  that is greater than  $BTD\_BIAS\_MIN$  (see Equation ( 4.8), which corresponds to the 1<sup>st</sup> percentile value from the ash/dust training data set as a function of  $\varepsilon_{tot}(11\mu m)$ ). This filter function is designed to

mitigate the impacts of possible errors associated with manually defining the edge of ash and dust clouds when  $\varepsilon_{tot}(11\mu m) < 0.5$ .

$$BTD\_BIAS\_MIN = \begin{cases} -0.700909\varepsilon_{tot}(11\mu m) + 0.0312235, & 0.0 \leq \varepsilon_{tot}(11\mu m) < 0.5 \\ -1000.0, & \varepsilon_{tot}(11\mu m) \geq 0.5 \end{cases} \quad (4.8)$$

4. All pixels with an observed 11 – 12  $\mu m$  BTD > 0 K must also have a  $\beta_{opaque}(12\mu m, 11\mu m)$  value < 1.36, which is the 99<sup>th</sup> percentile value from the ash/dust training data set.

The 11 – 12  $\mu m$  BTD (“split-window”) attributes of the quality controlled and filtered training data were analyzed to help quantify the limitations of traditional “split-window” ash/dust detection approaches and to help illustrate that the training data are representative of a wide range of conditions. The relative and absolute distribution of the 11 – 12  $\mu m$  BTD for the ash/dust (“yes”) and non-ash/dust (“no”) classes are shown in Figure 4.10. The distributions clearly indicate that there is significant overlap between the two classes such that even 11 – 12  $\mu m$  BTD values of -1 K are not totally unique to ash and dust clouds. In addition, many volcanic ash/dust pixels do not exhibit a negative “split-window” signature likely due to influences from background water vapor and/or cloud microphysical effects. While traditional threshold based “split-window” ash/dust detection algorithms are very simple to implement and may work well for a single case with a limited geographic extent, Figure 4.10c shows that the when applied to a global, multi-season data set, the detection skill (quantified using the Critical Success Index) of those algorithms is extremely limited. The Critical Success Index (CSI) is defined as the

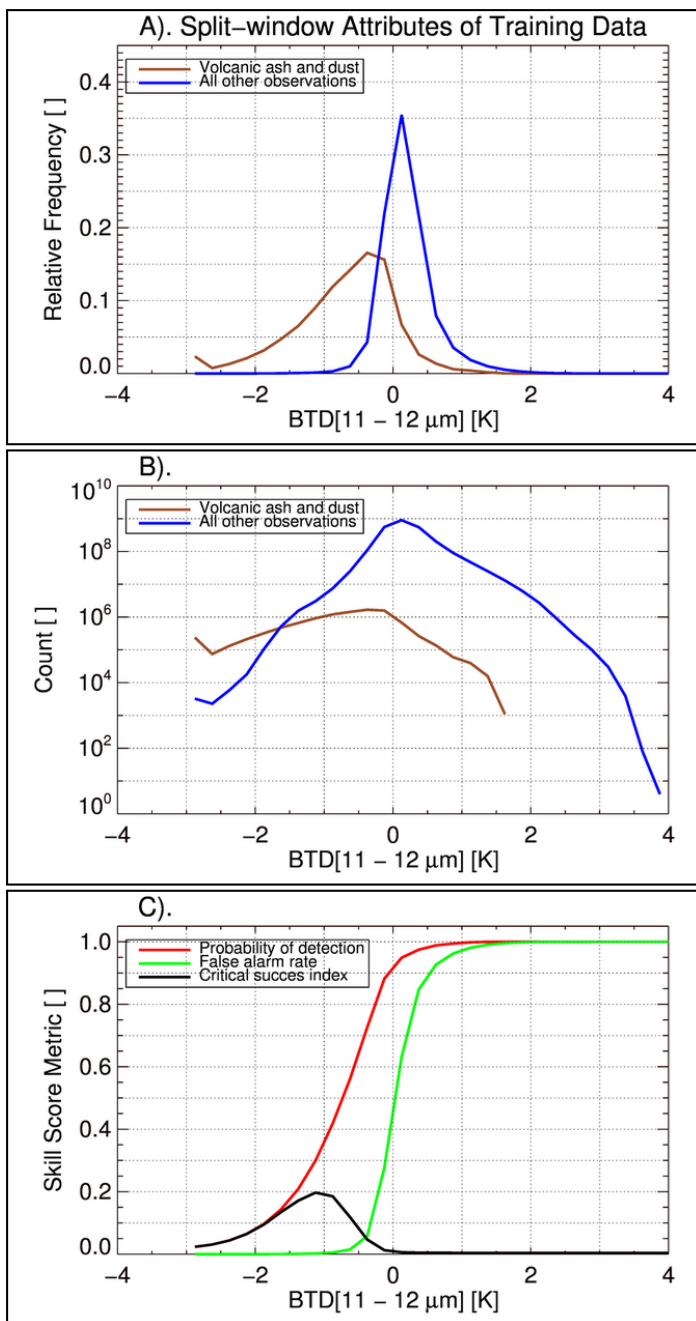


Figure 4.10: A). Normalized distribution of the 11 – 12 μm brightness temperature difference (BTD) of the data used to derive the ash/dust and the non-ash/dust class conditional probabilities, B). Same as panel A, except the distribution is not normalized and is shown using a log y-axis, C). Skill statistics of a simple threshold based 11 – 12 μm BTD ash/dust detection approach, applied to the training data set, is plotted as a function of the chosen threshold (classify as ash/dust if 11-12 μm BTD ≤ threshold on x-axis). The probability of detection (red), false alarm rate (green), and critical success index (black) are shown.

number of hits divided by the sum of hits, false alarms, and misses. The CSI does not take correct negatives into account, so it is an effective metric when the event of interest is observed far less often than the non-events and the tolerance for false alarms is low (volcanic ash false alarms are particularly undesirable). The maximum CSI of a threshold based “split-window” algorithm applied to our extensive training data set is about 0.20 when a threshold of -1.25 K is used. The Probability Of Detection (POD) for a threshold of -1.25 K is only about 0.30 with a False Alarm

Rate (FAR) of 0.002.

The features or classifiers ( $F_i$ ) used in our Bayes implementation are listed in

Table 4.5 as a function of satellite sensor. Even though the naïve Bayes formulation allows us to assume that each feature or classifier is independent, we utilize multivariate classifiers. The two and three-dimensional classifiers are very effective at capturing the most robust spectral indicators of ash and dust (see earlier discussion) without requiring large PDFs. Our methodology still takes advantage of the independence assumption, as we utilize far more than two or three predictors, which would not be practical without the naïve Bayes formulation. The conditional probabilities for each class are estimated from histograms of the training data set. The histogram bins are defined in Table 4.5.

Classifiers that are directly influenced by reflected sunlight were parsed into three different surface type categories (open water, snow/ice, and non-snow/ice land surfaces), while classifiers not directly influenced by reflected sunlight were sorted into two different surface type categories (open water and solid surfaces). Daily global snow/ice maps were constructed by combining the 4 km Interactive multisensor snow and Ice Mapping System (IMS) [Ramsay 1998], which at the time of this writing only provides coverage of the Northern Hemisphere, with the 25 km Special Sensor Microwave Imager (SSM/I)-Special Sensor Microwave Imager/Sounder (SSMIS) global ice concentration and snow extent data set [Nolin et al. 1998] to fill in the Southern Hemisphere. The surface types were chosen to broadly account for surface albedo effects on visible and near-infrared measurements during the day and differences in clear sky infrared radiative transfer error characteristics (errors are generally larger over land than open water).

Table 4.5: The top most portion of the table lists the individual radiative parameters utilized to construct SECO algorithm classifiers, along with the corresponding histogram binning scheme used to estimate the classifier PDFs. The multivariate classifier arrays (using the radiative parameter ID's shown in the top part of the table) are listed in the second part of the table as a function of satellite sensor and the conditions required for utilization. Sun glint is assumed to be present over water surfaces if the glint angle is less than  $40^\circ$ . Stray light is assumed to be present if the solar zenith angle exceeds  $90^\circ$  and the measured  $0.65 \mu\text{m}$  counts is greater than a sensor dependent threshold.

Parameter [Parameter ID]	Number of Histogram Bins	Starting Boundaries of Histogram Bins
$\epsilon_{\text{tot}}(11\mu\text{m})$ [1]	6	0.01, 0.03, 0.10, 0.20, 0.50, 0.90
$\beta_{\text{tot}}(12\mu\text{m}, 11\mu\text{m})$ [2]	42	-0.10 to 1.95 in increments of 0.05
$\beta_{\text{opaque}}(12\mu\text{m}, 11\mu\text{m})$ [3]	42	-0.10 to 1.95 in increments of 0.05
$\beta_{\text{tot } \sigma_8}(12\mu\text{m}, 11\mu\text{m})$ [4]	42	-0.10 to 1.95 in increments of 0.05
$\beta_{\text{tot } \sigma_7}(12\mu\text{m}, 11\mu\text{m})$ [5]	42	-0.10 to 1.95 in increments of 0.05
$\beta_{\text{tot}}(8.5\mu\text{m}, 11\mu\text{m})$ [6]	21	-0.10 to 1.90 in increments of 0.10
$\beta_{\text{opaque}}(8.5\mu\text{m}, 11\mu\text{m})$ [7]	21	-0.10 to 1.90 in increments of 0.10
$\beta_{\text{tot}}(7.3\mu\text{m}, 11\mu\text{m})$ [8]	21	-0.10 to 1.90 in increments of 0.10
$\rho(3.9\mu\text{m}, 0.65\mu\text{m})$ [9]	13	0.00 to 1.20 in increments of 0.10
$\epsilon_p(3.9\mu\text{m})$ [10]	25	0.80 to 2.00 in increments of 0.05
BTD(11-12 $\mu\text{m}$ ) [11]	33	-3.0 to 5.0 in increments of 0.25 K

Multivariate Classifier Arrays	Relevant Sensors	Conditions
[1] x [2] x [9]	AVHRR*	Only applied outside of sun glint when the solar zenith angle is less than $85^\circ$ .
[1] x [3] x [9]	COMS-MI	
[1] x [4] x [9]	GOES-Imager#	
[1] x [5] x [9]	GOES-R ABI	
[1] x [11] x [9]	Himawari-8/9 AHI	
	MODIS	
	MTSAT Imager	Only applied when the solar zenith angle is greater than $90^\circ$ and stray light is not detected.
	MSG SEVIRI	
	MTG FCI	
	VIIRS	
[1] x [2] x [10]	AVHRR*	
[1] x [3] x [10]	COMS-MI	
[1] x [4] x [10]	GOES-Imager#	Applied at all times.
[1] x [5] x [10]	GOES-R ABI	
[1] x [11] x [10]	Himawari-8/9 AHI	
	MODIS	
	MTSAT Imager	
	MSG SEVIRI	
	MTG FCI	Applied at all times.
	VIIRS	
[1] x [2] x [6]	GOES-R ABI	
[1] x [3] x [7]	Himawari-8/9 AHI	
	MODIS	
	MSG SEVIRI	
	MTG FCI	Only applied when both $\rho(3.9 \mu\text{m}, 0.65 \mu\text{m})$ and $\epsilon_p(3.9 \mu\text{m})$ are invalid.
	VIIRS	
[1] x [2]	AVHRR*	
[1] x [3]	COMS-MI	
[1] x [4]	GOES-Imager#	
[1] x [5]	GOES-R ABI	
[1] x [11]	Himawari-8/9 AHI	
	MODIS	Applied at all times.
	MTSAT Imager	
	MSG SEVIRI	
	MTG FCI	
	VIIRS	
	VIIRS	

\*The analogue to the 3.9- $\mu\text{m}$  band on AVHRR (the 3.75  $\mu\text{m}$  band) is currently not available on the MetOp-A and MetOp-B spacecraft during daytime operations.

#The 12  $\mu\text{m}$  channel is only available on the GOES-8, GOES-9, GOES-10, and GOES-11 spacecraft.

In addition, the classifiers that depend on  $\rho(3.9\mu\text{m}, 0.65\mu\text{m})$  are also parsed into two scattering angle ( $\Theta$ ) categories ( $\Theta < 90^\circ$  and  $\Theta \geq 90^\circ$ ) to roughly account for differences in the 0.65 and 3.9  $\mu\text{m}$  scattering phase functions. The scattering angle is defined as

$$\Theta = \cos^{-1}(-\cos\theta_{sun}\cos\theta_{sat} + \sin\theta_{sun}\sin\theta_{sat}\cos\phi), \quad (4.9)$$

where  $\theta_{sun}$  is the solar zenith angle,  $\theta_{sat}$  is the satellite zenith angle, and  $\phi$  is the relative azimuth angle. Experiments were conducted using more than two  $\Theta$  categories, but the results changed very little.

The SECO algorithm utilizes 5 - 8 classifiers, depending on the spectral channels provided by a given sensor. Each classifier has  $\epsilon_{tot}(11\mu\text{m})$  as the outermost dimension since uncertainties in the clear sky radiative transfer calculations influence the interpretation of the parameters. When the solar zenith angle is less than  $85^\circ$  and sun glint is not present, four different varieties of  $\beta(12\mu\text{m}, 11\mu\text{m})$  are paired with  $\rho(3.9\mu\text{m}, 0.65\mu\text{m})$  (see Table 4.5). Sun glint is deemed to be present if the pixel is located over open water and the glint angle ( $\Theta_{gl}$ ) is greater than  $40^\circ$ . The glint angle is defined in Equation (4.10).

$$\Theta_{gl} = \cos^{-1}(\cos\theta_{sun}\cos\theta_{sat} + \sin\theta_{sun}\sin\theta_{sat}\cos\phi), \quad (4.10)$$

It is important to note that the relationship between any two forms of  $\beta(\lambda_1, \lambda_2)$ , produced using the same  $\lambda_1$  and  $\lambda_2$ , is highly non-linear [Heidinger et al. 2010], so each form of  $\beta(12\mu\text{m}, 11\mu\text{m})$  coupled with  $\rho(3.9\mu\text{m}, 0.65\mu\text{m})$  will produce a different conditional probability. From a physical standpoint, each form of  $\beta(12\mu\text{m}, 11\mu\text{m})$  describes a different part of the solution space that defines which cloud property states

are possible given the measurements (and associated noise) and the clear sky radiative transfer modeling (and associated errors). For additional discussion of the cloud property solution space in the infrared consult Heidinger et al. [2010] and Chapter 3 of this dissertation. When the solar zenith angle ( $\theta_{\text{sun}}$ ) is greater than  $90^\circ$  the same four varieties of  $\beta(12\mu\text{m}, 11\mu\text{m})$  are paired with  $\varepsilon_p(3.9\mu\text{m})$ . In the day/night terminator region ( $85^\circ \leq \theta_{\text{sun}} \leq 90^\circ$ ) and in sun glint, a  $\varepsilon_{\text{tot}}(11\mu\text{m}) \times \beta(12\mu\text{m}, 11\mu\text{m})$  multivariate classifier is used. In addition, the  $\varepsilon_{\text{tot}}(11\mu\text{m}) \times \beta_{\text{tot}}(12\mu\text{m}, 11\mu\text{m}) \times \beta_{\text{tot}}(8.5\mu\text{m}, 11\mu\text{m})$ ,  $\varepsilon_{\text{tot}}(11\mu\text{m}) \times \beta_{\text{opaque}}(12\mu\text{m}, 11\mu\text{m}) \times \beta_{\text{opaque}}(8.5\mu\text{m}, 11\mu\text{m})$ , and  $\varepsilon_{\text{tot}}(11\mu\text{m}) \times \beta_{\text{tot}}(12\mu\text{m}, 11\mu\text{m}) \times \beta_{\text{tot}}(7.3\mu\text{m}, 11\mu\text{m})$  classifiers are used at all times of the day if the sensor spectral capabilities allow. While  $\beta(12\mu\text{m}, 11\mu\text{m})$  has been demonstrated to be a more robust metric for inferring cloud composition than the 11 – 12  $\mu\text{m}$  BTD [Chapter 3 of dissertation], multivariate 11 – 12  $\mu\text{m}$  BTD based classifiers are also used as there are occasions when the  $\beta(12\mu\text{m}, 11\mu\text{m})$  based metrics are less skillful either due to errors in clear sky radiative transfer modeling or “saturation” issues at large cloud optical depths. The 11 – 12  $\mu\text{m}$  BTD based classifiers are only used when the 11 – 12  $\mu\text{m}$  BTD is less than zero and the BTD data are parsed into 5 different 11  $\mu\text{m}$  clear sky brightness temperature bins ( $< 255$  K, 255-260 K, 260-265 K, 265-270 K, and  $> 270$  K) to account for the increased frequency of occurrence of negative “split-window” values in environments with cold backgrounds [Pavolonis et al. 2006].

By taking the ratio of the ash/dust conditional probability to the non-ash/dust conditional probability for each bin in the conditional probability look-up table, regions of the multivariate classifier space that favor volcanic ash/dust can be easily visualized. Figure 4.11 shows the conditional probability ratio of all of the multivariate classifiers

used over open water surfaces. In addition, Panels A through D are valid for  $\Theta \geq 90^\circ$ . Only the 0.10 – 0.20  $\varepsilon_{\text{tot}}(11\mu\text{m})$  bin is shown for the 3-dimensional classifiers (Panels A-K). The cyan to red portion of the color scheme is indicative of histogram bins where the ash/dust conditional probability is larger than the non-ash/dust conditional probability. Figure 4.11 indicates that the relationship between a given pair of variables is generally complicated and not conducive to using simple threshold functions to identify ash and dust in a deterministic manner. While  $\beta_{\text{tot}}(12\mu\text{m}, 11\mu\text{m})$  must have a valid value in order to estimate the ash/dust probability for a given satellite pixel, all other variants of  $\beta(\lambda_1, \lambda_2)$  are allowed to be invalid ( $\varepsilon(\lambda_1)$  and/or  $\varepsilon(\lambda_2) < 0.0$ ), as an invalid  $\beta(\lambda_1, \lambda_2)$  is still informative. For instance, an invalid  $\beta_{\text{tot}_\sigma 8}(12\mu\text{m}, 11\mu\text{m})$  is more likely to be associated with a single layer cloud than a valid value of  $\beta_{\text{tot}_\sigma 8}(12\mu\text{m}, 11\mu\text{m})$ . All invalid  $\beta(\lambda_1, \lambda_2)$  values are placed in the very first histogram bin for that particular  $\beta(\lambda_1, \lambda_2)$ . It is also worth noting that due to the maximum emissivity being capped at 0.99990 as a means of preventing arithmetic overflow when computing cloud optical depth (see Equation 3), the minimum valid value of  $\beta_{\text{opaque}}(\lambda_1, \lambda_2)$  is approximately 0.425 (e.g.  $\varepsilon(\lambda_1)=0.98$  per the definition of the opaque cloud assumption and  $\varepsilon(\lambda_2)=0.99990$  per the maximum allowed value).

As might be expected, the 3-dimensional classifiers (Panels A through K in Figure 4.11) can provide greater spectral separation between ash/dust and all other features in the training data set compared to the 2-dimensional (bi-spectral) classifiers (Panels L through O in Figure 4.11). Fortunately, the 2-dimensional classifiers are only utilized under a very limited set of conditions. Figure 4.11 also reveals that the classifiers that utilize the top of troposphere variant of  $\beta(\lambda_1, \lambda_2)$  provide the best opportunity to

produce an ash/dust conditional probability that is 1000-10,000 times *larger* than the non-ash/dust conditional probability. In contrast, the classifiers that utilize an “opaque cloud” version of  $\beta(\lambda_1, \lambda_2)$  generally provide the best opportunity to produce an ash/dust conditional probability that is 1000-10,000 times *smaller* than the non-ash/dust conditional probability. The  $\beta_{\text{tot}}(12\mu\text{m}, 11\mu\text{m}) \times \beta_{\text{tot}}(8.5\mu\text{m}, 11\mu\text{m})$  classifier (Panel I in Figure 4.11) has two distinct regions where the ash/dust conditional probability is at least 100 times greater than the non-ash/dust conditional probability. The dual maxima structure is primarily the result of small amounts of SO<sub>2</sub> combining with volcanic ash to create a spectral signature that is very similar to low-level liquid water clouds. The dual maxima pattern is most pronounced when  $\epsilon_{\text{tot}}(11\mu\text{m}) < 0.10$  (not shown), rendering the  $\beta(8.5\mu\text{m}, 11\mu\text{m})$ -based classifiers (Panels I and J in Figure 4.11) less useful in the transition region between little to no SO<sub>2</sub> influence and strong SO<sub>2</sub> influence. Thus, the  $\beta(8.5\mu\text{m}, 11\mu\text{m})$ -based classifiers are not used unless  $\epsilon_{\text{tot}}(11\mu\text{m}) > 0.10$  or  $\beta_{\text{tot}}(8.5\mu\text{m}, 11\mu\text{m}) \leq 1.05$  or  $\beta_{\text{tot}}(8.5\mu\text{m}, 11\mu\text{m}) \geq 2.0$ .

Analogous to Figure 4.11, Figure 4.12 shows the conditional probability ratio for land surfaces, where the snow and ice covered surfaces were excluded from the classifiers that are only valid during the day (Panels A through D). The snow/ice surface conditional probability ratios of the classifiers that are only valid during the day are shown in Figure 4.13. Over land surfaces, the classifiers that do not rely on the presence of sunlight (Panels E through O in Figure 4.12) exhibit ash/dust conditional probabilities that are rarely more than 1000 times larger than the corresponding non-ash/dust conditional probability. The differences between the land and water conditional probabilities can be largely attributed to the greater uncertainty in the clear sky radiance

calculations over land. Over snow and ice surfaces,  $\rho(3.9\mu\text{m}, 0.65\mu\text{m})$  is very small under clear sky conditions because snow and ice have a very large albedo at  $0.65\ \mu\text{m}$  and a very small albedo at  $3.9\ \mu\text{m}$ . Differences between Panels A through D in Figure 4.12 and Figure 4.13 are generally a result of differing surface albedo properties. While not shown, the difference between surface types becomes much smaller with increasing  $\epsilon_{\text{tot}}(11\mu\text{m})$ . Finally, the conditional probability ratios for the  $11 - 12\ \mu\text{m}$  BTD based classifiers (valid over land surfaces with a clear sky  $11\ \mu\text{m}$  brightness temperature  $> 270\ \text{K}$ ) are shown in Figure 4.14. As expected, large negative “split-window” values are far more likely to be associated with ash and dust than other features, especially when at larger  $\epsilon_{\text{tot}}(11\mu\text{m})$  values or when coupled with the near-infrared based spectral metrics. Far less separation between ash/dust and all other features is found when the  $11 - 12\ \mu\text{m}$  BTD is about  $-0.5\ \text{K}$  or larger.

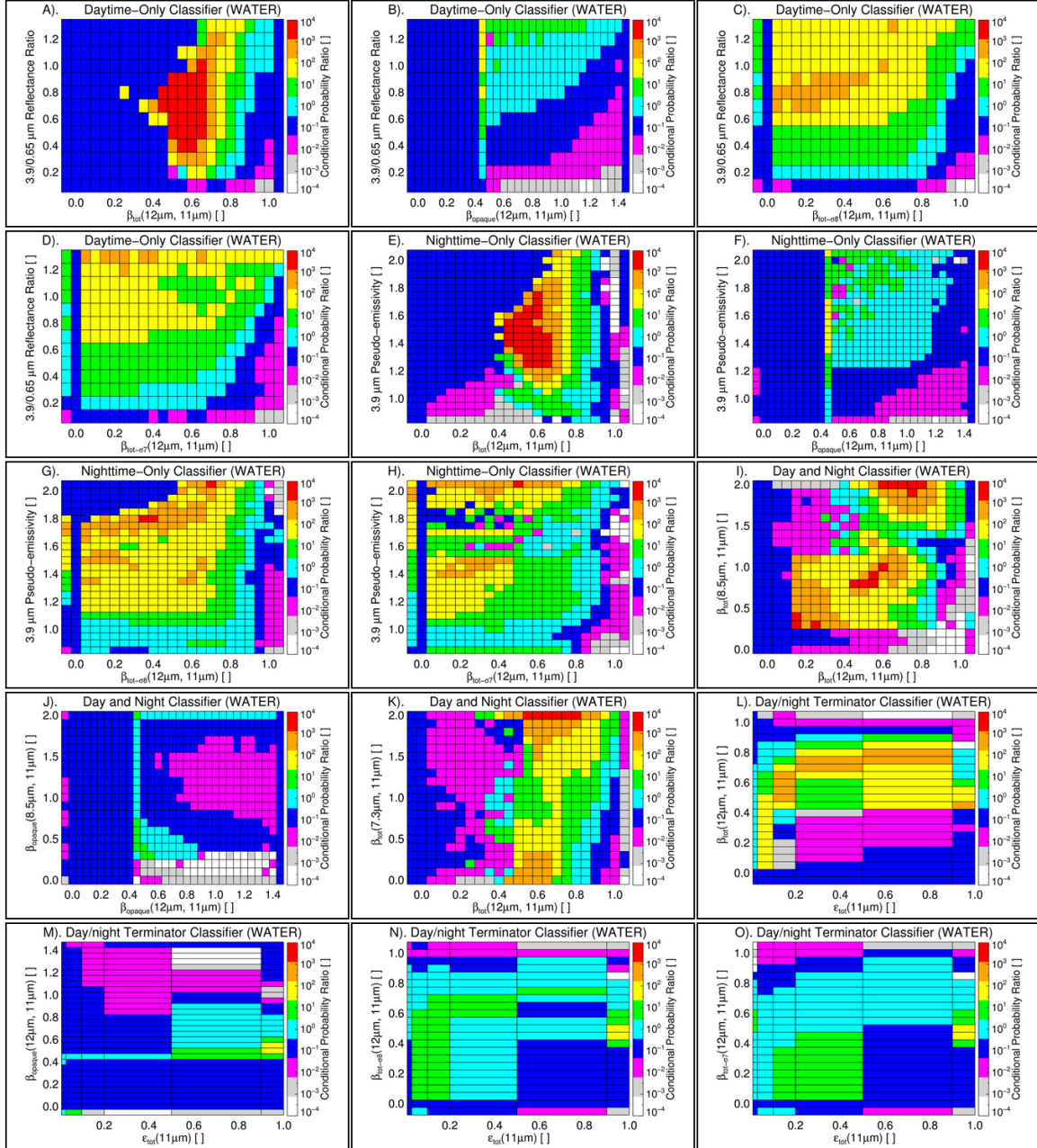


Figure 4.11: The ratio of the ash/dust class conditional probability to the class conditional probability of all other features is shown as a function of various multivariate spectral classifiers for an open water surface. The cyan/red portion of the color scheme indicates that the class conditional probability of ash/dust is greater than the class conditional probability of all non-ash/dust features for that histogram bin. A)  $\beta_{tot}(12\mu\text{m}, 11\mu\text{m})$  vs.  $\rho(3.9\mu\text{m}, 0.65\mu\text{m})$  (daytime classifier), B)  $\beta_{opaque}(12\mu\text{m}, 11\mu\text{m})$  vs.  $\rho(3.9\mu\text{m}, 0.65\mu\text{m})$  (daytime classifier), C)  $\beta_{tot\_s8}(12\mu\text{m}, 11\mu\text{m})$  vs.  $\rho(3.9\mu\text{m}, 0.65\mu\text{m})$  (daytime classifier), D)  $\beta_{tot\_s7}(12\mu\text{m}, 11\mu\text{m})$  vs.  $\rho(3.9\mu\text{m}, 0.65\mu\text{m})$  (daytime classifier), E)  $\beta_{tot}(12\mu\text{m}, 11\mu\text{m})$  vs.  $\epsilon_p(3.9\mu\text{m})$  (nighttime classifier), F)  $\beta_{opaque}(12\mu\text{m}, 11\mu\text{m})$  vs.  $\epsilon_p(3.9\mu\text{m})$  (nighttime classifier), G)  $\beta_{tot\_s8}(12\mu\text{m}, 11\mu\text{m})$  vs.  $\epsilon_p(3.9\mu\text{m})$  (nighttime classifier), H)  $\beta_{tot\_s7}(12\mu\text{m}, 11\mu\text{m})$  vs.  $\epsilon_p(3.9\mu\text{m})$  (nighttime classifier), I)  $\beta_{tot}(12\mu\text{m}, 11\mu\text{m})$  vs.  $\beta_{tot}(8.5\mu\text{m}, 11\mu\text{m})$  (day and night classifier), J)  $\beta_{opaque}(12\mu\text{m}, 11\mu\text{m})$  vs.  $\beta_{opaque}(8.5\mu\text{m}, 11\mu\text{m})$  (day and night classifier), K)  $\beta_{tot}(12\mu\text{m}, 11\mu\text{m})$  vs.  $\beta_{tot}(7.3\mu\text{m}, 11\mu\text{m})$  (day and night classifier), L)  $\epsilon_{tot}(11\mu\text{m})$  vs.  $\beta_{tot}(12\mu\text{m}, 11\mu\text{m})$  (twilight classifier only), M)  $\epsilon_{tot}(11\mu\text{m})$  vs.  $\beta_{opaque}(12\mu\text{m}, 11\mu\text{m})$  (twilight classifier only), N)  $\epsilon_{tot}(11\mu\text{m})$  vs.  $\beta_{tot\_s8}(12\mu\text{m}, 11\mu\text{m})$  (twilight classifier only), O)  $\epsilon_{tot}(11\mu\text{m})$  vs.  $\beta_{tot\_s7}(12\mu\text{m}, 11\mu\text{m})$  (twilight classifier only). Panels A through K are valid for  $0.10 < \epsilon_{tot}(11\mu\text{m}) < 0.20$ .

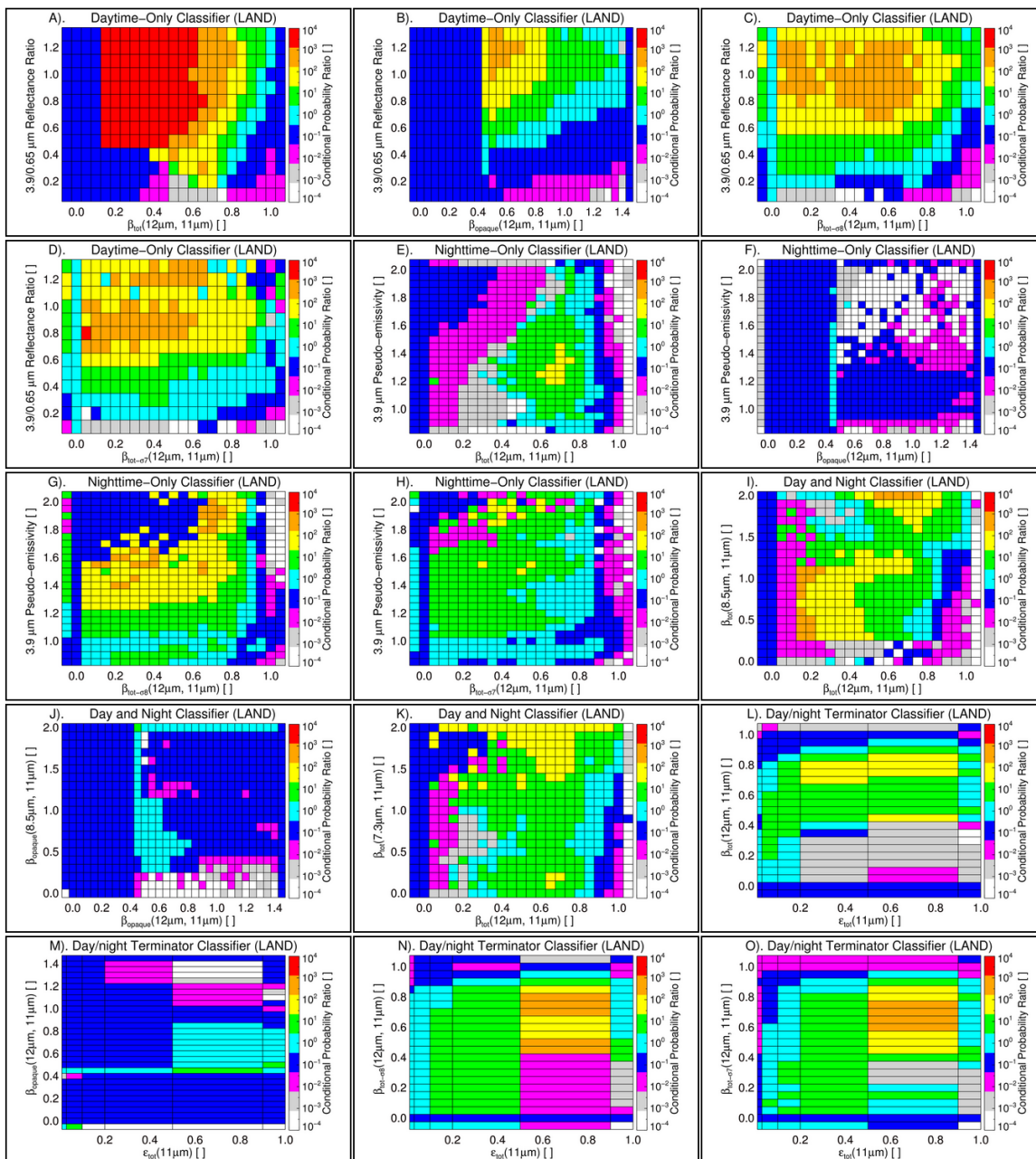


Figure 4.12: Same as Figure 4.11, except panels A through D are valid over all land surfaces excluding snow and ice and panel E through O are valid over all land surfaces including snow and ice.

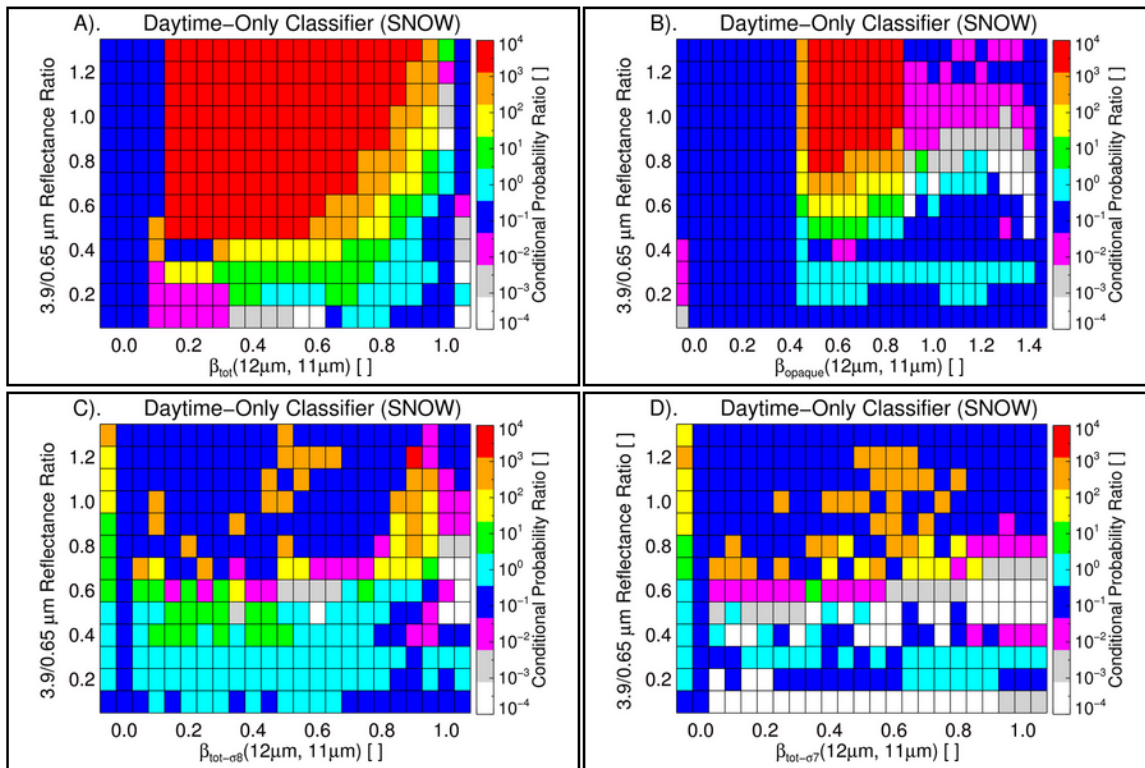


Figure 4.13: Same as panels A through D in Figure 4.11 and Figure 4.12, except over snow and ice surfaces (including frozen water).

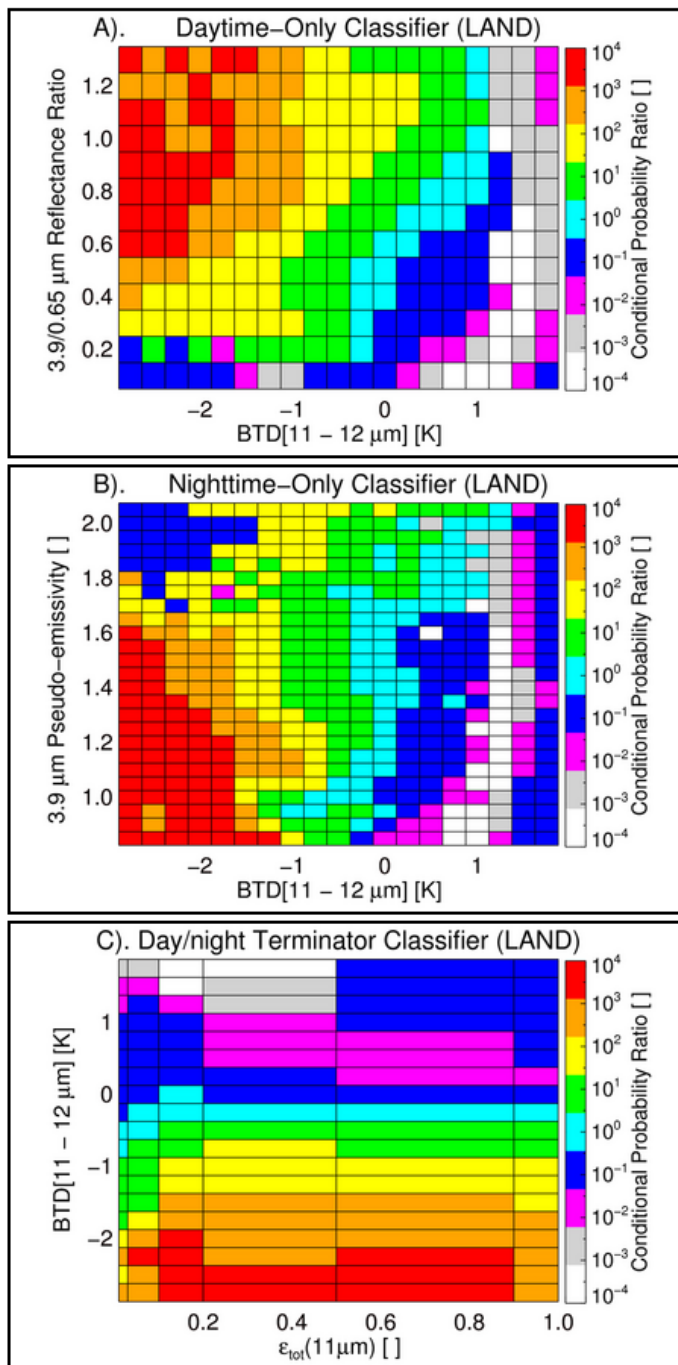


Figure 4.14: Analogous to Figure 4.11, Figure 4.12, and Figure 4.13 except the ash/dust to non-ash/dust conditional probability ratio for the BTD(11 - 12  $\mu\text{m}$ ) related classifiers are shown for a land surface with a clear sky 11  $\mu\text{m}$  brightness temperature > 270 K. A). BTD(11 - 12  $\mu\text{m}$ ) vs.  $\rho(3.9\mu\text{m}, 0.65\mu\text{m})$  (daytime classifier), B). BTD(11 - 12  $\mu\text{m}$ ) vs.  $\epsilon_p(3.9\mu\text{m})$  (nighttime classifier), and C). BTD(11 - 12  $\mu\text{m}$ ) vs.  $\epsilon_{\text{tot}}(11\mu\text{m})$  (twilight classifier only).

#### ***4.5. Analysis of Volcanic Ash/Dust Probabilities***

An initial assessment of the naïve Bayesian method, used to identify which satellite pixels are most likely to contain volcanic ash/dust, is conducted through the analysis of four ash/dust cases captured by MODIS. Each of the four cases (2 volcanic ash and 2 dust) is independent of the classifier training data, and the ash/dust probability is assessed within the context of human expert estimated horizontal cloud boundaries and the traditional “split-window” technique for detecting volcanic ash and dust. Ash/dust probability results are generated using four different spectral channel combinations that are commonly available on operational and research satellite radiometers.

1. 0.65 [daytime only], 3.9, 7.3, 8.5, 11, 12  $\mu\text{m}$  (SC1, SC=Spectral Combination)
2. 0.65 [daytime only], 3.9, 8.5, 11, 12  $\mu\text{m}$  (SC2)
3. 0.65 [daytime only], 3.9, 11, 12  $\mu\text{m}$  (SC3)
4. 11, 12  $\mu\text{m}$  (SC4)

The goal of the manual analysis of the ash/dust cloud boundaries was to define a Region of Interest (ROI) that contains the portion of the ash/dust cloud that can be manually identified in imagery, either directly or through spatial deduction. All conclusions drawn from the comparison to the manually determined ROI are derived from relative relationships. As such, small perturbations to the ROI do not impact the results as long as ash or dust pixels that exhibit a robust spectral signature (i.e. are obvious in the imagery) are not left out of the ROI.

##### *4.5.1. Volcanic Ash from Mount Cleveland (daytime)*

The ash/dust probabilities are analyzed using the previously discussed daytime scene with airborne volcanic ash (and SO<sub>2</sub>) from an explosive eruption of Mount

Cleveland, AK that began on February 19, 2001 at approximately 14:30 UTC [McGimsey et al. 2004]. The starting date and time of the *Terra* MODIS granule is February 19, 2001 at 23:10 UTC. The results, along with reference imagery, are shown in Figure 4.15. The bounds of the manually derived ROI are overlaid on each geo-referenced image (Panels A, B, C, D, F, H, and J) in Figure 4.15. While the spatial distribution of the ash optical depth is unknown, the 11  $\mu\text{m}$  brightness temperature image (Panel C) indicates that much of the cloud is quite tenuous (has a small optical depth). The ash/dust probability image (the transition from red to orange in the color bar indicates a transition to probabilities that are less than 10%) and the normalized histogram of ash/dust probability (inside and outside of the ROI) are shown for each of the four spectral combinations (SC1, SC2, SC3, and SC4) examined. Recall that probabilities are only computed for pixels that passed the pre-screening tests described earlier. The 11  $\mu\text{m}$  brightness temperature is shown in the geo-located images wherever the pixel probability is not computed. The histograms were created using the entire 5-minute MODIS granule, not just the sub-granule region shown in the geo-referenced images (for the sake of clarity) within Figure 4.15. The ash/dust probability is expressed as a percentage and log scaling is used in the figures to enhance details at low probabilities.

Not surprisingly, SC1 (Panels D and E), which utilizes the greatest number of spectral channels, produces the greatest area of probabilities that exceed 90% within the ROI. Regardless of the spectral channel combination used, the probability distribution demonstrates that the Bayesian method has good skill, as the amount of overlap between pixels inside and outside the ROI is relatively small, but does increase as the number of

spectral channels utilized decreases (moving from the second row from the top to the bottom of Figure 4.15), as one would expect if the spectral channels that are removed add value. Additional analysis was conducted to better quantify the performance of each spectral channel combination relative to the traditional “split-window” BTD. Performance related statistics (Panel A: CSI, Panel B: POD, and Panel C: FAR) are shown in Figure 4.16. The statistics are shown as a function of the threshold used to create a binary yes/no ash/dust mask from the probability derived from each spectral channel combination as well as the “split-window” BTD. The simple binary masks are not the end goal; it is just used to assess the performance of the Bayesian method by quantifying the amount of overlap between the ash/dust and non-ash/dust classes. The ash/dust probability threshold is shown on the top x-axis of Figure 4.16 and the 11 – 12  $\mu\text{m}$  BTD threshold is shown on the bottom x-axis. The SC1, SC2, SC3, SC4, and “split-window” BTD results are shown in black, red, blue, green, and magenta, respectively. The filled colored circles indicate which threshold, used to create a binary mask, produces the largest CSI. The ash/dust probability metric always produces a significantly larger maximum CSI than the “split-window” BTD. More specifically, SC1 produces the greatest maximum CSI (0.29), followed by SC4 (0.25), SC2 (0.24), SC3 (0.21), and the “split-window” BTD (0.13). The ranking of SC4 slightly ahead of SC2 and SC3 indicates that  $\beta_{\text{tot}}(7.3\mu\text{m}, 11\mu\text{m})$  is adding good value in this case, primarily due to the presence of  $\text{SO}_2$ , and the  $\rho(3.9\mu\text{m}, 0.65\mu\text{m})$  signal in certain portions of the cloud is weak ( $< 0.3$ ) as shown in Figure 4.7I. The weak  $\rho(3.9\mu\text{m}, 0.65\mu\text{m})$  signals are co-located with regions where the cloud is hardly identifiable in 11  $\mu\text{m}$  imagery, indicative of very low optical depths, where a strong  $\rho(3.9\mu\text{m}, 0.65\mu\text{m})$  signal is not expected [Pavolonis et al.

2006]. Finally, even though the same two spectral channels (11 and 12  $\mu\text{m}$ ) are used, SC4 is much more skillful at distinguishing ash/dust from all other features than the 11 – 12  $\mu\text{m}$  BTD alone, which illustrates the power of using  $\epsilon_{\text{tot}}(11\mu\text{m})$  and  $\beta$ -ratios in lieu of, or in addition to, BTDs.

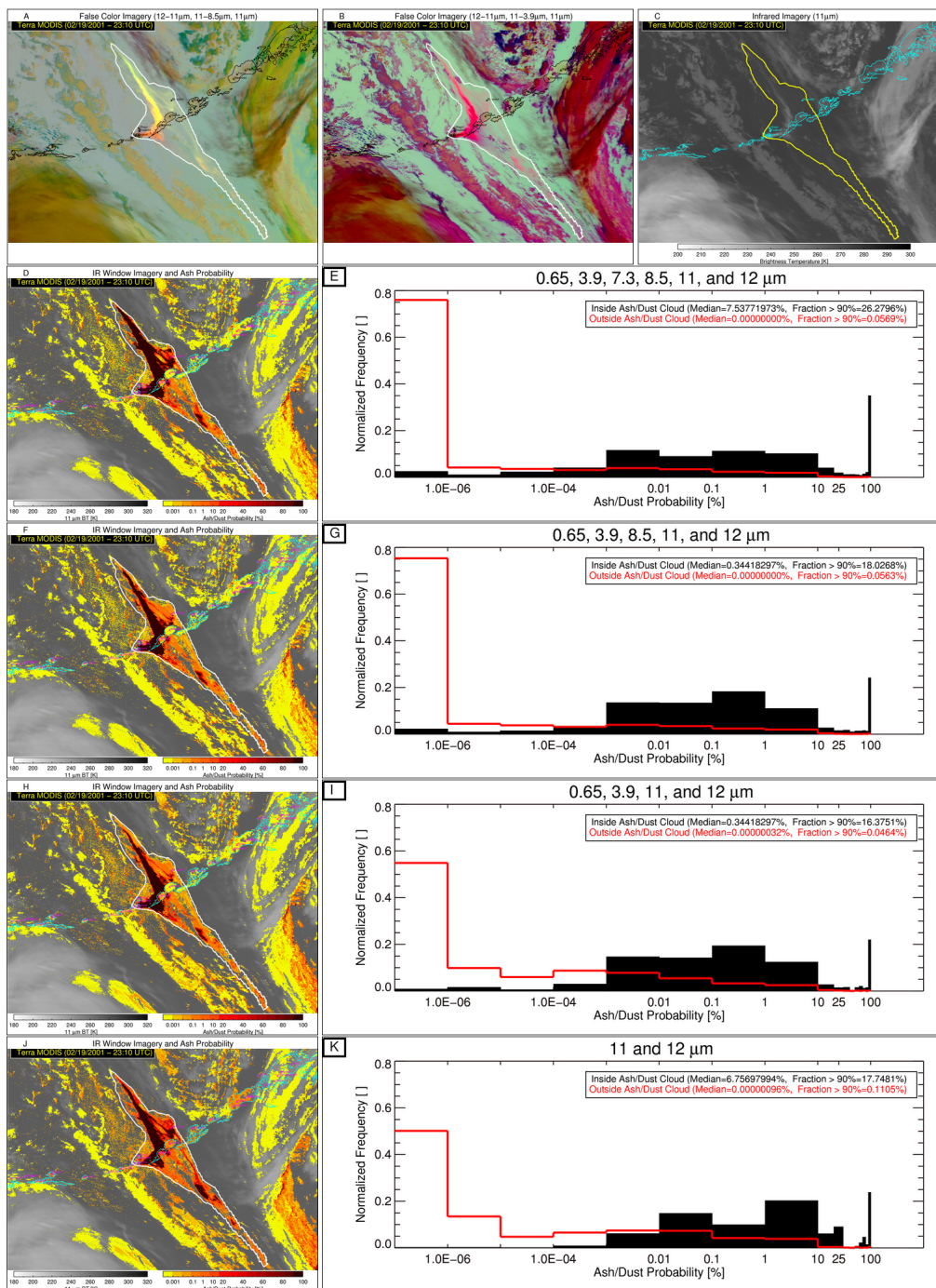


Figure 4.15: The results of the Bayesian method are shown for a Terra MODIS image from February 19, 2001 at 23:10 UTC. A). 12–11  $\mu\text{m}$ , 11–8.5  $\mu\text{m}$ , and 11  $\mu\text{m}$  false color image. B). 12–11  $\mu\text{m}$ , 11–3.9  $\mu\text{m}$ , and 11  $\mu\text{m}$  false color image. C). 11  $\mu\text{m}$  image. D). Ash/dust probability image for 0.65, 3.9, 7.3, 8.5, 11, 12  $\mu\text{m}$  channel combination. E). Histogram of ash/dust probability inside (black) and outside (red) of manually analyzed ash/dust cloud. The panels in the third through fifth rows are analogous to the second row, except for the 0.65, 3.9, 8.5, 11, 12  $\mu\text{m}$ , 0.65, 3.9, 11, 12  $\mu\text{m}$ , and 11, 12  $\mu\text{m}$  channel combinations, respectively. The outer bounds of the manually defined ash/dust cloud are overlaid on each geo-referenced image.

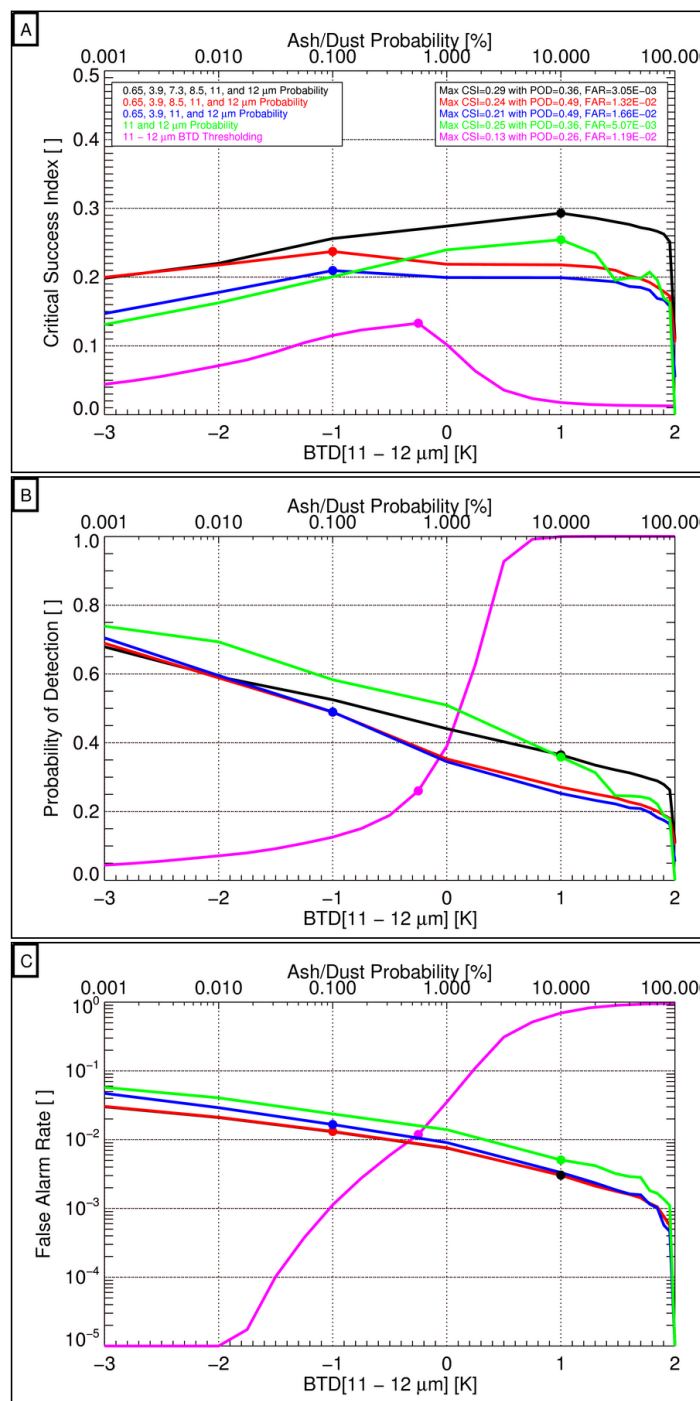


Figure 4.16: Skill statistics of threshold based ash/dust detection, applied to several different metrics, are shown as a function of the selected threshold. The thresholds are relevant to the following metrics: 0.65, 3.9, 7.3, 8.5, 11, 12 μm based probability (black), 0.65, 3.9, 8.5, 11, 12 μm based probability (red), 0.65, 3.9, 11, 12 μm based probability (blue), 11, 12 μm based probability (green), and BTD(11-12 μm). The statistics are valid for a 5-minute MODIS granule with a starting time of February 19, 2001 at 23:10 UTC. The bottom x-axis is BTD(11-12 μm) and the top x-axis is ash/dust probability. The critical success index (CSI) (A), probability of detection (B), and false alarm rate (C) are shown. The circles denote the threshold where the CSI is a maximum.

#### 4.5.2. Volcanic Ash from Mount Cleveland

In the 9.5 hours between *Terra* MODIS overpasses, volcanic ash and gases from the explosive February 19, 2001 eruption of Cleveland dispersed along a NW/SE axis and were advected northeastward by the atmospheric winds. Results from the February 20, 2001 08:45 UTC *Terra* MODIS (nighttime) overpass are shown in Figure 4.17. The 11  $\mu\text{m}$  brightness temperature image (Panel C) indicates that nearly the entire ash cloud is now highly semi-transparent to infrared radiation and quite difficult to see in single channel infrared imagery, more so than in the February 19, 2001 23:10 UTC *Terra* MODIS overpass shown earlier, likely due to dispersion and ash fallout processes. Similar to the February 19 Cleveland volcanic ash example, the overlap in the ash/dust probability distribution inside and outside of the ROI is rather small but does increase when less spectral channels are utilized. Performance metrics analogous to Figure 4.16 are shown in Figure 4.18. Once again the ash/dust probability metric always produces a significantly larger maximum CSI than the “split-window” BTD maximum value of 0.08. SC1, SC2, and SC3 produce maximum CSI of about 0.30, while SC4 has a maximum CSI of 0.24. The SC4 maximum CSI of 0.24 is three times greater than the “split-window” maximum of 0.08, further illustrating the value of using  $\epsilon_{\text{tot}}(11\mu\text{m})$  and  $\beta$ -ratios. Even though the CSI analysis indicates that additional spectral channels do not always have a large impact, it will be shown in Chapter 6 that the extra spectral channels do have noticeable positive impact on the final results of the complete SECO algorithm.

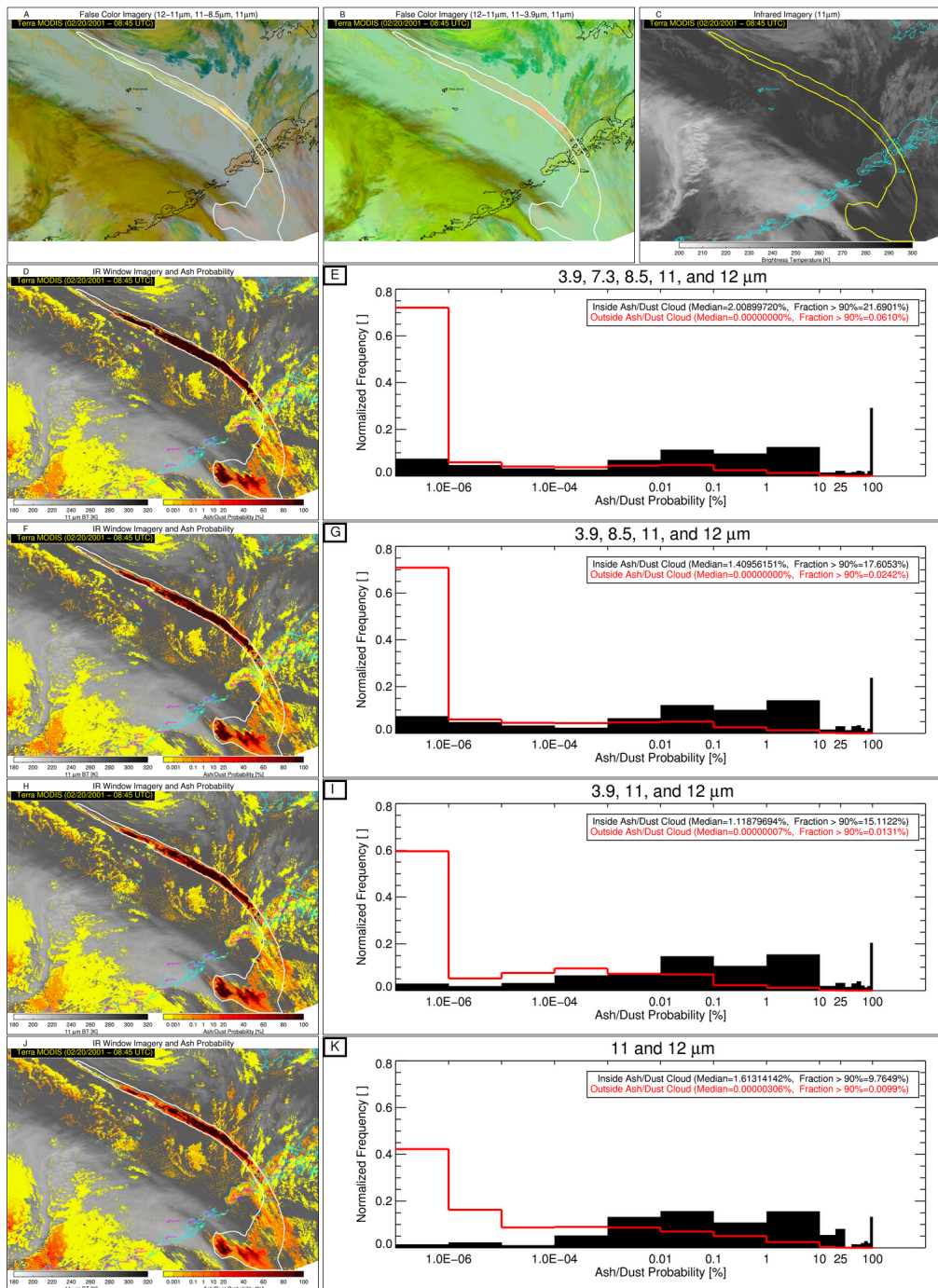


Figure 4.17: Same as Figure 4.15 except for a Terra MODIS image from February 20, 2001 at 08:45 UTC. Since this is a nighttime scene the 0.65  $\mu$ m channel is not utilized.

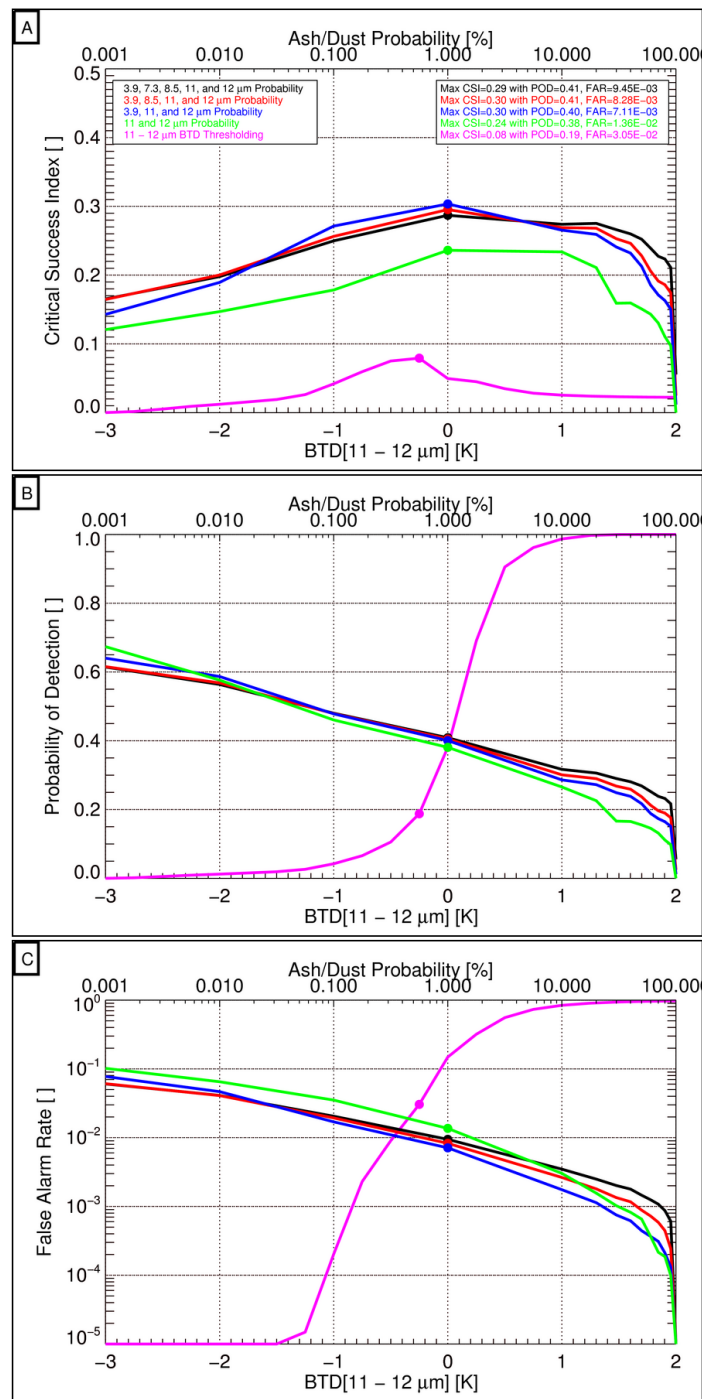


Figure 4.18: Same as Figure 4.16 except the statistics are valid for a 5 minute Terra MODIS granule with a starting time of February 20, 2001 at 08:45 UTC.

#### 4.5.3. South American Dust (daytime)

The Bayesian method was also applied to a dust case where sediments, primarily composed of gypsum, calcite, and halite [Piovano et al. 2002; da Silva et al. 2008], from dried up portions of Laguna Mar Chiquita, a saline lake in central Argentina, were lofted into the atmosphere by strong winds on July 29, 2012 (a small portion of the dust area may be the result of secondary sources). Not only is this case independent of the training data set, the training data set did not include any South American dust cases, let alone a case with a unique rock type that is associated with a relatively localized source. In addition, the dust is primarily located over land, where uncertainty in the clear sky radiance calculations is greater compared to water surfaces. Thus, this case is quite useful for demonstrating the robustness of the Bayesian method. The starting date and time of the *Aqua* MODIS granule used in this analysis is July 29, 2012 at 17:35 UTC (daytime). The results are shown in Figure 4.19 and Figure 4.20. Because of its relatively unique mineral composition the dust does not take on the typical reddish color in the 12-11  $\mu\text{m}$ , 11-8.5  $\mu\text{m}$ , 11  $\mu\text{m}$  false color image (Figure 4.19a). The manually analyzed bounds of the dust cloud were primarily determined from the 12-11  $\mu\text{m}$ , 11-3.9  $\mu\text{m}$ , 11  $\mu\text{m}$  false color image (Figure 4.19b) where the cloud is more readily apparent. The dust cloud ROI is also consistent with MODIS true color imagery (<https://earthdata.nasa.gov/labs/worldview/>). While the ash/dust probability within the dust cloud is generally quite large ( $> 80\%$ ), a fair number of larger values are also found outside of the ROI compared to the over-water Cleveland volcanic ash cases. The larger probabilities outside of the ROI are mainly caused by spectral variability in surface emissivity that resembles ash/dust clouds, coupled with errors in the clear sky radiance

calculations (largely driven by errors in land surface temperature). Nevertheless, the overlap in ash/dust probability inside and outside of the ROI is quite small, and increases when fewer spectral channels are used (see Figure 4.19). The maximum CSI associated with applying a threshold to the ash/dust probability (0.43, 0.43, 0.41, 0.46, for SC1, SC2, SC3, SC4, respectively) is still nearly twice the maximum CSI that can be achieved by applying a threshold to the “split-window” BTD (0.22) for this MODIS granule (Figure 4.20), regardless of the spectral channel combination used in estimating ash/dust probability. Despite the complexities introduced by a variety of complicated land surface types, the FAR associated with the maximum ash/dust CSI is very comparable to the over ocean Cleveland ash scenes, but the probability threshold required to achieve the maximum CSI does vary quite a bit from scene to scene. This issue is addressed in Chapter 6.

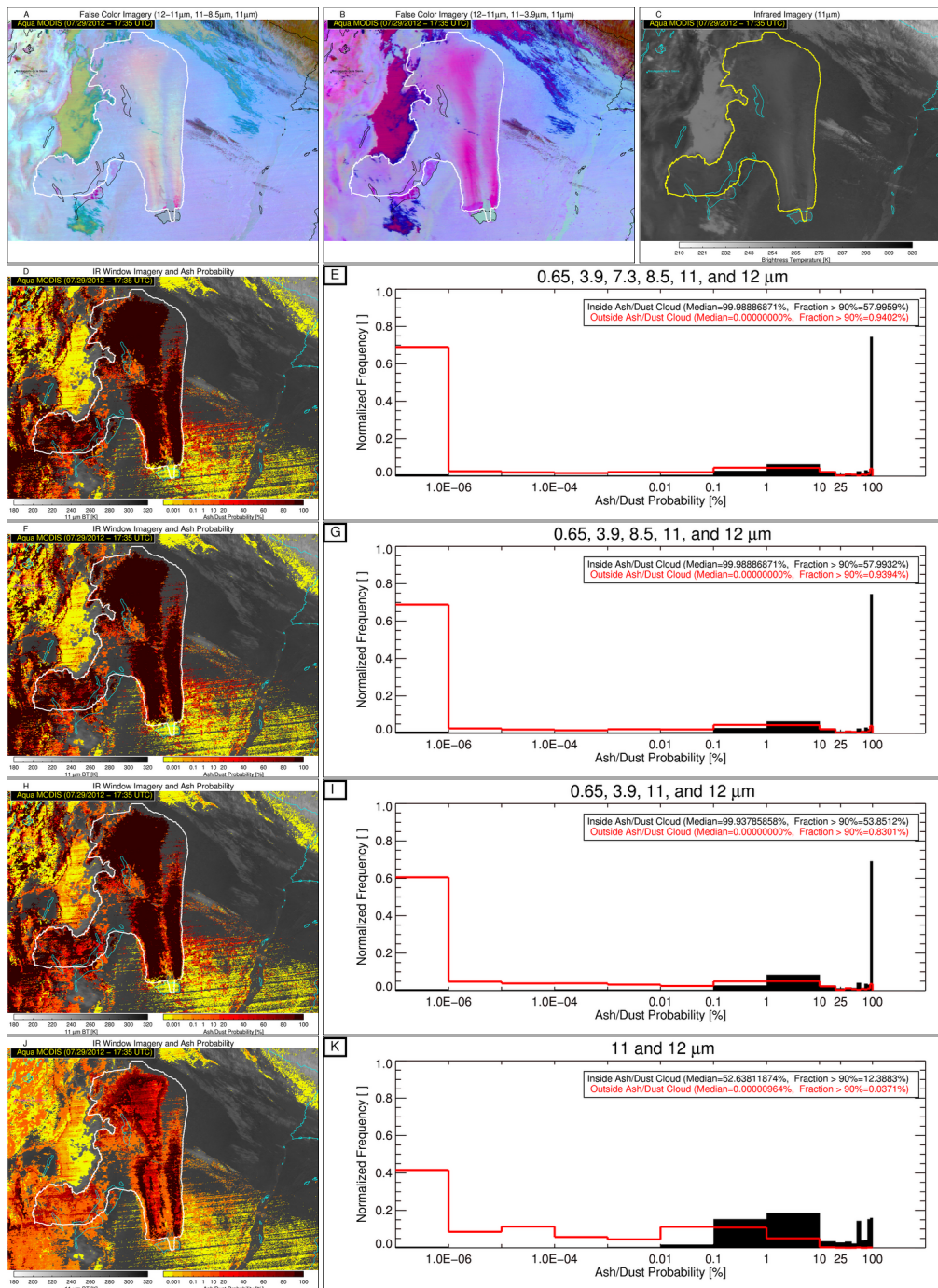


Figure 4.19: Same as Figure 4.15 except for an Aqua MODIS image from July 29, 2012 at 17:35 UTC.

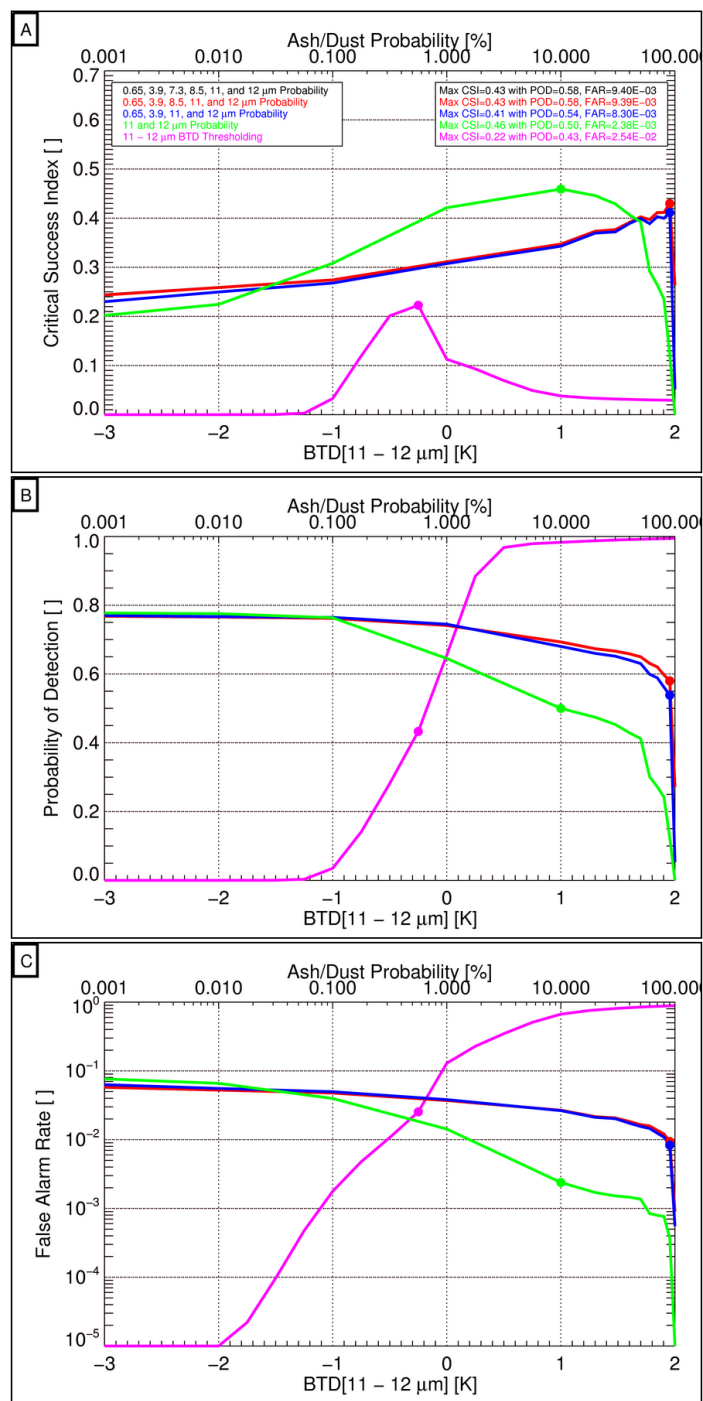


Figure 4.20: Same as Figure 4.16 except the statistics are valid for a 5 minute Aqua MODIS granule with a starting time of July 29, 2012 at 17:35 UTC.

Dust lofted from the western portion of the Argentinean Pampa (plain) by a nocturnal thunderstorm outflow boundary on January 24, 2014 was also examined. Feldspars and quartz tend to be the primary mineral components of dust that originates from the Argentinean Pampa [Ramsperger et al. 1998a; Ramsperger et al. 1998b]. The starting date and time of the *Terra* MODIS granule used in this analysis is January 24, 2014 at 03:55 UTC and the results are shown in Figure 4.21 and Figure 4.22. Similar to the Laguna Mar Chiquita dust scene, pixels outside of the manually derived ROI sometimes have a larger probability due to surface emissivity effects and errors in the clear sky radiative transfer (Figure 4.21). In addition, unlike the previous three cases, the SC4 derived ash/dust probabilities are not particularly skillful in this over land nighttime scene, likely as a result of less contrast between the temperature of the dust cloud and the background. The additional spectral information offered by SC1, SC2, and SC3 adds more value in the low temperature contrast situations commonly encountered at night. As shown in Figure 4.22, the maximum CSI of the SC1 (0.21), SC2 (0.21), and SC3 (0.22) derived ash/dust probabilities is more than twice the maximum CSI of the “split-window” BTM (0.10). The maximum CSI of SC4 does not improve upon the “split-window” BTM likely due to low signal to noise and clear sky radiative transfer errors. Overall, the Bayesian method has been demonstrated to be skillful in distinguishing ash/dust and non-ash/dust features, day and night, over land and over water. Pixel and cloud object filters that minimize the impact of clear sky radiative transfer errors, like those encountered in the two South American dust scenes, are described in Chapter 6.

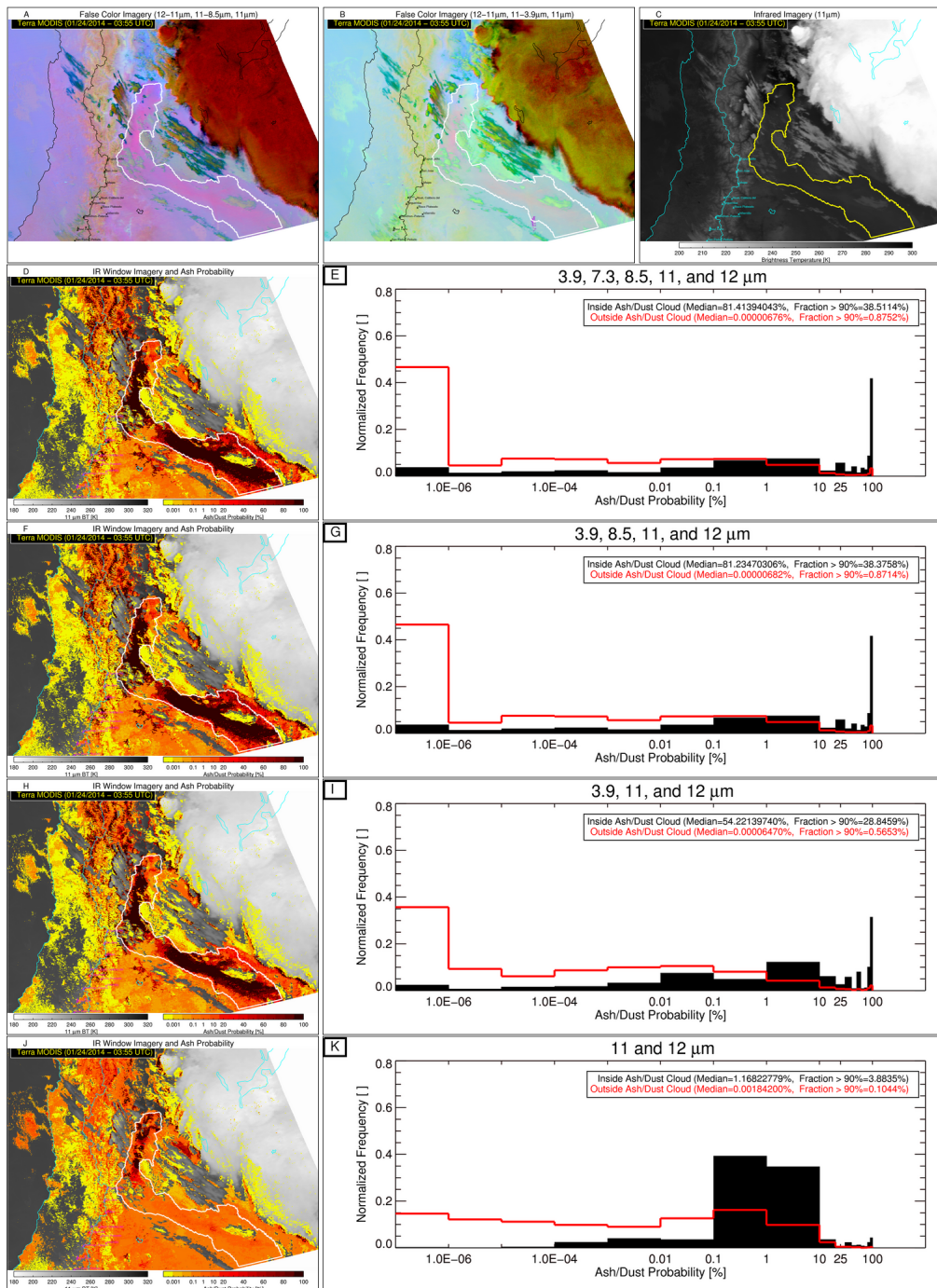


Figure 4.21: Same as Figure 4.15 except for a Terra MODIS image from January 24, 2014 at 03:55 UTC. Since this is a nighttime scene the 0.65  $\mu$ m channel is not utilized.

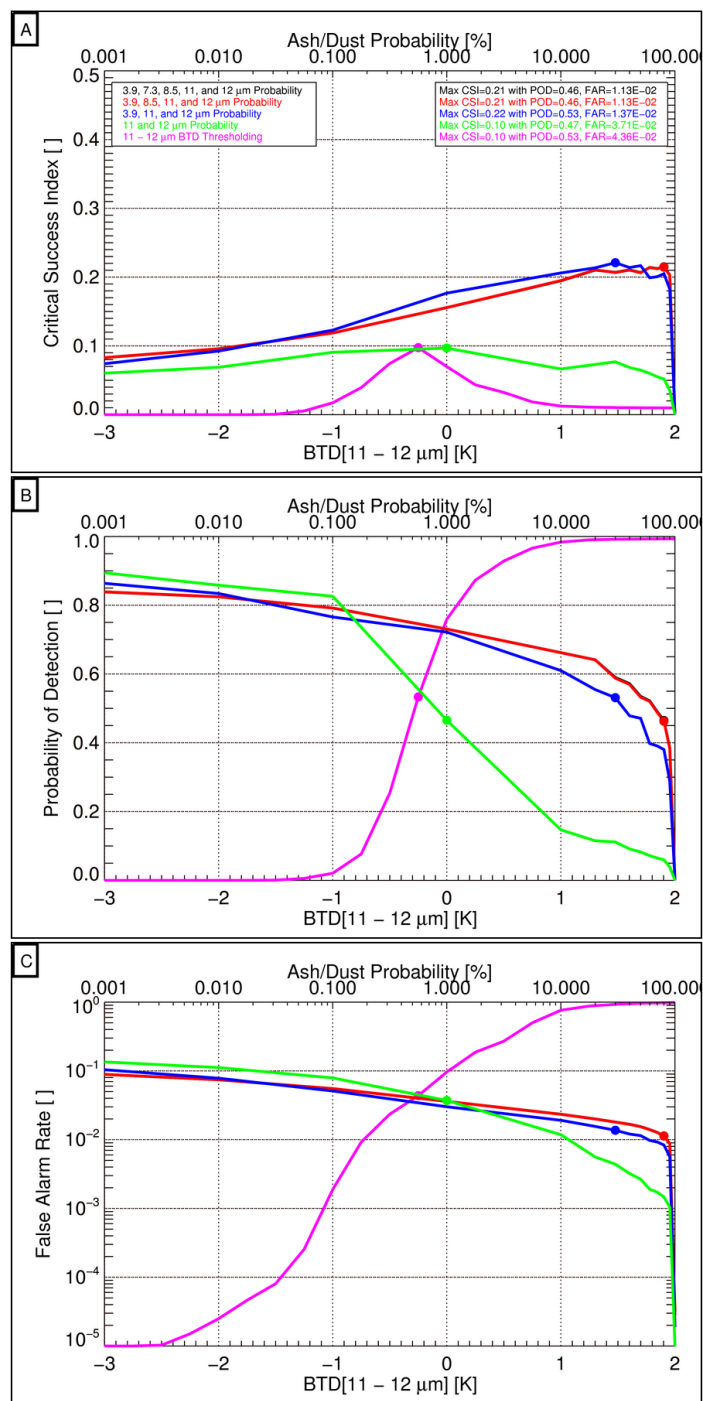


Figure 4.22: Same as Figure 4.16 except the statistics are valid for a 5 minute Terra MODIS granule with a starting time of January 24, 2014 at 03:55 UTC.

#### **4.6. Summary**

In an effort to open the door to new and improved research and operational volcanic ash and dust applications, the globally applicable Spectrally Enhanced Cloud Objects (SECO) algorithm was developed. The SECO volcanic ash and dust detection algorithm, which can be applied to nearly any satellite sensor at all times of the day, consists of four major components. The first two components, computation of advanced radiative metrics and estimation of the probability that a given pixel contains volcanic ash and/or dust, were described in this chapter. The remaining two parts, construction of cloud objects and the selection of volcanic ash/dust cloud objects, are described in Chapter 6. The methodology for computing advanced radiative metrics, such as effective absorption optical depth ratios ( $\beta$ -ratios) was described. Multispectral infrared measurements are expressed as  $\beta$ -ratios, as opposed to traditional brightness temperature differences (BTDs), because  $\beta$ -ratios provide increased sensitivity to cloud microphysical properties, including cloud composition. A naïve Bayesian approach was developed to take advantage of the volcanic ash/dust relevant cloud composition information that the  $\beta$ -ratios provide. Various empirically derived multivariate classifiers were constructed by coupling  $\beta$ -ratios, computed from the radiance measured at approximately 11 and 12  $\mu\text{m}$ , with visible and near infrared measurements (0.65 and/or 3.9  $\mu\text{m}$ ) or  $\beta$ -ratios that are computed using other spectral channel pairs (8.5/11  $\mu\text{m}$  and 7.3/11  $\mu\text{m}$ ). Several case studies showed that the naïve Bayesian approach is quite skillful even when only subsets of the allowable spectral channels are utilized. The skill of the Bayesian approach was also shown to greatly exceed the skill of the traditional “split-window” method used to detection volcanic ash and dust.

The ultimate objective of the automated SECO approach is to produce a binary volcanic ash/dust mask that is comparable in skill to a mask that is manually constructed by a human expert. Despite the success of the Bayesian method, it, alone, is not skillful enough to construct a human expert like binary mask by simply applying a probability threshold. As shown in Chapter 6, the Bayesian method must be combined with advanced spatial analysis to produce such a result.

## Chapter 5

### 5. Retrieval of Volcanic Ash and Dust Cloud Properties

#### 5.1. Introduction

In this chapter, satellite-based infrared measurements will be used to retrieve the radiative temperature, emissivity, and a microphysical parameter of volcanic ash and dust clouds (the term “cloud” will be used throughout this chapter in lieu of “aerosol layer” or “ash/dust plume”), analogous to the cirrus cloud retrievals performed by Heidinger and Pavolonis [2009] and Heidinger et al. [2010]. From these retrieved parameters, the cloud radiative height, effective particle radius, optical depth, and mass loading can be derived, subject to certain assumptions. The retrieval methodology was developed in preparation for the next generation of Geostationary Operational Environmental Satellite (GOES-R) and will serve as the official operational volcanic ash algorithm for GOES-R. The retrieval approach (hereafter referred to as the GOES-R approach), which has already been demonstrated in real-time (<http://volcano.ssec.wisc.edu/>) and used to support operations at the Anchorage and Washington Volcanic Ash Advisory Centers (VAACs), is unique in that it is fully automated, computationally efficient, globally applicable, explicitly accounts for major absorbing background atmospheric gases, and allows the effective cloud temperature to be a free parameter in the retrieval. The cloud radiative temperature has been treated as a constant in nearly all published imaging radiometer-based volcanic ash retrieval studies [e.g. Wen and Rose 1994; Prata and Grant 2001; Gu et al. 2005; Zhang et al. 2006; Corradini et al. 2008; Clarisse et al. 2010b]. In addition, like Yu et al. [2002] and Corradini et al. [2008], the GOES-R algorithm does not rely on the presence of the traditional “reverse absorption” signal (negative 11 – 12  $\mu\text{m}$

brightness temperature difference) [Prata 1989a; Prata 1989b]. A traditional “reverse absorption” signal need not be present because major background absorbing gases (e.g. H<sub>2</sub>O, CO<sub>2</sub>, and O<sub>3</sub>) are accounted for explicitly. The GOES-R approach does not depend on scene dependent off-line look-up tables, so it can easily be implemented operationally. Comparisons to other published methodologies like those of Wen and Rose [1994], Prata and Grant [2001], Corradini et al. [2008], Clarisse et al. [2010b], Francis et al. [2012], and Prata and Prata [2012] are valuable and will be performed at a later time. This chapter will focus on describing and justifying the GOES-R ash/dust retrieval methodology and physical basis. Further, as in Heidinger and Pavolonis [2009], spaceborne lidar measurements will be used to quantify the accuracy of the retrieval method presented in this chapter.

## ***5.2. Infrared Measurements***

Although the basic methodology described in this chapter applies to aircraft measurements of upwelling infrared radiation, we will focus on satellite based infrared measurements, which are generally better suited for global operational monitoring of volcanic ash and dust than research aircraft measurements. Three spectral channels centered near 11, 12, and 13.3  $\mu\text{m}$ , will be used to retrieve the ash and dust cloud properties. Heidinger et al. [2010] use this same channel combination to retrieve cirrus cloud properties and these channels are not sensitive to SO<sub>2</sub>, which simplifies the retrieval (e.g. fewer unknowns) when SO<sub>2</sub> is present, as may be the case in volcanic ash clouds. While the specific spectral characteristics of the channels will differ slightly from sensor to sensor, the channels considered in this chapter have approximate central wavelengths of 11, 12, and 13.3  $\mu\text{m}$  and are available on current sensors such as the

Moderate Resolution Imaging Spectroradiometer (MODIS) and the Spinning Enhanced Visible/Infrared Imager (SEVIRI) and will be available on all next generation geostationary sensors such as the GOES-R Advanced Baseline Imager (ABI) [Schmit et al., 2005]. Geostationary satellites, because of their high temporal refresh, are critical for monitoring volcanic ash and dust clouds. While certain instruments in low earth orbit have better spectral and/or spatial resolution, the temporal resolution is poor relative to geostationary satellites. It should be noted that the 11 and 12  $\mu\text{m}$  channel combination has been historically used to retrieve the optical depth and effective particle radius of volcanic ash and dust clouds (e.g. [Wen and Rose 1994; Prata and Grant 2001; Yu et al. 2002; Gu et al. 2003; Corradini et al. 2008]). However, Heidinger et al. [2010] showed that, for cirrus clouds, the addition of the 13.3  $\mu\text{m}$  channel adds considerable sensitivity to the cloud radiative temperature. Although the retrieval approach described in this chapter can be applied to hyperspectral infrared measurements (available on certain low earth orbit satellites), more advanced retrieval procedures can be applied to hyperspectral measurements (e.g. [Huang et al. 2004; Peyridieu et al. 2010; Clarisse et al. 2010b; DeSouza-Machado et al. 2010]) so this chapter is focused on more commonly available narrow band radiometer measurements. The algorithm described in this chapter will be demonstrated using SEVIRI, which is a 12-channel imaging radiometer with a spatial resolution of 3 km (in the infrared at nadir) and is located in a geostationary orbit with a coverage area that includes many volcanoes. For more information on SEVIRI, see <http://www.eumetsat.int/>. More specifically, volcanic ash from the 2010 eruptions of Eyjafjallajokull (Iceland) and Soufriere Hills (Caribbean) and airborne dust lofted from

the Sahara Desert will be used to illustrate algorithm results and co-located spaceborne lidar data will be used to objectively assess algorithm performance.

### 5.3. Infrared Radiative Transfer Theory

For reader convenience, a brief review of the infrared radiative transfer concepts first introduced in Chapter 3 is given. Assuming a satellite viewing perspective (e.g. upwelling radiation), a fully cloudy field of view, a non-scattering atmosphere (no molecular scattering), and a negligible contribution from downwelling cloud emission or molecular emission that is reflected by the surface and transmitted to the top of troposphere (Zhang and Menzel [2002] showed that this term is very small at infrared wavelengths), the cloudy radiative transfer equation for a given infrared channel or wavelength can be written as in Equation ( 5.1) (e.g. Chapter 3).

$$R_{obs}(\lambda) = \epsilon_{eff}(\lambda)R_{cld}(\lambda) + R_{clr}(\lambda)(1 - \epsilon_{eff}(\lambda)) \quad (5.1)$$

While sub-pixel cloudiness is noted as a potential source of error, only fully cloudy fields of view are considered in this since information on cloud fraction is not readily available. For a cloud fraction sensitivity analysis, see Heidinger and Pavolonis [2009]. In Equation ( 5.1), which is derived in Appendix A,  $\lambda$  is wavelength,  $R_{obs}$  is the observed radiance,  $R_{clr}$  is the clear sky radiance. The effective cloud emissivity [Cox 1976] is denoted by  $\epsilon_{eff}$ . The effects of cloud scattering are implicitly captured by the effective cloud emissivity (see Cox [1976]). To avoid using additional symbols, the angular dependence is simply implied.  $R_{cld}$  is given by

$$R_{cld}(\lambda) = R_{ac}(\lambda) + t_{ac}(\lambda)B(\lambda, T_{eff}). \quad (5.2)$$

In Equation ( 5.2),  $R_{ac}$  and  $t_{ac}$  are the above cloud upwelling atmospheric radiance and transmittance, respectively.  $B$  is the Planck Function, and  $T_{eff}$  is the effective cloud temperature. The effective cloud temperature is most often different from the thermodynamic cloud top temperature since the emission of radiation originates from a layer in the cloud. The depth of this layer depends upon the cloud extinction profile, which is generally unknown. The clear sky transmittance and radiance terms are determined using surface temperature, atmospheric temperature, water vapor, and ozone profiles from the Global Forecast Model (GFS) [Hamill et al. 2006], surface emissivity from the Seebor database [Seemann et al. 2008], the satellite zenith angle, and a regression based clear sky radiative transfer model [Hannon et al. 1996]. The procedure for determining the clear sky radiance and transmittance is the same as described in Heidinger and Pavolonis [2009] and Chapter 3 so no other details are given here.

The spectral variation of the effective cloud emissivity is directly related to cloud microphysical information (e.g. particle size, shape, composition, etc...). Effective absorption optical depth ratios, otherwise known as  $\beta$ -ratios, have been previously used to extract cloud microphysical information from infrared measurements [Inoue 1987; Parol et al. 1991; Giraud et al. 1997; Heidinger and Pavolonis 2009; and Chapter 3 of this dissertation]. For a given pair of spectral effective emissivities,  $\epsilon_{eff}(\lambda_1)$  and  $\epsilon_{eff}(\lambda_2)$ , the effective absorption optical depth ratio,  $\beta_{obs}$ , is defined in Equation ( 5.3).

$$\beta_{obs} = \frac{\ln[1 - \epsilon_{eff}(\lambda_1)]}{\ln[1 - \epsilon_{eff}(\lambda_2)]} = \frac{\tau_{abs, eff}(\lambda_1)}{\tau_{abs, eff}(\lambda_2)} \quad ( 5.3)$$

Notice that Equation ( 5.3) can simply be interpreted as the ratio of effective absorption optical depth ( $\tau_{abs,eff}$ ) at two different wavelengths. An appealing quality of  $\beta_{obs}$ , is that it

can be interpreted in terms of the single scatter properties, which can be computed for a given cloud composition and particle distribution. Following Van de Hulst [1980] and Parol et al. [1991], a spectral ratio of scaled extinction coefficients can be calculated from the single scatter properties (single scatter albedo, asymmetry parameter, and extinction cross section), as follows.

$$\beta_{theo} = \frac{[1.0 - \omega(\lambda_1)g(\lambda_1)]\sigma_{ext}(\lambda_1)}{[1.0 - \omega(\lambda_2)g(\lambda_2)]\sigma_{ext}(\lambda_2)} \quad (5.4)$$

In Equation ( 5.4),  $\beta_{theo}$  is the spectral ratio of scaled extinction coefficients,  $\omega$  is the single scatter albedo,  $g$  is the asymmetry parameter, and  $\sigma_{ext}$  is the extinction cross section. As shown in Chapter 3, at wavelengths in the 8 – 15  $\mu\text{m}$  range, where multiple scattering effects are small,  $\beta_{theo}$ , captures the essence of the cloudy radiative transfer such that

$$\beta_{obs} \approx \beta_{theo}. \quad (5.5)$$

Equation ( 5.5) allows  $\beta_{obs}$  to be used to infer information on the cloud particle distribution. In addition, Equations ( 5.1) - ( 5.5) allow for an efficient retrieval without the need for large, scene dependent, look-up tables.

#### **5.4. Retrieval Forward Model**

Following Equation ( 5.1), the infrared radiative transfer equation is shown for each spectral channel used in the retrieval in Equations ( 5.6) – ( 5.8).

$$R_{obs}(11\mu\text{m}) = \varepsilon_{eff}(11\mu\text{m})R_{cld}(11\mu\text{m}) + R_{clr}(11\mu\text{m})(1 - \varepsilon_{eff}(11\mu\text{m})) \quad (5.6)$$

$$R_{obs}(12\mu\text{m}) = \varepsilon_{eff}(12\mu\text{m})R_{cld}(12\mu\text{m}) + R_{clr}(12\mu\text{m})(1 - \varepsilon_{eff}(12\mu\text{m})) \quad (5.7)$$

$$R_{obs}(13.3\mu m) = \epsilon_{eff}(13.3\mu m)R_{cl}(13.3\mu m) + R_{clr}(13.3\mu m)(1 - \epsilon_{eff}(13.3\mu m)) \quad (5.8)$$

The algorithm is designed to directly retrieve the 11  $\mu m$  effective cloud emissivity and  $\beta_{obs}(12/11 \mu m)$ , in addition to  $T_{eff}$ , so Equation ( 5.3) is used to express the 12  $\mu m$  effective cloud emissivity as a function of the 11  $\mu m$  effective cloud emissivity and  $\beta_{obs}(12/11 \mu m)$ , as shown in Equation ( 5.9).

$$\epsilon_{eff}(12\mu m) = 1 - [1 - \epsilon_{eff}(11\mu m)]^{\beta_{obs}(12/11\mu m)} \quad (5.9)$$

Similarly the 13.3  $\mu m$  effective cloud emissivity can be expressed as a function of the 11  $\mu m$  effective cloud emissivity and  $\beta_{obs}(13.3/11 \mu m)$ , as shown in Equations ( 5.10).

$$\epsilon_{eff}(13.3\mu m) = 1 - [1 - \epsilon_{eff}(11\mu m)]^{\beta_{obs}(13.3/11\mu m)} \quad (5.10)$$

The single scatter properties (recall Equations ( 5.4) and ( 5.5)) are then used to relate  $\beta_{obs}(12/11 \mu m)$  to  $\beta_{obs}(13.3/11 \mu m)$  such that only  $T_{eff}$ ,  $\epsilon_{eff}(11 \mu m)$ , and  $\beta_{obs}(12/11 \mu m)$  are solved for in the retrieval. More specifically,  $\beta_{obs}(13.3/11 \mu m)$  is related to  $\beta_{obs}(12/11 \mu m)$  via a 4<sup>th</sup> order polynomial fit (see Equation ( 5.11)) to the single scatter property derived beta relationship ( $\beta_{theo}(13.3/11 \mu m)$  vs.  $\beta_{theo}(12/11 \mu m)$ ). The polynomial coefficients ( $c_0$ ,  $c_1$ ,  $c_2$ ,  $c_3$ , and  $c_4$ ) are a function of the microphysical model chosen, and will be discussed in a later section in this chapter.

$$\beta(13.3/11\mu m) = c_4[\beta(12/11\mu m)]^4 + c_3[\beta(12/11\mu m)]^3 + c_2[\beta(12/11\mu m)]^2 + c_1[\beta(12/11\mu m)] + c_0 \quad (5.11)$$

### 5.5. *Optimal Estimation Retrieval Method*

The retrieval of  $T_{eff}$ ,  $\epsilon_{eff}(11 \mu m)$ , and  $\beta_{obs}(12/11 \mu m)$  is formally performed using the optimal estimation approach described by Rodgers [1976]. Heidinger and Pavolonis [2009] utilize this same technique to retrieve cirrus cloud properties. In addition, Turner

[2008] used optimal estimation to retrieve dust cloud properties from ground based infrared measurements. There are many more examples of optimal estimation being used in satellite remote sensing applications. The benefits of this approach are that it is flexible and allows new observations or retrieved parameters to be added or removed from the retrieval scheme. Another benefit of this approach is that it generates estimates of the uncertainty in the retrieval. Each step in the optimal estimation iteration changes each element of vector of retrieved parameters ( $T_{\text{eff}}$ ,  $\epsilon_{\text{eff}}(11 \mu\text{m})$ , and  $\beta_{\text{obs}}(12/11 \mu\text{m})$ ) according to the following relationship.

$$\delta x = S_x \{ K^T S_y^{-1} [y - f(x)] + S_a^{-1} (x_a - x) \} \quad (5.12)$$

In Equation ( 5.12),  $\mathbf{y}$  is the vector of observations,  $\mathbf{x}$  is the vector of retrieved parameters,  $f(\mathbf{x})$  represents the forward model, which is a function of  $\mathbf{x}$ , and  $\mathbf{x}_a$  is the *a priori* representation of  $\mathbf{x}$ . The matrices  $\mathbf{S}_x$ ,  $\mathbf{S}_y$ , and  $\mathbf{S}_a$  are the error covariance matrices of the retrieved parameters, the measurements, and the *a priori* values, respectively. The kernel matrix,  $\mathbf{K}$ , contains the forward model Jacobians. In our retrieval,  $\mathbf{x} = [T_{\text{eff}}, \epsilon(11\mu\text{m}), \beta_{\text{obs}}(13.3/11\mu\text{m})]$ . Using “BT” to denote brightness temperature and “BTD” to denote brightness temperature difference, the observation vector,  $\mathbf{y}$  is  $[BT(11\mu\text{m}), BTD(11-12\mu\text{m}), BTD(11-13.3\mu\text{m})]$ . The forward model vector,  $f(\mathbf{x})$ , is constructed in the same manner as  $\mathbf{y}$  for each of the channel combinations. The kernel matrix is defined in Equations ( 5.13).

$$\mathbf{K} = \begin{pmatrix} \frac{\partial BT(11\mu m)}{\partial T_{eff}} & \frac{\partial BT(11\mu m)}{\partial \epsilon_{eff}(11\mu m)} & \frac{\partial BT(11\mu m)}{\partial \beta_{obs}(12/11\mu m)} \\ \frac{\partial BT(11-12\mu m)}{\partial T_{eff}} & \frac{\partial BT(11-12\mu m)}{\partial \epsilon_{eff}(11\mu m)} & \frac{\partial BT(11-12\mu m)}{\partial \beta_{obs}(12/11\mu m)} \\ \frac{\partial BT(11-13.3\mu m)}{\partial T_{eff}} & \frac{\partial BT(11-13.3\mu m)}{\partial \epsilon_{eff}(11\mu m)} & \frac{\partial BT(11-13.3\mu m)}{\partial \beta_{obs}(12/11\mu m)} \end{pmatrix} \quad (5.13)$$

Given our choice of forward model, analytical expressions for the Jacobians can be derived. The Jacobian analytical expressions can be found in Appendix D. Once the Kernel Matrix has been calculated, the error covariance matrix of  $\mathbf{x}$  can be determined using Equation ( 5.14) [Rodgers, 1976]. The method used to determine  $S_a$  and  $S_y$  will be described shortly.

$$S_x = (S_a^{-1} + K^T S_y^{-1} K)^{-1} \quad (5.14)$$

The optimal estimation approach is run until the following convergence criterion is met.

$$\left\| \sum \delta x S_x^{-1} \delta x \right\| \leq \frac{p}{2} \quad (5.15)$$

In Equation ( 5.15),  $p$  is the size of  $\mathbf{x}$ , which is 3 in our case. This convergence criterion is same used by Rodgers [1976]. If the retrieval does not converge after 10 iterations, it is deemed a failed retrieval (retrievals very rarely fail to converge) and all retrieved parameters are set to the *a priori* values. Further,  $\delta x$  is constrained such that the maximum allowed absolute changes in the retrieved parameters,  $T_{eff}$ ,  $\epsilon(11\mu m)$ , and  $\beta(12/11\mu m)$ , are 20.0 K, 0.3, 0.2, respectively. Once the retrieval vector is updated by  $\delta x$ , the retrieved parameters are constrained to be within a physically plausible range.

The *a priori* values and their associated uncertainties act to constrain the retrieved parameters when the measurements contain little or no information on one or more of the

retrieved parameters. However, prior, independent, knowledge of ash and dust cloud properties is generally not available and climatological values are not very useful since ash and dust cloud properties are highly variable in space and time. Thus, a large uncertainty is assigned to each *a priori* parameter, so that the measurements are highly weighted. Ideally, ash cloud property estimates from more accurate (but less frequent) measurements (satellite or otherwise) would be used to automatically determine the *a priori* values and uncertainties. However, combining measurements from different satellites or measurement platforms is not a trivial endeavor and will be the subject of future research. Model simulated ash cloud properties can also potentially be used as a first guess, but quantifying model errors is a difficult task and requires significant additional research. The *a priori* values and associated uncertainty estimates are shown in Table 5.1. The choice of *a priori* value for  $T_{\text{eff}}$  and  $\epsilon(11\mu\text{m})$  assumes that most ash and dust clouds are semi-transparent to infrared radiation and accounts for the satellite zenith angle. The *a priori* value of  $\beta(12/11\mu\text{m})$  is chosen as 0.8, which, as will be shown in the next section, approximately corresponds to the center of the range of sensitivity for effective particle size. The actual *a priori* values, however, are not critically important since the *a priori* error estimates ( $\sigma_{x_{\text{ap}}}$ ) are assumed to be significant (see Table 5.1). As in Heidinger and Pavolonis [2009], the *a priori* error covariance matrix (Equation ( 5.16)) is taken to be diagonal (e.g. errors in the first guess of each parameter are uncorrelated). The procedure for assigning the *a priori* values and uncertainty will be refined in the future.

$$S_a = \begin{pmatrix} \sigma^2_{T_{\text{eff}} - ap} & 0.0 & 0.0 \\ 0.0 & \sigma^2_{\varepsilon(11\mu\text{m}) - ap} & 0.0 \\ 0.0 & 0.0 & \sigma^2_{\beta(12/11\mu\text{m}) - ap} \end{pmatrix} \quad (5.16)$$

Table 5.1: First guess values and associated uncertainties of each retrieved parameter.  $\theta_{\text{sat}}$  is the satellite zenith angle. If an upper level  $\text{SO}_2$  signal is present (see Chapter 3),  $T_{\text{eff}}(2)$  is utilized, otherwise  $T_{\text{eff}}(1)$  is used.

Retrieved Parameter ( $\mathbf{x}$ )	First Guess ( $\mathbf{x}_{\text{ap}}$ )	First Guess Uncertainty ( $\sigma_{\text{ap}}^2$ )
$T_{\text{eff}}(1)$	BT(11 $\mu\text{m}$ ) – 15 K	(50 K) <sup>2</sup>
$T_{\text{eff}}(2)$	Temperature at tropopause + 2km	(50 K) <sup>2</sup>
$\varepsilon_{\text{eff}}(11 \mu\text{m})$	$1.0 - \exp(-0.5/\cos(\theta_{\text{sat}}))$	(1.0) <sup>2</sup>
$\beta_{\text{obs}}(12/11 \mu\text{m})$	0.8	(0.6) <sup>2</sup>

The optimal estimation procedure also requires an estimate of the error covariance matrix of the forward model (Equation ( 5.17)).

$$S_y = \begin{pmatrix} \sigma^2_{BT(11\mu\text{m})} & 0.0 & 0.0 \\ 0.0 & \sigma^2_{BTD(11 - 12\mu\text{m})} & 0.0 \\ 0.0 & 0.0 & \sigma^2_{BTD(11 - 13.3\mu\text{m})} \end{pmatrix} \quad (5.17)$$

As in Heidinger and Pavolonis [2009], the total uncertainty in the forward model is assumed to be composed of a linear combination of three major sources (see Equation ( 5.18)): instrumental, clear sky radiative transfer modeling, and pixel heterogeneity.

$$\sigma^2 = \sigma^2_{\text{instr}} + [1 - \varepsilon(11\mu\text{m})]\sigma^2_{\text{clr}} + \sigma^2_{\text{hetero}} \quad (5.18)$$

In Equation ( 5.18), the instrument uncertainty is given by  $\sigma^2_{\text{instr}}$ , the clear sky radiative transfer uncertainty is denoted by  $\sigma^2_{\text{clr}}$ , and the uncertainty due to pixel heterogeneity is given by  $\sigma^2_{\text{hetero}}$ . The impact of the clear sky radiative transfer uncertainty is

approximately inversely proportional to the cloud emissivity, so it is weighted by the 11- $\mu\text{m}$  cloud emissivity,  $\epsilon(11\mu\text{m})$ . As discussed in Heidinger and Pavolonis [2009], the off-diagonal elements (correlated uncertainty) of the forward model error covariance matrix are very difficult to determine, so only the diagonal elements (uncorrelated uncertainty) are considered. The uncertainty in the clear sky radiative transfer ( $\sigma_{\text{clr}}^2$ ), which is a function of the accuracy of the radiative transfer model, the GFS fields, and the surface emissivity database, is determined through an offline clear sky radiance bias analysis, separately for land and water surfaces (see Heidinger and Pavolonis [2009]). In general, there is much greater uncertainty in land surface temperature than sea surface temperature so the clear sky uncertainty over land is greater than over water. The forward model uncertainty due to spatial heterogeneity ( $\sigma_{\text{hetero}}^2$ ) is approximated by the spatial variance of each observation used in the retrieval over a 3 x 3 pixel box centered on the current pixel of interest. The last forward model error term is that due to instrumental effects,  $\sigma_{\text{instr}}^2$ . This term includes noise, calibration, and spectral response errors that impact the ability of the forward model to fit the measurements. The clear sky and instrument uncertainty estimates for SEVIRI are given in Table 5.2. The instrumental uncertainty was taken from satellite operator, EUMETSAT: [http://www.eumetsat.int/idcplg?IdcService=GET\\_FILE&dDocName=PDF\\_MSG\\_SEVIRI\\_RADIOM\\_NOISE&RevisionSelectionMethod=LatestReleased](http://www.eumetsat.int/idcplg?IdcService=GET_FILE&dDocName=PDF_MSG_SEVIRI_RADIOM_NOISE&RevisionSelectionMethod=LatestReleased).

Table 5.2: Instrument and forward model errors for each observation used in the retrieval.

Observation (y)	Instrument Error ( $\sigma_{\text{instr}}$ )	Clear Sky Error (water) ( $\sigma_{\text{clr}}$ )	Clear Sky Error (land) ( $\sigma_{\text{clr}}$ )
BT(11 $\mu\text{m}$ )	(0.11 K) <sup>2</sup>	(0.50 K) <sup>2</sup>	(5.00 K) <sup>2</sup>
BTD(11-12 $\mu\text{m}$ )	(0.26 K) <sup>2</sup>	(0.25 K) <sup>2</sup>	(1.00 K) <sup>2</sup>
BTD(11-13.3 $\mu\text{m}$ )	(0.55 K) <sup>2</sup>	(1.50 K) <sup>2</sup>	(4.00 K) <sup>2</sup>

### 5.6. Microphysical Models

The microphysical relationships needed to determine  $\beta_{\text{obs}}(13.3/11 \mu\text{m})$  from the retrieved  $\beta_{\text{obs}}(12/11 \mu\text{m})$  (see Equation 11) and to calculate the effective particle radius [Hansen and Travis 1974] and mass loading from the retrieved  $\epsilon_{\text{eff}}(11 \mu\text{m})$  and  $\beta_{\text{obs}}(12/11 \mu\text{m})$  were constructed for 4 different rocks: andesite, rhyolite, gypsum, and kaolinite. Pollack et al. [1973] provided the indices of refraction for andesite and rhyolite and Roush et al. [1991] provided the indices of refraction of the other rocks. Regardless of the composition, the size distribution was assumed to be lognormal.

$$n(r) = \frac{N_o}{\sqrt{2\pi}} \frac{1}{r \ln \sigma_g} \exp\left(-\frac{(\ln r - \ln r_g)^2}{2(\ln \sigma_g)^2}\right) \quad (5.19)$$

In equation ( 5.19),  $N_o$  is the total number of particles,  $r$  is particle radius,  $r_g$  is the geometric mean radius, and  $\sigma_g$  is the geometric standard deviation. In this study, the geometric standard deviation is always set to 2.1 ( $\ln(\sigma_g)=0.74$ ). Lognormal distributions with a geometric standard deviation of  $\sim 2$  have commonly been used to model and fit volcanic ash and dust particle distributions (e.g. [Hobbs et al. 1991; Wen and Rose 1994; Pavolonis et al. 2006; Prata and Grant 2001; Pavolonis 2010; Clarisse et al. 2010b]). The

geometric radius,  $r_g$ , can be determined from the effective particle radius [Hansen and Travis 1974],  $r_{eff}$ , using

$$r_g = \frac{r_{eff}}{\exp\left(\frac{5}{2}(\ln \sigma_g)^2\right)}. \quad (5.20)$$

The total number of particles per unit area,  $N_o$ , can be calculated from the retrieved effective cloud emissivity,  $\varepsilon_{eff}(11 \mu\text{m})$  and  $\beta_{obs}(12/11 \mu\text{m})$  using

$$N_o = \frac{\tau(11\mu\text{m})}{\sigma_{ext}(11\mu\text{m})}, \quad (5.21)$$

where  $\tau(11\mu\text{m})$  is the effective cloud optical depth at 11  $\mu\text{m}$  and  $\sigma_{ext}(11\mu\text{m})$  is the extinction cross section at 11  $\mu\text{m}$ . The effective cloud optical depth, corrected for satellite viewing zenith angle,  $\theta_{sat}$ , is easily computed from the retrieved effective cloud emissivity using Equation (5.22).

$$\tau(11\mu\text{m}) = -\cos(\theta_{sat}) \ln[1.0 - \varepsilon(11\mu\text{m})] \quad (5.22)$$

As will be shown shortly, the single scatter properties can be expressed as a function of  $\beta_{theo}(12/11 \mu\text{m})$ , which allows  $\sigma_{ext}(11\mu\text{m})$  to be determined.

The ash and dust particles were assumed to be spherical and Mie theory is used to compute the single scatter properties for each rock type over a range of effective radii (0.5 – 20.0  $\mu\text{m}$ ). Of course, real volcanic ash and dust particles actually take on a variety of irregular shapes that are very difficult to model. Fortunately, in the infrared (especially at wavelengths larger than 10  $\mu\text{m}$ ), the sensitivity to particle habit and composition has been shown to be much smaller than the sensitivity to particle size [Wen and Rose 1994; Corradini et al. 2008; Clarisse et al. 2010b; Newman et al. 2012], so, as

in other studies, the particles are treated as spheres. The Mie calculations in the wavelength range of 8 – 15  $\mu\text{m}$  are performed with a wave number spacing of 10  $\text{cm}^{-1}$ . Instrument specific single scatter properties for each channel required by the retrieval algorithm are compiled by integrating over the corresponding instrument specific spectral response functions for those channels.

For a given rock type, the theoretical beta relationship (Equation ( 5.4)) over a range of effective radii is used to derive the empirical coefficients needed to evaluate Equation ( 5.11). Figure 5.1 shows  $\beta_{\text{theo}}(13.3/11 \mu\text{m})$  as a function of  $\beta_{\text{theo}}(12/11 \mu\text{m})$  for each rock type. The coefficients required by Equation ( 5.11) are determined by fitting a 4<sup>th</sup> order polynomial to the points. The relationships shown in Figure 5.1 are valid for the SEVIRI sensor on-board the Met-9 satellite. The relationship between  $\beta_{\text{theo}}(12/11 \mu\text{m})$  and  $\beta_{\text{theo}}(13.3/11 \mu\text{m})$  has the same primary attribute,  $\beta_{\text{theo}}(12/11 \mu\text{m}) > \beta_{\text{theo}}(13.3/11 \mu\text{m})$  for a given  $r_{\text{eff}}$ , for all rock types. In an analogous manner,  $\beta_{\text{obs}}(12/11 \mu\text{m})$  is also used to determine the effective particle radius ( $r_{\text{eff}}$ ) and the 11- $\mu\text{m}$  extinction cross-section ( $\sigma_{\text{ext}}(11\mu\text{m})$ ). Those relationships are shown for each rock type in Figure 5.2 and Figure 5.3, respectively. The empirical relationships depicted in Figure 5.2 and Figure 5.3 are valid for Met-9 SEVIRI, but empirical fits of the same general form are used for other instruments. Thus, polynomial coefficients for each instrument of interest are computed and stored in a data file and a single version of the retrieval code is used for all instruments that meet the channel requirements.

Figure 5.2 shows that the sensitivity to effective radius is generally greatest in the 1 – 6  $\mu\text{m}$  range (e.g. relatively large changes in  $\beta_{\text{theo}}(12/11 \mu\text{m})$  are associated with relatively small changes in  $r_{\text{eff}}$ ). Once the  $r_{\text{eff}}$  exceeds  $\sim 15 \mu\text{m}$ , relatively small changes

in  $\beta_{\text{theo}}(12/11 \text{ } \mu\text{m})$  are associated with larger changes in  $r_{\text{eff}}$  and retrievals of  $r_{\text{eff}}$  greater 15  $\mu\text{m}$  cannot be performed reliably. It is also more difficult to separate ash/dust clouds from liquid water and ice clouds when  $r_{\text{eff}}$  exceeds 15  $\mu\text{m}$  [Chapter 3 of this dissertation]. Thus, the maximum allowed retrieved  $r_{\text{eff}}$  in the GOES-R approach is 15  $\mu\text{m}$ . This does not mean that a volume of particles with an actual  $r_{\text{eff}} > 15 \text{ } \mu\text{m}$  does not contribute to the measured top of atmosphere radiation. Figure 5.3 shows that particles of all sizes greater than about 1  $\mu\text{m}$  have a non-trivial extinction coefficient. In fact, the larger the effective radius, the greater the extinction of radiation. While fundamental (given the physical relationship between particle size and wavelength), this is an important point to make in this manuscript since the lack of sensitivity to effective radii larger than about 15  $\mu\text{m}$  is sometimes misinterpreted to mean that larger particles within a size distribution do not significantly contribute to the measured radiance in the infrared, which is not correct. The infrared cloud optical depth is greatly influenced by emission and scattering from larger particles.

As in previous studies, ash mass loading in  $\text{g}/\text{m}^2$  is computed using

$$ML = (1 \times 10^6) \frac{4}{3} \pi \rho_{\text{ash}} \int_{r_1}^{r_2} r^3 n(r) dr. \quad (5.23)$$

In Equation ( 5.23), ML is the mass loading in  $\text{g}/\text{m}^2$  and  $\rho_{\text{ash}}$  is the density of ash, which is taken to be  $2.6 \text{ g}/\text{cm}^3$  [Neal et al., 1994]. The particle radius,  $r$ , is expressed in units of  $\mu\text{m}$ . The units of  $n(r)$  are the number of particles per  $\mu\text{m}^2$  per  $\mu\text{m}$ . The factor,  $1 \times 10^6$ , in Equation ( 5.23), is needed to convert the units to  $\text{g}/\text{m}^2$ . Given that the maximum effective radius that can be retrieved is 15  $\mu\text{m}$ , the mass loading will likely be

underestimated if the actual effective radius exceeds 15  $\mu\text{m}$  simply because the number of larger volume particles will be underestimated.

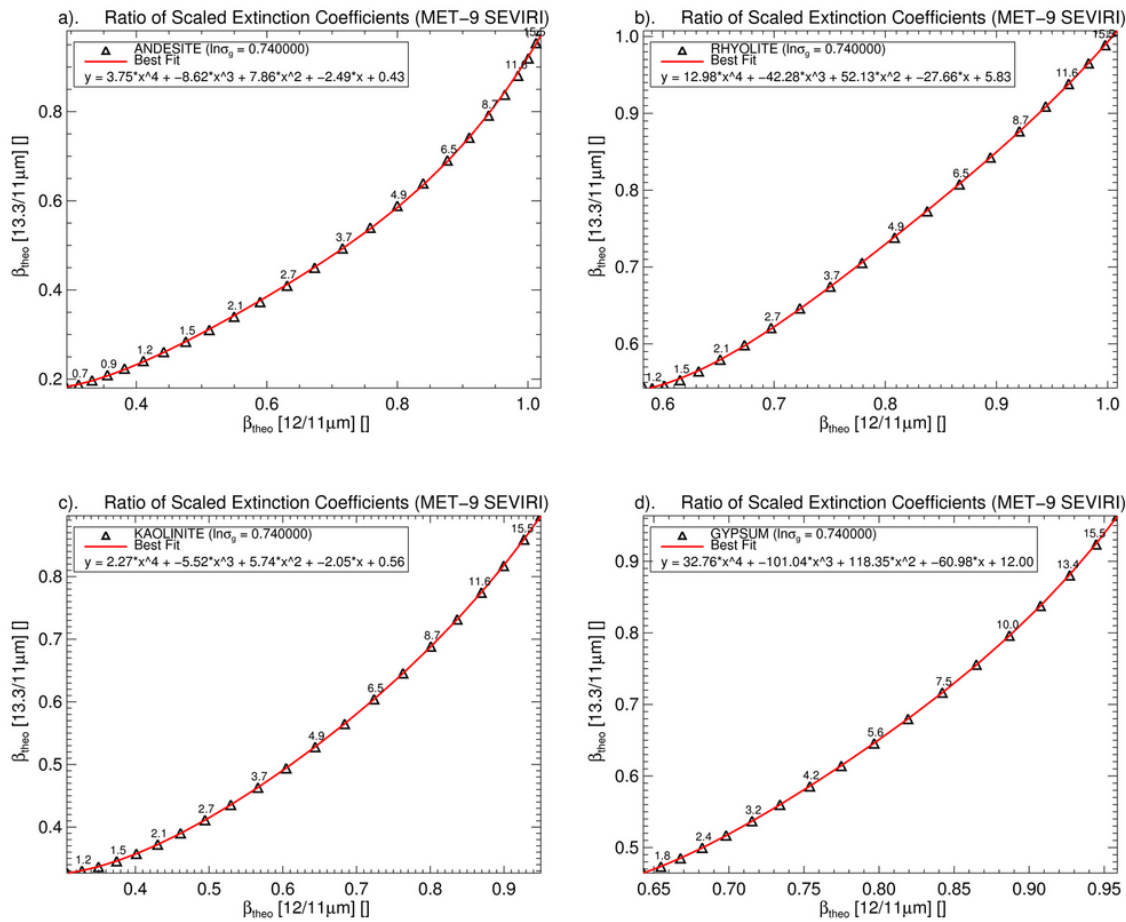


Figure 5.1: The black triangles show the 13.3/11  $\mu\text{m}$  scaled extinction ratio ( $\beta_{theo}(13.3/11\mu\text{m})$ ) as a function of the 12/11  $\mu\text{m}$  scaled extinction ratio ( $\beta_{theo}(12/11\mu\text{m})$ ) for 4 different rock types over a range of effective radii (1 – 15  $\mu\text{m}$ ). A fourth order polynomial fit is shown in red. The numbers adjacent to the triangles indicate the effective radius in  $\mu\text{m}$ . Andesite, rhyolite, kaolinite, and gypsum are shown in panels a-d, respectively.  $\beta_{theo}(12/11\mu\text{m})$  and  $\beta_{theo}(13.3/11\mu\text{m})$  were derived from the single scatter properties as described in the text.

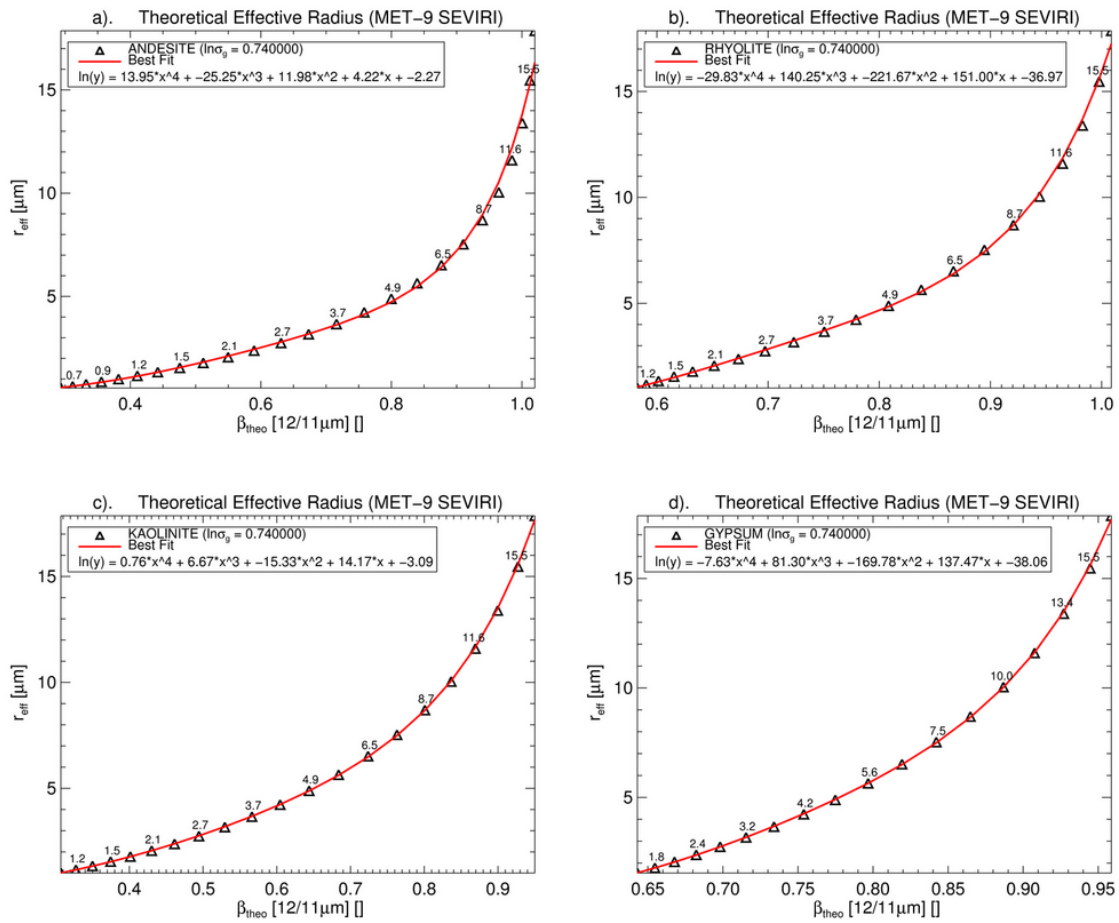


Figure 5.2: The same as Figure 5.1 except the effective particle radius ( $r_{\text{eff}}$ ) is shown as a function of  $\beta_{\text{theo}}(12/11 \mu\text{m})$ .

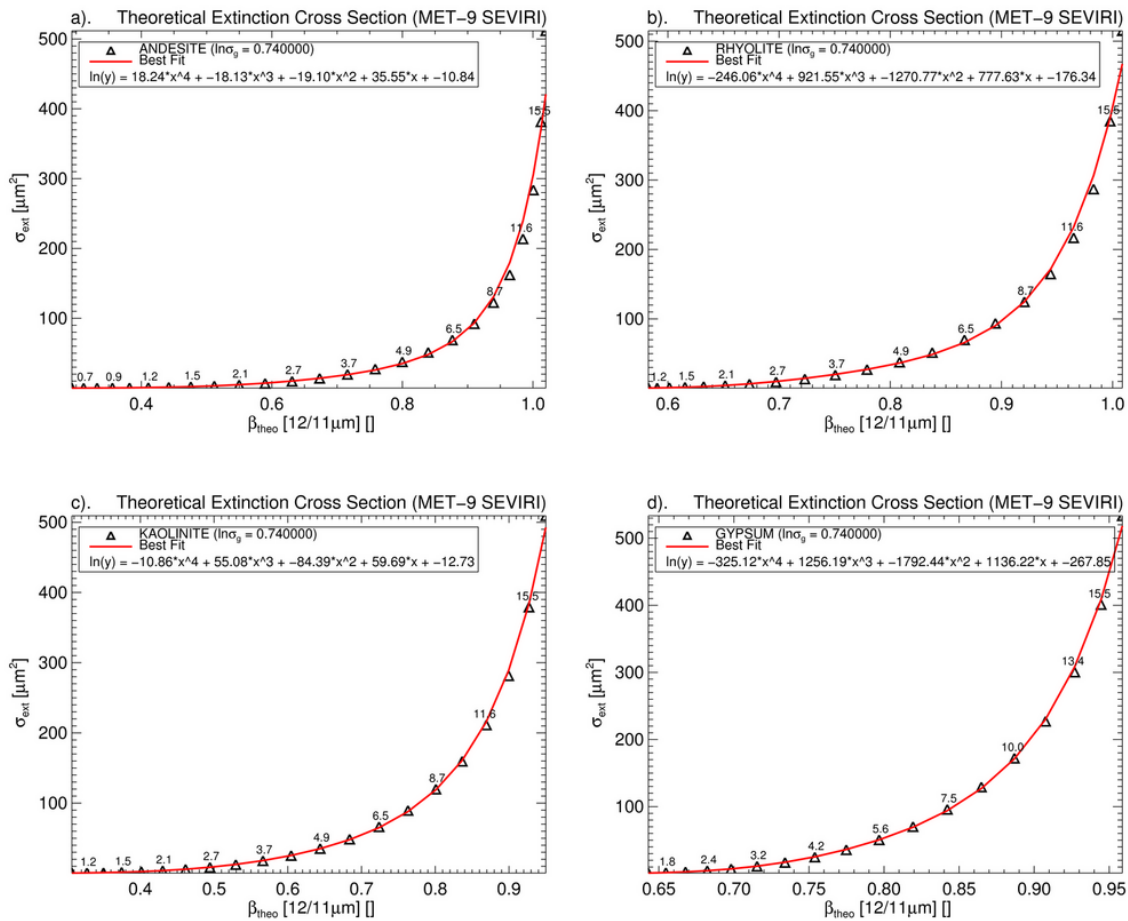


Figure 5.3: The same as Figure 5.1 except the extinction cross section ( $\sigma_{ext}$ ) is shown as a function of  $\beta_{theo}$ (12/11  $\mu\text{m}$ ).

## 5.7. Results and Error Analysis

The optimal estimation retrieval algorithm is applied to all satellite pixels that either have an ash/dust probability (see Chapter 4) that exceeds  $1.0 \times 10^6\%$  or an 11 – 12  $\mu\text{m}$  BTD that is less than 0 K.

### 5.7.1. Eyjafjallajökull – May 8, 2010 (04:00 UTC)

The April 14 – May 21, 2010 eruption of Eyjafjallajökull [Gudmundsson et al. 2010] in southern Iceland had an extensive impact on aviation. Ash clouds from 2010 eruption of Eyjafjallajökull have been studied using ground [Ansmann et al. 2010;

Arason et al. 2011; Gasteiger et al. 2011], airborne [Schumann et al. 2011; Turnbull et al. 2012; Newman et al. 2012; Marengo et al. 2011; Johnson et al. 2012], and satellite [Winker et al. 2012; Francis et al. 2012; Stohl et al. 2011; Newman et al. 2012; Prata and Prata 2012] observations. In this study, the GOES-R retrieval results will primarily be compared to ash cloud properties inferred from the Cloud Aerosol Lidar with Orthogonal Polarization (CALIOP) [Hunt et al. 2009] on board the Cloud Aerosol Lidar and Infrared Pathfinder Satellite Observation (CALIPSO) [Winker et al., 2010] since those data provide detailed information on cloud vertical structure and are readily and freely available. In addition, unlike fixed location ground-based measurements and aircraft measurements, CALIOP samples ash and dust clouds globally over a large range of background conditions. Thus, just as described by Heidinger and Pavolonis [2009], the CALIOP data set is an ideal starting point for algorithm validation. Quantitative comparisons to aircraft observations will be performed in the future when those data sets are more readily available to the broader scientific community. Detailed comparisons to ground-based measurements and other published satellite retrieval data sets will also be the focus of future research.

Figure 5.4, Figure 5.5, and Figure 5.6 show the results of the GOES-R ash cloud property retrieval on May 8, 2010 at 04:00 UTC. Satellite imagery and the core retrieval outputs,  $T_{\text{eff}}$  (K),  $\epsilon(11\mu\text{m})$ ,  $\beta(12/11\mu\text{m})$ , and associated uncertainties are shown in Figure 5.4. The andesite rock type was used to generate the results shown in Figure 5.4. Consistent with Heidinger and Pavolonis [2009], the uncertainties are expressed as the ratio of the estimated 1- $\sigma$ -retrieval error and the *a priori* error estimate, where a value of 1.0 indicates that the uncertainties are identical and the retrieval added no value (ratios

much less than 1.0 indicate that the retrieval added considerable value). Figure 5.5 shows the ash cloud height, mass loading, and effective particle radius, which were derived from  $T_{\text{eff}}$ ,  $\epsilon(11\mu\text{m})$ , and  $\beta(12/11\mu\text{m})$  as described earlier. In order to help assess the sensitivity to rock type, the height (km above sea level), mass loading ( $\text{g}/\text{m}^2$ ), and effective radius ( $\mu\text{m}$ ) results are shown for three different rock types, andesite (left column), rhyolite (center column), and kaolinite (right column). Finally, Figure 5.6 shows the 532 nm total attenuated backscatter from a CALIOP cross-section through the ash cloud at 04:00 UTC. The ash cloud height results from each composition are overlaid on the cross section shown in the bottom panel of Figure 5.6. SEVIRI parallax effects were accounted for when co-locating SEVIRI and CALIOP and measurement times never differed by more than 7.5 minutes. For reference, the CALIPSO ground track is overlaid on each panel in Figure 5.4 and (black line) Figure 5.5.

Figure 5.4 (panels c and d) shows that  $T_{\text{eff}}$  is generally much less than the 11  $\mu\text{m}$  brightness temperature and  $\epsilon(11\mu\text{m})$  is generally less than 0.5, meaning the cloud is semi-transparent to infrared radiation and deviates strongly from blackbody behavior. This is true for nearly all ash/dust clouds analyzed in this chapter. Also seen in Figure 5.4 (panels g-i), is that the uncertainty ratio for each of the retrieved parameters is generally  $< 0.90$ , indicating that the retrieval is adding skill to the first guess. This scene is particularly interesting because the retrieval results indicate that there is considerable spatial variability in the ash cloud properties along the CALIPSO ground track, with higher heights (lower  $T_{\text{eff}}$ ), lower loadings (smaller  $\epsilon(11\mu\text{m})$  and  $\beta(12/11\mu\text{m})$ ), and smaller effective radii in the southwest portion of the ground track compared to the northeast portion. Figure 5.6 shows that the GOES-R retrievals are very consistent with

the 1/3 km 532 nm CALIOP total attenuated backscatter profile which shows a more strongly attenuating lower level ash cloud in the northeast part of the overpass segment and much higher ash cloud layers with weaker attenuation in the southwest. The overall cloud height variation is captured by the GOES-R retrieval regardless of the assumed rock type. The retrieved mass loading and effective radius, however, are more sensitive to rock type, with kaolinite producing much larger (in some cases a factor of 2 larger) mass loadings and effective radii than andesite or rhyolite (see Figure 5.5). A more rigorous, quantitative, validation analysis will be shown later as a function of the rock type. One of the main limitations of our methodology, and all previously published passive satellite sensor ash/dust retrieval algorithms, is that ash/dust cloud properties can only be retrieved if ash/dust is the highest cloud layer. In this scene the false color image (dust RGB) (Figure 5.4a) indicates that cirrus clouds overlap the ash cloud just south of Iceland. Thus, ash cloud properties could not be determined for this part of the ash cloud.

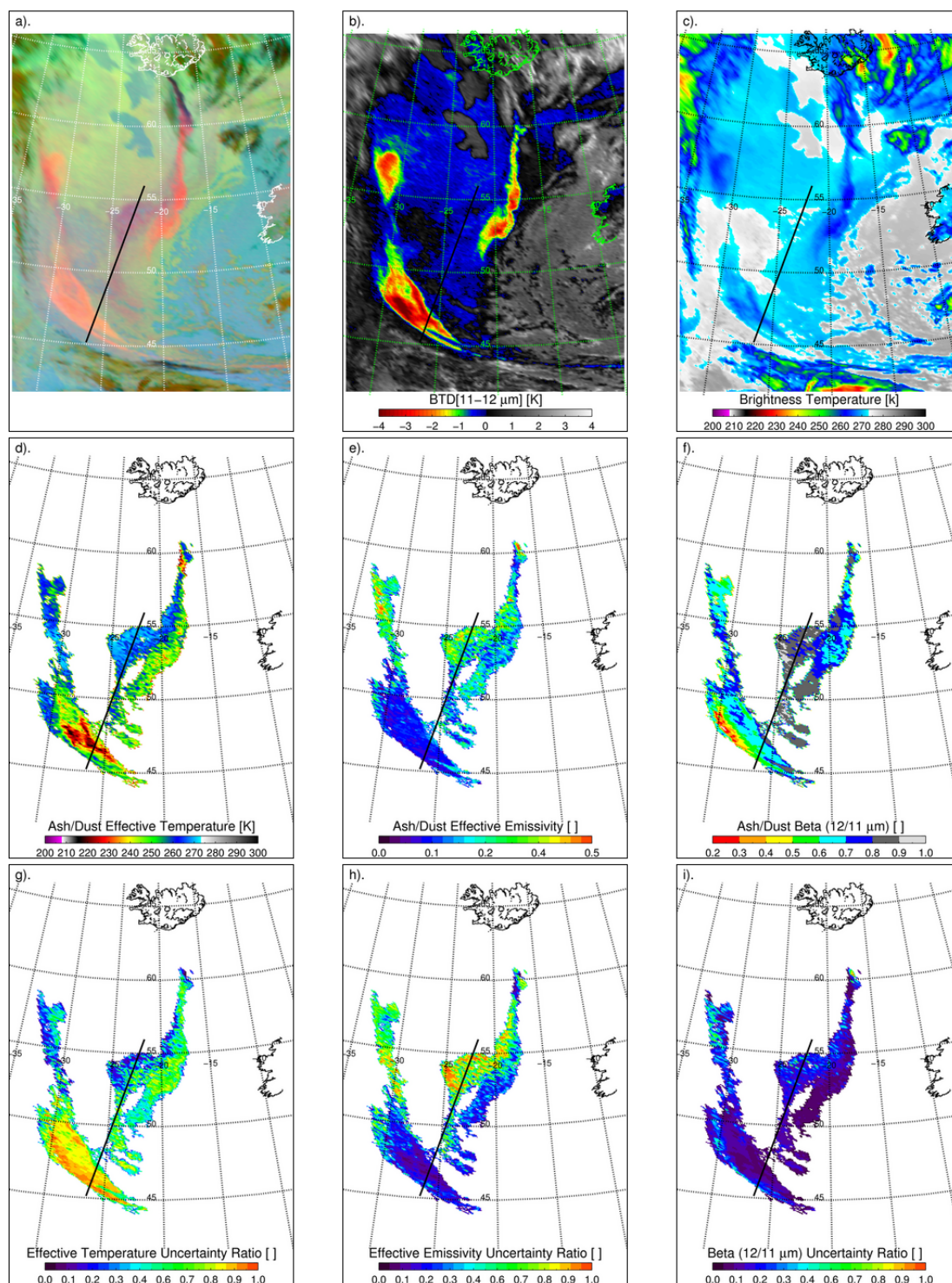


Figure 5.4: SEVIRI images from 0400 UTC on May 8, 2010. (a) Dust RGB image. (b) “Split-window” imagery. (c) 11  $\mu\text{m}$  imagery. (d) Retrieved effective cloud temperature. (e) Retrieved effective cloud emissivity. (f) Retrieved 12/11  $\mu\text{m}$  effective optical depth ratio. (g) Retrieved effective cloud temperature uncertainty ratio. (h) Retrieved effective cloud emissivity uncertainty ratio. (i) Retrieved 12/11  $\mu\text{m}$  effective optical depth ratio uncertainty ratio. The black solid line through the cloud represents a CALIPSO overpass. The andesite rock type was used to generate these results.

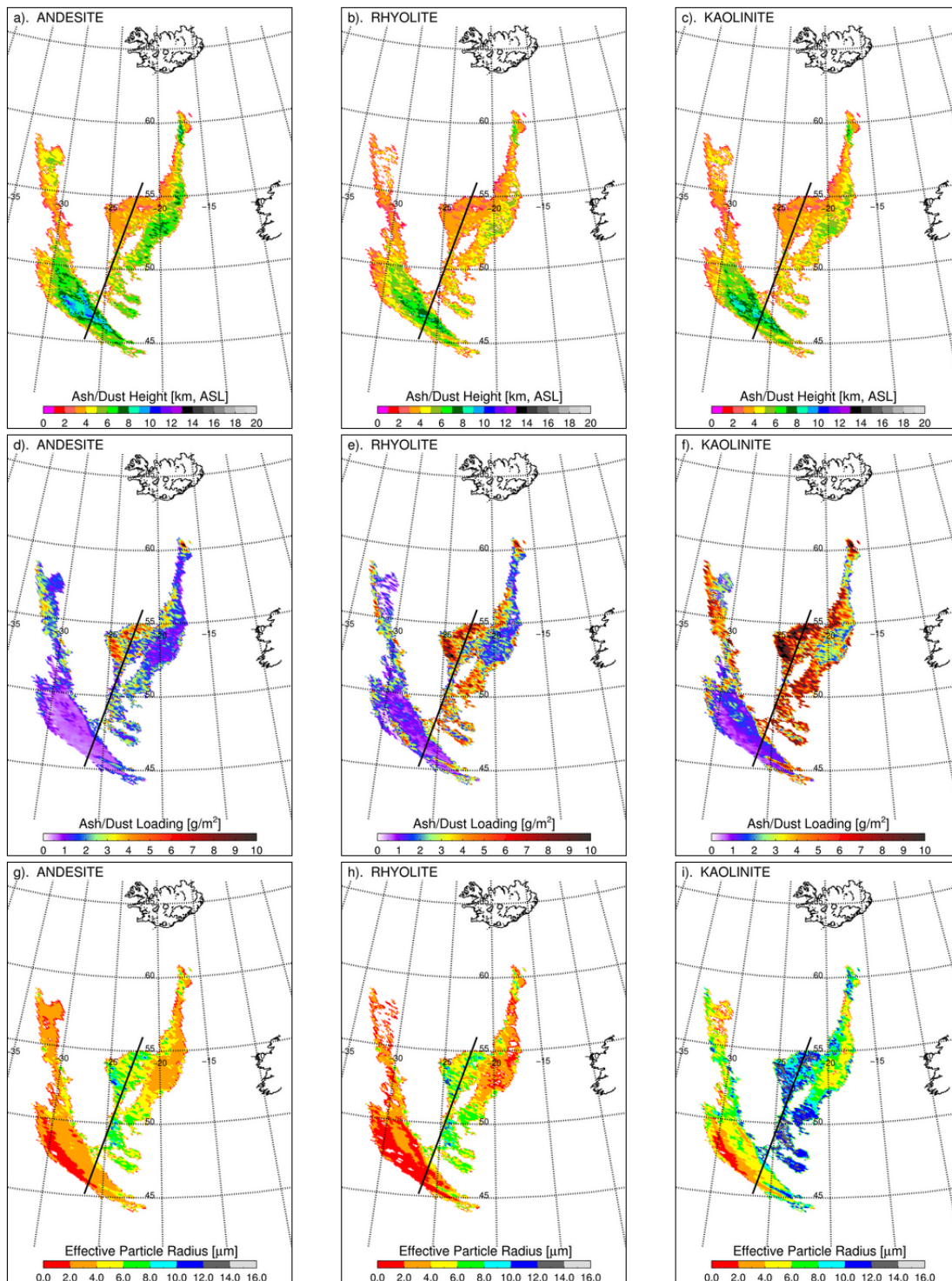


Figure 5.5: SEVIRI images from 0400 UTC on May 8, 2010. (a-c) Retrieved effective cloud height as a function of rock type (andesite, rhyolite, and kaolinite, respectively). (d-f) Retrieved cloud mass loading as a function of rock type (andesite, rhyolite, and kaolinite, respectively). (g-i) Retrieved cloud effective radius as a function of rock type (andesite, rhyolite, and kaolinite, respectively). The black solid line through the cloud represents a CALIPSO overpass.

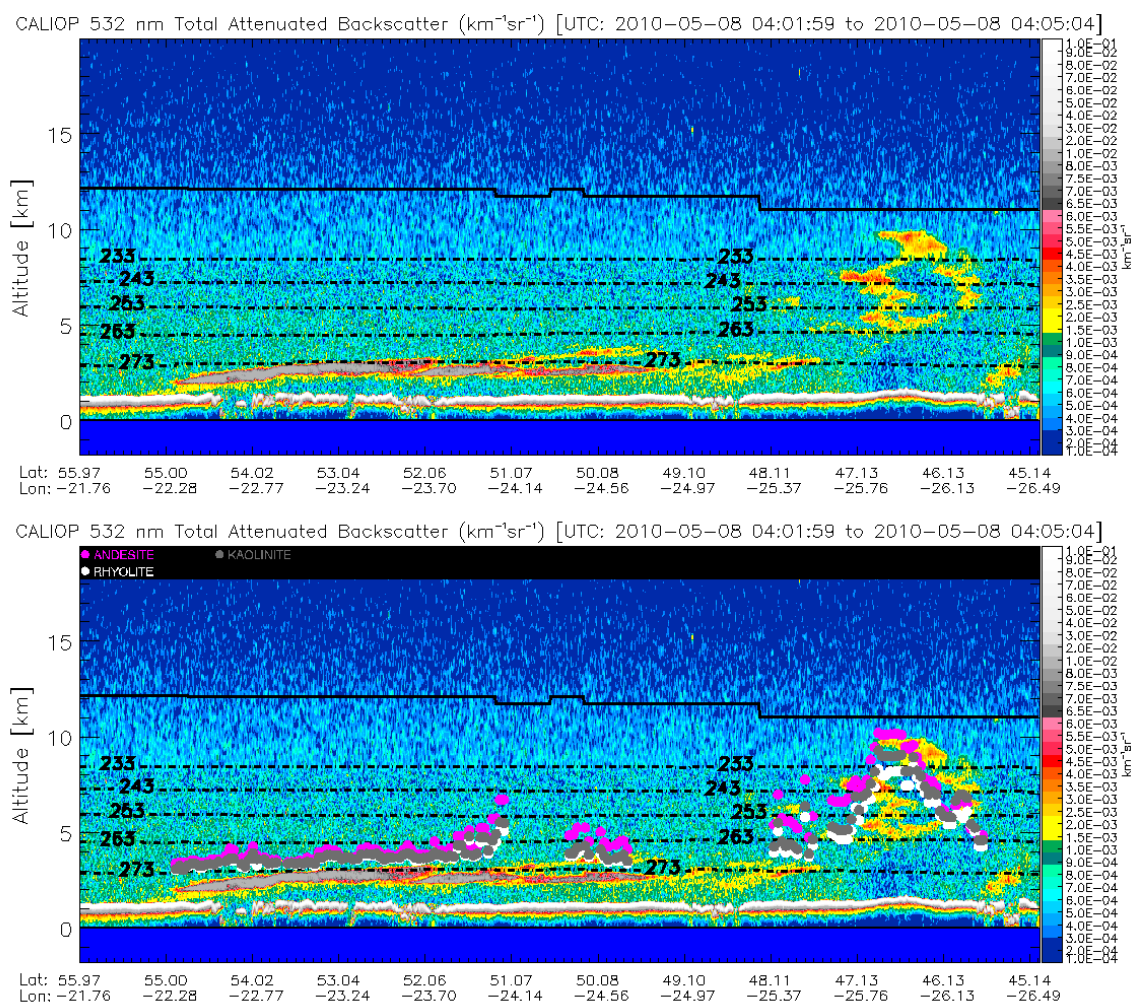


Figure 5.6: A CALIOP 532 nm total attenuated backscatter cross-section from 04:01:59 UTC – 04:05:04 UTC on May 8, 2012. The cross section is shown with (bottom) and without (top) the retrieved SEVIRI cloud heights (as a function of the assumed rock type) overlaid. Magenta circles represent andesite. White circles denote rhyolite. Gray circles represent kaolinite. In both panels, the solid black line denotes the tropopause and the dashed black lines represent select atmospheric isotherms (in Kelvin).

### 5.7.2. Soufriere Hills – February 12, 2010 (05:30 UTC)

Soufriere Hills is located in the eastern Caribbean, on the island of Montserrat. On February 11, 2010 a major partial lava dome collapse occurred, resulting in pyroclastic flows and a high-level ash cloud [Montserrat Volcano Observatory: <http://www.mvo.ms>]. Figure 5.7, Figure 5.8, and Figure 5.9 show the results of the

GOES-R ash cloud property retrieval on February 12, 2010 at 05:30 UTC in the same manner as the Eyjafjallajökull example. The andesite rock type was assumed to generate the results shown in Figure 5.7. The meteorological background for this eruption is considerably different than that observed south of Iceland on May 8, 2010. A radiosonde from the nearby island of Guadeloupe indicated that the total precipitable water was 27.18 mm, more than twice that observed at Keflavikur-Flugvollur in southern Iceland on May 8, 2010 (13.28 mm). As seen in Figure 5.7b, a significant portion of the ash cloud is characterized by a positive  $BTD(11-12\mu\text{m})$ , consistent with a larger water vapor loading. Recall that the retrieval accounts for background variables such as water vapor so it should not be adversely impacted by positive values of  $BTD(11-12\mu\text{m})$ . As in the Eyjafjallajökull example,  $T_{\text{eff}}$  is generally much less than the  $11\ \mu\text{m}$  brightness temperature and subsequently  $\epsilon(11\mu\text{m})$  is also generally small, as is commonly the case with dispersed ash clouds (see Figure 5.7, panels c and d). Most of the Soufriere Hills cloud is characterized by  $\beta(12/11\mu\text{m})$  values greater than 0.8. The uncertainty ratios indicate that the retrieval is adding considerable skill to the first guess for all retrieved parameters over most of the cloud. In the isolated patches where the  $T_{\text{eff}}$  uncertainty ratio is greater than 0.9 the  $\epsilon(11\mu\text{m})$  and  $\beta(12/11\mu\text{m})$  uncertainty ratios are very small and vice-versa, such that all three uncertainty ratios are never simultaneously large. There are a couple small holes in the cloud where conditions were such that ash was not detected using the procedure described earlier, and no retrieval was performed. Once again, the retrieved effective radius, and hence the mass loading, is far more sensitive to the assumed rock type than the cloud height (see Figure 5.8). The retrieved cloud heights are also in good agreement with the CALIOP cross section (Figure 5.9) through the optically

thin eastern portion of the cloud, with andesite producing a slightly better match than rhyolite and kaolinite. The low heights ( $< 2$  km) sometimes observed on the very edge of the Soufriere Hills cloud are likely caused by sub-pixel cloudiness (e.g. cloud fraction  $< 1.0$  within a given satellite pixel), which is not accounted for in the retrieval. Retrieval results and uncertainty estimates at the very edge of clouds should be used with caution, especially when the size of a satellite pixel is large, as it is in this case (SEVIRI pixels have a horizontal resolution of 10 km or greater in this region).

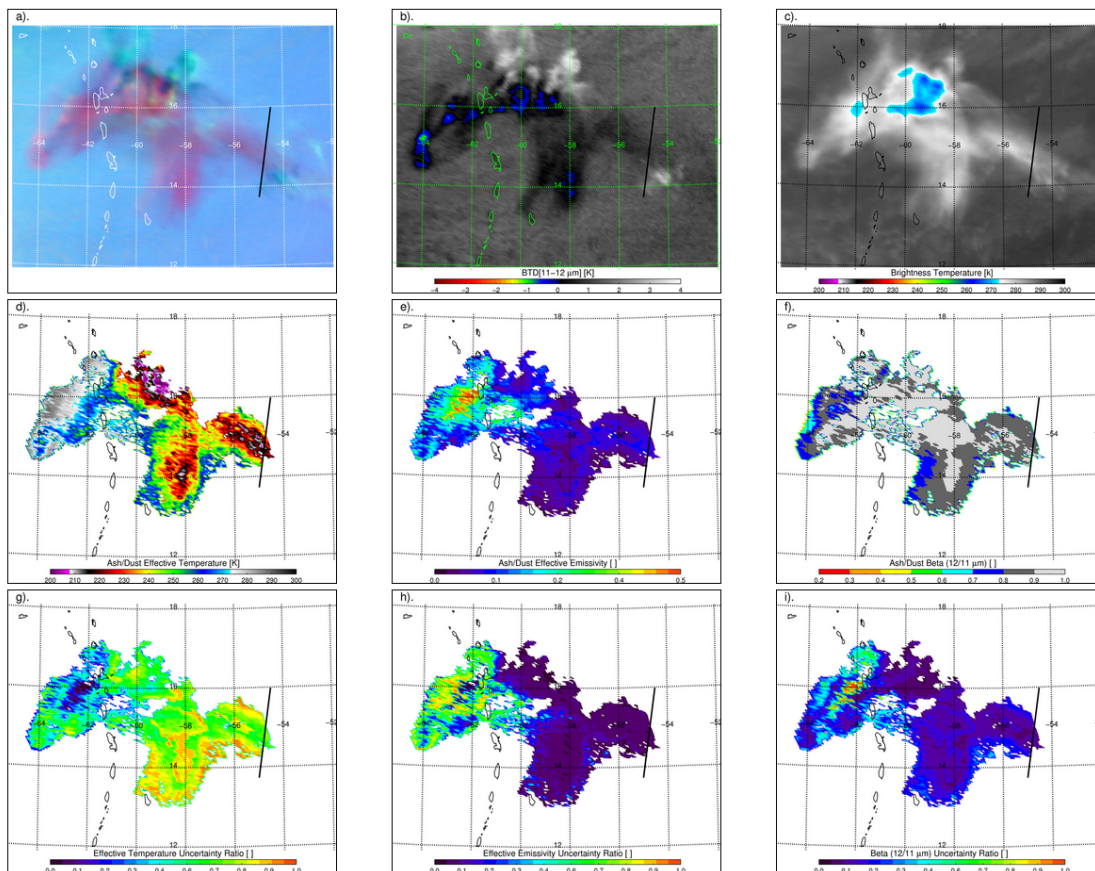


Figure 5.7: Same as Figure 5.4 except for the eastern Caribbean on 0530 UTC on February 12, 2010. The andesite rock type was used to generate these results.

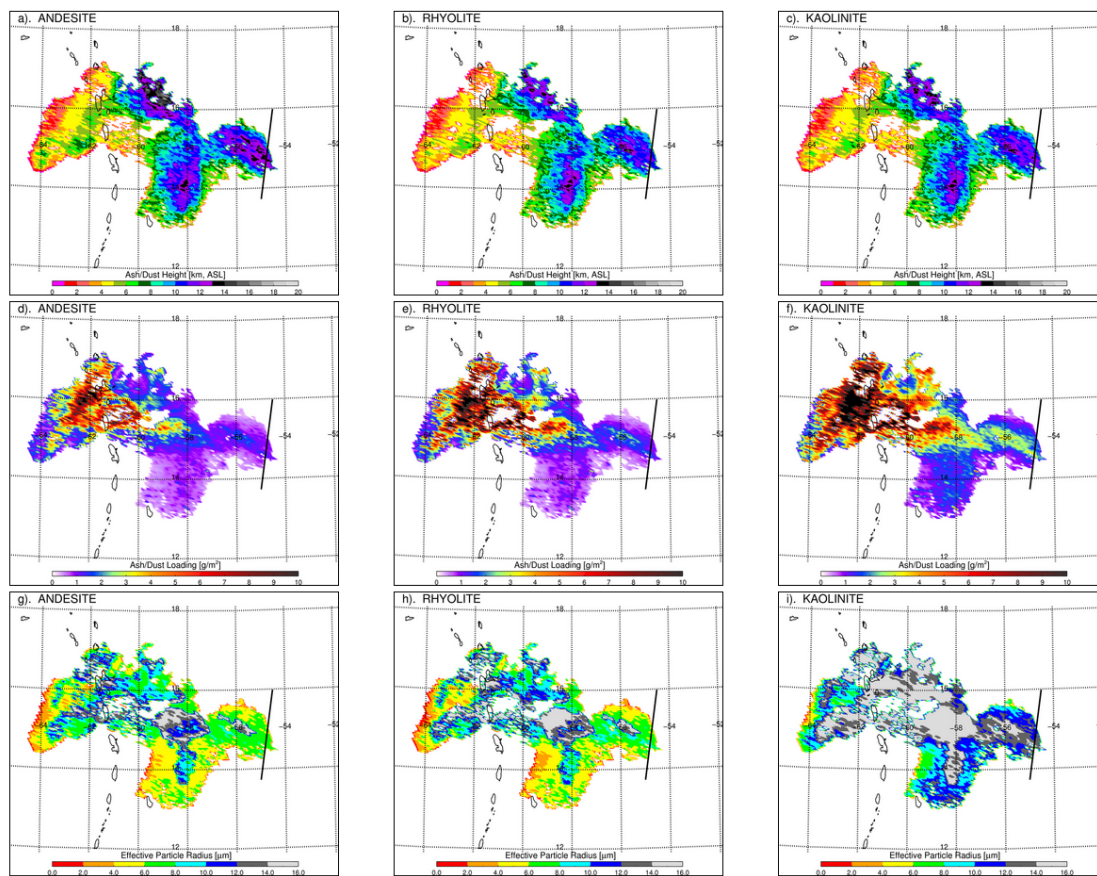


Figure 5.8: Same as Figure 5.5 except for the eastern Caribbean on 0530 UTC on February 12, 2010.

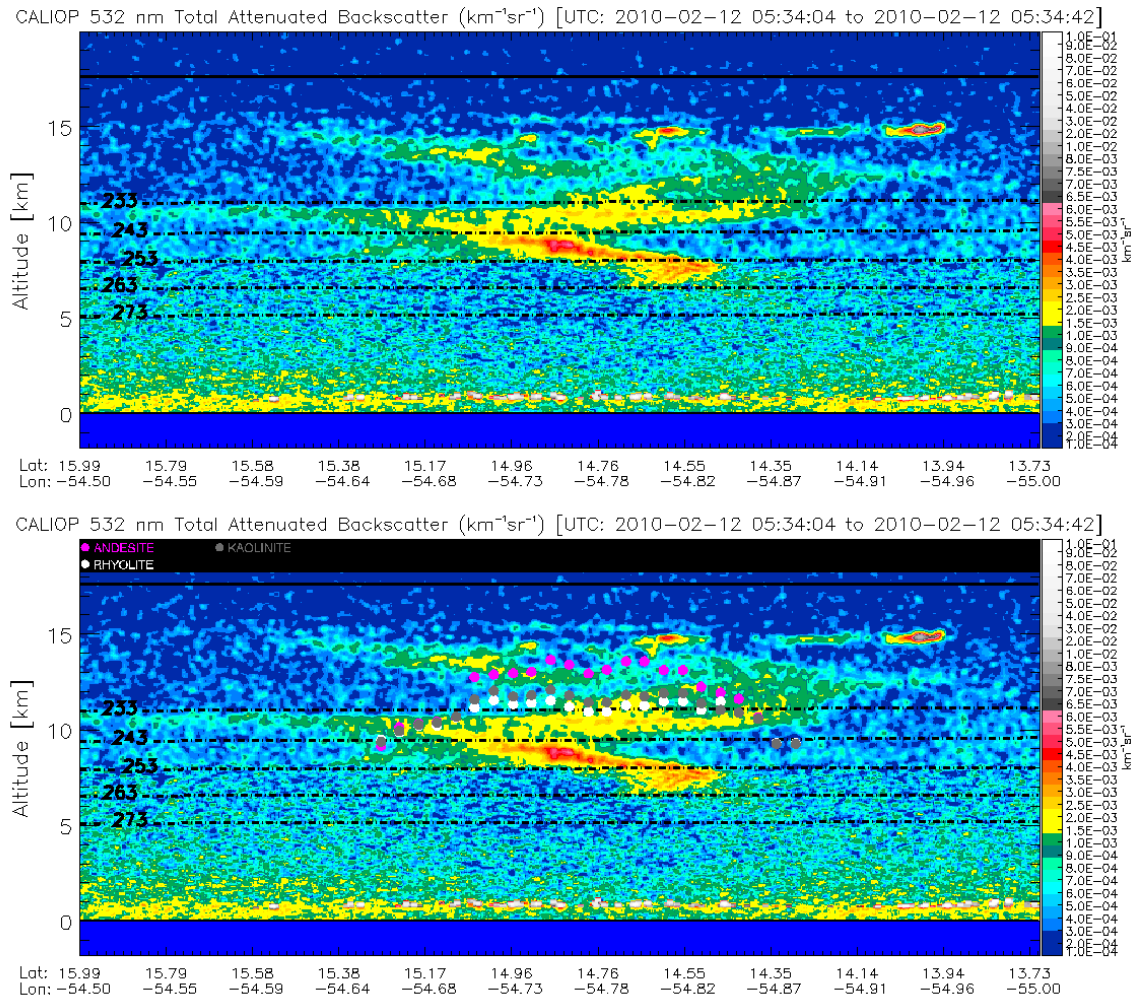


Figure 5.9: Same as Figure 5.6 except for 05:34:04 UTC – 05:34:42 UTC on February 12, 2010.

### 5.7.3. Saharan Dust – June 22, 2007 (02:45 UTC)

While the retrieval methodology described in this chapter was developed, primarily, for volcanic ash cloud applications, it can also be used to estimate dust cloud properties. Figure 5.10, Figure 5.11, and Figure 5.12 illustrate how the retrieval works on a Saharan dust cloud near the west coast of Africa, captured by SEVIRI on June 22, 2007 at 02:45 UTC. It should be noted that the horizontal resolution of the GFS model data used in this case study is  $1^\circ$  ( $0.5^\circ$  data were used for the previous two cases), so the

retrieved properties are slightly “blocky” as a result. As with the Eyjafjallajökull and Soufriere Hills volcanic ash clouds, the retrieved  $T_{\text{eff}}$  (Figure 5.10c) throughout the Saharan dust cloud is often much less than the 11  $\mu\text{m}$  brightness temperature (Figure 5.10d) and  $\epsilon(11\mu\text{m})$  rarely exceeds 0.3 (Figure 5.10e). The kaolinite rock type was used to generate the results shown in Figure 5.10. The  $T_{\text{eff}}$  uncertainty ratio often exceeds 0.9 (medium and dark orange colors in Figure 5.10g) when  $\epsilon(11\mu\text{m})$  is smaller than about 0.05 (see Figure 5.10e), indicating that the retrieval of  $T_{\text{eff}}$  adds little to no value to the first guess for the most optically thin portions of this dust cloud. In contrast, the  $\epsilon(11\mu\text{m})$  and  $\beta(12/11\mu\text{m})$  uncertainty ratios (Figure 5.10h and Figure 5.10i, respectively) are nearly always less than 0.7, regardless of cloud opacity. The uncertainty ratio for all three retrieved parameters is generally greater over land than water because, as described earlier, the uncertainty in the modeled clear sky brightness temperatures is much greater over land than water.

Figure 5.11 shows that the retrieval of cloud height, mass loading, and effective particle radius is quite sensitive to the rock type. In particular, using gypsum as the rock type results in lower cloud heights (higher  $T_{\text{eff}}$ ), which must be radiatively compensated for by larger values of  $\epsilon(11\mu\text{m})$  (not shown). The larger gypsum derived mass loadings are caused by the larger values of  $\epsilon(11\mu\text{m})$ . This particular Saharan dust scene was chosen for analysis because the CALIPSO overpass includes observations over water and land (Figure 5.12). Figure 5.12 shows that the retrieved cloud heights tend to be overestimated near the coastline when using kaolinite or andesite. Coastlines are challenging in that surface temperature can vary greatly over relatively small distances. The spatial variability of surface temperature is not captured well by course

resolution global models like the GFS (the horizontal resolution of the GFS data used for this scene is 1.0 degree). Thus, larger errors in the modeled clear sky brightness temperatures are likely. Over the land portion of this segment the rock type has only a small impact on the retrieved height, consistent with a  $T_{\text{eff}}$  that does not deviate much from the first guess value. In fact,  $T_{\text{eff}}$  is generally within 5 K of the first guess along the land portion of the CALIOP cross section. Over the water, using gypsum causes the cloud height to be underestimated more than kaolinite, perhaps suggesting that kaolinite is more likely to be the dominant rock type of this cloud. Turner [2008] found that the dominant rock type of Saharan dust clouds was kaolinite. Interestingly, even though this cloud is not composed of andesite, the cloud heights retrieved using the andesite composition are generally consistent with kaolinite. Using andesite, however, will cause the effective radius, and consequently the mass loading, to be underestimated relative to kaolinite. This case study does show that the general retrieval approach can be applied to dust clouds.

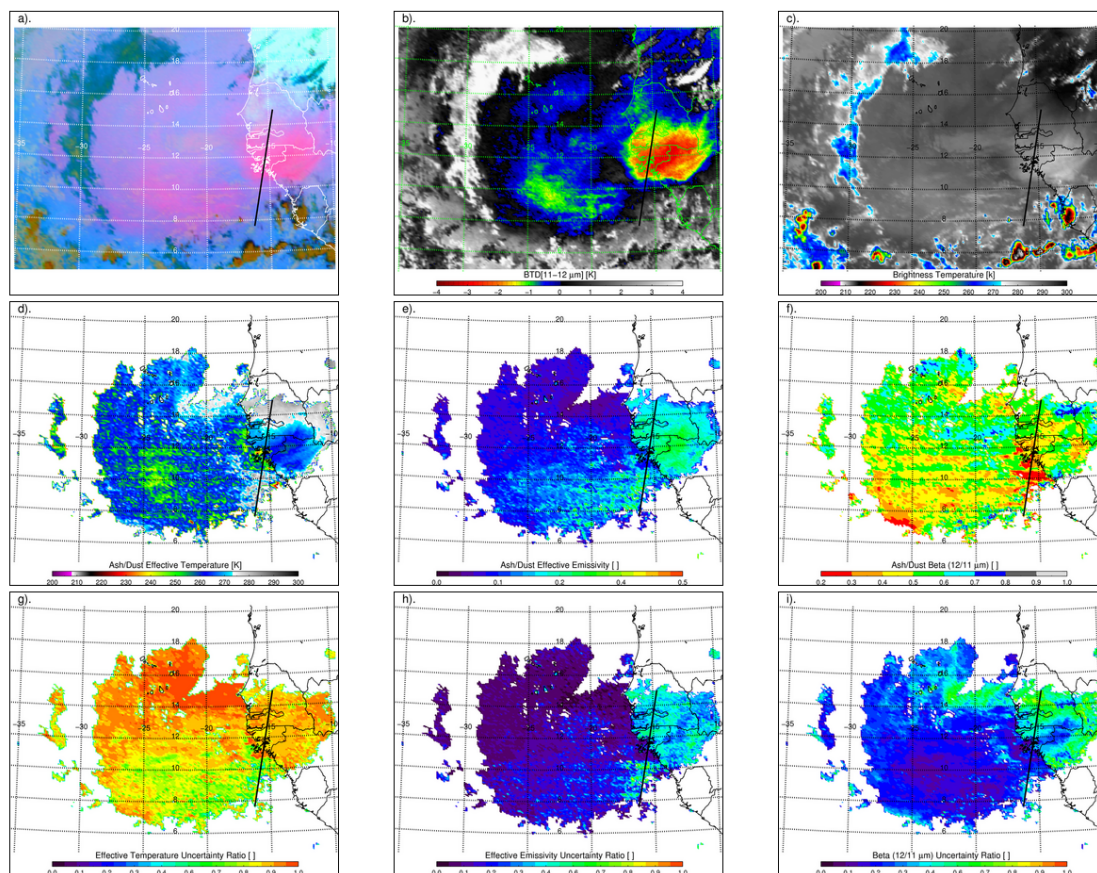


Figure 5.10: Same as Figure 5.4 except for a dust outbreak near the west coast of Africa on 0245 UTC on June 22, 2007. The kaolinite rock type was used to generate these results.

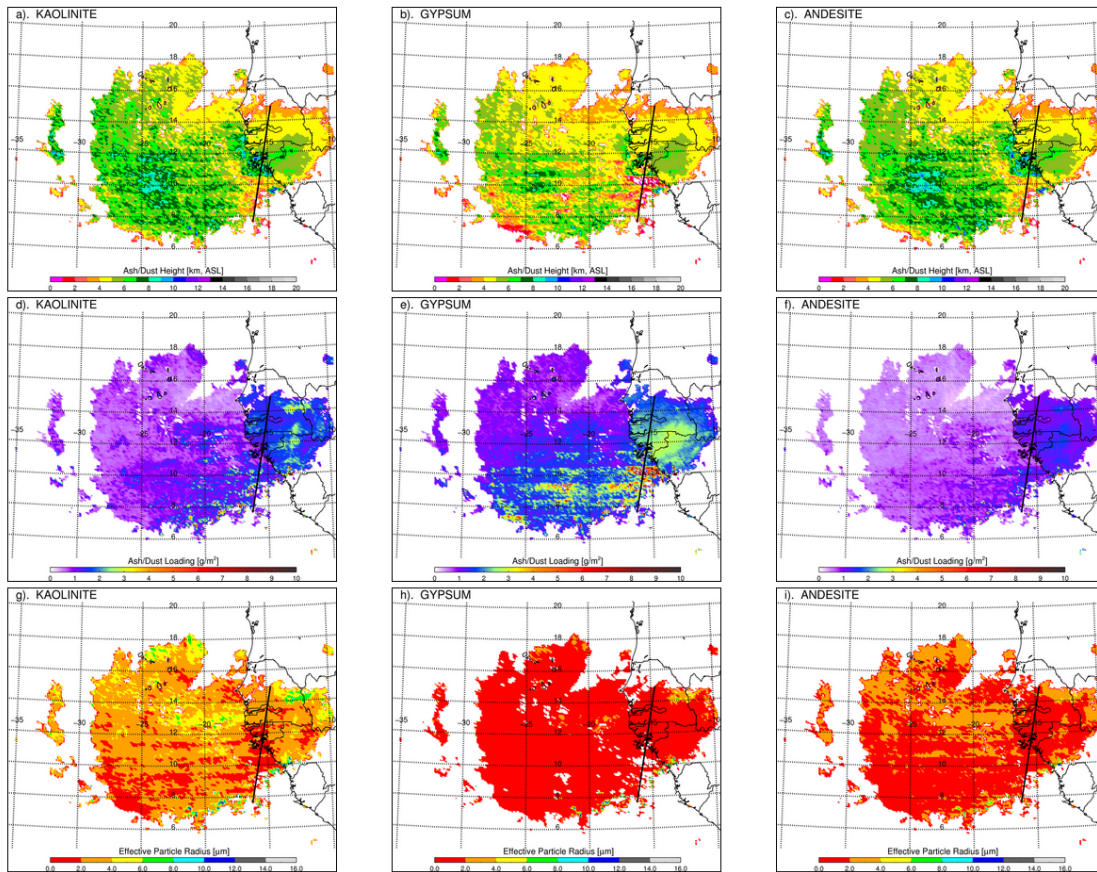


Figure 5.11: SEVIRI images near the west coast of Africa on 0245 UTC on June 22, 2007. (a-c) Retrieved effective cloud height as a function of rock type (kaolinite, gypsum, and andesite, respectively). (d-f) Retrieved cloud mass loading as a function of rock type (kaolinite, gypsum, and andesite, respectively). (g-i) Retrieved cloud effective radius as a function of rock type (kaolinite, gypsum, and andesite, respectively). The black solid line through the cloud represents a CALIPSO overpass.

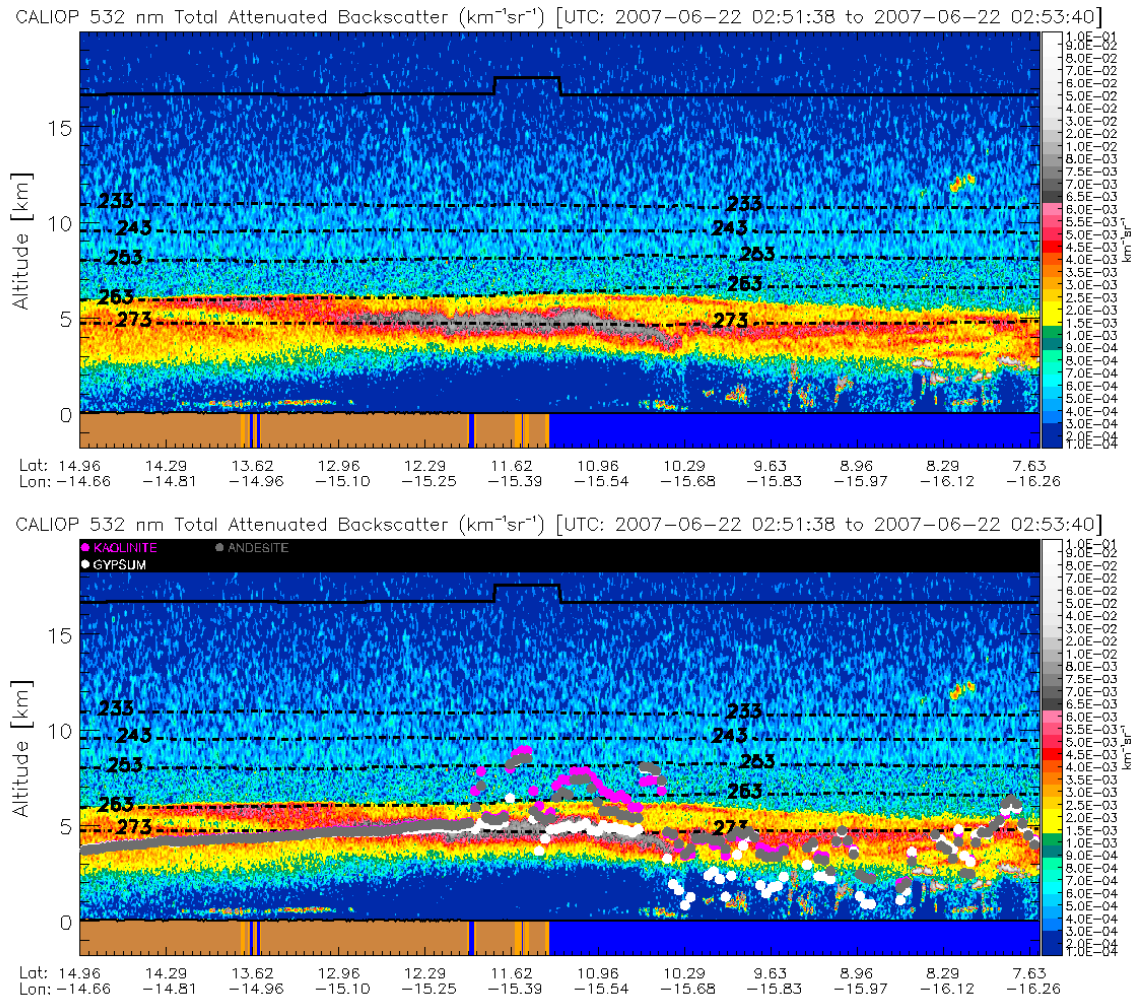


Figure 5.12: Same as Figure 5.6 except for 02:51:38 UTC – 02:53:40 UTC on June 22, 2007. Unlike Figure 5.6, magenta circles represent kaolinite, white circles denote gypsum and gray circles represent andesite.

#### 5.7.4. Statistical Comparison to CALIOP

More rigorous comparisons to CALIOP derived cloud properties are used to quantitatively assess the GOES-R retrieval algorithm. A total of 15 CALIPSO ash cloud overpasses from the May 6-16 portion of the 2010 Eyjafjallajökull eruption and the CALIPSO overpass from the Soufriere Hills ash clouds shown in Figure 5.7 were manually chosen for this analysis. The only criterion used in the manual selection process was that ash had to be the highest cloud layer. When fully automated techniques

have been developed to mine the CALIOP data record for ash clouds, this analysis can be readily expanded. Currently, confidently identifying ash clouds in CALIOP data is a manually intensive process that requires side-by-side close examination of CALIOP and infrared imagery, as ash clouds are very difficult to identify using CALIOP alone [Winker et al. 2012]. The CALIPSO overpasses of Eyjafjallajökull ash clouds are conveniently well known due to the high impact of that eruption on air traffic, which is not the case with many other eruptions sampled by CALIOP. The 16-ash cloud overpasses result in a total of 796 data points, which is large relative to previously published quantitative, ash cloud, validation efforts (e.g. [Francis et al. 2012]; Prata and Prata 2012)).

A combination of the 5-km CALIOP cloud and aerosol cloud layers products [Vaughan et al. 2009] are used to determine the vertical extent of the highest cloud layer along each segment through the ash clouds. A combination of the cloud and aerosol layers products is needed since some ash clouds will be classified as aerosol and some will be classified as clouds (liquid or ice) by the classification algorithm [e.g. Winker et al. 2012]. In addition, effective cloud emissivity for a given SEVIRI spectral band or bands can be computed using a combination of CALIOP vertical cloud boundaries and co-located SEVIRI infrared measurements [e.g. Heidinger and Pavolonis 2009; Garnier et al. 2012]. We utilize the method of Heidinger and Pavolons [2009] to compute the  $\epsilon(11\mu\text{m})$ , and  $\beta(12/11\mu\text{m})$  of the highest cloud layer. The  $\epsilon(11\mu\text{m})$ , and  $\beta(12/11\mu\text{m})$  computed from a combination of CALIOP and SEVIRI will be consistently more accurate than the  $\epsilon(11\mu\text{m})$ , and  $\beta(12/11\mu\text{m})$  retrieved using SEVIRI alone (with the GOES-R retrieval approach) because CALIOP vertical cloud boundaries provide a very

tight constraint on  $T_{\text{eff}}$  and no cloud microphysical assumptions are needed (see Equations ( 5.1) - ( 5.2)). In the GOES-R retrieval,  $T_{\text{eff}}$  is a very loosely constrained free parameter and cloud microphysical assumptions related to particle composition, shape, and size are needed (e.g. Figure 5.1). No microphysical assumptions are needed to determine cloud top height,  $\epsilon(11\mu\text{m})$ , and  $\beta(12/11\mu\text{m})$  from CALIOP or a combination of CALIOP and SEVIRI (in the case of  $\epsilon(11\mu\text{m})$ , and  $\beta(12/11\mu\text{m})$ ). The determination of mass loading from the CALIOP + SEVIRI derived  $\epsilon(11\mu\text{m})$  and  $\beta(12/11\mu\text{m})$  does require the same assumptions about particle composition, size, and shape utilized when computing mass loading from SEVIRI alone.

A comparison between the GOES-R ash cloud heights and the CALIOP cloud top heights are shown in Figure 5.13 as a function of the  $\epsilon(11\mu\text{m})$  computed from a combination of CALIOP and SEVIRI, the cloud geometrical thickness provided by CALIOP, and the rock type (andesite, rhyolite, or kaolinite) used in the GOES-R retrieval. The cloud heights retrieved using the GOES-R approach are generally in good agreement with CALIOP, regardless of the rock type used in the retrieval (although andesite seems to have a slight edge). The GOES-R heights are negatively biased (-0.77 km for andesite) relative to the CALIOP cloud top, which is expected given the high vertical resolution of CALIOP and the coarse vertical resolution of SEVIRI (the measured radiation originates from a thicker layer within the cloud). Not surprisingly, the most optically thin clouds ( $\epsilon(11\mu\text{m}) < 0.05$ ) are responsible for most of the low bias. Clouds with a larger geometric thickness are also more prone to underestimation since the measured infrared radiation is now emanating from a thicker layer below the cloud top. The GOES-R approach sometimes slightly over-estimates the cloud top height, especially

for ash clouds with tops lower than 5 km. The over-estimation can generally be attributed to underlying stratus clouds that are colder than the surface. Underlying cloud layers are not accounted for in the retrieval at this time, but future versions of the retrieval will account for underlying clouds.

Figure 5.14 shows a comparison between  $\epsilon(11\mu\text{m})$  retrieved using the GOES-R algorithm and  $\epsilon(11\mu\text{m})$  computed from a combination of CALIOP and SEVIRI. The results are shown as a function of the CALIOP cloud top height, CALIOP geometric cloud thickness, and the rock type (andesite, rhyolite, or kaolinite) used to perform the GOES-R retrieval. The GOES-R bias in  $\epsilon(11\mu\text{m})$  is very small, especially when the retrieval is performed using andesite (bias = -0.006). The standard deviation (or precision) of the GOES-R – CALIOP difference is considerably larger because a positive bias is observed when the CALIOP derived  $\epsilon(11\mu\text{m}) < 0.3$  and a negative bias is observed when  $\epsilon(11\mu\text{m}) > 0.3$ . Closer inspection of the CALIOP cross sections used in this analysis reveals that the positive bias at smaller emissivity values is likely a result of the presence of multiple, geometrically thin, ash cloud layers with very little vertical separation. While underlying cloud layers are accounted for in the computation of the combined CALIOP/SEVIRI  $11\mu\text{m}$  cloud emissivity, they are not accounted for in the GOES-R retrieval. Conversely, the negative bias observed at larger emissivity values is caused by the under-estimation of  $T_{\text{eff}}$  (over-estimation of cloud height) discussed earlier.

A comparison between the GOES-R  $\beta(12/11\mu\text{m})$  and the  $\beta(12/11\mu\text{m})$  computed using a combination of CALIOP and SEVIRI are shown in Figure 5.15 as a function of the CALIOP cloud top height, the  $\epsilon(11\mu\text{m})$  computed from a combination of CALIOP and SEVIRI measurements, and rock type. With the exception of a few outliers (mainly

low to mid level ash clouds), the  $\beta(12/11\mu\text{m})$  retrieved using the GOES-R algorithm is in very close agreement with the CALIOP  $\beta(12/11\mu\text{m})$ , regardless of the rock type used in the retrieval (bias = 0.002 for andesite). Since the effective particle radius is determined directly from  $\beta(12/11\mu\text{m})$  (see Figure 5.1), these results imply that the effective particle radius can be computed with a similarly small bias for a given known rock type. Given that  $\beta(12/11\mu\text{m})$  (and hence the effective particle radius) is largely unbiased, the bias in mass loading will primarily be a result of the bias in  $\epsilon(11\mu\text{m})$ , which is heavily influenced by underlying cloud layers. Thus, the mass loading of an ash cloud (with a known rock type and particle density) that overlays another cloud layer or layers will be positively biased when  $\epsilon(11\mu\text{m}) < 0.3$  and negatively biased when  $\epsilon(11\mu\text{m}) > 0.3$ . Accounting for underlying cloud layers, even crudely, should help reduce the overall bias.

The comparison between the ash mass loading derived from a combination of CALIOP and SEVIRI and SEVIRI alone is shown in Figure 5.16. The andesite rock type results in the lowest bias (no large systematic bias) and spread. Relative to the combined CALIOP/SEVIRI retrievals, the SEVIRI alone retrievals tend to underestimate the ash loading of lower level ash clouds and over-estimate the loading of higher-level clouds. A closer inspection of the cases used in this analysis indicates that multiple cloud layers (usually ash with underlying meteorological cloud layers) are often present when the differences are larger. We are able to account for multiple distinct cloud layers in the combined CALIOP/SEVIRI retrieval with much greater skill compared to the SEVIRI alone retrieval.

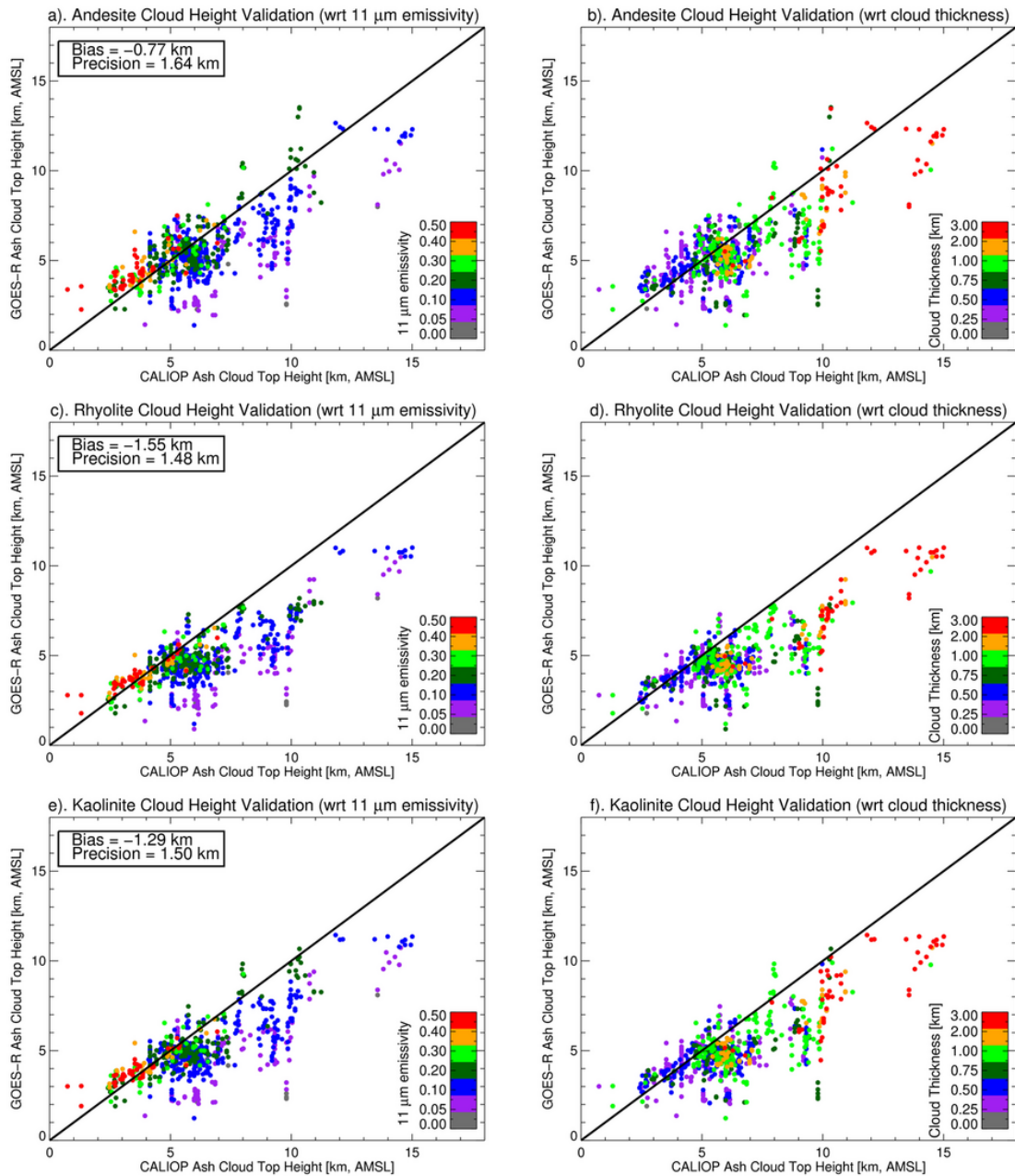


Figure 5.13: A comparison of SEVIRI ash cloud heights retrieved using the GOES-R approach and CALIOP measured cloud top heights is shown as a function of the nadir  $11\ \mu\text{m}$  cloud emissivity derived from a combination of CALIOP and SEVIRI (first column) and the cloud geometric thickness given by CALIOP (second column). Each color represents a different  $11\text{-}\mu\text{m}$  cloud emissivity or cloud thickness bin. The results are also shown as a function of the rock type assumed by the retrieval (top=andesite, middle=rhyolite, bottom=kaolinite). The 1:1 line is shown in black. A total of 796 data points were used in this analysis.

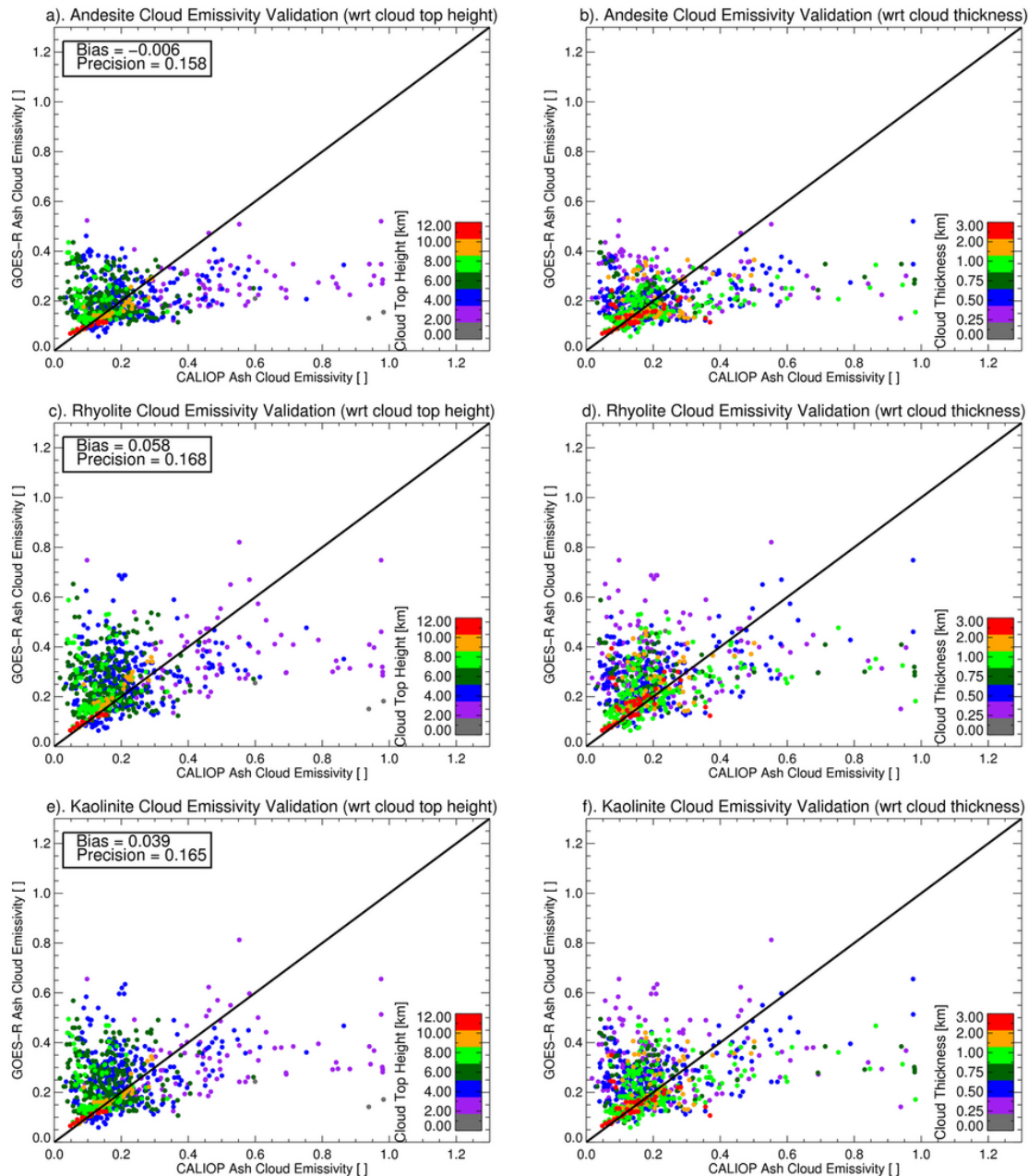


Figure 5.14: A comparison of SEVIRI ash cloud emissivity retrieved using the GOES-R approach and the  $11\ \mu\text{m}$  cloud emissivity derived from a combination of CALIOP and SEVIRI are shown as a function of the CALIOP measured cloud top height (first column) and the cloud geometric thickness given by CALIOP (second column). Each color represents a different cloud top height or cloud thickness bin. The results are also shown as a function of the rock type assumed by the retrieval (top=andesite, middle=rhyolite, bottom=kaolinite). The 1:1 line is shown in black. A total of 796 data points were used in this analysis.

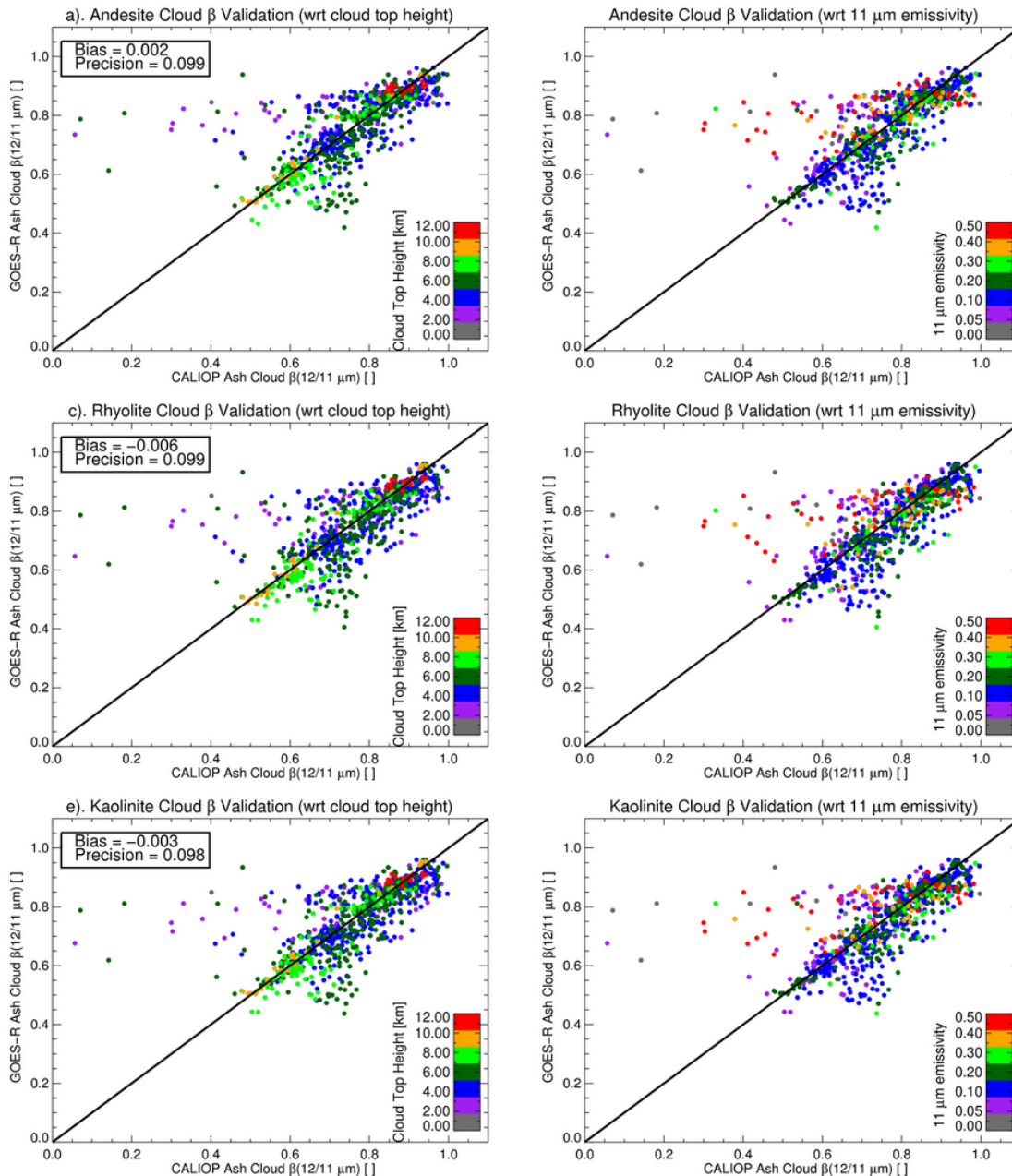


Figure 5.15: A comparison of SEVIRI ash 12/11  $\mu\text{m}$   $\beta$ -ratios retrieved using the GOES-R approach and the 12/11  $\mu\text{m}$   $\beta$ -ratios computed using a combination of CALIOP and SEVIRI is shown as a function of the cloud top height measured by CALIOP (first column) and the nadir 11  $\mu\text{m}$  cloud emissivity derived from a combination of CALIOP and SEVIRI (second column). Each color represents a different cloud top height or 11- $\mu\text{m}$  cloud emissivity bin. The results are also shown as a function of the rock type assumed by the retrieval (top=andesite, middle=rhyolite, bottom=kaolinite). The 1:1 line is shown in black. A total of 796 data points were used in this analysis.

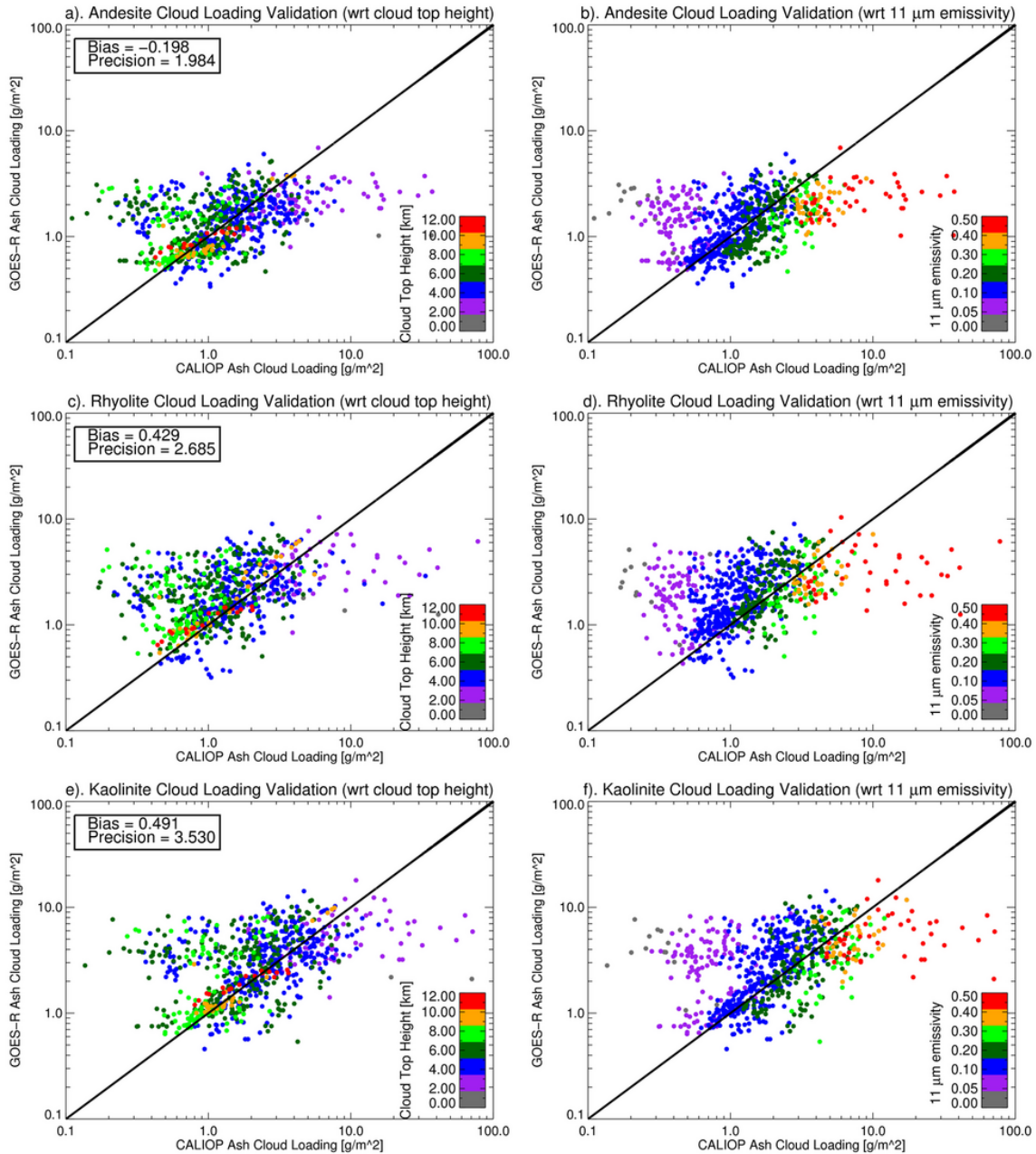


Figure 5.16: A comparison of SEVIRI ash mass loading retrieved using the GOES-R approach and the ash mass loading computed using a combination of CALIOP and SEVIRI is shown as a function of the cloud top height measured by CALIOP (first column) and the nadir 11  $\mu\text{m}$  cloud emissivity derived from a combination of CALIOP and SEVIRI (second column). Each color represents a different cloud top height or 11- $\mu\text{m}$  cloud emissivity bin. The results are also shown as a function of the rock type assumed by the retrieval (top=andesite, middle=rhyolite, bottom=kaolinite). The 1:1 line is shown in black. A total of 796 data points were used in this analysis.

### 5.8. *Summary*

A fully automated algorithm to retrieve the radiative temperature, emissivity, and a microphysical parameter of volcanic ash and dust clouds using satellite-based infrared measurements was developed. From these retrieved parameters, the cloud radiative height, effective particle radius, optical depth, and mass loading can be derived, subject to certain assumptions. An optimal estimation framework is utilized, which allows uncertainties in the measurements and forward model to be taken into account and uncertainty estimates for each of the retrieved parameters to be determined. Background atmospheric water vapor, surface temperature, and surface emissivity are explicitly accounted for on a pixel-by-pixel basis, so the algorithm is globally applicable.

Using SEVIRI, the retrieval algorithm was applied to ash clouds from the 2010 eruption of Eyjafjallajökull and the 2010 eruption of Soufriere Hills and a Saharan dust cloud. In an effort to determine the accuracy of the retrieval, the results were compared to CALIOP derived cloud properties. The retrieved cloud heights were found to generally be within 1 - 2 km (with little bias) of CALIOP derived cloud top heights for low and mid level ash clouds (< 7 km) and within 3 - 4 km (with a negative bias) for high level clouds (> 7 km). These results are consistent with the work of Francis et al. [2012]. The 11  $\mu\text{m}$  cloud emissivity had a tendency to be positively biased relative to the cloud emissivity computed using CALIOP for clouds with a small 11  $\mu\text{m}$  optical depth (< 0.3) and negatively biased for clouds with an intermediate to large optical depth (> 0.3), although nearly all clouds analyzed were semi-transparent to infrared radiation. The bias in the retrieved cloud emissivity is likely caused by complexities related to underlying cloud layers. The 12/11 $\mu\text{m}$  optical depth ratio ( $\beta(12/11\mu\text{m})$ ), which is directly related to

the effective particle radius, closely agreed with the  $\beta(12/11\mu\text{m})$  computed using CALIOP, and was found to be unbiased. Consequently, the effective particle radius should also be largely unbiased. The mass loading was biased in a similar manner as the cloud emissivity, which is expected since  $\beta(12/11\mu\text{m})$  was shown to be accurate and unbiased. In addition, better overall agreement between the retrieved and CALIOP derived cloud properties was found when andesite rock was used to represent ash clouds and kaolinite was used to represent dust clouds.

While the retrieval described in this chapter was designed to use spectral channels approximately centered at 11, 12, and 13.3  $\mu\text{m}$ , the general retrieval framework can be applied to other channel combinations. For instance a water vapor absorption band (e.g. 6.7  $\mu\text{m}$ ) can be substituted for the 12  $\mu\text{m}$  or 13.3  $\mu\text{m}$  channels so that ash and dust cloud properties can be retrieved using a greater number of satellite sensors. Measurements from different sensors can also be combined to allow the retrieval to be performed using high spatial resolution sensors that lack a 13.3  $\mu\text{m}$  band by approximating a 13.3  $\mu\text{m}$  band from low spatial resolution hyperspectral infrared sounding instruments located on the same spacecraft (e.g. Advanced Very High Resolution Radiometer (AVHRR) + Infrared Atmospheric Sounding Interferometer (IASI); Visible Infrared Radiometer Suite (VIIRS) + Cross Track Infrared Sounder (CrIS); MODerate Resolution Imaging Spectroradiometer (MODIS) + Atmospheric Infrared Sounder (AIRS)). Hyperspectral instruments can also potentially be used to provide a better first guess for the retrieval.

As recent case studies [Stohl et al. 2011; Schmehl et al. 2012; Denlinger et al. 2012; Webley et al. 2012] have shown, the ash/dust cloud property retrievals, like those presented here, can be used to initialize (improve the volcano source term, data

assimilation applications, initialize trajectories, etc...) and validate dispersion and transport models. A globally robust, fully automated, ash/dust detection method is needed to facilitate using satellite retrievals of ash and dust cloud properties to improve operational modeling capabilities. Such a method is described in the next chapter.

## Chapter 6

### 6. Volcanic Ash Cloud Objects

#### 6.1. Introduction

A fully automated, satellite-based, volcanic ash and dust detection technique, known as the Spectrally Enhanced Cloud Objects (SECO) algorithm, is developed. The development of the SECO algorithm is motivated by the lack of a highly skilled, globally applicable, automated volcanic ash and dust detection technique that can be applied to nearly any geostationary or low earth orbit satellite sensor with infrared measurement capabilities day or night [Chapter 4]. The SECO algorithm is designed to deterministically identify volcanic ash and dust in manner that is more consistent with human expert interpretation of satellite imagery than traditional techniques. The SECO approach does not attempt to distinguish between volcanic ashes and dust because they generally have very similar spectral signatures at the wavelengths utilized by the SECO algorithm.

In Chapter 4, several sophisticated satellite metrics, derived from measurements with central wavelengths of approximately 0.65, 3.9, 7.3, 8.5, 11, and 12  $\mu\text{m}$ , were utilized in a naïve Bayesian procedure to determine the probability that a given satellite pixel contains volcanic ash and/or non-volcanic dust. The Bayesian method can utilize all of those spectral channels or several different channel subsets as dictated by sensor capabilities, solar zenith angle, and/or intellectual curiosity (see Table 4.1). The Bayesian method was trained empirically using a very large MODerate Resolution Imaging Spectroradiometer (MODIS) based data set where the horizontal bounds of volcanic ash and dust clouds were manually analyzed. Analysis showed that the

Bayesian method was skilled at distinguishing between volcanic ash/dust features and all other features (e.g., the probability was generally much greater inside actual volcanic ash and dust clouds than outside), much more so than the traditional “split-window” method [e.g. Prata 1989a; Prata 1989b] technique, even when spectral channel subsets were used. The traditional “split-window” method consists of computing the difference in brightness temperature between measurements taken at approximately 11 and 12  $\mu\text{m}$  and applying a threshold. Volcanic ash and dust typically absorb, and hence emit, more radiation at 11  $\mu\text{m}$  than 12  $\mu\text{m}$ , resulting in a split-window brightness temperature difference that is less than 0 K in the absence of competing absorption/emission/reflection effects at those wavelengths. Conversely, liquid water and ice clouds, generated by meteorological processes (meteorological clouds), typically have a “split-window” brightness temperature difference that is greater than 0 K. Thus, a “split-window” threshold of about 0 K is typically used for ash/dust detection. Unfortunately, competing absorption/emission/reflection effects and measurement errors greatly limit the accuracy of the “split-window” technique.

A human-like (i.e., high probability of detection with an extremely low false alarm rate) capability for distinguishing volcanic and dust from all other features is needed for advanced, automated applications such as volcanic eruption alerting and data assimilation. Despite the success of the pixel-level Bayesian method, it, alone, is not sufficient to produce a human-like deterministic volcanic ash/dust assessment by simply applying a probability threshold. The Bayesian method must be combined with advanced spatial analysis to produce such a result. In this Chapter, the remaining components of the SECO algorithm that utilize advanced spatial analysis are described, and the results

are shown to be consistent with human expert interpretation of multispectral satellite imagery, especially with respect to false alarm rate. Data from the MODIS are used to introduce the remaining components of the SECO algorithm and assess the impact of using various spectral channel subsets.

## 6.2. Review of Multispectral Parameters

In Chapter 4 (hereafter Ch4), several advanced multi-spectral parameters were introduced and subsequently utilized in the naïve Bayesian method for determining the probability that volcanic ash and/or dust is present in a given satellite pixel. These parameters and the underlying physical concepts are also invoked in this paper so a brief review is given here. The multi-spectral infrared measurements were generally expressed as  $\beta$ -ratios, as opposed to traditional brightness temperature differences (BTDs), because  $\beta$ -ratios provide increased sensitivity to cloud microphysical properties, including cloud composition [Chapter 3]. As shown in ( 6.1), a  $\beta$ -ratio is simply the ratio of effective (scattering is implicitly accounted for) absorption optical depth at two different wavelengths.

$$\beta_{obs} = \frac{\ln[1 - \varepsilon_{eff}(\lambda_1)]}{\ln[1 - \varepsilon_{eff}(\lambda_2)]} = \frac{\tau_{abs, eff}(\lambda_1)}{\tau_{abs, eff}(\lambda_2)} \quad (6.1)$$

The effective absorption optical depth for a given wavelength [ $\tau_{eff}(\lambda)$ ] is easily computed from the effective cloud emissivity [ $\varepsilon_{eff}(\lambda)$ ] (see ( 6.1)), but computation of  $\varepsilon_{eff}(\lambda)$  requires knowledge of the clear sky top of atmosphere radiance and transmittance (integrated radiance and transmittance from the surface or a given atmospheric level to the top of the atmosphere) combined with the effective cloud height (and the corresponding effective cloud temperature). The clear sky transmittance and radiance are determined using the

methods described in Chapter 3. The effective height (“radiative center”) of the cloud is unknown, so  $\beta$ -ratios are computed using the “top of troposphere” and “opaque” cloud assumptions as described in Ch4. The “top of troposphere”  $\beta$ -ratio,  $\beta_{\text{tot}}(\lambda_1, \lambda_2)$ , is computed by assuming that the cloud radiative center is located at the top of the troposphere. The “opaque cloud”  $\beta$ -ratio,  $\beta_{\text{opaque}}(\lambda_1, \lambda_2)$ , is computed by assuming that the cloud radiative center is located at the highest level of the troposphere that results in  $\epsilon_{\text{eff}}(\lambda_1)$  or  $\epsilon_{\text{eff}}(\lambda_2)$  being equal to 0.98 (using (4.1)). As shown in Ch4,  $\beta_{\text{tot}}(12\mu\text{m}, 11\mu\text{m})$ ,  $\beta_{\text{opaque}}(12\mu\text{m}, 11\mu\text{m})$ ,  $\beta_{\text{tot}}(8.5\mu\text{m}, 11\mu\text{m})$ , and  $\beta_{\text{tot}}(7.3\mu\text{m}, 11\mu\text{m})$  are particularly useful for discriminating volcanic ash and dust from other features. In addition, the 11  $\mu\text{m}$  effective cloud emissivity, computed using the “top of troposphere” assumption [ $\epsilon_{\text{tot}}(11\mu\text{m})$ ], is a good indicator of how much the observed radiance deviates from the estimated clear sky radiance. Such information is important for correctly interpreting multispectral signatures related to cloud composition.

In addition to the infrared-based metrics, useful information on cloud composition can also be gleaned from visible (daytime only) and near-infrared (day and night) observations that are available on nearly every meteorological satellite sensor. When the solar zenith angle is less than  $85^\circ$  and sun glint is not pronounced, the ratio of the 3.9  $\mu\text{m}$  reflectance and the 0.65  $\mu\text{m}$  reflectance [ $\rho(3.9\mu\text{m}, 0.65\mu\text{m}) = \text{ref}[3.9\mu\text{m}]/\text{ref}[0.65\mu\text{m}]$ ] is used in combination with “split-window” (11 and 12  $\mu\text{m}$ ) observations to enhance the spectral contrast between volcanic ash/dust and all other features (see Pavolonis et al. [2006] and Ch4 for a more detailed description). At solar zenith angles greater than  $90^\circ$ , and in the absence of stray light influences (significant sunlight impinging on the sensor when the solar zenith angle exceeds  $90^\circ$ ), the 3.9  $\mu\text{m}$  pseudo-emissivity [ $\epsilon_p(3.9\mu\text{m})$ ] is

used in conjunction with “split-window” measurements to help identify ash and dust clouds. The  $\varepsilon_p(3.9\mu\text{m})$  parameter is simply defined as the ratio of the measured 3.9- $\mu\text{m}$  radiance to the estimated 3.9- $\mu\text{m}$  blackbody radiance [ $\varepsilon_p(3.9\mu\text{m}) = R(3.9\mu\text{m})/R_{\text{bb}}(3.9\mu\text{m})$ ] (see Heidinger et al. [2012] and Ch4 for more information). The spatial standard deviation of the 11  $\mu\text{m}$  brightness temperature [ $\text{BT}_{\text{sdev}}(11\mu\text{m})$ ] and the 0.65  $\mu\text{m}$  reflectance [ $\text{ref}_{\text{sdev}}(0.65\mu\text{m})$ ] are also utilized as metrics in an effort to mitigate cloud edge related measurement errors (e.g., small band to band co-registration errors can have a large impact in regions with sharp spatial gradients). The standard deviations are computed using a 3 x 3 pixel window centered on the pixel of interest.

### **6.3. Review of Ash/Dust Cloud Property Retrieval**

The remaining components of the SECO algorithm also leverage information on retrieved cloud properties and their associated uncertainty. The optimal estimation retrieval algorithm described in Chapter 5 is applied to all satellite pixels that either have an ash/dust probability that exceeds  $1.0 \times 10^{-6}\%$  or an 11 – 12  $\mu\text{m}$  BTD that is less than 0 K. The retrieved mass loading and the uncertainty in the retrieved cloud emissivity, expressed as the ratio of the 1-sigma retrieval uncertainty to the *a priori* uncertainty, are useful for assessing the impact a given pixel will have on the total mass of ash and/or dust computed from a collection of pixels. While the methodology explicitly described in Chapter 5 requires measurements at 11, 12, and 13.3  $\mu\text{m}$ , the retrieval algorithm is flexible and can be applied without the 13.3  $\mu\text{m}$  channel, which is not available on many satellite sensors.

#### ***6.4. Cloud Object Analysis***

The majority of volcanic ash and dust clouds are composed of a small subset of pixels that are spectrally unique (e.g., very unlikely to be associated with any other feature) and a larger subset of pixels that, to varying degrees, are spectrally non-unique (e.g., can sometimes be associated with other features). When very few spectrally unique pixels are present, as is common in well-dispersed ash and dust clouds, it is very difficult to achieve a useful probability of detection without significantly increasing the false alarm rate. One of the aims of the SECO algorithm is to associate spectrally non-unique pixels with the correct feature (ash/dust vs. everything else) through spatial connectivity with spectrally unique pixels. In order to achieve this goal, cloud objects are constructed. In the SECO algorithm, a cloud object is defined as a collection of spatially connected satellite pixels that meet certain criteria. The methodology described in Wielicki and Welch [1986] is used to efficiently construct cloud objects in a single pass through the data. In Wielicki and Welch, a cloud is deemed unique when it has no edge pixels adjacent to another cloud. The cloud object procedure also allows for diagonal spatial connectivity between two pixels and no constraints are placed on the size of cloud objects. The most challenging aspect of the cloud object generation procedure is establishing which pixels are suitable for inclusion into cloud objects. The volcanic ash/dust probability determined using the methods described in Ch4 play a critical role in constructing cloud objects and interpreting cloud object properties.

##### ***6.4.1. Cloud Object Membership***

As shown in Ch4, the volcanic ash/dust probability, while generally quite skillful, does not always provide robust separation from non-ash/dust features. In other words,

there are instances where high probabilities are associated with non-ash/dust features and low probabilities are associated with ash/dust features. The lack of separation is generally caused by a combination of ambiguity in the multi-spectral signature of ash/dust (other surface and atmospheric features sometimes have a very similar spectral signature as volcanic ash and dust) and uncertainty in the clear sky radiative transfer required to construct our advanced spectral metrics. Unidentified measurement errors can also be problematic. Over land, complexities related to surface temperature and emissivity can further increase the overlap of the probability distributions derived from observations inside and outside of the volcanic ash/dust cloud. Thus, determination of cloud object membership using a simple probability threshold is not optimal.

In lieu of a single probability threshold, the probability information is combined with several other variables to determine which pixels can belong to a cloud object. The cloud object selection criteria were developed heuristically using physical reasoning. Given the extremely large size of the data set used to train the Bayesian method, development of objective multivariate selection criteria was impractical. The cloud object membership criteria are based on the following physical reasoning. Larger (more conservative) volcanic ash/dust probability thresholds should be utilized when the observed 11  $\mu\text{m}$  radiance deviates very little from the clear sky value (e.g.,  $\epsilon_{\text{tot}}(11\mu\text{m})$  is small) *and* the observed 11 – 12  $\mu\text{m}$  BTD does not exhibit, at the very least, a semi-robust ash/dust signature *and* the calculated clear sky minus the observed 11 – 12  $\mu\text{m}$  BTD (hereafter referred to as BTD\_Bias) is small *and* the uncertainty in the retrieved cloud emissivity is large (meaning that addition of this pixel to the cloud object will add significant uncertainty to the total mass of volcanic ash or dust in the cloud object).

Local spatial contrast metrics are also used in the cloud object membership decision-making process and extra consideration (the probability threshold is lowered) is given to pixels that exhibit an SO<sub>2</sub> signal (SO<sub>2</sub> and volcanic ash are often, though not always, co-located). All pixels that have an ash/dust probability that exceeds at least one of the thresholds computed using the functions in Appendix E are allowed to be part of a cloud object.

Figure 6.1 helps demonstrate how the cloud object construction process works. A volcanic ash cloud (with SO<sub>2</sub>) from the February 19, 2001 eruption of Mount Cleveland in the Aleutian Islands (Alaska) can be seen in the false color images shown in the top row of Figure 6.1. As in Ch4, the satellite data for this scene are from *Terra* MODIS. The approximate horizontal boundary of the ash cloud, determined through manual analysis of the false color imagery, is overlaid in white. The cloud boundary contour is also referred to as the Region of Interest (ROI), as ROI software is used in the manual analysis process. Interpretation of the false color imagery, including imagery for this particular case, is discussed in detail in P14. The volcanic ash/dust probability computed using the method of Ch4 is shown in Figure 6.1d. As described in Ch4, the naïve Bayesian method for determining the probability is not applied to pixels that clearly lie outside of certain theoretical constraints (when the ash/dust probability is not computed, the corresponding 11 μm image is shown). The end result of sorting eligible pixels into cloud objects is visualized by imaging the median ash/dust probability of the pixels that compose the object. More specifically, the median probability of the object is assigned to each pixel in the object (e.g., the same color associated with a given median object probability is assigned to each pixel in the object) as shown in Figure 6.1e. While many

pixels with a valid probability do not meet the object membership criteria, several cloud objects of various sizes are constructed inside and outside of the ROI. The volcanic ash cloud shown in Figure 6.1 is fairly well dispersed and, as such, is composed entirely of optically thin cloud elements [Chapter 4]. In some regions of the volcanic ash cloud, the optical depth of the cloud for a given set of conditions falls below the quantitative detection limit (the presence of ash in some regions is primarily inferred through spatial deduction), resulting in multiple cloud objects within the ROI. Note, however, that the cloud objects within the ROI generally have a much greater median probability than the objects outside of the ROI. In addition, the pixels selected for cloud object membership need not have a robust traditional “split-window” signal. In fact, many of the pixels retained for further analysis have *positive* 11 – 12  $\mu\text{m}$  BTD (see Figure 6.1c). Retaining pixels with positive 11 – 12  $\mu\text{m}$  BTD is critical because there are several factors that can cause volcanic ash/dust to have positive 11 – 12  $\mu\text{m}$  BTD (e.g., water vapor absorption, underlying or co-located liquid water or ice particles, large particle sizes, mineral composition effects, etc.). The  $\beta$ -ratio parameters used in the naïve Bayesian approach account for many of the factors that cause the “split-window” BTD to be positive.

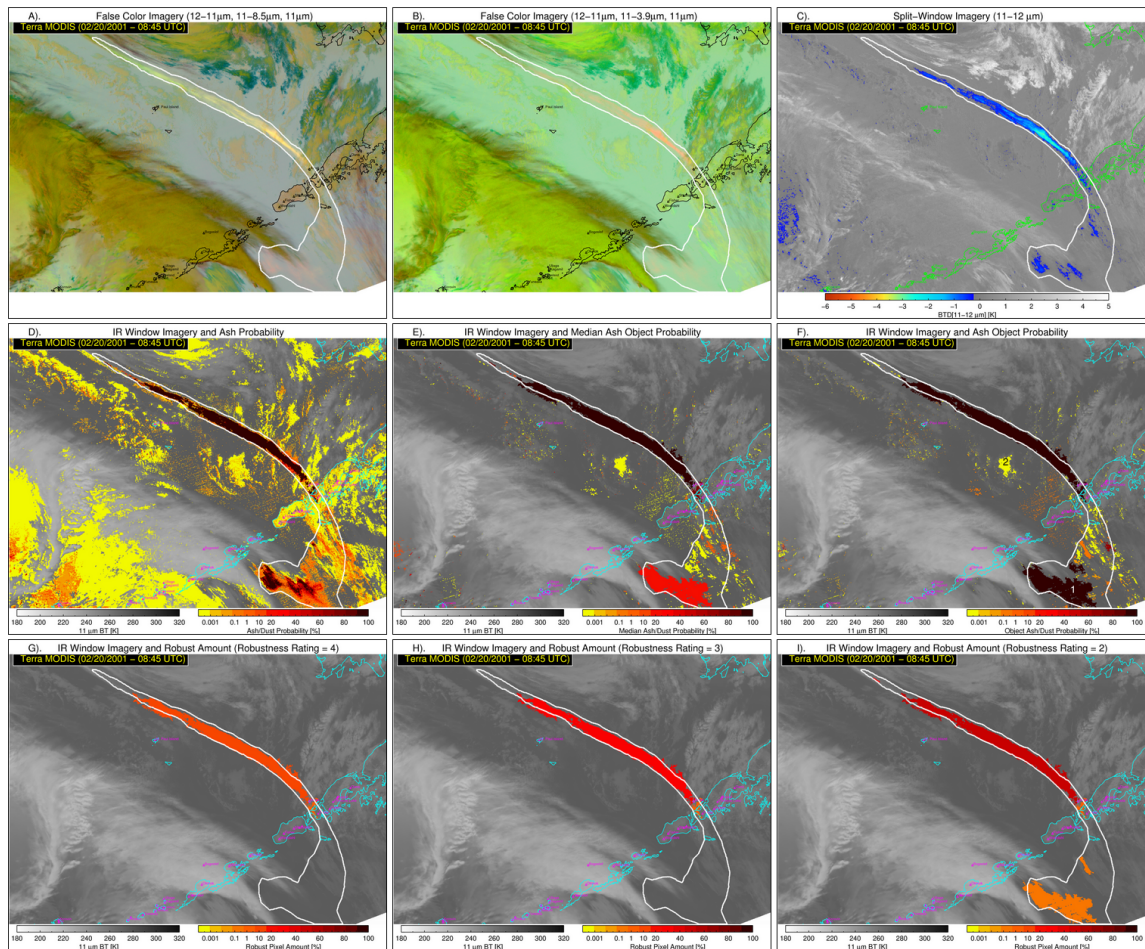


Figure 6.1: Images of the primary metrics utilized to construct cloud objects and apply a binary ash/dust classifier to each cloud object are shown. All parameters were derived from a Terra MODIS image from February 20, 2001 at 08:45 UTC. The approximate visual bounds of a volcanic ash cloud produced by an eruption of Mount Cleveland (Alaska) are overlaid on each image in white. A). 12-11 $\mu\text{m}$ , 11-8.5 $\mu\text{m}$ , and 11 $\mu\text{m}$  false color image. B). 12-11 $\mu\text{m}$ , 11-3.9 $\mu\text{m}$ , and 11 $\mu\text{m}$  false color image. C). Image of BTD(11-12 $\mu\text{m}$ ). D). Ash/dust pixel probability image. E). Median ash/dust probability of pixels that compose each cloud object. F). The probability that the cloud object is part of a volcanic ash/dust cloud. G). The fraction of cloud object pixels that have a spectrally robust ash/dust signature using the most strict definition of spectral robustness. H). The fraction of cloud object pixels that have a spectrally robust ash/dust signature using the second most strict definition of spectral robustness. I). The fraction of cloud object pixels that have a spectrally robust ash/dust signature using the third strictest definition of spectral robustness. In Panels D-I the 11  $\mu\text{m}$  brightness temperature image is shown when the variable of interest is invalid. Two objects of interest are labeled “1” and “2” in Panel F. The 3.9, 7.3, 8.5, 11, and 12  $\mu\text{m}$  channels were used to generate these results.

#### 6.4.2. *Cloud Object Statistics*

Several key cloud object properties are used to determine if a given cloud object, and all of the pixels that compose the object, are part of an actual volcanic ash or dust cloud. More specifically, the cloud object size (in pixel counts), median volcanic ash/dust probability of pixels within the object, cloud object probability, and spectral robustness ratings are utilized by the cloud object selection procedure. The size of the cloud object and the median pixel probability are trivial to calculate and require no further explanation. The remaining two object properties are described in greater detail.

The cloud object probability is defined as, the probability that a given cloud object is, itself, an ash/dust cloud or is part of a larger ash/dust cloud. The cloud object probability addresses the following question. Given a collection of spatially connected satellite pixels, what is the probability that the resulting spatially aggregated multispectral signature is associated with volcanic ash or dust? This differs from the median probability metric that quantifies the extent to which individual pixels in the object have a spectral signature that is associated with volcanic ash or dust. This concept is best explained using an example. Suppose that a large (1000 pixels or greater) cloud object is composed primarily of pixels that have a weak to moderate volcanic ash/dust multispectral signature such that the probability that a given individual pixel contains volcanic ash or dust is, at most, 50%. The resulting median probability for that object would then be less than 50%. The object probability, however, can be much greater than 50% because, while the probability of an individual pixel is not strongly indicative of ash/dust, the occurrence of a spatially coherent aggregate of pixels with a weak to moderate volcanic ash/dust multispectral signature is far less likely to be observed outside of

volcanic ash and dust clouds. This concept is also akin to how humans visually identify very optically thin cirrus clouds in an otherwise blue sky (during the day). If a 1 km spatial grid were applied to the cirrus cloud area, analogous to a region of satellite pixels, and if a person's view were restricted to a given grid cell, it would be very difficult to *confidently* determine if that grid cell contained cirrus or clear sky. Conversely, when the entire collection of grid cells is viewed (analogous to a cloud object), spatial coherence makes the cirrus cloud much easier to identify, despite the fact that the amount of sunlight attenuated within many of the grid cells is too small to produce the contrast required for *confident* visual identification.

#### 6.4.2.1. Bayesian Method

The methodology for computing the cloud object ash/dust probability is as follows. A naïve Bayesian method is used to estimate the probability that a given *cloud object* is an ash or dust cloud. The naïve Bayesian method is formulated by assuming that the features ( $\mathbf{F}$ ) are independent within each class. The general naïve Bayesian approach is motivated and described in Ch4, so only the details required to understand the cloud object implementation are described in this chapter.

Using the naïve Bayes formulation, the probability of ash or dust given an observed set of independent features [ $P(C_{yes}|\mathbf{F})$ ] is calculated using ( 6.2) (the term,  $P(C_{yes}|\mathbf{F})$ , is also commonly referred to as the posterior probability).

$$P(C_{yes} | \mathbf{F}) = \frac{P(C_{yes}) \prod_{i=1}^N P(F_i | C_{yes})}{P(\mathbf{F})} \quad (6.2)$$

In ( 6.2),  $P(C_{yes})$  is the prior probability that a given cloud object is part of an ash or dust cloud without knowledge of  $\mathbf{F}$ ,  $P(F_i|C_{yes})$  is the estimated probability of observing a given feature ( $F_i$ ) when an ash or dust cloud object is present (a total of  $N$  features are used), and  $P(\mathbf{F})$  is the probability of a given set of features being observed and is computed using ( 6.3).

$$P(\mathbf{F}) = P(C_{yes}) \prod_{i=1}^N P(F_i | C_{yes}) + P(C_{no}) \prod_{i=1}^N P(F_i | C_{no}) \quad (6.3)$$

In ( 6.3),  $P(C_{no})$  is the prior probability that a given cloud object is *not* part of a volcanic ash or dust cloud [i.e.,  $P(C_{no}) = 1 - P(C_{yes})$ ] and  $P(F_i|C_{no})$  is the estimated probability of observing a given feature ( $F_i$ ) when an ash or dust cloud object is *not* present. As in Ch4, the prior probability of ash/dust [ $P(C_{yes})$ ] is assumed to be 0.1%. The rationale used in selecting the prior probability is described in Ch4. As with the determination of the pixel level ash/dust probability [Chapter 4], the object based ash/dust conditional probability is often many orders of magnitude greater than the non-ash/dust conditional probability, rendering the impact of the prior probabilities minimal.

#### 6.4.2.2. Cloud Object Classifiers

The class conditional probability density functions (PDFs) are empirically constructed, for each classifier ( $F_i$ ), from the same extensive MODIS-based training data set described in detail in Ch4. The top ten most common spectral states, by areal coverage, within a cloud object, are used as classifiers. There are many different ways to define spectral state (spectral state definition – SSD). Consistent with Ch4, we utilize several different multivariate definitions of spectral state. Each of the SSDs is listed in

Table 6.1 as a function of sensor capabilities and solar illumination. The satellite sensor acronyms are defined in Table 4.2.

The object conditional probability for the “yes” and “no” classes are drawn from a series of empirically derived 2-dimensional PDFs. The first dimension of the conditional probability PDFs corresponds to the spectral state location (SSL), or where in the SSD parameter space that portion of the cloud object resides (the multivariate SSDs shown in Table 6.1 are collapsed into a single vector) and the second dimension corresponds to the size of the geographic area within the object that belongs to a given SSL. The starting location of the area bins in  $\text{km}^2$  is 1.0, 10.0, 50.0, 100.0, 500.0, 1000.0, and 5000.0. A maximum of 7 SSDs can be used if the sensor has the 0.65, 3.9, 7.3, 8.5, 11, and 12  $\mu\text{m}$  channels (0.65  $\mu\text{m}$  is only relevant in sunlit conditions). For each SSD, the top ten SSLs within a cloud object are used as classifiers. Thus, a maximum of 70 classifiers ( $F_i$ ) can be used. If an object has less than 10 SSLs, for a given SSD, then less than 10 SSLs are used (the cloud object area corresponding to a given SSL must be greater than 1  $\text{km}^2$ ). In addition, when the SSL is defined by a  $\varepsilon_{\text{tot}}(11\mu\text{m})$  that is less than 0.03, the conditional probability for the “yes” and “no” classes is set to 1.0 to avoid using pixels that exhibit very little deviation from clear sky conditions at 11  $\mu\text{m}$  in the object selection process.

Table 6.1: The top most portion of the table lists the individual radiative parameters utilized to construct cloud object classifiers, along with the corresponding histogram-binning scheme used to estimate the classifier PDFs. The multivariate classifier variables (using the radiative parameter IDs shown in the top part of the table) are listed in the second part of the table as a function of satellite sensor and the conditions required for utilization. Sun glint is assumed to be present over water surfaces if the glint angle is less than  $40^\circ$ . Stray light is assumed to be present if the solar zenith angle exceeds  $90^\circ$  and the measured  $0.65 \mu\text{m}$  counts is greater than a sensor dependent threshold. Please see Table 4.2 for a list of sensor acronyms.

Parameter [Parameter ID]	Number of Histogram Bins	Starting Boundaries of Histogram Bins
$\epsilon_{\text{tot}}(11\mu\text{m})$ [1]	4	0.00, 0.03, 0.10, 0.30
$\beta_{\text{tot}}(12\mu\text{m}, 11\mu\text{m})$ [2]	7	0.00, 0.70, 0.80, 0.90, 0.95, 0.98, 1.00
$\beta_{\text{opaque}}(12\mu\text{m}, 11\mu\text{m})$ [3]	7	0.00, 0.50, 0.90, 1.00, 1.10, 1.20, 1.30
$\beta_{\text{tot}}(8.5\mu\text{m}, 11\mu\text{m})$ [4]	5	0.00, 0.90, 1.10, 1.30, 1.80
$\beta_{\text{opaque}}(8.5\mu\text{m}, 11\mu\text{m})$ [5]	5	0.00, 0.90, 1.10, 1.30, 1.80
$\beta_{\text{tot}}(7.3\mu\text{m}, 11\mu\text{m})$ [6]	5	0.00, 1.00, 1.50, 2.00, 3.00
$\rho(3.9\mu\text{m}, 0.65\mu\text{m})$ [7]	5	0.00, 0.20, 0.50, 0.80, 1.00
$\epsilon_p(3.9\mu\text{m})$ [8]	5	0.00, 0.90, 1.00, 1.20, 1.40
BTD(11-12 $\mu\text{m}$ ) [9]	7	-20.00, -2.00, -1.00, -0.75, -0.50, -0.25, 0.00 K
$\text{BT}_{\text{sdev}}(11\mu\text{m})$ [10]	11	0.0, 0.25, 0.50, 0.75, 1.0, 2.0, 3.0, 4.0, 5.0, 6.0, 7.0 K
$\text{ref}_{\text{sdev}}(0.65 \mu\text{m})$ [11]	11	0.0, 1.0, 2.0, 3.0, 4.0, 5.0, 6.0, 7.0, 8.0, 9.0, 10.0 %
Indicators of Spectral State	Relevant Sensors	Conditions
[1] x [2] x [7] [1] x [3] x [7] [1] x [9] x [7] [1] x [11]	AVHRR* COMS-MI GOES-Imager# GOES-R ABI Himawari-8/9 AHI MODIS MTSAT Imager MSG SEVIRI MTG FCI VIIRS	Only applied when at least 25% of the cloud object pixels are outside of sun glint and have a solar zenith angle that is less than $85^\circ$ .
[1] x [2] x [8] [1] x [3] x [8] [1] x [9] x [8] [1] x [10]	AVHRR* COMS-MI GOES-Imager# GOES-R ABI Himawari-8/9 AHI MODIS MTSAT Imager MSG SEVIRI MTG FCI VIIRS	Only applied when at least 25% of the cloud object pixels have a solar zenith angle greater than $90^\circ$ while not under the influence of stray light.
[1] x [2] x [4] [1] x [3] x [5]	GOES-R ABI Himawari-8/9 AHI MODIS MSG SEVIRI MTG FCI VIIRS	Applied at all times.
[1] x [2] x [6]	GOES-R ABI Himawari-8/9 AHI MODIS MSG SEVIRI MTG FCI	Applied at all times.
[1] x [2] [1] x [3] [1] x [9] [1] x [10]	AVHRR* COMS-MI GOES-Imager# GOES-R ABI Himawari-8/9 AHI MODIS MTSAT Imager MSG SEVIRI MTG FCI VIIRS	Only applied when less than 25% of the cloud object pixels fail to meet the daytime or nighttime requirements.

\*The analogue to the 3.9- $\mu\text{m}$  band on AVHRR (the 3.75  $\mu\text{m}$  band) is currently not available on the MetOp-A and MetOp-B spacecraft during daytime operations.

#The 12  $\mu\text{m}$  channel is only available on the GOES-8, GOES-9, GOES-10, and GOES-11 spacecraft.

#### 6.4.2.3. Cloud Object Probability Illustration

The cloud object probability is shown in Figure 6.1F. Several cloud objects within the ROI have a very large probability ( $\sim 100\%$ ), while all of the cloud objects outside of the ROI generally have much lower probabilities. The ten most common (by area) SSLs within the cloud object (labeled with a “1” in Figure 6.1F) are shown in Figure 6.2 using six different SSDs. Note that cloud object “1” is located inside the ROI. Each bar in each panel of Figure 6.2 represents a classifier in the cloud object based Bayesian method. The magnitude of each bar depicts the area within the cloud object that falls within a given SSL (the area is shown on the y-axis on the left). The bar color represents the ratio of the ash/dust conditional probability to the non-ash/dust conditional probability, where the cyan to red color range indicates that the ash/dust conditional probability is greater than or equal to the non-ash/dust conditional probability. The specific parameters that define the SSL are also labeled on each bar. The box-and-whisker plot of the pixel ash/dust probability distribution within a given SSL in the cloud object is overlaid in black and referenced to the y-axis on the right of each panel. Figure 6.2 indicates that even SSLs that are generally associated with pixel-level ash/dust probabilities that are less than 50% often have conditional probabilities that favor ash/dust (or vice versa). It is no surprise that the posterior cloud object probability is  $\sim 100\%$ , as the posterior cloud object probability computed using a single SSD (or single panel in Figure 6.2) is also quite large ( $>95\%$  in most cases). This analysis was repeated for the cloud object that resides outside of the ROI in Figure 6.1F and is labeled with a “2” (Figure 6.3). Unlike object “1,” less than ten SSLs were identified in object “2” and the observed features do not favor volcanic ash/dust, regardless of the method used to define

spectral state. The posterior cloud object probability is close to zero, as one might expect for a meteorological cloud feature. The analysis shown in Figure 6.1F, Figure 6.2, and Figure 6.3 indicates that the cloud object implementation of the Bayesian method produces reasonable results and enhances the pixel-level probability information.

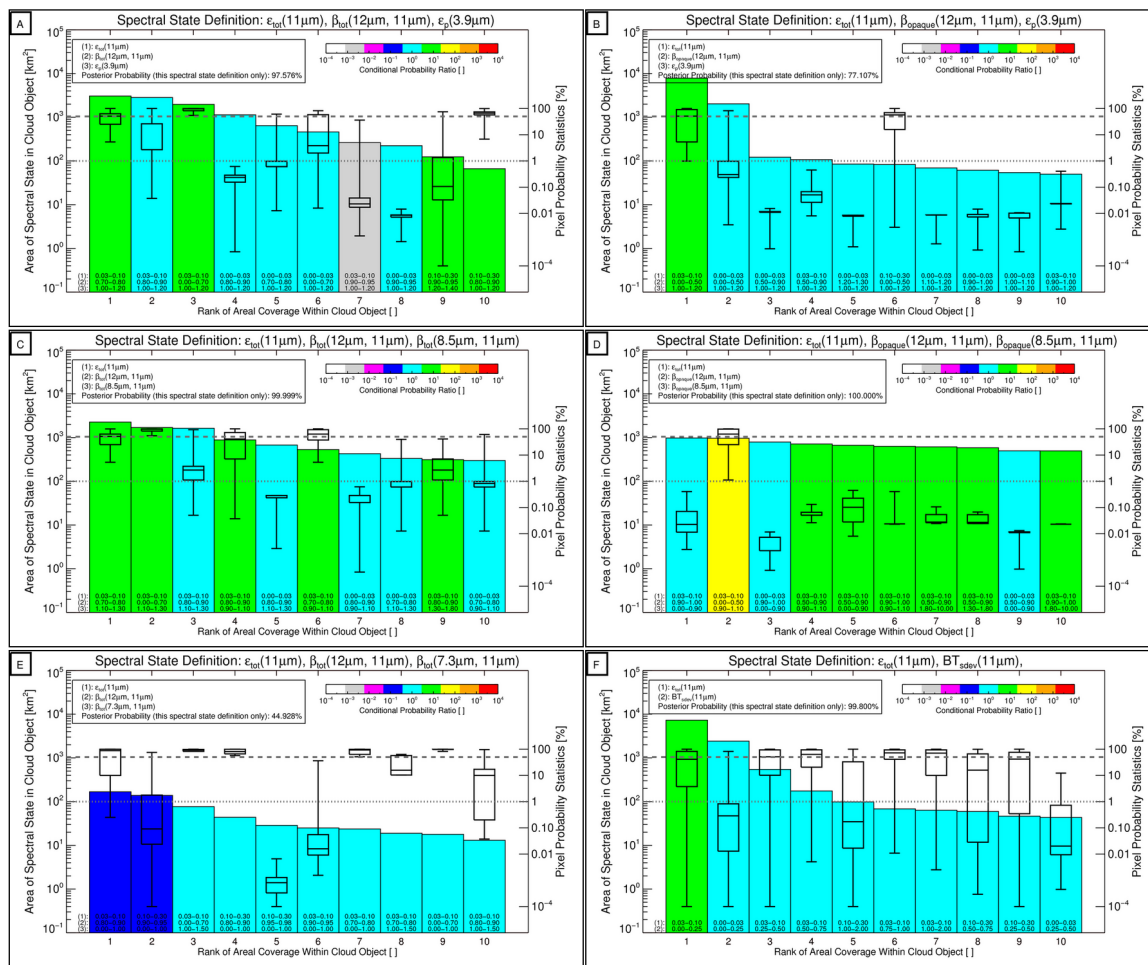


Figure 6.2: The procedure used to determine the probability that a cloud object is part of a volcanic ash or dust cloud is illustrated. Each panel represents a different method for quantifying the spectral states within a cloud object (see panel titles for spectral state definition). The ten most common spectral states (for a given definition) within the cloud object labeled “1” in Figure 6.1F are denoted by the colored bars. The magnitude of the bar is representative of the area within the cloud object that exhibits a given spectral state (the area is shown on the y-axis on the left). The bar color represents the ratio of the ash/dust conditional probability to the non-ash/dust conditional probability, where the cyan to red color range indicates that the ash/dust conditional probability is greater than or equal to the non-ash/dust conditional probability. The specific parameters that define each spectral state are also labeled at the bottom of each bar. Finally, the box-and-whisker plot of the pixel ash/dust probability distribution within a given spectral state in the cloud object is overlaid in black and referenced to the y-axis on the right of each panel. The dotted and dashed horizontal gray lines indicate a pixel probability value of 1% and 50%, respectively.

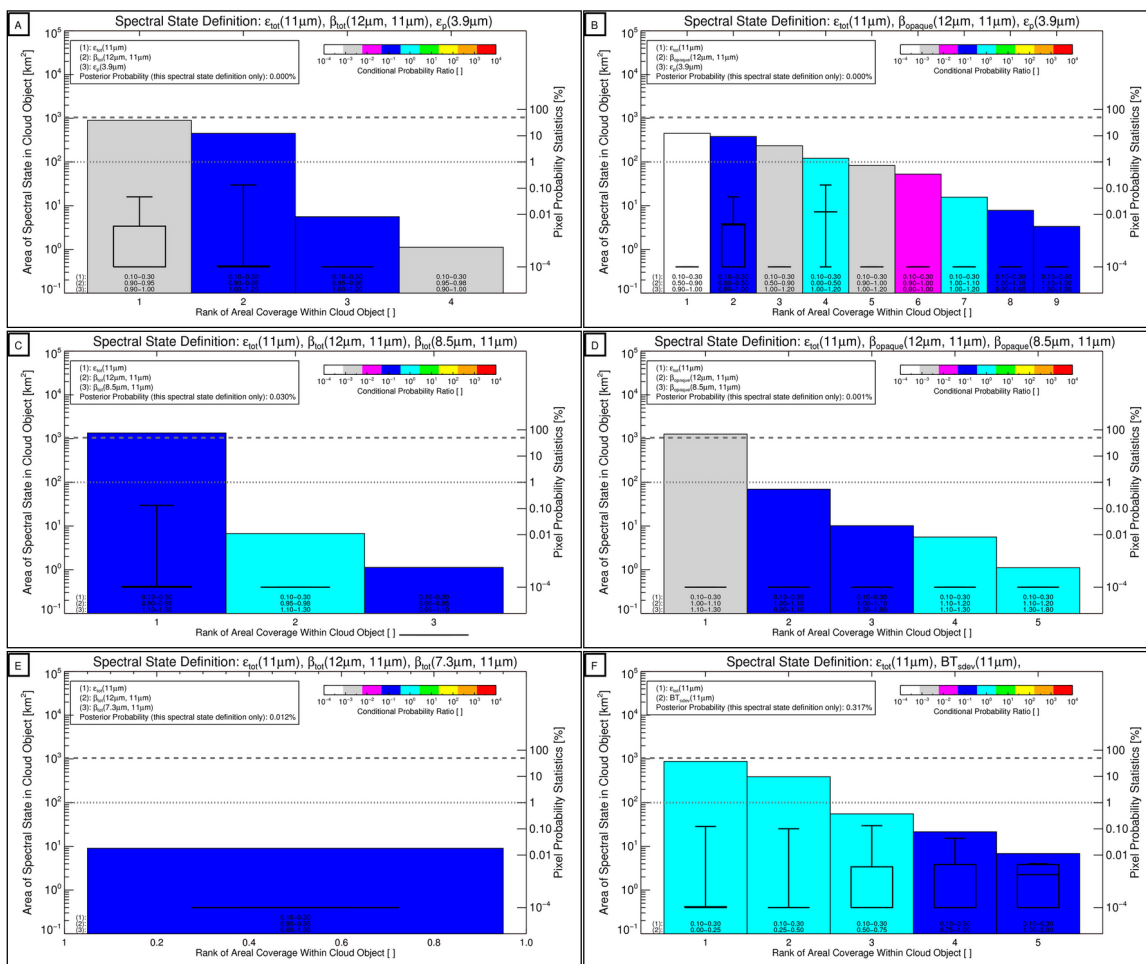


Figure 6.3: Same as Figure 6.2, except for the cloud object labeled with a “2” in Figure 6.1F. Less than 10 spectral states were found in object “2,” regardless of the mechanism for defining spectral state.

#### 6.4.2.4. Spectral Robustness

Another method for quantitatively rating the overall spectral robustness of a given cloud object, with respect to volcanic ash and dust, is to determine how many pixels in the object exhibit a multi-spectral signature that is very rarely observed outside of volcanic ash and dust clouds. Although the pixel level Bayesian model was shown to be quite skillful, a pixel level ash/dust probability close to 100% does not always correspond to volcanic ash or dust, primarily because the naïve Bayesian method cannot perfectly

account for land surface emissivity effects, errors in the computation of clear sky radiances, and measurement artifacts. Thus, seven additional metrics are used along with the pixel level ash/dust probability to rate the spectral robustness of a given pixel. The additional metrics utilized are: the 11  $\mu\text{m}$  clear sky brightness temperature [ $\text{BT}_{\text{clr}}(11\mu\text{m})$ ],  $\epsilon_{\text{tot}}(11\mu\text{m})$ ,  $\text{BT}_{\text{sdev}}(11\mu\text{m})$ ,  $\text{BTD}(11\text{-}12\mu\text{m})$ ,  $\text{BTD}(8.5\text{-}11\mu\text{m})$ ,  $\beta_{\text{tot}}(7.3\mu\text{m}, 11\mu\text{m})$ , and  $\beta_{\text{tot}}(8.5\mu\text{m}, 11\mu\text{m})$ . These metrics were chosen because the values of many different combinations of these variables are rarely observed outside of volcanic ash and dust clouds, including in association with measurement artifacts such as noise and band-to-band co-registration errors and errors in the clear sky radiative transfer. In addition, only a small number of histogram bins are required, for each metric, to keep track of values that are potentially associated with a robust ash/dust spectral signature, making it practical to construct an 8-dimensional histogram. The histogram bins are defined in Table 6.2. The MODIS-based training dataset described in Ch4 was used to construct an 8-dimensional histogram from volcanic ash/dust pixels and separately from all other pixels in the training data set. Even though the training data set is very large the 8-dimensional histogram is likely under-sampled, which is one of the reasons that a naïve Bayesian approach, with lower dimensional classification features, is utilized to assign pixel and object probabilities. The 8-dimensional histograms, however, are only utilized to identify pixels that have a discretized (i.e., individual values are assigned to a histogram bin) 8-element state vector that was observed inside of ash and/or dust clouds in the training data, but otherwise were rarely observed in the training data. Several satellite sensors lack the spectral channels required to compute the  $\text{BTD}(8.5\text{-}11\mu\text{m})$ ,  $\beta_{\text{tot}}(7.3\mu\text{m}, 11\mu\text{m})$ , and  $\beta_{\text{tot}}(8.5\mu\text{m}, 11\mu\text{m})$  parameters (see Table 6.1). When the 7.3

and/or 8.5  $\mu\text{m}$  channels are not available, all observations are assigned to the first histogram bin of the parameter or parameters that cannot be computed.

*Table 6.2: The radiative parameters that define an 8-element state vector, where each element is discretized using the associated histogram-binning scheme, are shown.*

Parameter [Dimension Index]	Number of Histogram Bins	Starting Boundaries of Histogram Bins
$BT_{\text{clr}}(11\mu\text{m})$ [1]	4	160, 250, 270, 290 [K]
$\epsilon_{\text{tot}}(11\mu\text{m})$ [2]	8	0.00, 0.05, 0.08, 0.10, 0.20, 0.40, 0.60, 0.80
$BT_{\text{sdev}}(11\mu\text{m})$ [3]	6	0.00, 0.50, 1.00, 2.00, 5.00, 10.00 [K]
BTD(11-12 $\mu\text{m}$ ) [4]	14	-50.00, -25.00, -2.50, -2.00, -1.50, -1.00, -0.75, -0.50, -0.25, -0.10, 0.0, 0.25, 0.50, 1.00 [K]
BTD(8.5-12 $\mu\text{m}$ ) [5]	11	-50.00, -25.00, -1.50, -1.25, -1.00, -0.75, -0.50, -0.25, 0.00, 0.25, 0.50 [K]
$\beta_{\text{tot}}(7.3\mu\text{m}, 11\mu\text{m})$ [6]	5	0.00, 0.10, 1.50, 1.80, 2.00
$\beta_{\text{tot}}(8.5\mu\text{m}, 11\mu\text{m})$ [7]	8	0.00, 0.10, 0.80, 0.90, 1.00, 1.50, 1.80, 2.00
$P(C_{\text{ves}} F)$ [8]	10	0, 10, 50, 90, 99, 99.9, 99.99, 99.999, 99.9999, 99.99999 [%]

The 8-dimensional histograms are used to derive a spectral robustness rating for each histogram bin that ranges from 0 (not robust) to 4 (very robust). The robustness rating was derived separately for desert surfaces since multi-spectral surface emissivity signatures over desert can closely resemble volcanic ash and dust clouds and errors in the clear sky radiative transfer calculations are generally greatest over desert. For non-desert surfaces, the ash/dust histogram contains about 10 million observations and the non-ash/dust histogram contains 2.3 billion observations. For desert surfaces, the ash/dust histogram contains about 100,000 observations and the non-ash/dust histogram contains 4.7 million observations. The discrepancy in sampling was considered when choosing guidelines that map each histogram bin into a robustness rating. For a given histogram bin, the number of ash/dust observations ( $N_{\text{ash}}$ ), the number of non-ash/dust observations ( $N_{\text{other}}$ ), and the number of non-ash/dust observations normalized by the total number of observations (ash/dust + non-ash/dust) in that bin ( $R_{\text{other}}$ ) are used to assign the robustness

rating (RR). Each bin is assigned the highest robustness rating possible using the following rules.

$$RR = \left\{ \begin{array}{l} 4, \quad N_{ash} > 5 \text{ and } N_{other} = 0 \\ \\ N_{ash} > 0 \text{ and } N_{other} = 0 \text{ or} \\ N_{ash} > 1 \text{ and } N_{other} < 2 \text{ or} \\ 3, \quad N_{ash} > 5 \text{ and } N_{other} < 50 \text{ and } R_{other} < 0.01 \text{ or} \\ N_{ash} > 5 \text{ and } N_{other} < 10 \text{ and } R_{other} < 0.10 \\ \\ N_{ash} > 0 \text{ and } N_{other} < 10 \text{ or} \\ 2, \quad N_{ash} > 5 \text{ and } N_{other} < 100 \text{ and } R_{other} < 0.01 \text{ or} \\ N_{ash} > 5 \text{ and } N_{other} < 50 \text{ and } R_{other} < 0.10 \\ \\ N_{ash} > 0 \text{ and } N_{other} < 100 \text{ or} \\ 1, \quad N_{ash} > 5 \text{ and } N_{other} < 500 \text{ and } R_{other} < 0.50 \\ \\ 0, \quad otherwise \end{array} \right. \quad (6.4)$$

Each pixel in a given cloud object is assigned a robustness rating using the 8-dimensional robustness look-up table generated from the data used to train the Bayesian methods. The total number of pixels in each robustness category can then be computed for each cloud object. Returning to the nighttime Cleveland volcanic ash example, the fraction of each cloud object that achieves robustness rating 2 through 4 is shown in the bottom row of Figure 6.1, with robustness rating decreasing from left to right. The robustness counter is incremented for a given rating (0-4) if a rating at or above that level is achieved. For instance, a robustness rating of 3 results in the object counter for rating values 0-3 being incremented. In Figure 6.1 (Panels G-I) the robustness fraction is only displayed if it is greater than 0%, otherwise the 11  $\mu\text{m}$  brightness temperature is displayed. Only two cloud objects were found to include pixels with a robustness rating of 3 or greater, and both objects were located inside the ROI. Five cloud objects, all

within the ROI, were found to contain pixels with a robustness rating of 2 or greater. Not surprisingly, the two objects with level 3 or greater robust pixels correspond to regions of the ash cloud that are readily apparent in the false color and “split-window” images. The cloud objects that at most contained pixels with a robustness rating of 2 have a much less impressive visual appearance in the multi-spectral imagery. Thus, the robustness rating of all of the objects is qualitatively consistent with how a human expert would rate the strength of the volcanic ash spectral signature at various locations in the cloud. Finally, the robustness rating procedure allows for a greater degree of sensor dependent customization without the need of re-training the Bayesian model. Thus, the SECO method can be effectively applied to new sensors immediately, simply by adjusting the robustness rating look-up table until the false alarm rate is as low as expected.

#### *6.4.2.5. Identifying Potential Clear Sky Objects*

As discussed in Ch4, errors in the clear sky radiative transfer calculations can be large at times, especially over land surfaces. Thus, some “cloud” objects may actually be composed entirely of clear sky pixels when the clear sky radiances are significantly over-estimated. If the spectral variability of the surface emissivity is similar to volcanic ash and dust, the clear sky object can potentially be misclassified as volcanic ash/dust. A spatial analysis technique is used to address this issue. The difference between the clear sky  $11\ \mu\text{m}$  BT and the observed  $11\ \mu\text{m}$  BT, referred to as the clear sky bias or  $\text{BT}_{\text{bias}}$ , is assessed at various locations inside and outside of cloud objects. More specifically, the mean “in object” and “environmental”  $\text{BT}_{\text{bias}}$  is computed for each object. The “in object”  $\text{BT}_{\text{bias}}$  ( $\text{BT}_{\text{bias\_obj}}$ ) is computed from object pixels that have a pixel-level ash/dust probability smaller than 10%. The “environmental”  $\text{BT}_{\text{bias}}$  ( $\text{BT}_{\text{bias\_env}}$ ) is computed from

nearby (e.g. within 12 pixels of the edge of the object of interest) out of object pixels that have an ash/dust probability less than 0.10 and are likely to be free of meteorological cloud. Meteorological cloud cover is assessed using the metrics described in Heidinger et al. [2012]. Each cloud object is assigned a cloud flag (CF) ranging from 0 (confidently clear) to 3 (confidently cloudy) depending on the  $BT_{bias\_obj}$  and the difference between  $BT_{bias\_obj}$  and  $BT_{bias\_env}$  ( $BTD_{bias\_diff}$ ). The binary cloud object classifier utilizes the cloud flag. The guidelines for assigning the cloud flag are provided below.

$$CF = \begin{cases} 3 & BT_{bias\_obj} > 18K \text{ or } BTD_{bias\_diff} > 6K \\ 2 & 4 < BTD_{bias\_diff} \leq 6 \\ 1 & 2 < BTD_{bias\_diff} \leq 4 \\ 0 & BTD_{bias\_diff} \leq 2 \end{cases} \quad (6.5)$$

#### 6.4.3. Binary Classification of Cloud Objects

Using the various cloud object statistics described earlier, a simple binary cloud object classifier was developed. Cloud objects can be classified as volcanic ash/dust or not. If a cloud object is classified as volcanic ash/dust all pixels that compose the cloud object are classified as volcanic ash/dust. The basic binary classifier, also referred to as the cloud object selection procedure, is a function of the cloud object size (in pixels), the median ash/dust pixel probability, the cloud object referenced probability of ash/dust, the cloud confidence flag, and the robustness rating metrics. Many different threshold combinations are utilized based on heuristic analysis of the training data set and subsequent global real-time testing of the SECO algorithm. All of the threshold combinations utilized in the cloud object selection process are listed in Table 6.3. Each

row in the table represents a set of cloud object selection criteria. During the cloud object selection process the “greater than” operator is applied to all criteria except the maximum cloud object size and cloud confidence. The “less than or equal to” operator is applied to the maximum cloud object size and the “greater than or equal to” operator is applied to the cloud confidence flag. If any single set of selection criteria is met, the cloud object is selected.

*Table 6.3: Each row in the table represents a set of cloud object selection criteria. During the cloud object selection process the “greater than” operator is applied to all criteria except “Max Size” and “Cloud Flag.” The “less than or equal to” operator is applied to “Max Size” and the “greater than or equal to” operator is applied to “Cloud Flag.” If any single set of selection criteria is met, the cloud object is selected. The center of the cloud object must be within 50/10/5 km of a volcano in order to use the criteria listed below the V50/V10/V5 headers.*

Min Size (#pix)	Max Size (#pix)	Median Prob %	Object Prob %	Cloud Flag (CF)	RR4 Ct	RR4 Frac	RR3 Ct	RR3 Frac	RR2 Ct	RR2 Frac	RR1 Ct	RR1 Frac
25	∞	0	80	2	4	0.0000	14	0.0000	0	0.0000	0	0.0000
25	∞	80	0	2	4	0.0000	14	0.0000	0	0.0000	0	0.0000
250	∞	0	80	2	0	0.0100	0	0.0000	0	0.0000	0	0.0000
250	∞	80	0	2	0	0.0100	0	0.0000	0	0.0000	0	0.0000
100	∞	0	80	2	0	0.0050	0	0.0100	0	0.0000	0	0.0000
100	∞	80	0	2	0	0.0050	0	0.0100	0	0.0000	0	0.0000
5000	∞	20	99	2	-1	-0.10	-1	-0.10	10	0.0000	3000	0.0000
250	∞	0	80	0	100	0.0000	0	0.0000	0	0.0000	0	0.0000
250	∞	80	0	0	100	0.0000	0	0.0000	0	0.0000	0	0.0000
500	∞	0	80	0	0	0.0000	500	0.0000	0	0.0000	0	0.0000
500	∞	80	0	0	0	0.0000	500	0.0000	0	0.0000	0	0.0000
100	1000	80	80	2	-1	-0.10	0	0.0100	0	0.0133	0	0.0500
250	500	0	80	2	0	0.0000	0	0.0055	0	0.0133	0	0.0500
250	500	80	0	2	0	0.0000	0	0.0055	0	0.0133	0	0.0500
100	250	0	80	2	0	0.0050	0	0.0100	0	0.0000	0	0.0000
100	250	80	0	2	0	0.0050	0	0.0100	0	0.0000	0	0.0000
25	250	0	80	2	0	0.0000	0	0.0000	0	0.0133	0	0.0500
25	250	80	0	2	0	0.0000	0	0.0000	0	0.0133	0	0.0500
15	25	80	80	2	4	0.0000	14	0.0000	0	0.0000	0	0.0000
10	25	80	80	2	0	0.0000	0	0.0000	0	0.0133	0	0.0500
<b>V50</b>												
10	25	80	0	3	-1	-0.10	-1	-0.10	0	0.2500	0	0.5000
10	25	80	80	3	-1	-0.10	-1	-0.10	0	0.1000	0	0.5000
0	10	80	0	3	-1	-0.10	-1	-0.10	0	0.2500	0	0.5000
0	10	80	80	3	-1	-0.10	-1	-0.10	0	0.1000	0	0.5000
<b>V10</b>												
10	25	0	80	3	0	0.0000	0	0.0000	0	0.0133	0	0.0500
10	25	80	0	3	0	0.0000	0	0.0000	0	0.0133	0	0.0500
<b>V5</b>												
0	10	80	0	3	0	0.0000	0	0.0000	0	0.0133	0	0.0500
0	10	0	80	3	0	0.0000	0	0.0000	0	0.0133	0	0.0500

#pix: number of pixels, Prob: ash/dust probability, RR: Robustness rating, Ct: count, Frac: fraction

### 6.5. Case Studies

An initial assessment of the complete SECO volcanic ash/dust detection algorithm is conducted by analyzing four ash/dust cases captured by MODIS. The same four cases shown in Ch4 are utilized. Each of the four cases (2 volcanic ash and 2 dust) is independent of the classifier training data, and the ash/dust probability is assessed within the context of human expert estimated horizontal cloud boundaries and the traditional “split-window” technique for detecting volcanic ash and dust. As in Ch4, results from the SECO algorithm were generated using four different spectral channel combinations that are commonly available on operational and research satellite radiometers.

1. 0.65 [daytime only], 3.9, 7.3, 8.5, 11, 12  $\mu\text{m}$  (SC1, SC=Spectral Combination)
2. 0.65 [daytime only], 3.9, 8.5, 11, 12  $\mu\text{m}$  (SC2)
3. 0.65 [daytime only], 3.9, 11, 12  $\mu\text{m}$  (SC3)
4. 11, 12  $\mu\text{m}$  (SC4)

The results from the manual analysis first presented in Ch4 are once again utilized. As described in Ch4, the goal of the manual analysis of the ash/dust cloud boundaries was to define a ROI that contains the portion of the ash/dust cloud that can be manually identified in multispectral imagery, either directly or through spatial deduction. All conclusions drawn from the comparison to the manually determined ROI are derived from relative relationships. As such, small perturbations to the ROI do not impact the results as long as ash or dust pixels that exhibit a robust spectral signature (i.e., are obvious in the imagery) are not left out of the ROI.

### 6.5.1. Volcanic Ash from Mount Cleveland (nighttime)

SECO algorithm results from each spectral channel combination are shown in Figure 6.4 for the same nighttime Cleveland volcanic ash scene discussed earlier. The binary classifier results are displayed using the pixel level ash/dust probability and the 11  $\mu\text{m}$  brightness temperature imagery. Where the binary classifier indicates volcanic ash or dust is present, the pixel level probability is displayed; otherwise the 11  $\mu\text{m}$  brightness temperature is displayed. As in Ch4, the Critical Success Index (CSI), which is defined as the number of hits divided by the sum of hits, false alarms, and misses, is utilized to quantify the skill of the SECO algorithm relative to the manual analysis. The CSI does not take correct negatives into account, so it is an effective metric when the event of interest is observed far less often than the non-events and the tolerance for false alarms is low (volcanic ash false alarms are particularly undesirable). The “split-window” results were derived using the traditional threshold method. The BT(11-12 $\mu\text{m}$ ) threshold, however, was selected such that it maximized the CSI for each 5-minute MODIS granule. Thus, the *best possible*, case specific, “split-window” results are shown (which will not necessarily be known in real-time). The Probability of Detection (POD) and False Alarm Rate (FAR) are also computed. The MODIS overpass shown in Figure 6.4 occurred about 18.25 hours after the start of the eruption of Mount Cleveland. As a result, the volcanic ash cloud has been advected northeastward of the volcano by the atmospheric winds and the entire ash cloud is highly semi-transparent to infrared radiation due to dispersion and fallout processes. In fact, portions of the southern part of cloud can only be confidently identified in multispectral false color imagery through spatial deduction.

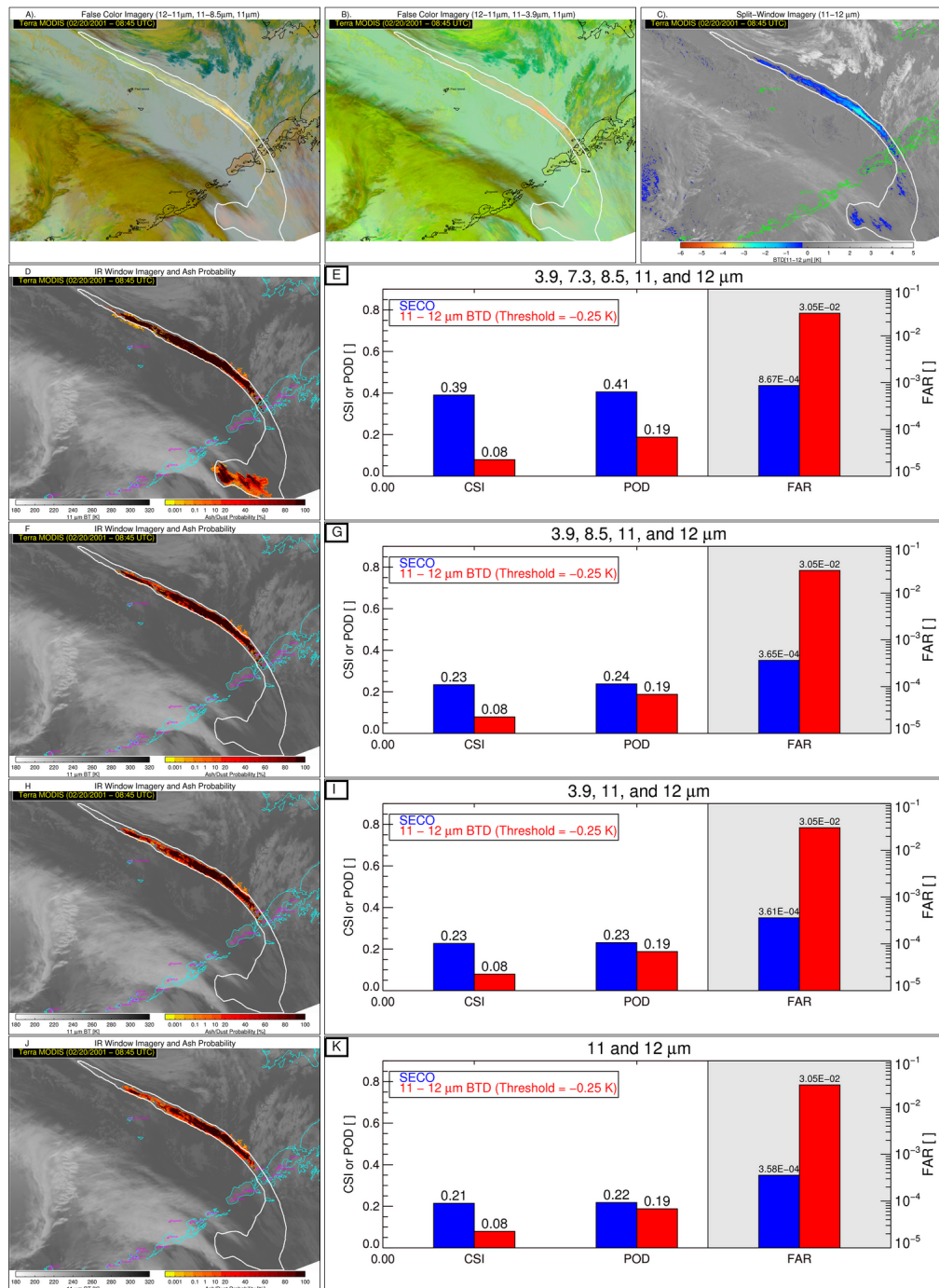


Figure 6.4: The results of the SECO volcanic ash and dust detection algorithm are shown for a Terra MODIS image from February 20, 2001 at 08:45 UTC. A). 12-11 μm, 11-8.5 μm, and 11 μm false color image. B). 12-11 μm, 11-3.9 μm, and 11 μm false color image. C). Image of BTd(11-12μm). D). Ash/dust pixel probability image for 0.65, 3.9, 7.3, 8.5, 11, 12 μm channel combination. E). The SECO algorithm skill (blue bars) measured against manual analysis of multi-spectral imagery is expressed as the Critical Success Index (CSI), Probability of Detection (POD), and False Alarm Rate (FAR). The skill of the traditional “split-window” method using the BTd(11-12μm) threshold that produces the greatest CSI for this particular scene is also shown (red bars). The panels in the third through fifth rows are analogous to the second row, except for the 3.9, 8.5, 11, 12 μm, 3.9, 11, 12 μm, and 11, 12 μm channel combinations, respectively. The outer bounds of the manually defined ash/dust cloud are overlaid on each geo-referenced image.

Figure 6.4 shows that the SECO algorithm is much more skilled than the “split-window” approach, that was intentionally optimized for this particular scene, regardless of the spectral channel combination. In this scene the CSI of the SECO algorithm is 0.39, 0.23, 0.23, and 0.21 for the SC1, SC2, SC3, and SC4 implementations, respectively. The “split-window” approach only achieves a CSI of 0.08; making the CSI of the SC1 implementation of the SECO algorithm almost five times greater than the “split-window” approach. Even when the SECO algorithm utilizes the exact same spectral channels as the “split-window” approach (the SC4 implementation), the skill of the SECO algorithm is much greater, which underscores the value of using  $\beta$ -ratios in lieu of BTD’s and cloud objects in lieu of individual pixels. Unlike the “split-window” approach, all SECO algorithm ash/dust detections occur within the ROI or just barely outside of the ROI (this is true for the entire 5-minute MODIS granule) and the 11 – 12  $\mu\text{m}$  BTD need not be negative in order to detect volcanic ash. The POD of the SECO method is greater than the “split-window” method, regardless of the channel combination utilized. Further, the FAR of the SECO method is nearly two orders of magnitude less than the “split-window” technique and the proximity of the SECO “false alarms” to the edge of the manually analyzed cloud casts some doubt as to their true nature.

As expected, the skill of the SECO approach decreases when spectral channels are removed. In fact, the portion of the ash cloud south of Alaska’s Aleutian Islands is only partially detected using the SC1 implementation. Only the SC1 implementation results in the object labeled “1” in Figure 6.1F having a sufficient number of spectrally robust pixels to be selected. However, as Figure 6.5 shows, even the two-channel SC4 implementation results in many cloud objects within the ROI. While many of those

objects lack the properties required for selection by the basic cloud object selection procedure, the mere presence of those objects within the ROI means that the prospect of improving the POD of the SECO algorithm through improvements in the cloud object selection procedure is good. For instance, future versions of the SECO cloud object selection procedure will include the ability to utilize the results from previous images, regardless of sensor.

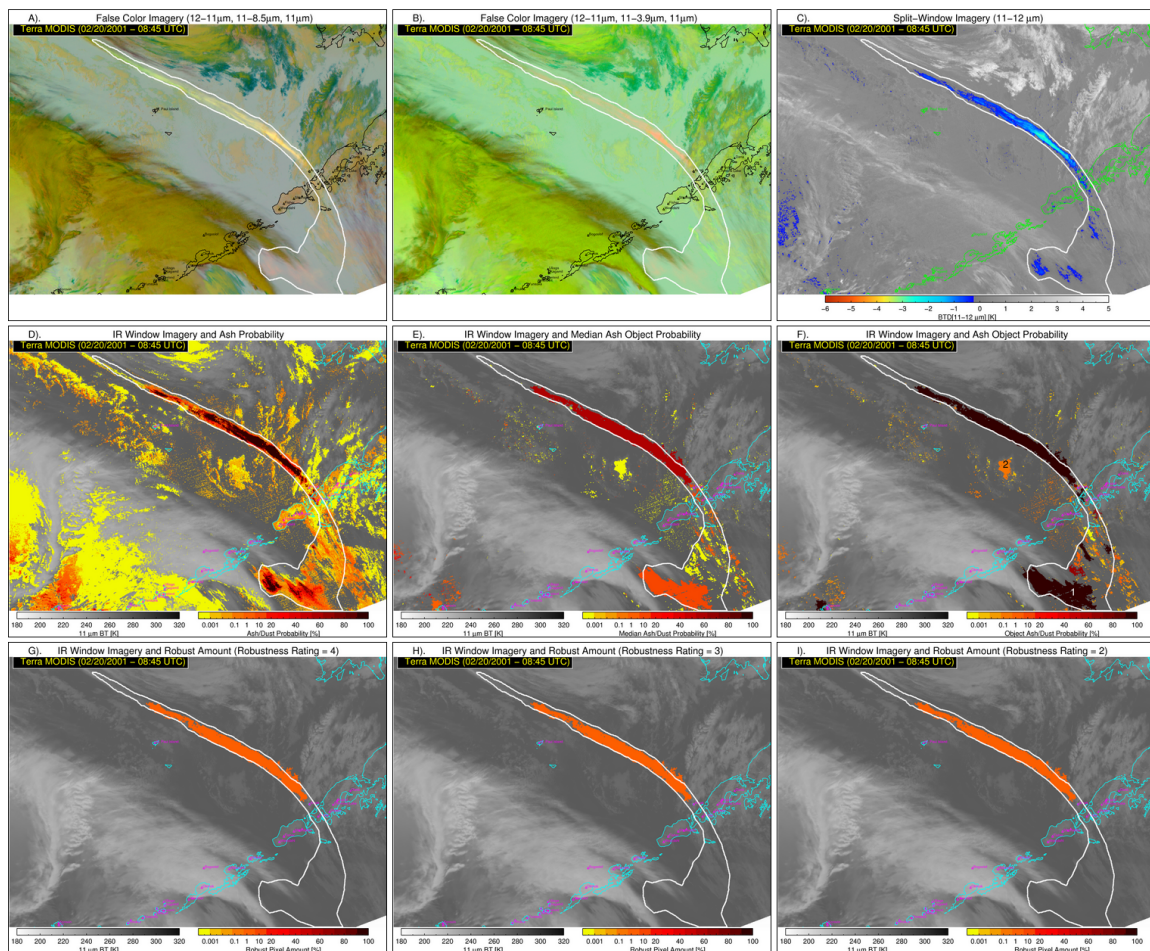


Figure 6.5: Same as Figure 6.1, except only the 11 and 12  $\mu$ m channels were used to generate these results.

### 6.5.2. Volcanic Ash from Mount Cleveland (daytime)

As in Ch4, the *Terra* MODIS overpass of the Cleveland ash cloud that occurred about 9.5 hours prior to the nighttime Cleveland example was also analyzed. The exact starting date and time of the *Terra* MODIS granule is February 19, 2001 at 23:10 UTC and the overpass occurred under sunlit conditions and at a time when the Cleveland plume was less dispersed. SECO algorithm results from each spectral channel combination are shown in Figure 6.6. As in the previous example, the SECO algorithm is much more skilled than the “split-window” approach, regardless of the spectral channel combination. In this scene the CSI of the SECO algorithm is 0.63, 0.61, 0.59, and 0.58 for the SC1, SC2, SC3, and SC4 implementations, respectively. The “split-window” approach achieves a CSI of 0.13; making the CSI of the SC1 implementation of the SECO algorithm more than five times greater than the “split-window” approach. Even when the SECO algorithm utilizes the exact same spectral channels as the “split-window” approach (the SC4 implementation), the skill of the SECO algorithm is much greater, which again underscores the value of using  $\beta$ -ratios in lieu of BTDs and cloud objects in lieu of individual pixels. All SECO “false alarms” once again reside along the edge of the manually analyzed ROI, while the “split-window” false alarms are located well outside of the ROI. The CSI of the SECO approach does decrease when less spectral channels are used, but not by a substantial amount.

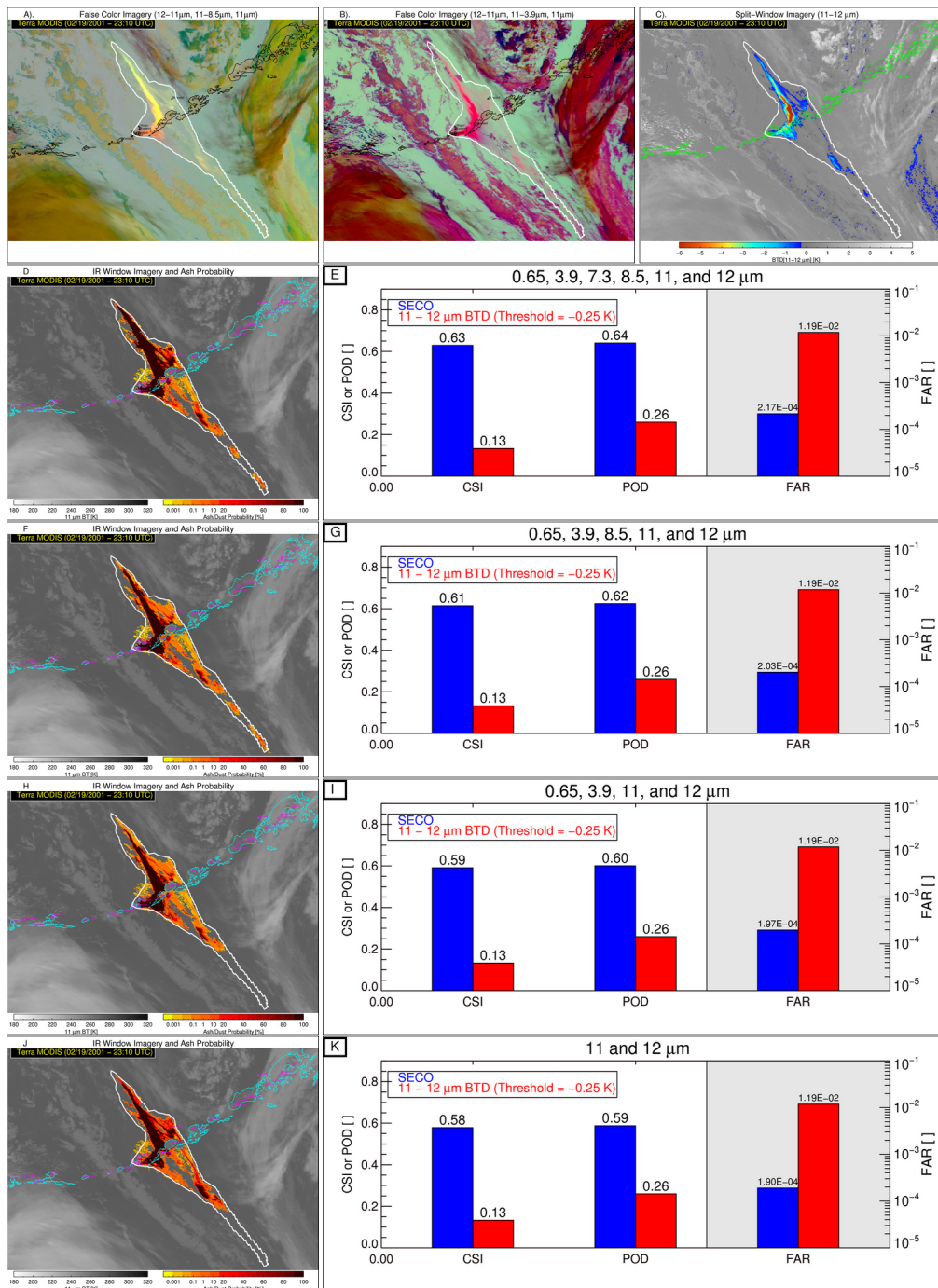


Figure 6.6: Same as Figure 6.4, except the results are shown for a sunlit (the 0.65  $\mu\text{m}$  channel is used) Terra MODIS image from February 19, 2001 at 23:10.

### 6.5.3. South American Dust (daytime)

When the complete SECO algorithm is applied to the South American suspended lake sediment case from Ch4, the SECO algorithm significantly improves upon the “split-window” technique, except when the SC4 implementation is used (Figure 6.7). The SC4 channel combination results in no pixels being classified as dust, which illustrates the value of using additional spectral channels, especially over complicated land surfaces. There is essentially no difference between the SC1 and SC2 results, with both channel combinations having a CSI of 0.54. The FAR of the SC1 and SC2 results ( $2.03 \times 10^{-3}$ ), however, is larger compared to the Cleveland ash results because the western edge of the dust cloud is over-estimated relative to the manual analysis. Errors in the clear sky radiance calculations combined with surface emissivity effects lead to the western-most cloud object being partially composed of pixels that are outside of the identifiable bounds of the dust cloud. No other false alarms were found and the SC1 and SC2 FAR is still an order of magnitude smaller than the “split-window” FAR. The SC3 implementation has a CSI of 0.50 with very few false alarms, all of which are located right along the boundary of the manually analyzed cloud. This case shows that the SECO method is effective over complicated land surfaces during sunlit conditions.

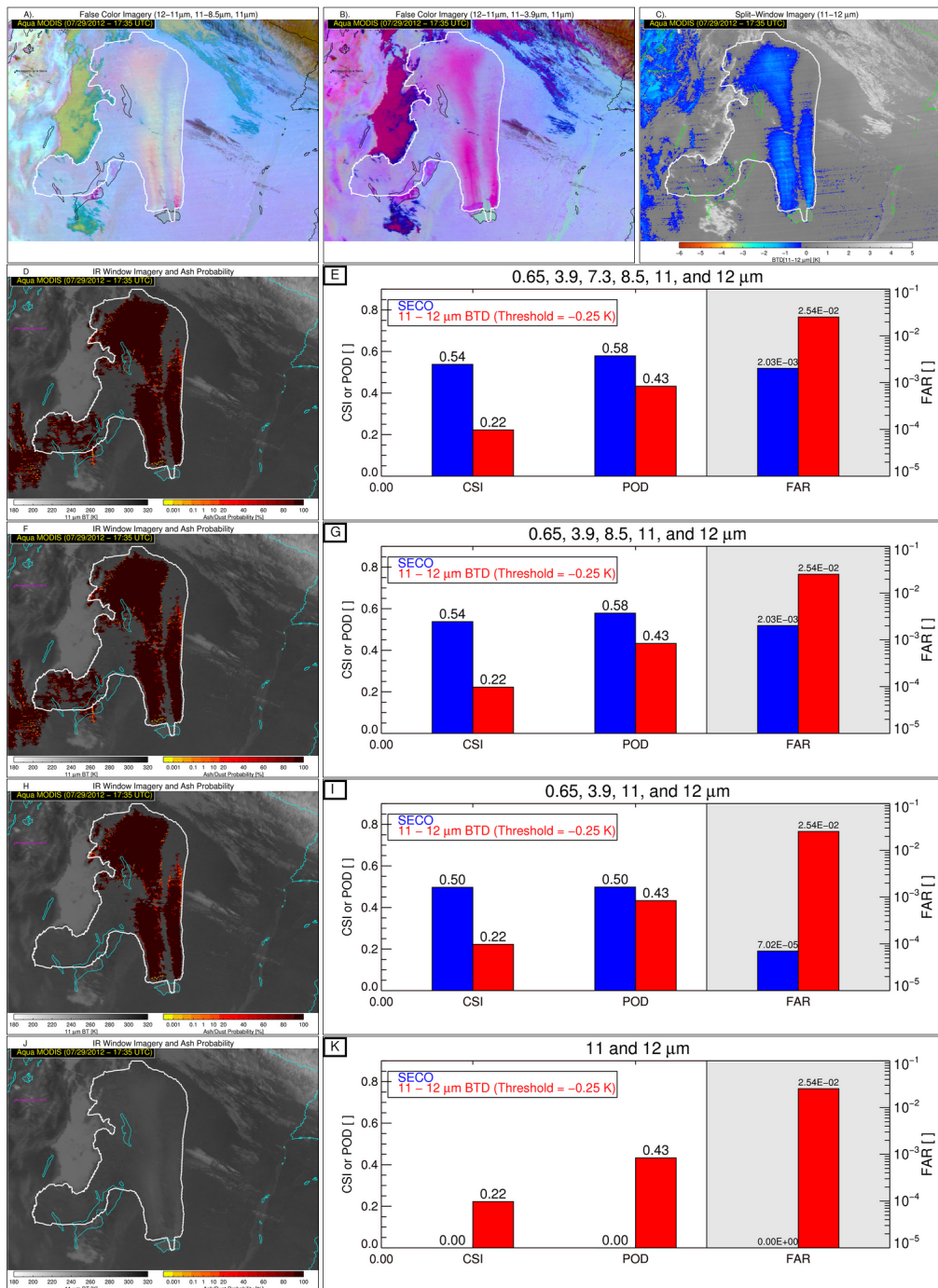


Figure 6.7: Same as Figure 6.4, except the results are shown for a sunlit (the 0.65 μm channel is used) Aqua MODIS image from July 29, 2012 at 17:35.

#### *6.5.4. South American Dust (nighttime)*

In Ch4, a nocturnal South American dust cloud, generated by an outflow boundary, was analyzed. This same case is revisited using the complete SECO algorithm (Figure 6.8). The dust cloud in this scene has 11  $\mu\text{m}$  BT values that deviate only slightly from the clear sky values; therefore this case is very challenging. As a result, only the SC1 and SC2 implementations of the SECO algorithm are able to detect any dust. The CSI of the SC1 implementation is more than three times greater than the “split-window,” primarily due to the very low FAR of the SC1 implementation compared to the “split-window” technique. The SC2 implementation is only a slight improvement to the “split-window” approach, but the much higher POD of the “split-window” comes with a FAR that is three orders of magnitude greater than the SC2 FAR. Despite the severe detection deficiency of the SC3 and SC4 implementations, neither implementation produces any false alarms. Improvements to the cloud object selection procedure may lead to improved detection capabilities for all channel combinations.

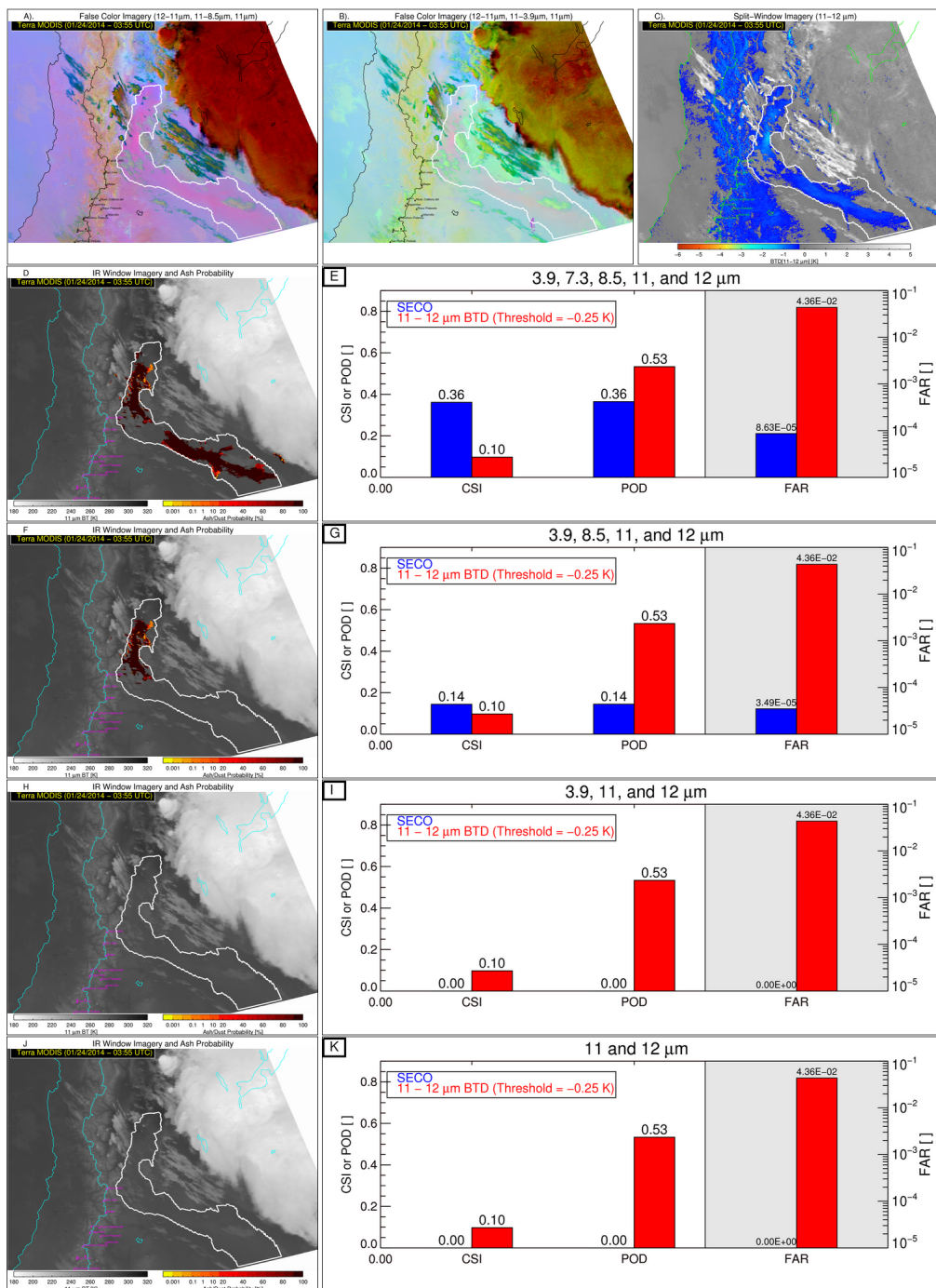


Figure 6.8: Same as Figure 6.4, except the results are shown for a Terra MODIS image from January 24, 2014 at 03:55.

## 6.6. Global Analysis

The skill score of the SECO method, with the full complement of spectral channels (the SC1 implementation), was assessed using a full day of *Aqua* MODIS data from January 26, 2011. All data from this day are independent of the training data set. On January 26, 2011 four volcanoes produced ash clouds that were identifiable in MODIS false color imagery. Kizimen and Karymsky volcanoes on the Kamchatka Peninsula of Russia and Sakurajima (Japan) produced small ash plumes that were identifiable in MODIS multispectral imagery. The existence of these plumes in MODIS false color imagery is consistent with the volcanic activity reported by the Smithsonian Global Volcanism Program ([http://www.volcano.si.edu/reports\\_weekly.cfm#vn\\_300130](http://www.volcano.si.edu/reports_weekly.cfm#vn_300130)). In addition, more significant ash emissions were produced by the eruption of Shinmoe-dake, a stratovolcano of the Kirishima volcano group in Japan [Miyabuchi et al. 2013]. Mainly optically thin regions of African (Saharan) and Asian dust were also present in MODIS false color (and true color) imagery at times, but the horizontal bounds of the dust over the desert surface are difficult to determine, therefore the 16 5-minute MODIS granules (out of a total of 288) that possibly contained regions of dust were excluded from the skill score analysis. Thus, only the Kizimen, Karymsky, Sakurajima, and Shinmoe-dake ash clouds were manually analyzed.

The global ash detection results are visualized for both orbital nodes (ascending and descending) of *Aqua* MODIS. The ascending node (Figure 6.9) consists primarily of sunlit observations (except at high latitudes in the Northern Hemisphere) and the descending node consists of nighttime observations (except at high latitudes in the Southern Hemisphere). In the ascending node, the SECO algorithm detects dust clouds

over the Sahara and Asia. The presence of dust in these regions is confirmed in the false color imagery (especially when viewed at full resolution). No other regions of ash or dust are detected (no false alarms). However, the SECO algorithm does miss some areas of low optical depth dust over Africa and Asia because the cloud objects associated with these low optical clouds did not exhibit the necessary spectral attributes to be chosen by the cloud object selection procedure. The SECO algorithm also misses weak ash plumes from Kizimen and Karymsky (Figure 6.10) for the same reason the low optical depth dust clouds are missed. The 11  $\mu\text{m}$  brightness temperatures in the over-land portion of the Kizimen and Karymsky plumes are very similar to the calculated clear sky 11  $\mu\text{m}$  brightness temperature. Thus, the cloud objects, denoted by the median cloud object probability, within the ROI in Figure 6.10D are not selected. No other volcanic ash clouds are present in the ascending node multispectral imagery. In the future, the detection of low optical depth ash/dust clouds or ash/dust clouds that exhibit very little thermal contrast with the estimated clear sky brightness temperatures can potentially be improved through incorporation of information from multispectral satellite data collected at previous times.

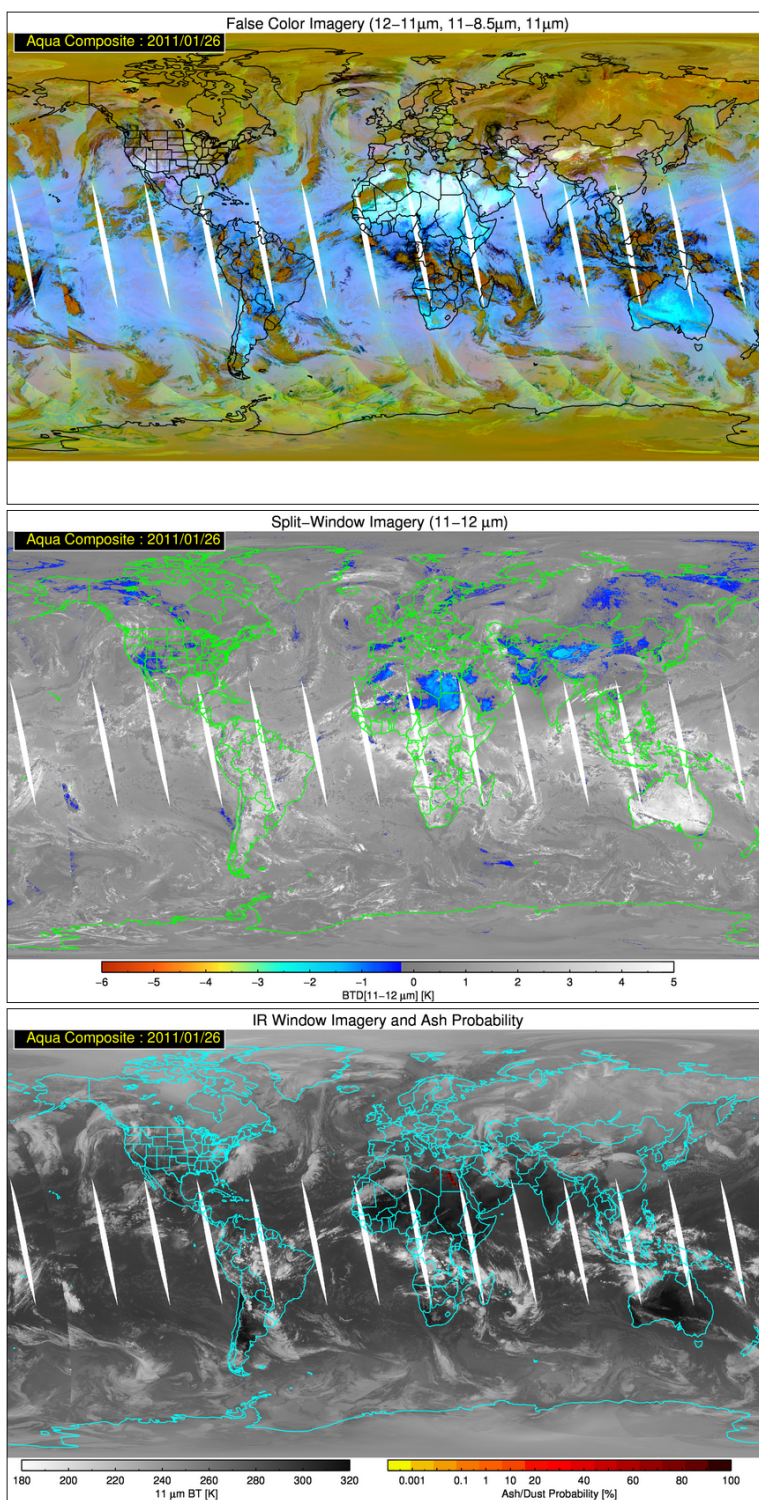


Figure 6.9: False color imagery constructed from the 12-11, 11-8.5, 11 $\mu$ m channel combination (top), 11-12 $\mu$ m “split-window” imagery (middle), and the results of the SECO ash/dust detection algorithm using the 0.65, 3.9, 7.3, 8.5, 11, and 12  $\mu$ m channel combination are shown for all Aqua MODIS ascending (afternoon) node overpasses on January 26, 2011. The SECO results are displayed by overlaying the pixel-level probability of ash/dust over the 11  $\mu$ m brightness temperature image in locations where the SECO algorithm detected ash or dust.

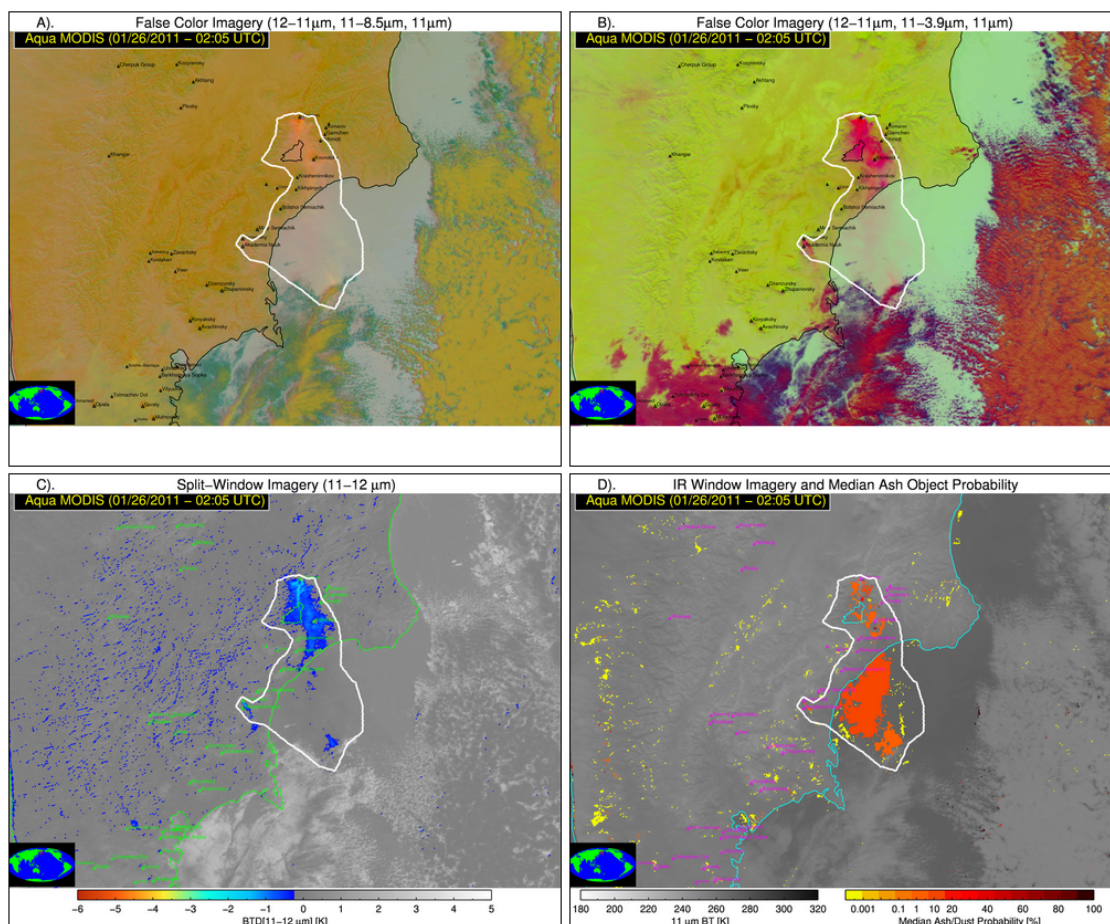


Figure 6.10: Volcanic ash plumes produced by eruptions of Kizimen and Karymsky on the Kamchatka Peninsula (Russia), which were captured by Aqua MODIS on January 26, 2011 (02:05 UTC), are examined in greater detail. A). The 12-11, 11-8.5, 11µm false color image. B). The 12-11, 11-3.9, 11µm false color image. C). The 11-12µm “split-window” brightness temperature difference. D). The median cloud object probability from the 0.65, 3.9, 7.3, 8.5, 11, and 12 µm implementation of the SECO algorithm overlaid on the corresponding 11 µm brightness image.

In the descending node (Figure 6.11), the SECO algorithm detects ash clouds associated with the eruptions of Sakurajima (very minor ash emission) and Shinmoe-dake (more significant ash emission) in Japan. No other regions of volcanic ash or dust are detected. Volcanic ash clouds from the Japanese volcanoes are examined in greater detail (Figure 6.12). While the areal extent of the volcanic ash detected by the SECO algorithm is much smaller than the manually defined ROI (Figure 6.12D), the SECO algorithm does

correctly detect ash in regions that do not exhibit a robust “split-window” signature (Figure 6.12C). Portions of the ash cloud that overlap low meteorological clouds are missed, as are optically thick (and perhaps ice topped) portions near Shinmoe-dake. The Sakurajima ash plume, which is detected by the SECO algorithm is only composed of about 200 pixels and is barely noticeable in the far western part of the images in Figure 6.12. Note that the SECO algorithm does not detect any volcanic ash outside of the ROI. An ash plume from Kizimen is also noticeable in multi-spectral imagery, albeit barely (Figure 6.13). The SECO algorithm does not detect the Kizimen ash plume, as it simply exhibits very little contrast with the surrounding environment, especially over land. The ROI does, however, contain a few cloud objects (Figure 6.13D), so this very weak plume can potentially be detected using a more sophisticated cloud object selection procedure.

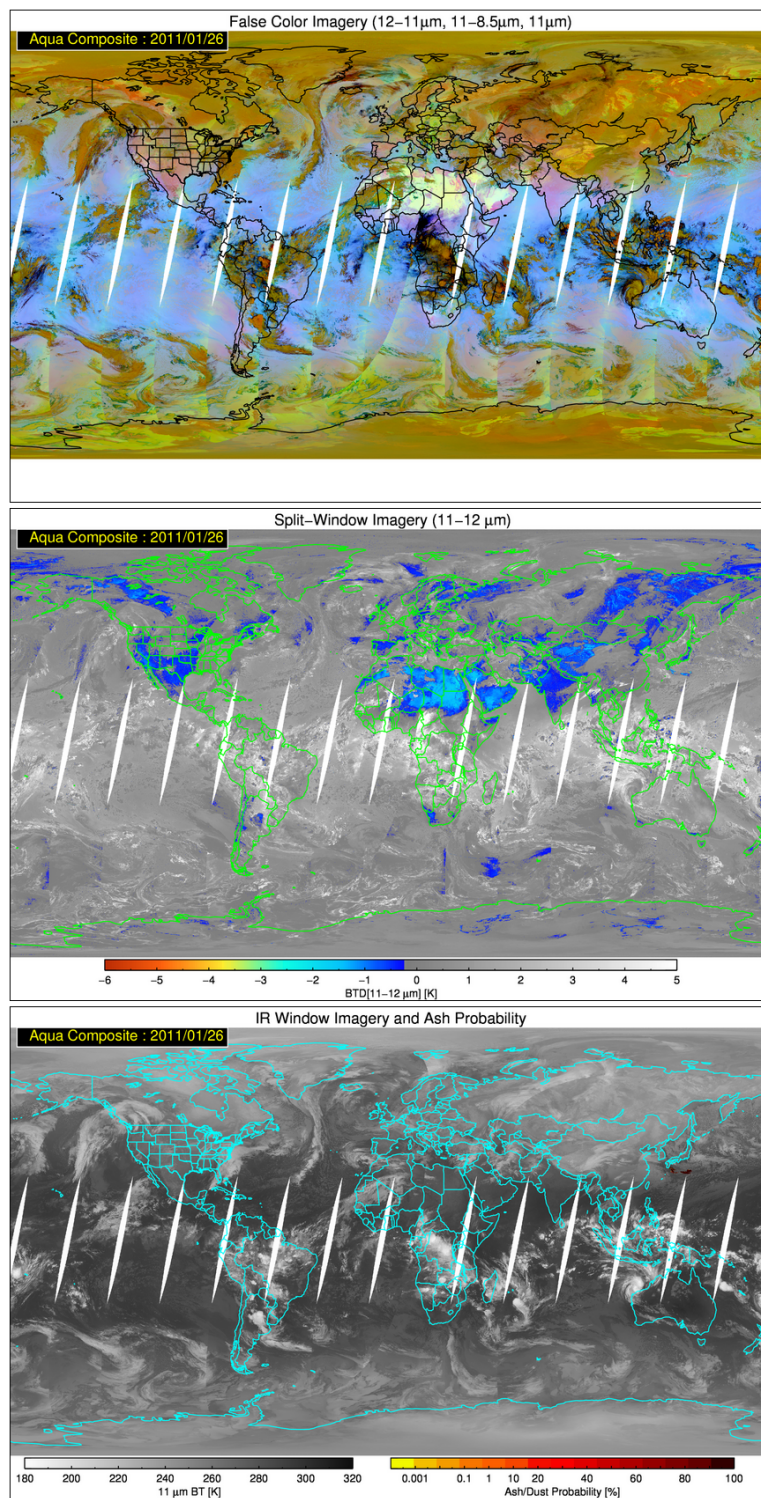


Figure 6.11: Same as Figure 6.9 except for all descending (overnight) Aqua MODIS overpasses on January 26, 2011.

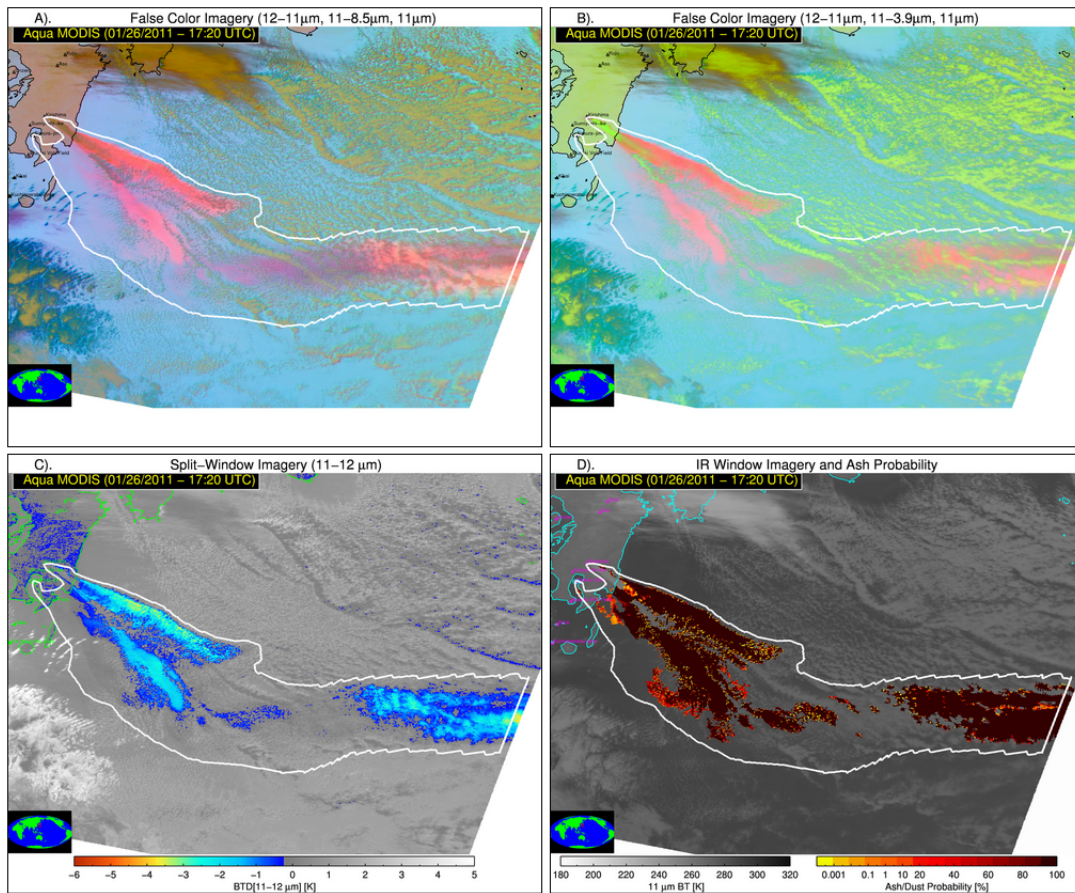


Figure 6.12: Volcanic ash produced by a minor emission from Sakurajima and a more significant emission from Shinmoe-dake in Japan, which was captured by Aqua MODIS on January 26, 2011 (17:20 UTC), are examined in greater detail. A). The 12-11, 11-8.5, 11 $\mu\text{m}$  false color image. B). The 12-11, 11-3.9, 11 $\mu\text{m}$  false color image. C). The 11-12 $\mu\text{m}$  “split-window” brightness temperature difference. D). Volcanic ash detected by the 3.9, 7.3, 8.5, 11, and 12  $\mu\text{m}$  implementation of the SECO algorithm is denoted by valid values of pixel-level ash/dust probability in lieu of the 11  $\mu\text{m}$  brightness temperature value.

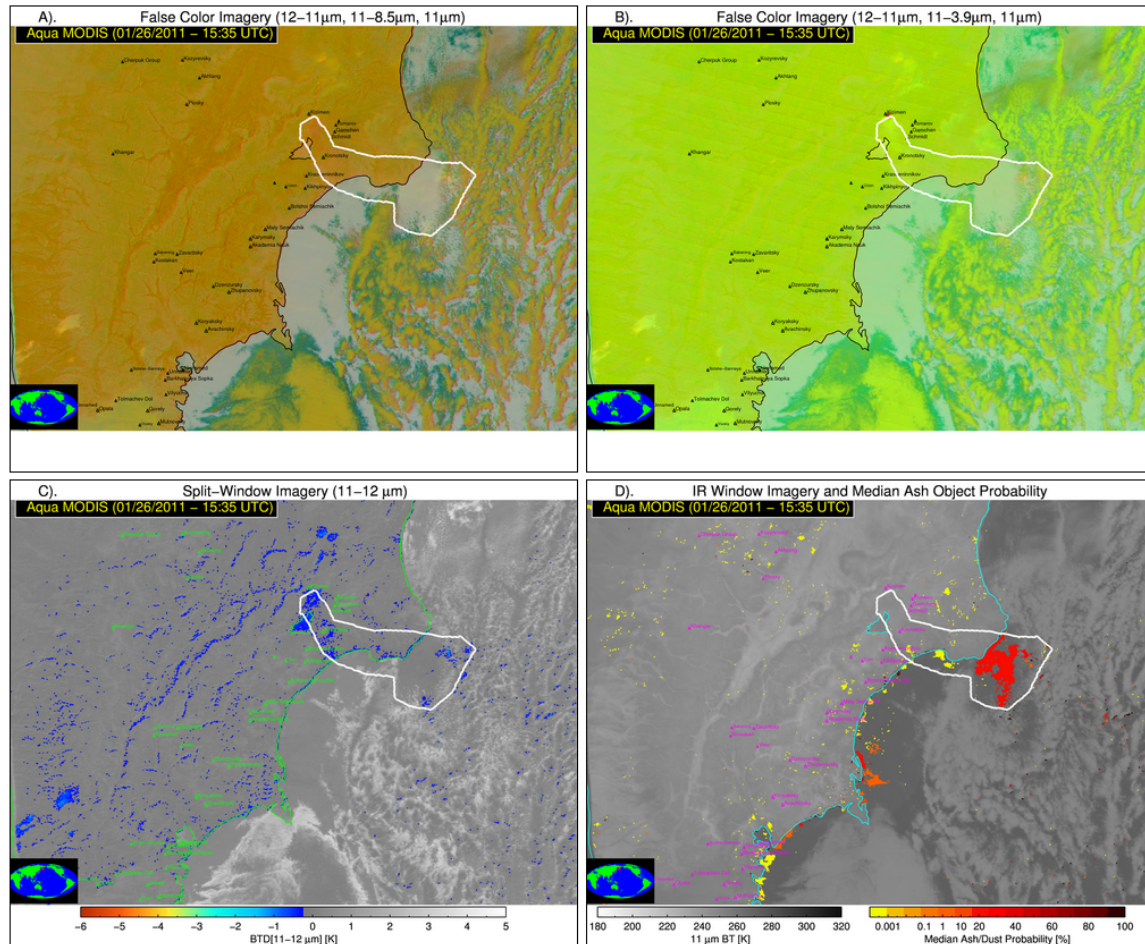
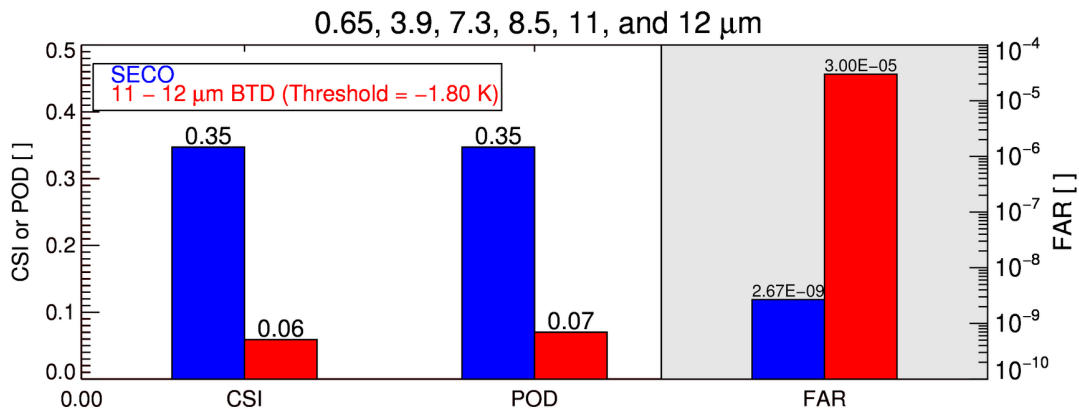


Figure 6.13: Same as Figure 6.10, except for the January 26, 2011 15:35 UTC Aqua MODIS overpass.

Excluding the 16 MODIS granules that contained diffuse dust clouds with ill-defined edges, the skill score of the SC4 implementation of the SECO algorithm and the “split-window” approach were determined using the global January 26, 2011 Aqua MODIS dataset. The results are shown in Figure 6.14. The SECO approach (0.35) has a CSI that is more than five times greater than the “split-window” technique. The “split-window” ash/dust detection threshold was set at -1.80 K because that threshold resulted in the greatest CSI in this global analysis. The threshold of -1.80 K is exceptionally conservative; yet more than 20,000 false alarms are associated with the FAR of  $3.0 \times 10^{-5}$ .

The SECO method only produced a total of 2 false alarm pixels, both of which were located near the edge of the Japanese ash ROI. A total of about 736,982,000 pixels were included in this analysis. While the SECO POD (0.35) greatly exceeds the “split-window” POD (0.07), the SECO POD is rather low. The low PODs can be attributed the superior ability of the human expert to identify specific objects in images. Many of the additional regions of volcanic ash or dust identified by the human expert are extremely tenuous or are identified through spatial deduction. In addition, the small buffer applied when manually drawing the cloud edges has a significant effect on the POD, especially for large clouds. The main goal of the skill score analysis was to quantitatively demonstrate that the SECO algorithm has a very low false alarm rate and significantly improves upon the traditional “split-window” approach. Both of those goals have been achieved.



*Figure 6.14: SECO and “split-window” algorithm performance statistics (CSI, POD, FAR) measured against manual analysis of multi-spectral imagery for an entire day of Aqua MODIS overpasses on January 26, 2011. Only MODIS granules that likely contain diffuse dust clouds with ill-defined edges are excluded. The SECO results, using the 0.65, 3.8, 7.3, 8.5, 11, and 12  $\mu\text{m}$  channel combination, are shown in blue and the “split-window” results obtained using the BTD(11-12 $\mu\text{m}$ ) threshold that produced the greatest CSI for this particular day of data are shown in red.*

### **6.7. Summary**

The SECO algorithm combines radiative transfer theory, Bayesian methods, and image processing/computer vision concepts to identify volcanic ash and dust clouds in multispectral satellite data with skill that is generally comparable to a human expert, especially with respect to false alarm rate. The volcanic ash/dust probability determined using the naïve Bayesian approach described in Ch4, in combination with results from a cloud property retrieval algorithm [Chapter 5], is used to identify satellite pixels that might contain volcanic ash and/or dust. All pixels that potentially contain ash or dust are sorted into cloud objects. A cloud object is a collection of spatially connected satellite pixels that meet a specified set of criteria. An ash/no ash (or dust/no dust) classification is then assigned on a cloud object basis. The majority of volcanic ash and dust clouds are composed of a small subset of pixels that are spectrally unique (e.g., very unlikely to be associated with any other feature) and a larger subset of pixels that, to varying degrees, are spectrally non-unique (e.g., can sometimes be associated with other features). In essence, a cloud object is assigned to the volcanic ash/dust class if the object contains a specified number of pixels that exhibit a spectral signature that is unambiguously associated with volcanic ash or dust (volcanic ash and dust exhibit very similar spectral signatures in weather satellite data). The resulting pixel level ash/no ash (or dust/no dust) classification is used to screen out any ash cloud property retrievals that were performed outside of volcanic ash or dust clouds. The SECO method is globally applicable and can be applied to virtually any low earth orbit or geostationary satellite sensor. Further, the SECO approach was quantitatively proven to be more skillful than pixel based approaches, including the commonly used “split-window” technique. More specifically,

the SECO method has a much higher probability of detection than the traditional “split-window” method while maintaining a near zero false alarm rate. The performance of the SECO approach is extremely promising and well suited to a variety of new and improved applications.

## Chapter 7

### 7. Analysis of Ash Cloud Properties

#### 7.1. 2008 Eruption of Kasatochi, Alaska

##### 7.1.1. Eruption Overview

On August 7-8, 2008, Kasatochi volcano erupted with little warning, injecting volcanic gases and ash high into the atmosphere. Kasatochi volcano is located on Kasatochi Island in the Aleutian Islands of Alaska (see Figure 7.1). Prior to the 2008 eruption, Kasatochi Island served as a major nesting area for sea birds. Aside from yearly visits from scientists from the U.S. Fish and Wildlife Service, Kasatochi Island

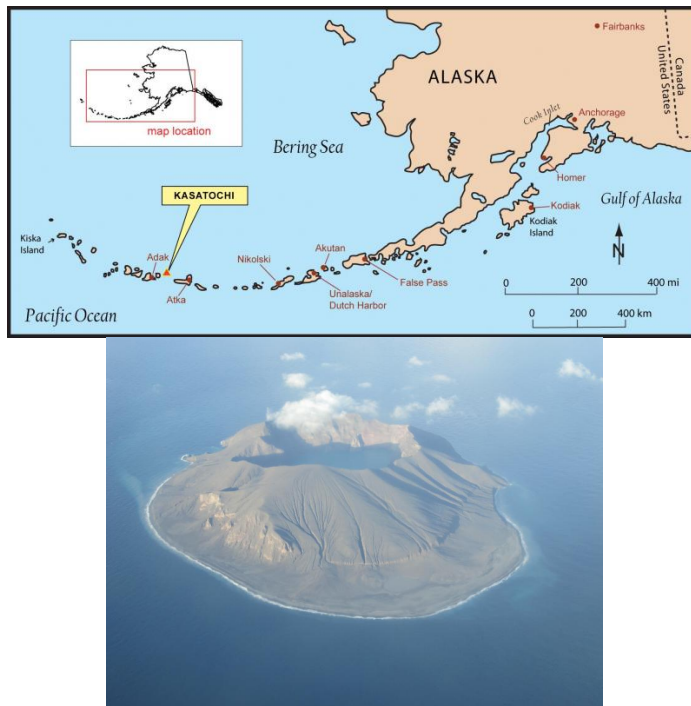


Figure 7.1: Top: Map showing the location of Kasatochi Island (Source: AVO/ADGGS). Bottom: Aerial photo of Kasatochi Island on December 5, 2013 (Source: Richard Zimmer)

was uninhabited by humans [Buchheit and Ford 2008]. Waythomas et al. [2010] provide a thorough review of the eruption, which was the first known eruption of Kasatochi in recorded history. An overview of the Kasatochi eruption is described throughout the remainder of this section.

Three distinct explosions, each lasting

approximately 60 minutes or less were observed [Waythomas et al. 2010]. The first explosion, which was evident in satellite imagery at 22:23 UTC on 7 August, was primarily driven by magma coming into contact with lake water inside the crater of the volcano [Waythomas et al. 2010]. The particulate composition of the resulting cloud was dominated by water. The cloud top was estimated to be 14 km ASL and the water at cloud top was in the form of ice (Figure 7.2). The cloud from the second explosive event was first observed in satellite imagery at 02:10 UTC on 8 August (height was estimated to be 14 km ASL by Waythomas et al. [2010]). The primary mechanism (phreatomagmatic – water/magma interaction versus magmatic) for this explosion is unclear [Waythomas et al. 2010]. As Figure 7.2 shows, the resulting cloud initially appeared dark in visible satellite imagery, which is consistent with volcanic ash being the dominant particulate, as volcanic ash absorbs more visible light than liquid water or ice [Pavolonis et al. 2006]. Subsequent visible satellite images, however, indicated that the cloud albedo increased significantly, consistent with the formation of ice. The clouds from the first two explosive events were observed to move to the southwest of the volcano and disperse (the cloud optical depth decreased significantly) without ever displaying a multispectral signature that was clearly indicative of volcanic ash.

The third and final explosive event was first observed in satellite imagery at 04:43 UTC on 8 August. This event was interpreted to be a magmatic eruption from a dry vent [Waythomas et al. 2010]. As a result, the cloud appeared very dark in visible satellite imagery (Figure 7.2), which is a strong indicator of ash being the dominant particulate in the cloud. Using the parallax induced horizontal displacement of the cloud in geostationary satellite imagery; the height of the cloud from the third explosion was

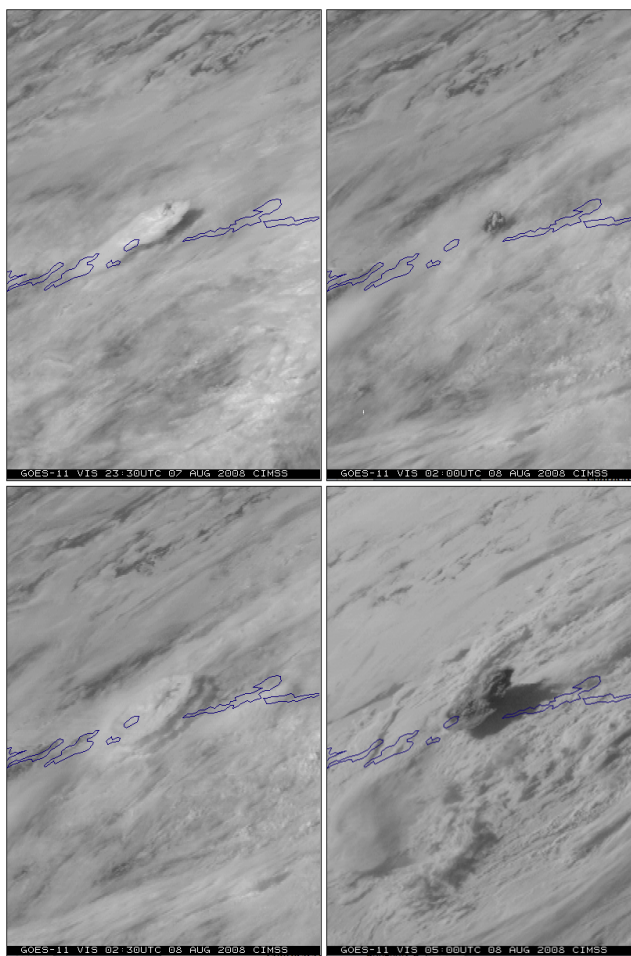


*Figure 7.2: GOES-11 visible satellite images capturing the three explosive events during the August 7-8, 2008 eruption of Kasatochi. The cloud produced by Event 1 is shown at 23:30 UTC on 7 August (top left). The cloud produced by Event 2 is shown at 02:00 UTC and 02:30 UTC on 8 August (top right and bottom left, respectively). The cloud produced by Event 3 is shown at 05:00 UTC on 8 August. The clouds of interest are located in the center of each image. Source: CIMSS Satellite Blog*

estimated to be 18 km ASL [Waythomas et al. 2010]. Airborne ash that may have remained as a result of the first two explosive events could not be distinguished from the cloud produced by the third event. After the third explosive event the eruption entered a phase characterized by continuous production of ash and gases until about 20:00 UTC on 8 August [Waythomas et al. 2010]. The maximum height of the ash clouds produced during the continuous phase was estimated to be 10 km ASL, making it difficult to distinguish between ashes produced by the third explosive event and the continuous phase of the eruption [Waythomas et

al. 2010]. In the days that followed the third explosive event, the volcanic ash clouds from Kasatochi maintained an infrared signature that is very consistent with the presence of volcanic ash. Ultra-violet [Krotkov et al. 2010] and infrared [Karagulian et al. 2010; Prata et al. 2010] satellite measurements indicated that the Kasatochi cloud also contained large amounts of SO<sub>2</sub>.

Volcanic ash and gases, primarily from the third and most explosive Kasatochi event dispersed over great distances in the months that followed. Aviation across the North Pacific and northern North America was disrupted for 5 days following the start of the eruption, resulting in at least 40 flight cancellations that stranded over 6000 passengers [Associated Press and Anchorage Daily News reports]. On numerous occasions airlines had to re-route planes to avoid possible areas of volcanic ash [Guffanti et al. 2010b]. In addition, several pilots reported possible encounters with volcanic ash clouds [Guffanti et al. 2010b].

The Kasatochi eruption was selected for analysis because the ash and gas emissions and subsequent dispersion were reasonably well observed by low earth orbit and geostationary-based imaging radiometers, lidars, and by humans (e.g. pilots). Further, the Kasatochi literature is rich with observational and model based analysis of the gas and ash clouds produced by the third explosive event, allowing for interesting comparisons. The volcanic ash detection and ash cloud property retrieval algorithms described in Chapters 3-6 were applied to data from the Moderate Resolution Imaging Spectroradiometer (MODIS). The spectral channels available on MODIS allow all of the algorithms to run in the most capable configuration. Corrandini et al. [2010] also used MODIS to study the Kasatochi ash cloud. While Prata et al. [2010] used the Atmospheric Infrared Sounder (AIRS), which is located on the same spacecraft as one of the two MODIS instruments to estimate the Kasatochi ash cloud properties. Thus, the use of MODIS in our study facilitates comparisons to published analyses.

### *7.1.2. Comparison to Independent Observations*

Prior to describing the evolution of the Kasatochi ash cloud in space and time, the ash cloud properties derived using the methods presented in this dissertation are assessed relative to some independent observations of the Kasatochi clouds. While quantitative validation studies for each algorithm have already been presented, an additional assessment is performed using some independent observations that are unique to the Kasatochi case.

#### *7.1.2.1. True Color Imagery*

The algorithm used to retrieve the ash cloud properties (height, mass loading, and effective particle radius) only utilizes infrared channels. One possible way to assess the quality of the mass loading estimates is to compare them against true color imagery, which is available from MODIS. In true color images, calibrated reflectance measurements from the red light (0.65  $\mu\text{m}$ ), green light (0.55  $\mu\text{m}$ ), and blue light (0.47  $\mu\text{m}$ ) centered channels are displayed on the corresponding red-green-blue color guns. The resulting image is a decent proxy of a color photograph. Similar to a photograph, liquid water or ice clouds that appear bright white can be considered optically thick. Thick layers of volcanic ash on the other hand will appear brown, similar to when viewed by the human eye. Thus, true color images are useful for identifying areas of optically thick volcanic ash, assuming a higher cloud layer does not obscure the volcanic ash. Optically thin layers of volcanic ash are not nearly as distinct in true color imagery, especially when underlying liquid water or ice clouds are present as the energy scattered back to space by the underlying clouds dominates the measured signal at these

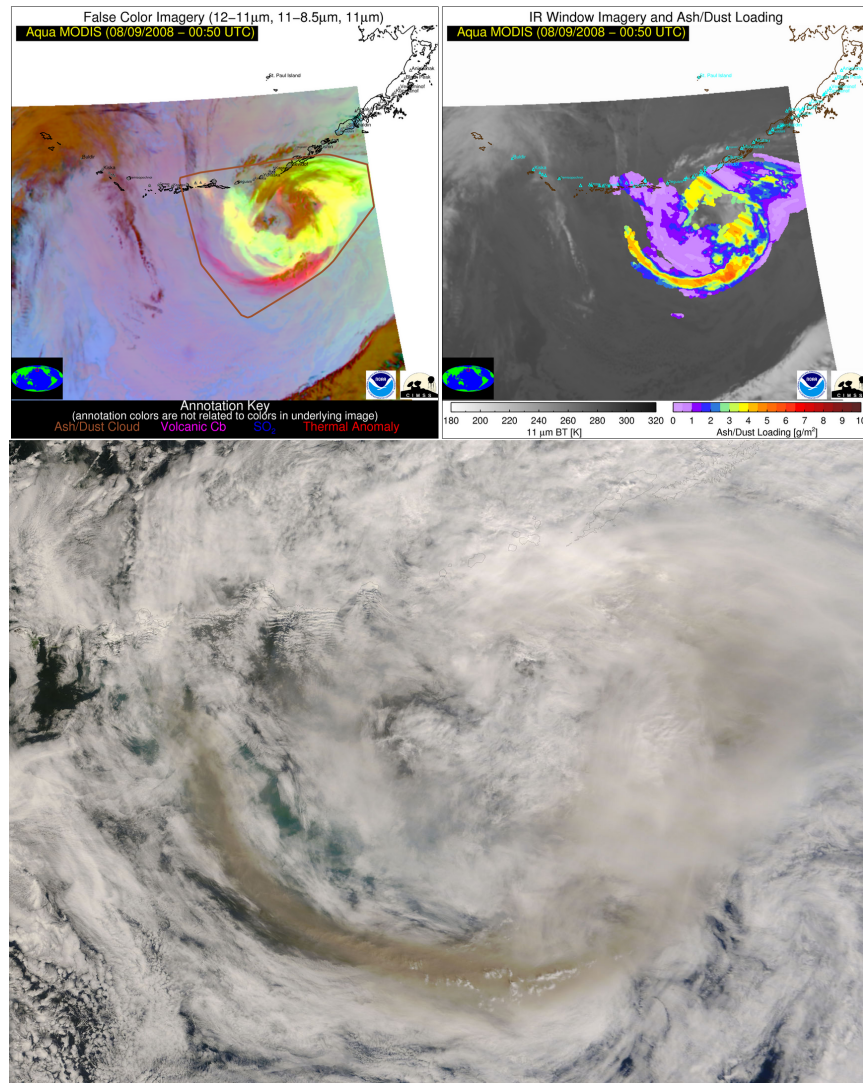


*Figure 7.3: A comparison between the retrieved ash mass loading (top right) and the corresponding true color imagery (bottom) for a 9 August 2008 Aqua MODIS overpass (at 00:50 UTC) with Kasatochi volcanic ash is shown. Infrared-based false color imagery is also shown in the top left panel. The true color imagery was obtained from NASA.*

wavelengths (infrared observations generally maintain sensitivity to optically thin ash layers more so than visible wavelength observations).

The goal of the true color imagery comparison is to qualitatively determine if the spatial pattern in ash mass loading, derived solely from infrared measurements, is consistent with the location of optically thick volcanic ash in the corresponding true color

image (Figure 7.3). An *Aqua* MODIS overpass on 9 August 2008 at 00:50 UTC (~20 hours after the third explosive event) was selected for analysis. In Figure 7.3, the most optically thick portion of the ash cloud identifiable in the true color image corresponds to an “axis” of larger retrieved mass loadings. Conversely, much smaller mass loadings are co-located with parts of the cloud that have a tenuous appearance in the true color imagery. Thus, the infrared-based mass loading retrievals and the true color imagery, which is spectrally independent of the retrieval, are generally consistent. It is also worth noting that the overall horizontal extent of the volcanic ash is far easier to visually ascertain in infrared false color imagery compared to the true color image for reasons described earlier (Figure 7.3). As demonstrated throughout this dissertation, the qualitative sensitivity of the infrared measurements also translates to quantitative sensitivity.

#### *7.1.2.2. Pilot Reports*

On 11 August 2008, with portions of the Kasatochi cloud now dispersed over Canada and parts of the northern United States, numerous pilots reported seeing volcanic ash or brown colored haze layers (consistent with volcanic ash) that smelled of sulphur (consistent with the presence of SO<sub>2</sub> and possibly H<sub>2</sub>S) above 8 km ASL [Guffanti et al. 2010b]. Several of the pilot reports were associated with volcanic cloud sightings in Montana, Wyoming, and South Dakota on 11 August. The volcanic ash cloud properties derived from an *Aqua* MODIS overpass that occurred about 10-15 hours after the pilot reports from Montana, Wyoming, and South Dakota are shown in Figure 7.4. The false color image shows that the U.S. portion of the volcanic cloud is located further to the east over the Dakotas and Nebraska (geostationary satellite image sequences confirm the

eastward movement). The automated algorithms described in this dissertation are able to detect and characterize several regions of volcanic ash that have a horizontal position that is consistent with the imagery. In general, less than  $0.5 \text{ g/m}^2$  of ash (although not resolved by the color scale, most mass loading values are  $< 0.1 \text{ g/m}^2$ ) with cloud top heights around 12 – 14 km ASL were found using the retrieval approach described in Chapter 5. This result is therefore consistent with the 11 August 2008 pilot reports of tenuous volcanic ash layers with bases of 9 km ASL or greater. Some portions of the Kasatochi cloud that are identifiable in the false color image are not detected by the automated algorithm (Figure 7.4), which illustrates that very low optical depth ash clouds are difficult to automatically detect, especially over land surfaces where uncertainties in the clear sky radiance calculations are greater.

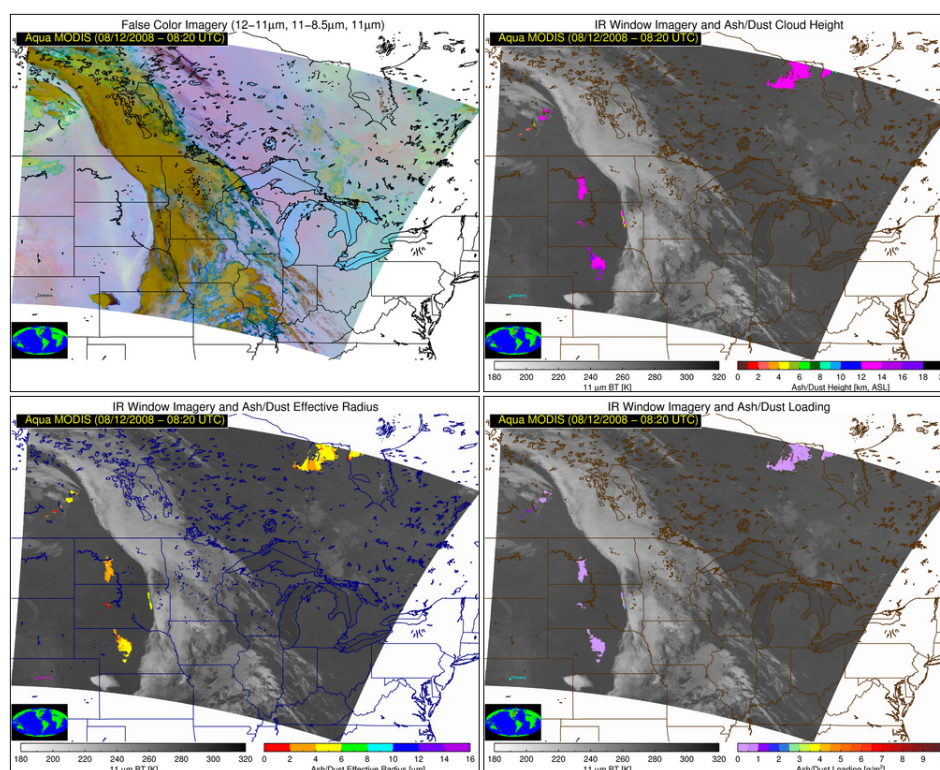


Figure 7.4: Volcanic ash cloud properties as derived from an Aqua MODIS overpass on August 12, 2008 at 08:20 UTC. A false 12-11 $\mu\text{m}$ , 11-8.5 $\mu\text{m}$ , 11 $\mu\text{m}$  false color image (top left), ash cloud height (top right), ash effective particle radius (bottom left), and ash mass loading (bottom right) are shown.

More detailed information about the Kasatochi volcanic cloud was ascertained from a 757 jet aircraft encounter over northern British Columbia on 11 August at about 01:00 UTC [Guffanti et al 2010b]. The crew of the 757 reported seeing a yellowish brown aerosol layer from the flight deck while cruising at about 10 km ASL. They also reported smelling sulfur. The plane descended to about 8.5 km ASL in order to escape the cloud. A subsequent inspection of the planes engines and other systems revealed no damage, but particles adhering to the engine cowl and air conditioning pack were found during the inspection process and a sample of these particles was sent to the United States Geological Survey (USGS) for further analysis [Guffanti et al. 2010b]. The USGS analysis determined that some of the collected particles were volcanic in origin and consistent with the composition of Kasatochi tephra deposits [Guffanti et al. 2010b]. Thus, volcanic ash was deemed to be present in the cloud encountered by the 757.

The traditional “split-window” technique for detecting volcanic ash was not able to provide any conclusive information related to the presence of volcanic ash in northern British Columbia near the time of the encounter. At the time of the encounter, the British Columbia portion of the cloud was thought to be primarily composed of SO<sub>2</sub>. The volcanic ash cloud properties derived from an *Aqua* MODIS overpass on 10 August 2008 at 21:25 (about 3.5 hours prior to the 757 encounter), however, indicate that volcanic ash was present in the vicinity of the encounter location (Figure 7.5). In the 3.5 hours between the MODIS overpass and the crew of the 757 observing the volcanic cloud, geostationary satellite imagery shows that sections of the cloud in British Columbia moved northward towards the future location of the 757. The MODIS retrievals indicate that generally light amounts of ash ( $< 1 \text{ g/m}^2$ ) with cloud top heights of 10-14 km ASL

are present in the general vicinity of the encounter location (Figure 7.5). Some of the larger mass loading ( $> 1\text{g/m}^2$ ) values is likely an artifact of cirrus contaminating the retrieval (the cirrus are easily identifiable in the corresponding false color image). In general, the MODIS based retrieval results are very consistent with the in-situ samples inadvertently collected by the 757.

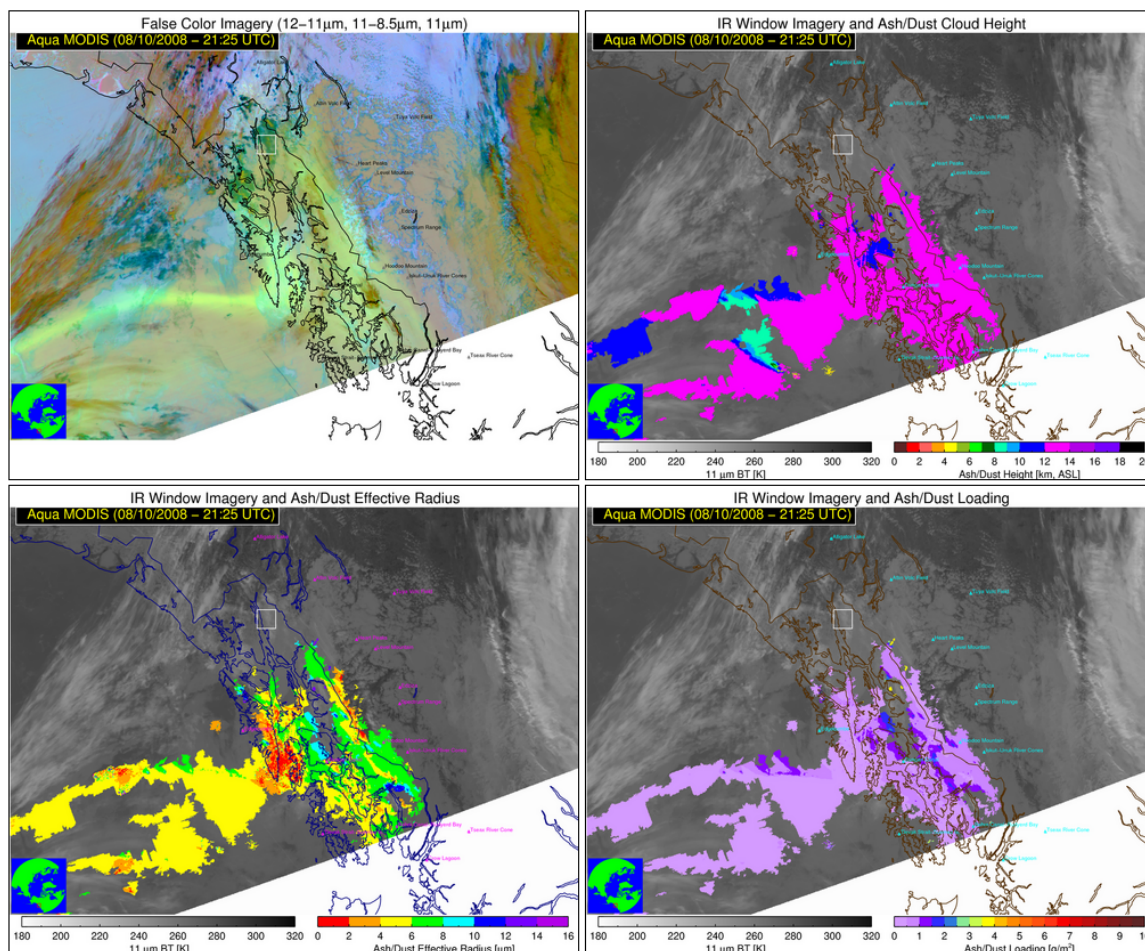


Figure 7.5: Volcanic ash cloud properties as derived from an Aqua MODIS overpass on August 10, 2008 at 21:25 UTC. A false 12-11µm, 11-8.5µm, 11µm false color image (top left), ash cloud height (top right), ash effective particle radius (bottom left), and ash mass loading (bottom right) are shown. The approximate location of a 757 encounter with volcanic ash at 01:00 UTC on 11 August 2008 is denoted by the white square.

### 7.1.2.3. Lidar

The Kasatochi cloud was also observed by the University of Wisconsin High Spectral Resolution Lidar (HSRL), which, in 2008, was deployed on the roof of the Space Science and Engineering Center (SSEC) in Madison, WI USA. The HSRL is a unique lidar that provides absolutely calibrated profiles of particulate backscatter cross section and depolarization [Eloranta 2005]. Conventional lidars measure the total attenuated backscatter (from molecular and particulate matter), which at any given location in the vertical profile is at least somewhat dependent on the full vertical profile of attenuating matter (molecular and particulate). Conversely, the HSRL particulate backscatter measurements at a given vertical location are not compromised by attenuation in other parts of the vertical profile (at least up until the lidar beam is completely attenuated) and the small field of view of the HSRL greatly limits the effects of multiple scattering. Thus, the HSRL provides exceptionally accurate measurements of the vertical location and optical depth of cloud and aerosol layers. In addition, the HSRL depolarization ratio provides robust information on particle shape at a given location above the lidar. The depolarization measurements provide information about cloud composition, as very low depolarization ratios are indicative of spherical particles and higher depolarization ratios are measured when non-spherical particles such as volcanic ash dominate the composition. As of May 2014, the University of Wisconsin HSRL measurements have not been used in any published Kasatochi related study.

Karagulian et al. [2010] and Krotkok et al. [2010] conclude that by 11 August 2008 sulphate aerosol, formed from oxidation of  $\text{SO}_2$  by homogeneous gas phase reactions [McKeen and Liu 1984], was the dominant particulate composition in the

Kasatochi clouds. Karagulian et al. [2010] were unable to unambiguously detect volcanic ash after 10 August 2008 using high spectral resolution infrared measurements from the Infrared Atmospheric Sounding Interferometer (IASI). Krotkov et al. [2010] interpreted the very low depolarization measured by the spaceborne lidar, CALIOP (see Chapter 5 for an overview of CALIOP), to be indicative of spherical sulphate aerosols dominating the particulate composition. As shown in Figure 7.4 and Figure 7.5, the remote sensing methods described in this dissertation were still able to detect volcanic ash after 10 August 2008, which was qualitatively consistent with pilot reports and with particles inadvertently collected by a 757 that flew into the Kasatochi cloud. The HSRL measurements are used to investigate the cloud composition problem in more detail.

The Kasatochi cloud elements depicted in Figure 7.4, and in ultra-violet based SO<sub>2</sub> products [e.g. Guffanti et al 2010b], moved eastward into southern WI along with a line of convection on 13 August 2008. The properties of the overpassing Kasatochi cloud were subsequently measured by the HSRL between 5-6 UTC and 7-8 UTC on 13 August, when optically thick meteorological cloud layers did not completely attenuate the HSRL beam (Figure 7.6). The HSRL shows a cloud layer between 11.5 and 12.5 km ASL that has a depolarization ratio of about 15-30%, which is strongly indicative of non-spherical volcanic ash particles being the dominant particulate component of the cloud (Figure 7.6). Clouds composed primarily of spherical particles will have depolarization ratios that are about 3% or less, whereas ice clouds typically have a depolarization ratio of 20% or greater in HSRL data since ice crystals are non-spherical [Burton et al. 2012]. The presence of volcanic ash over the Midwest U.S. on 12 August 2008, as inferred from the

MODIS measurements (Figure 7.4), is consistent with the HSRL observations of the same region of the Kasatochi cloud 24 hours later.

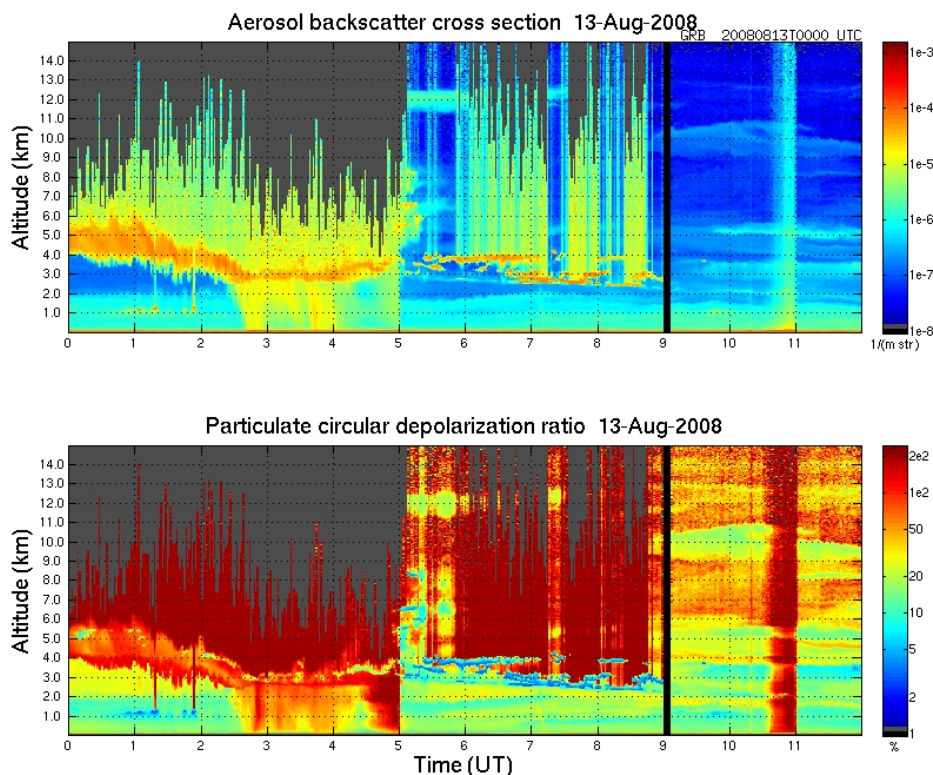
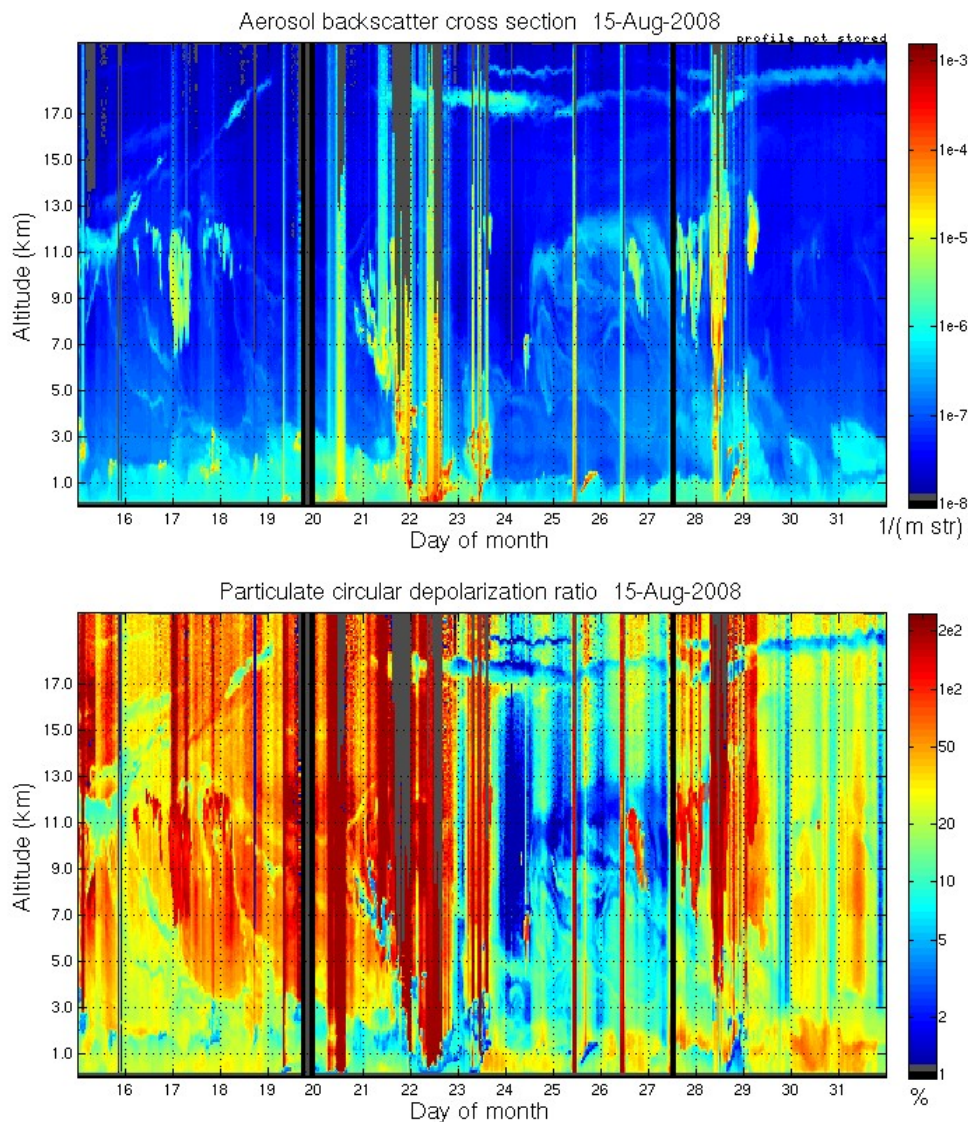


Figure 7.6: HSRL aerosol backscatter cross section (top) and particulate circular depolarization ratio (bottom) from 0-12 UTC on 13 August 2008 in Madison, WI. Clouds produced by the eruption of Kasatochi volcano were definitively observed by the HSRL above 11 km ASL between 5-6 UTC and 7-8 UTC. The black region just after 9 UTC indicates missing data.

The time series of HSRL measurements from August 15-31, 2008 provides additional insight into the evolution of the particulates in the Kasatochi cloud (Figure 7.7). Two primary clusters of intriguing upper troposphere to lower stratospheric (11-18 km ASL) clouds drifted over the HSRL during the second half of August. The first cluster was observed from August 15-19 and had a depolarization ratio of about 10-30%, which again suggests that non-spherical particles dominated the particulate composition (Figure

7.7). The appearance of the August 15-19 clouds is consistent with the location of the SO<sub>2</sub> cloud on these days [Krotkov et al. 2010; Karagulian et al. 2010], leaving little doubt that these features are part of the Kasatochi cloud. The second cluster of clouds was observed above 17 km ASL from 23 August to 1 September. Unlike the first cloud cluster, the depolarization ratio is generally less than about 7%, suggesting that spherical particles are the more dominant particulate composition. Thus, the particulate component of the Kasatochi cloud sampled by the HSRL was not dominated by spherical sulfate particles until the last third of August 2008. Given that the HSRL spatial sampling is limited to a vertical column above a single point, it is certainly possible that the HSRL fortuitously sampled portions of the Kasatochi cloud that had a particulate component dominated by ash. As such, the HSRL results do not necessarily conflict with the conclusions of Karagulian et al. [2010] and Krotkov [2010], but do provide additional confidence that our MODIS derived cloud properties are more sensitive to low optical depth ash clouds than other methods.



*Figure 7.7: HSRL aerosol backscatter cross section (top) and particulate circular depolarization ratio (bottom) from August 15-31, 2008 in Madison, WI. Clouds produced by the eruption of Kasatochi volcano were definitively observed by the HSRL above 11 km ASL between August 15-19 and August 22-31.*

Finally, while CALIOP provides an unprecedented view of clouds, one has to wonder if the depolarization ratios can always be interpreted in a straightforward manner given the significant effects of multiple scattering, attenuation, and instrument noise. On 16 August 2008 and 28 August 2008 CALIOP sampled the Kasatochi volcanic cloud within 200 km of Madison, WI (the location of the HSRL). Figure 7.8 shows that the

CALIOP depolarization ratio of the Kasatochi layer on 16 August is very small (consistent with spherical particles in the absence of competing effects) and indistinguishable from the depolarization ratio observed on 28 August. Note that the CALIOP cloud layers are located at very similar altitudes (11-15 km ASL on 16 August and > 17 km ASL on 28 August) as the cloud layers sampled by the HSRL (Figure 7.8), which provides confidence that the cloud layers sampled by both instruments can be fairly compared. As highlighted earlier, the difference between the HSRL depolarization ratios observed at those same times is significant, strongly suggestive of different dominant particulates. While it is possible that the CALIOP/HSRL differences can be attributed to inexact spatial co-location, the difference is large and worthy of consideration when interpreting CALIOP depolarization ratios.

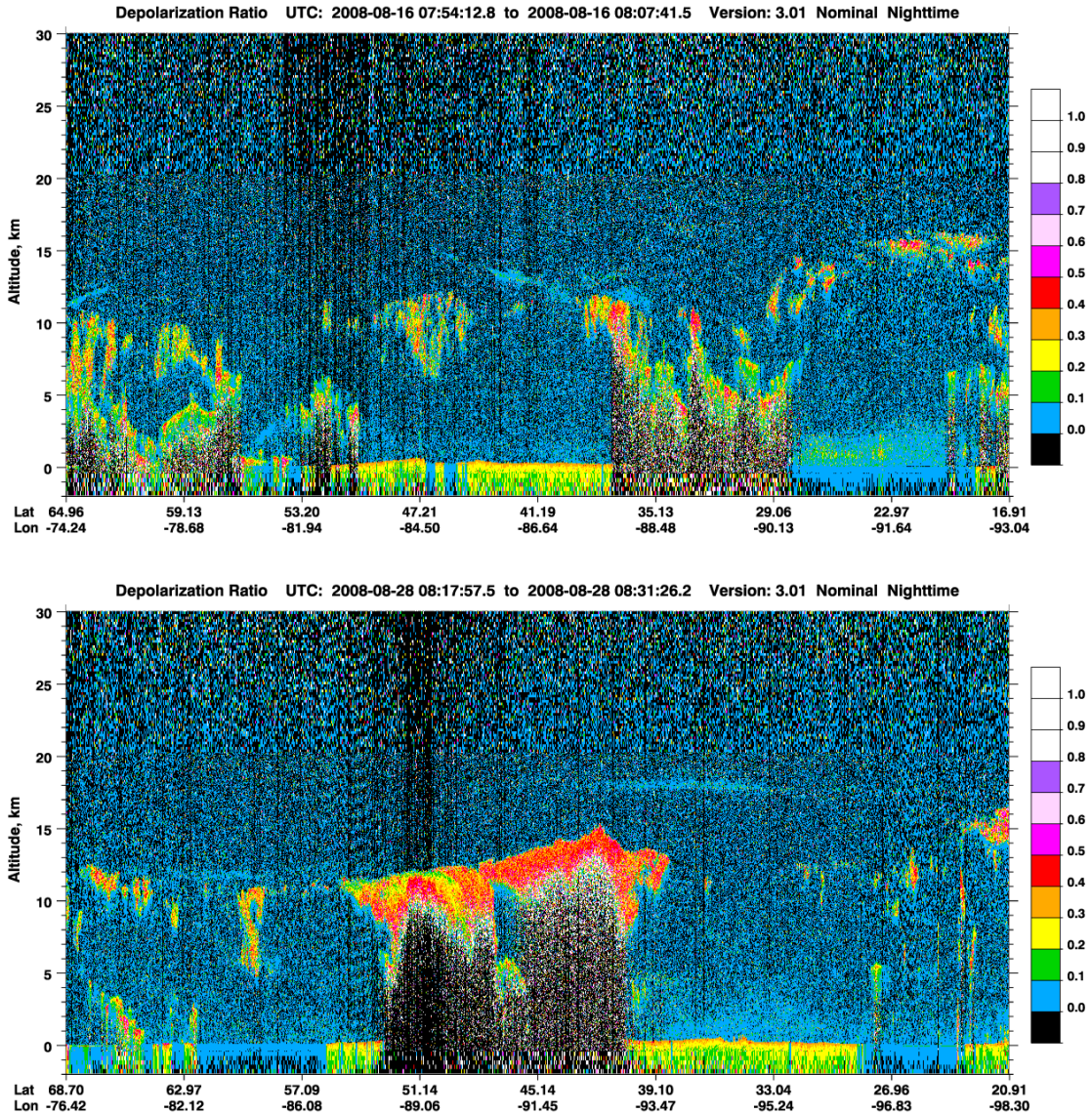


Figure 7.8: The CALIOP depolarization ratio from August 16, 2008 at 07:54-08:08 UTC (top) and August 28, 2008 at 08:18-08:31 UTC (bottom) is shown. Kasatochi clouds within 200 km of Madison, WI were sampled by CALIOP. In the top figure the Kasatochi cloud of interest is located above 11 km ASL and is centered on  $41.19^{\circ}$  latitude,  $-86.64^{\circ}$  longitude. In the bottom figure the Kasatochi cloud of interest is the sole identifiable feature above 17 km ASL.

### 7.1.3. Ash Cloud Evolution

Previous validation efforts and comparisons to independent observations of the Kasatochi cloud indicate that the ash detection and cloud property retrieval methods

described in Chapters 3-6 are well suited to analyzing the spatial and temporal evolution of the Kasatochi ash cloud and may provide new insights into the physical behavior of the cloud. As described earlier, in an effort to maximize accuracy and facilitate comparisons to published results, the algorithms were applied to MODIS on-board the *Aqua* (sun synchronous) low earth orbit satellite. The MODIS retrievals assumed the ash was composed of andesite, which matches the composition of the tephra deposits collected from Kasatochi Island [Waythomas et al. 2010]. The MODIS-derived areal extent, height, mass loading, and effective particle radius of the ash cloud are analyzed.

Composite maps of the MODIS-derived ash mass loading (overlaid on 11  $\mu\text{m}$  brightness temperature imagery) and the corresponding false color imagery were created using MODIS overpasses that occurred between August 8-11, 2008 (Figure 7.9 and Figure 7.10). Each map represents one of the two orbital nodes on a given day (descending overnight node or ascending afternoon node). The image sequence demonstrates that the horizontal location of ash, determined using the Spectrally Enhanced Cloud Objects (SECO) approach described in Chapter 4 and Chapter 6, is very consistent with the false color imagery. As shown in Chapter 6, the lack of obvious false alarms and the high detection rate of the SECO approach are very unique.

The overall spatial area of the cloud was found to increase significantly with time while the mass loading decreased considerably. The area of the ash cloud is comparable to the  $\text{SO}_2$  cloud that was detected by ultra-violet satellite measurements [Krotkov et al. 2010], which differs from published accounts of a much smaller detectable ash cloud (using variants of the traditional “split-window” approach) compared to the  $\text{SO}_2$  cloud [e.g. Guffanti et al. 2010b]. The dispersal pattern of the cloud was strongly influenced by

a mid-latitude cyclone over the North Pacific. From August 8-9, 2008, the Kasatochi cloud moved slowly to the southeast while rotating counter-clockwise in the response to the developing mid-latitude cyclone (the counter-clockwise rotation is readily apparent in geostationary satellite movies). On August 10-11, 2008, a large portion of the ash cloud wrapped around the center of the cyclone as the spatial lag between the upper level cyclonic circulation to the west and the near surface cyclonic circulation to the east decreased as the cyclone matured. Parts of the ash cloud to the north of the primary cloud shield, associated with the mid-latitude cyclone, were advected towards the northeast and subsequently formed an elongated north/south band in response to upper tropospheric/lower stratospheric wind shear.

The composite maps of the retrieved ash cloud height (Figure 7.11 and Figure 7.12) indicate that the highest layer of ash was generally located in the upper troposphere to lower stratosphere (10-16 km ASL). Areas of lower ash layers were generally only observed towards the outer fringes of the cloud prior to 10 August. The location of the lower cloud heights was also well correlated with the red colors in the false color imagery. As discussed in Chapter 4, areas of volcanic ash that are horizontally co-located with SO<sub>2</sub> will appear yellow in 12-11 $\mu$ m, 11-8.5 $\mu$ m, 11 $\mu$ m false color imagery while ash that is not co-located with SO<sub>2</sub> will appear red. The areas of mid-troposphere volcanic ash decreased rapidly in time, likely in response to being removed from the atmosphere by some combination of gravitational sedimentation, wet deposition, and dry deposition [e.g. Langmann et al. 2010]. The impacts of the volcanic ash on the mid-latitude cyclone or other weather systems, primarily via cloud microphysical effects [e.g. Campbell et al. 2012], are unfortunately not easily ascertained from any single data set. However, the

combination of the MODIS data set, other data sets, and modeling may eventually be able to address questions related to weather modification via volcanic clouds.

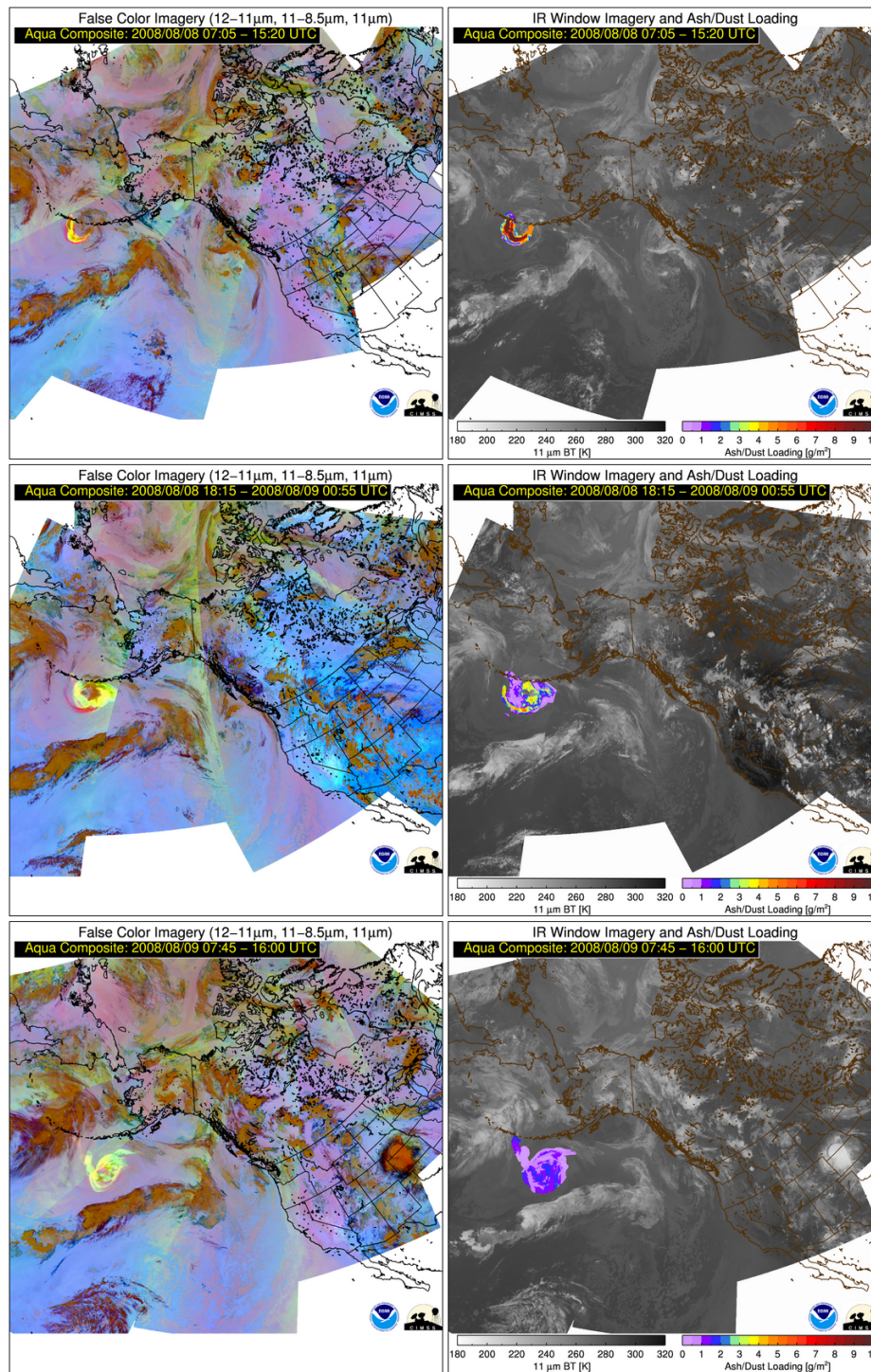


Figure 7.9: Composite maps of 12-11µm, 11-8.5 µm, 11 µm false color imagery (left column) and volcanic ash mass loading (right column) from three different Aqua MODIS overpasses. The 8 August 2008 AM overpasses (top), 8 August 2008 PM overpasses (middle), and 9 August AM overpasses (bottom) are shown. The ash mass loading is overlaid on 11 µm brightness temperature imagery.

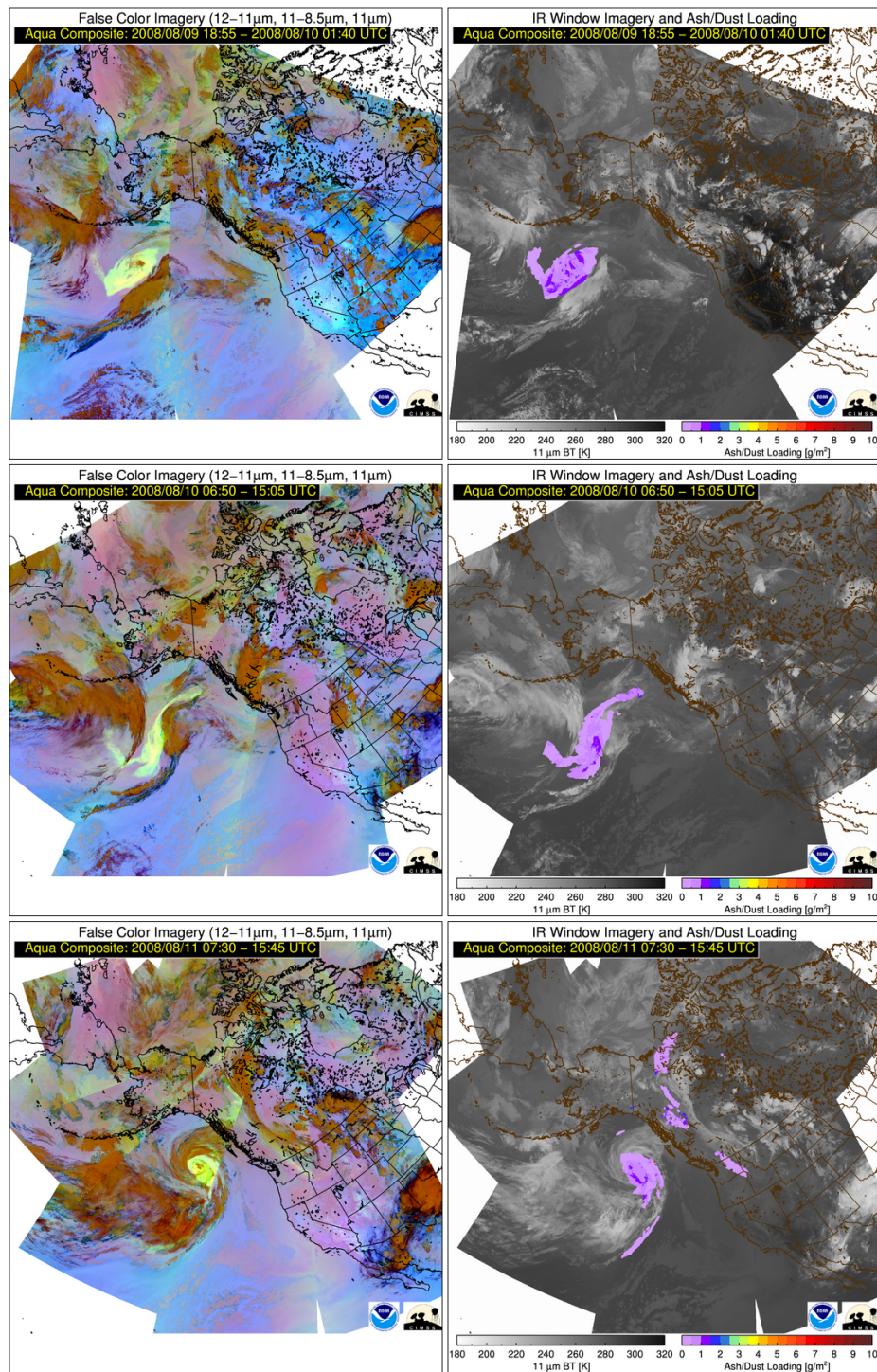


Figure 7.10: Composite maps of 12-11µm, 11-8.5 µm, 11 µm false color imagery (left column) and volcanic ash mass loading (right column) from three different Aqua MODIS overpasses. The 9 August 2008 PM overpasses (top), 10 August 2008 AM overpasses (middle), and 11 August AM overpasses (bottom) are shown. The ash mass loading is overlaid on 11 µm brightness temperature imagery.

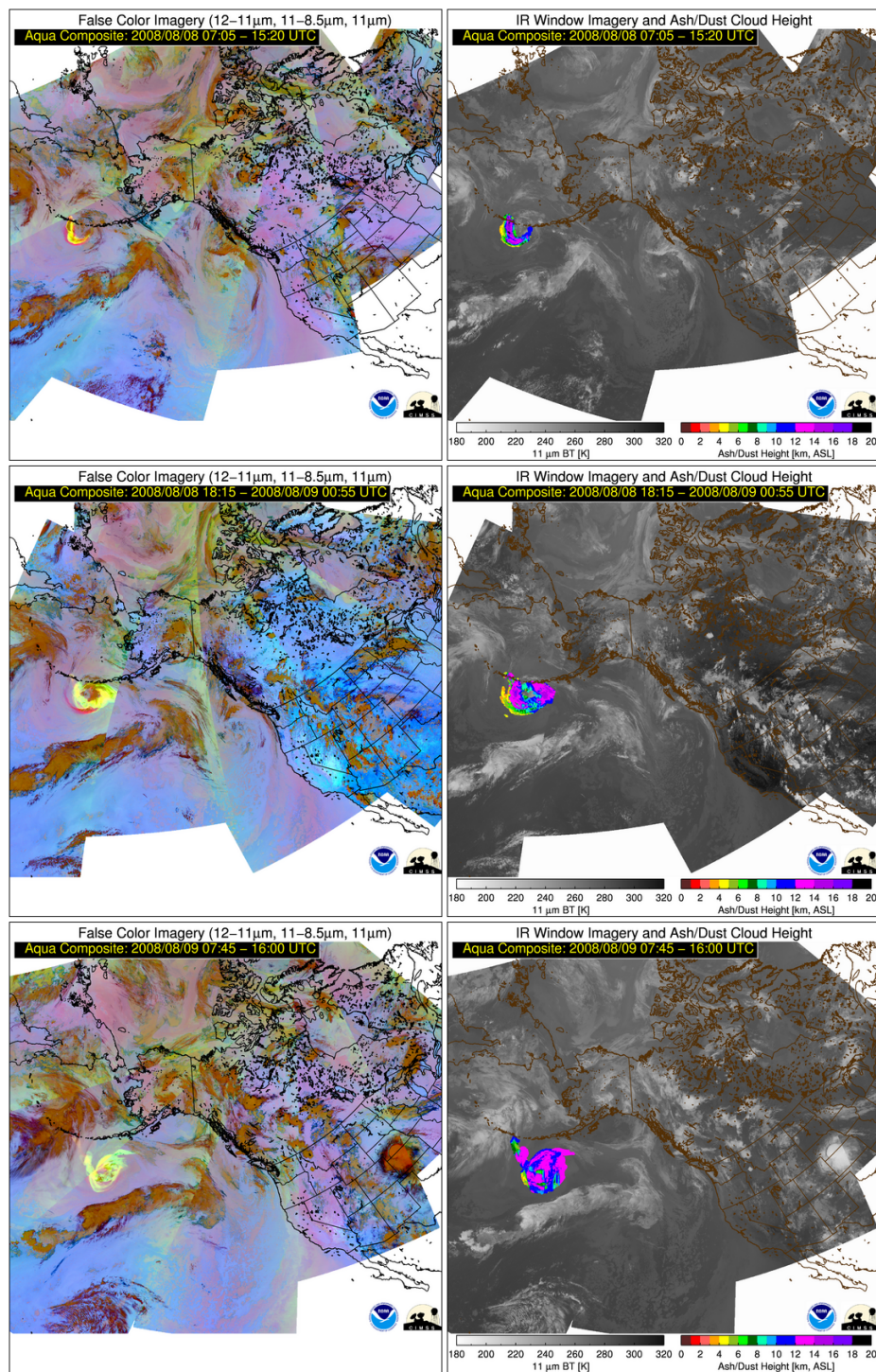


Figure 7.11: Same as Figure 7.9 except the retrieved ash cloud height is shown in the right column.

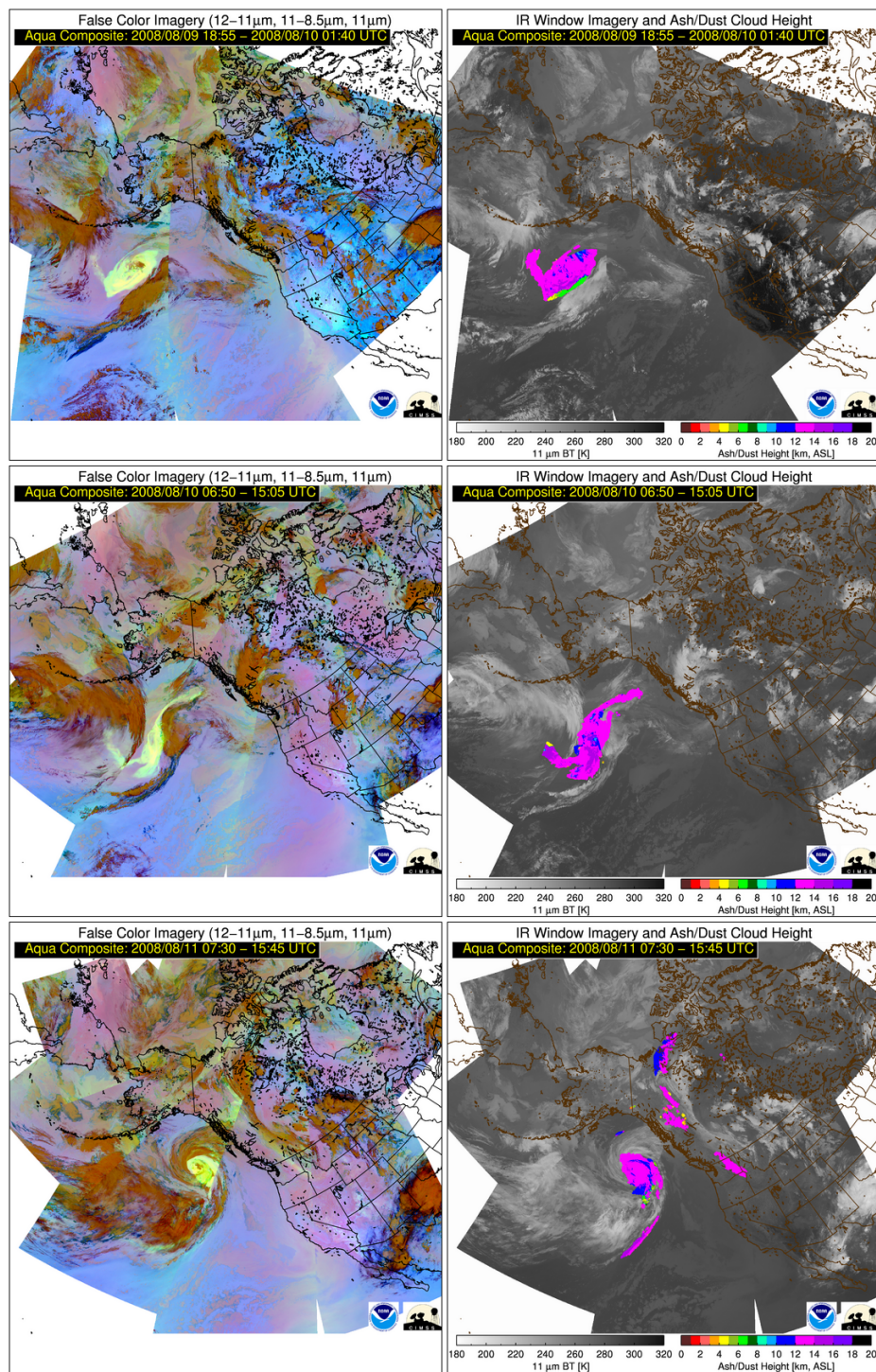


Figure 7.12: Same as Figure 7.10 except the retrieved ash cloud height is shown in the right column.

The total mass and area of volcanic ash were computed as a function of time (Figure 7.13). The total mass was determined simply by multiplying the mass loading (mass per unit area) in a given pixel by the pixel area and summing the result for all pixels deemed to contain volcanic ash. In Chapter 5, the mass loading retrieval was shown to be largely unbiased. As such, the total mass estimates should also be generally unbiased given the

demonstrated skill of the SECO ash detection approach. The total mass is expressed in terra grams (Tg), the total area in  $\text{km}^2$ , and time in hours since the start of the third explosive event at ~04:40 UTC on 8 August 2008

[Waythomas et al. 2010]. The total ash (black line in Figure 7.13) mass rapidly decreases with

time from ~1.0 Tg to 0.38 Tg in the first 60 hours after the start of the third explosive event, while the total ash cloud area (red line in Figure 7.13) increases approximately exponentially to ~80,000  $\text{km}^2$  (roughly the size of Texas and Louisiana combined) 80 hours after the eruption. The maximum total mass estimate of ~1 Tg is likely an

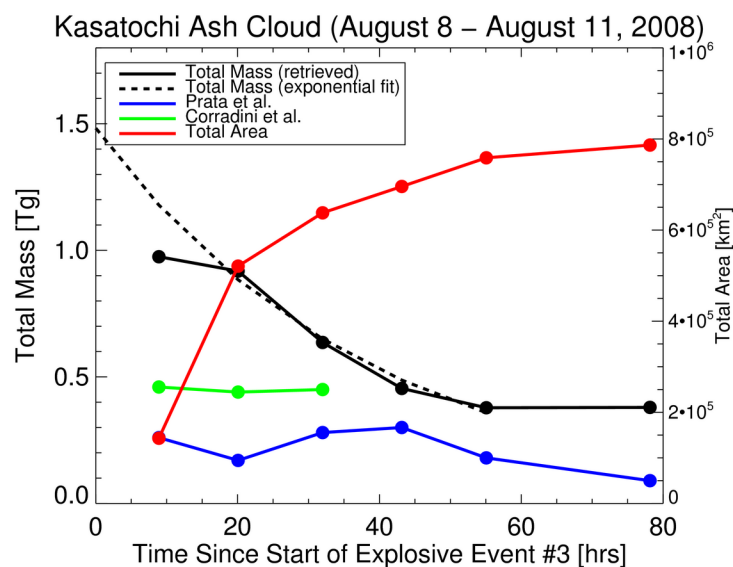


Figure 7.13: The total mass and area of airborne volcanic ash are shown as a function of the time since the third and final explosive event observed during the August 7-8, 2008 eruption of Kasatochi volcano. The total mass estimated using the methods described in this dissertation (black), the total mass reported by Corradini et al. [2010] (green), the total mass reported by Prata et al. [2010] (blue), and the total ash cloud area (red) are shown.

underestimate as the ability to retrieve cloud optical depths greater than 5 with infrared measurements is quite limited. From 20 hours onwards (the second point on the black line in Figure 7.13), optical depth saturation is no longer an issue (e.g. Figure 7.9), therefore the total mass estimates are likely more accurate. Waythomas et al. [2010] utilized observations of tephra deposits to estimate that the bulk volume of erupted products was 0.15-0.28 km<sup>3</sup> (0.15 km<sup>3</sup> is a conservative lower bound so the actual volume is unlikely to be smaller). Using a particle density of 2.6 g/cm<sup>3</sup> [Neal et al. 1994] yields a total erupted mass of 390 – 728 Tg. The significant difference between the total mass estimated from fall deposits and the total mass extrapolated from the MODIS estimates can largely be attributed to large pyroclasts (larger than 1 mm) that quickly fall out of the eruptive column within the first 30 minutes [Rose 1993]. The saturation of the cloud optical depth information also certainly contributes. Nevertheless, it appears that the total eruptive mass derived from Waythomas et al. [2010] decreased by almost three orders of magnitude in the first 24 hours, as inferred from the MODIS estimates at ~20 hours after the third explosive event.

The initial mass of SO<sub>2</sub> in the Kasatochi cloud was estimated to be 2.2 Tg [Krotkov et al. 2010]. If the total ash mass estimate at 9 hours after the third explosive event (first point on black line in Figure 7.13) is representative of the initial mass of fine-grained ash (Mastin et al. [2009] define fine ash as particles with a diameter < 63 μm) and the total mass estimate at that time is underestimated due to cloud optical depth saturation, then the total mass of fine ash is possibly comparable to the total mass of SO<sub>2</sub>. Further, the mass fraction of the initial mass that is composed of fine-grained ash is approximated as  $10^0/10^2 \approx 0.01$ . The fraction of the total mass associated with fine-

grained ash is an extremely important parameter for dispersion models [e.g. Mastin et al. 2009] and the order of magnitude estimate presented here represents the first attempt to obtain this information for the 2008 Kasatochi eruption. Without a reasonable estimate of fine ash fraction, models can greatly over-estimate the atmospheric ash content. For instance, the total Kasatochi ash mass simulated by Langmann et al. [2010], using a three-dimensional atmospheric chemistry-aerosol model, is consistently three orders of magnitude larger than our MODIS-based results out to 80 hours after the third explosive event. Langmann et al. [2010] assumed that 95% of the 600 Tg of pyroclasts released by the eruption in their experiment had a diameter of 1 - 16  $\mu\text{m}$ , resulting in a very large fine ash fraction that is not supported by satellite observations.

Prata et al. [2010] and Corradini et al. [2010] also estimated the total mass of ash (blue and green lines, respectively, in Figure 7.13) in the Kasatochi cloud. Prata et al. [2010] (hereafter Prata10) utilized infrared measurements from AIRS to compute the total mass of ash in the 3 days following the third explosive event. Corradini et al. [2010] (hereafter Corradini10) provided MODIS-based (only infrared channels were used) estimates of total mass out to 30 hours after the third explosive event. The Prata10 and Corradini10 ash detection and ash cloud property retrieval approaches differ from the algorithms presented in Chapters 3-6. For instance, in the ash retrieval, the surface temperature and cloud temperature are assumed to be spatially uniform and background atmospheric water vapor is accounted for empirically by Prata10 and Corradini10. In addition, the ash detection methods utilized by Prata10 and Corradini10 are most effective when a robust “split-window” brightness temperature difference is present. The

ash detection approach described in Chapters 4 and 6 does not rely on the presence of a robust “split-window” signal.

The Prata10 and Corradini10 total mass time series’ differ considerably from the time series derived using the methods described in Chapters 3-6 (hereafter referred to as the SECO method). The *maximum* total mass from Prata10 (0.31 Tg) never exceeds the *minimum* total mass derived using the SECO method (0.38 Tg). While the Corradini10 total mass estimates are always greater than the corresponding Prata10 estimates; they are always less than the SECO derived values. Further, the total mass of ash does not always decrease with time in the Prata10 and Corradini10 results as one would expect given that the ash producing eruptive event (the source of ash) ended ~15 hours after the start of the third explosive event [Waythomas et al 2010]. Closer examination of the spatial pattern of the Prata10 and Corradini10 ash mass loading for a given *Aqua* overpass reveals that the remote sensing techniques utilized by Prata10 and Corradini10, at times, significantly underestimates the areal extent of the ash cloud as readily inferred from visual analysis of the corresponding satellite imagery (see Figures 7-8 in Prata10 and Figure 5 in Corradini10). The underestimation of the ash cloud area, and hence the total mass, is largely due to well-understood limitations of their ash detection methods. These limitations often prevent optically thick ash and well dispersed optically thin ash from being detected. Prata10 and Corradini10 acknowledge that limitations in the ash detection approaches that they employ result in an underestimation of the ash cloud area and total mass. Visual inspection of Figures 7-8 in Prata10 and Figure 5 in Corradini10 also reveals some significant differences in the retrieved mass loadings when all three methods perform the retrieval. The nature of these differences cannot be

explored without a detailed pixel-by-pixel inter-comparison conducted in a collaborative manner, which is not currently possible. The swath width of the AIRS instrument utilized by Prata10, which is 680 km smaller than the MODIS swath width, may also partially explain why the Prata10 estimates are so much lower.

Additional statistical properties of the ash cloud were analyzed with respect to time after the start of the third explosive event (Figure 7.14). The 25<sup>th</sup>, 50<sup>th</sup>, and 75<sup>th</sup> percentiles of the ash mass loading (Figure 7.14, top), effective particle radius (Figure 7.14, middle), and cloud top height (Figure 7.14, bottom) were analyzed. The 25<sup>th</sup>, 50<sup>th</sup>, and 75<sup>th</sup> percentiles of mass loading and effective radius generally decrease with time, consistent with ash removal (Figure 7.14, top and middle). The interquartile range of ash cloud top height generally decreases with time, indicative of removal

of lower and middle tropospheric ash (Figure 7.14, bottom). After 55 hours, the total ash mass is essentially constant at

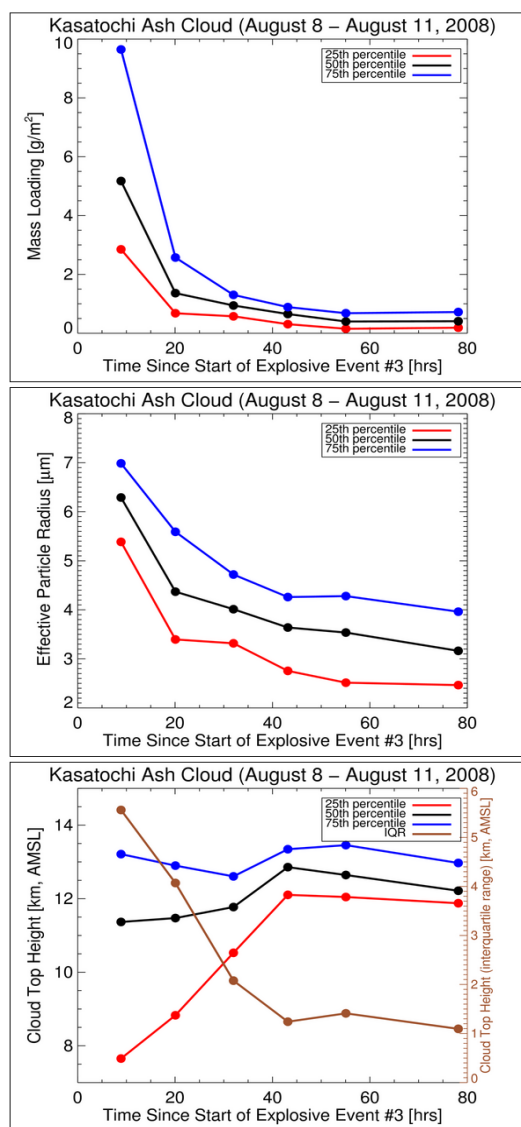


Figure 7.14: The 25<sup>th</sup> (red), 50<sup>th</sup> (black), and 75<sup>th</sup> (blue) percentiles of ash mass loading (top), effective particle radius (middle), and cloud top height (bottom) are shown as a function of time since the start of the third explosive event from the 2008 Eruption of Kasatochi. The interquartile range of cloud top height (brown) is also shown in the bottom panel.

~0.38 Tg (Figure 7.13). Further, nearly all of the detected ash is near or above the tropopause (Figure 7.14, bottom) and the median ash effective radius is indicative of a cloud dominated by smaller particles (Figure 7.14, middle). One would not expect the total ash mass to decrease significantly if much of the remaining ash is dominated by smaller particles located in the stratosphere (above most of the weather), as the terminal settling velocity of ash particles with a diameter of 15  $\mu\text{m}$  or less is only of the order  $10^{-1}$  to  $10^{-3}$  m/s [Rose and Durant 2011].

#### *7.1.4. Summary*

When applied to the 2008 Kasatochi volcanic ash cloud, the new satellite remote methods presented in this dissertation produce results that are consistent with independent observations, imagery, and physical expectations. The new remote sensing methods address some of the long-standing limitations of traditionally used methods and, as such, have a significant impact on the inferred ash cloud properties. The ash cloud area and total mass of ash were found to be significantly larger than reported in earlier studies of the Kasatochi eruption. The larger detected area and mass is mainly a result of improved ash detection at large ( $> 5$ ) and small ( $< 0.1$ ) optical depths, where traditional approaches most often fail [e.g. Pavolonis et al. 2006]. Further, previous studies concluded that sulphate particles were the dominant particulate constituent of the Kasatochi cloud within three days of the last explosive event [Krotkov et al. 2010; Karagulian et al. 2010; Prata et al. 2010]. The results derived using the new satellite remote sensing methods and independent ground-based lidar measurements are more consistent with ash being the dominant particulate composition out to about 7 days after the last explosive event. The new remote sensing methods were also used to derive an

estimate of fine ash fraction for the Kasatochi eruption. The satellite-derived fine ash fraction of  $\sim 0.01$  was much smaller than what has been used to model the Kasatochi ash cloud [Langmann et al. 2010], which likely explains why the modeled total mass of ash and ash cloud area greatly exceeds the satellite estimates. This underscores the importance of observations to better constrain model parameters.

## ***7.2. Excursion: Analysis of Ash Cloud Geometric Thickness***

Prior to the availability of CALIOP measurements (see Chapter 5), information on the vertical extent (e.g. geometric thickness) of dispersed ash clouds was simply not available. Thus, CALIOP has provided the first opportunity to characterize ash cloud geometric thickness to a meaningful extent. Figure 7.15 shows the CALIOP-derived distribution of geometric ash cloud thickness for observations of ash cloud from the 2010 eruption of Eyjafjallajökull and observations of additional ash clouds produced by a variety of eruptions including Cordon Caulle (2011), Grimsvotn (2011), Kasatochi (2008), Okmok (2008), Soufriere Hills (2010), and Redoubt (2009). The Eyjafjallajökull distribution (Figure 7.15, top) indicates that 75% of the ash layers sampled by CALIOP are less than 1 km thick. Similarly, the distribution from the other volcanic events indicates that 73% of ash layers sampled are less than 1 km thick (Figure 7.15, bottom). The majority of the ash layers sampled were well dispersed from the volcano. These results show that the majority of dispersed ash clouds have a geometric thickness that most forecast models would be unable to resolve. Thus, current dispersion model forecasts might be prone to over-estimating the vertical extent of dispersed ash clouds, which has very important implications for aviation.

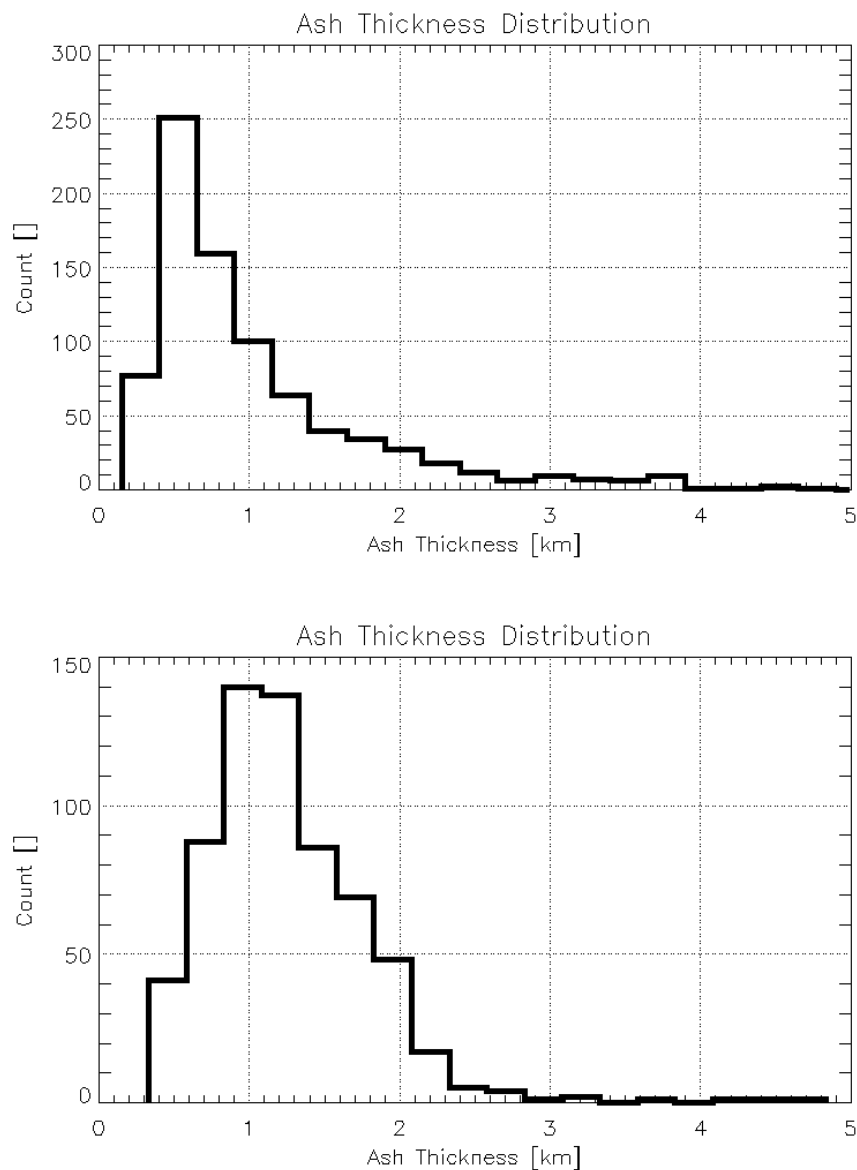


*Figure 7.15: The CALIOP-derived distribution of geometric ash cloud thickness is shown for Eyjafjallajökull observations (top) and observations of additional ash clouds produced by a variety of eruptions including Cordon Caulle (2011), Grimsvotn (2011), Kasatochi (2008), Okmok (2008), Soufriere Hills (2010), and Redoubt (2009) (bottom). The distribution shown in the top panel indicates that 75% of the ash layers sampled by CALIOP are less than 1 km thick. Similarly, the bottom panel distribution indicates that 73% of ash layers sampled are less than 1 km thick. The majority of the ash layers sampled were well dispersed from the volcano.*

## Chapter 8

### 8. Summary and Conclusions

The five objectives of this research, described in Chapter 2, were accomplished. An alternative data space that increases the sensitivity of space-based infrared measurements to cloud microphysics was developed. Traditionally, infrared brightness temperatures (BTs) and brightness temperature differences (BTDs) have been used to infer cloud composition from satellites. It was shown that BTDs are fundamentally limited and that a more physically based infrared approach can lead to significant increases in sensitivity to cloud microphysics, especially for optically thin clouds. In lieu of BTDs, a derived radiative parameter,  $\beta$ , which is directly related to particle size, habit, and composition, is utilized. This is the first study to explore the use of  $\beta$  for inferring cloud composition in the total absence of cloud vertical boundary information. The results showed that even in the absence of cloud vertical boundary information, one could significantly increase the sensitivity to cloud microphysics by converting the measured radiances to effective emissivity and constructing effective absorption optical depth ratios from a pair of spectral emissivities in the 8 – 12  $\mu\text{m}$  “window.” The increase in sensitivity to cloud microphysics is relative to brightness temperature differences (BTDs) constructed from the same spectral pairs. A paper describing this component of the research has been published Pavolonis [2010].

Multispectral satellite measurements were used to estimate the probability that a given satellite pixel contains volcanic ash and quantitatively show that the probabilities provide a more robust framework for distinguishing volcanic ash from all other features, relative to the traditional “split-window” approach. More specifically, a naïve Bayesian

approach was developed to take advantage of the volcanic ash relevant cloud composition information that the  $\beta$ -ratios derived in Chapter 3 provide. Various empirically derived multivariate classifiers were constructed by coupling  $\beta$ -ratios, computed from the radiance measured at approximately 11 and 12  $\mu\text{m}$ , with visible and near infrared measurements or  $\beta$ -ratios that are computed using other spectral channel pairs in the infrared. Several case studies showed that the naïve Bayesian approach is quite skillful even when subsets of the allowable spectral channels are utilized. In each of those cases, the statistical skill of the Bayesian approach was shown to greatly exceed the traditional “split-window” method used to detect volcanic ash.

An algorithm that utilizes infrared satellite measurements to retrieve ash cloud height, mass loading, and effective particle radius was developed. The fully automated algorithm directly retrieves the cloud radiative temperature, emissivity, and a microphysical parameter. From these retrieved parameters, the cloud radiative height, effective particle radius, optical depth, and mass loading can be derived, subject to certain assumptions. An optimal estimation framework is utilized, which allows uncertainties in the measurements and forward model to be taken into account and uncertainty estimates for each of the retrieved parameters to be determined. Background atmospheric water vapor, surface temperature, and surface emissivity are explicitly accounted for on a pixel-by-pixel basis, so the algorithm is globally applicable. In addition, the retrieval algorithm is unique because it allows the cloud temperature to be a free parameter. The retrieval algorithm is demonstrated using the Spinning Enhanced Visible and Infrared Imager (SEVIRI). Ash clouds from the 2010 eruption of Eyjafjallajökull in Iceland and the 2010 eruption of Soufriere Hills in the eastern Caribbean were analyzed, and the accuracy of

the retrieval was evaluated using spaceborne lidar measurements. The validation analysis shows that the retrieved ash cloud height, emissivity, and effective particle radius generally agrees well with lidar measurements, especially when andesite rock is used to model the cloud microphysics. The ash cloud property retrieval algorithm, which is also described in Pavolonis et al. [2013], will serve as the operational algorithm for the next generation of Geostationary Operational Environmental Satellites (GOES-R).

Building upon previous results, the Spectrally Enhanced Cloud Objects (SECO) volcanic ash detection algorithm was developed. The SECO algorithm combines radiative transfer theory, Bayesian methods, and image processing/computer vision concepts to identify volcanic ash clouds in satellite data with skill that is generally comparable to a human expert, especially with respect to false alarm rate. The volcanic ash probability determined using the naïve Bayesian approach, in combination with results from the ash cloud property retrieval algorithm, is used to identify satellite pixels that might contain volcanic ash. All pixels that potentially contain volcanic ash are sorted into cloud objects. A cloud object is a collection of spatially connected satellite pixels that meet a specified set of criteria. An ash/no ash classification is then assigned on a cloud object basis. The majority of volcanic ash clouds are composed of a small subset of pixels that are spectrally unique (e.g., very unlikely to be associated with any other feature) and a larger subset of pixels that, to varying degrees, are spectrally non-unique (e.g., can sometimes be associated with other features). In essence, a cloud object is assigned to the volcanic ash class if the object contains a specified number of pixels that exhibit a spectral signature that is unambiguously associated with volcanic ash or dust (volcanic ash and dust exhibit very similar spectral signatures in weather satellite

data). The resulting pixel level ash/no ash classification is used to screen out any ash cloud property retrievals that were performed outside of volcanic ash or dust clouds. The SECO method is globally applicable and can be applied to virtually any low earth orbit or geostationary satellite sensor. Further, the SECO approach was quantitatively proven to be more skillful than pixel based approaches, including the commonly used “split-window” technique. More specifically, the SECO method has a much higher probability of detection than the traditional “split-window” method while maintaining a near zero false alarm rate. The performance of the SECO approach is extremely promising and well suited to a variety of new and improved applications.

The SECO algorithm was applied to MODIS and the spatial and temporal evolution of the ash clouds produced by the 2008 eruption of Kasatochi volcano in Alaska was analyzed. The SECO results were found to be consistent with independent observations (lidar, true color imagery, and pilot reports), imagery, and physical expectations (e.g. area of stratospheric ash cloud should increase with time, total mass of ash should decrease with time after the end of the eruption). The SECO algorithm addresses some of the long-standing limitations of traditionally used methods and, as such, has a significant impact on the inferred ash cloud properties. The ash cloud area and total mass of ash were found to be significantly larger than reported in earlier studies of the Kasatochi eruption [Corradini et al. 2010; Prata et al. 2010]. Further, previous studies concluded that sulphate particles were the dominant particulate constituent of the Kasatochi cloud within three days of the last explosive event [Krotkov et al. 2010; Karagulian et al. 2010; Prata et al. 2010]. The results derived using the SECO algorithm and independent ground-based lidar measurements are more consistent with ash being the

dominant particulate composition out to about 7 days after the last explosive event. The SECO algorithm was also used to derive an estimate of fine ash fraction for the Kasatochi eruption. The satellite-derived fine ash fraction of  $\sim 0.01$  was much smaller than what has been used to model the Kasatochi ash cloud [Langmann et al. 2010], which likely explains why the modeled total mass of ash and ash cloud area greatly exceeds the satellite estimates. This underscores the importance of observations to better constrain model parameters.

This study has resulted in the development of a promising new theoretical framework for retrieving volcanic ash cloud properties from satellite measurements. Several components of the research can be generalized and applied to other problems such as dust cloud monitoring, SO<sub>2</sub> detection/tracking, and cloud thermodynamic phase determination. The new framework is well suited for advanced applications such as automated volcanic ash cloud alerting and constraining Eulerian and Lagrangian model forecasts of volcanic ash dispersion and removal. In fact, the SECO algorithm has already been used to develop an automated volcanic ash-alerting tool. Since May of 2013, the alerting tool has detected several eruptions that otherwise went undetected. By mid 2014 all Volcanic Ash Advisory Centers will have a subscription to the alerts. The SECO derived products have also been used in model validation studies [Bursik et al. 2012; Denlinger et al. 2012; Schmehl et al. 2012], but much more work is needed to couple observations with models.

While the SECO algorithm software was designed to allow satellite data from multiple times to be used when constructing and classifying cloud objects, this capability has yet to be explored in any detail. SECO algorithm results from previous image times

can be used to provide prior knowledge on the likely spatial locations of volcanic ash, allowing for improved ash detection at the lowest detectable optical depths and in very complex scenes. Ash cloud properties from previous times can also serve as a first guess in the optimal estimation procedure. In addition, time trends in cloud vertical growth [e.g. Cintineo et al. 2014] may offer a means to detect clouds that contain volcanic ash, but cannot be detected using spectral methods due to a combination cloud optical depth saturation and the presence of ice. The temporal evolution of cloud properties during an eruption may also allow the mass eruption rate to be determined in a fully automated objective manner [Puget et al. 2013]. Mass eruption rate is a critical input for dispersion models and current techniques to estimate mass eruption rate are based on very simple empirical relationships that are prone to large errors [Mastin et al. 2009].

Detailed comparisons to other remote sensing approaches are also an important next step. Given the complexity of satellite remote sensing algorithms, inter-comparison work must be done collaboratively through sharing of data sets and algorithm software. Fortunately, with support from the World Meteorological Organization (WMO), a volcanic ash algorithm inter-comparison and validation workshop will be held in October 2014. The SECO algorithms will be part of the inter-comparison activity. The inter-comparison activity will allow the volcanic ash remote sensing community to better characterize errors in detection and retrieval methodologies and further develop best scientific practices.

As stated in Chapter 2, the primary motivation of this research was to reduce the probability of catastrophic aircraft encounters with clouds that contain volcanic ash and enhance the economic resilience to aviation disruptions caused by volcanic eruptions.

The improved ash detection algorithm has led to the development of an automated volcanic ash-alerting tool that has helped increase the timeliness of volcanic ash advisories to aviation users. In addition, a more accurate characterization of dispersed ash clouds has been achieved, allowing aviation interests to better plan for volcanic ash related disruptions to normal operations. Nevertheless, much more work lies ahead, but with a variety of in-situ, remote sensing, and modeling efforts now well aligned and internationally coordinated, the future of volcanic cloud research is bright and full of possibilities.

## Appendix A: Derivation of the all-sky infrared radiative transfer equation

For upwelling infrared radiation, the surface reflectance term is generally quite small (Zhang and Menzel [2002]) and molecular scattering is negligible, so the top of atmosphere clear sky radiance,  $R_{clr}(\lambda)$ , can be expressed as

$$R_{clr}(\lambda) = \varepsilon_{sfc}(\lambda)B(\lambda, T_{sfc})t_{atmos}(\lambda) + R_{atmos}(\lambda). \quad [A.1]$$

In Equation [ A.1],  $\lambda$  is the wavelength,  $\varepsilon_{sfc}(\lambda)$  is the surface emissivity,  $B$  is the Planck Function,  $T_{sfc}$  is the surface temperature,  $t_{atmos}(\lambda)$  is the surface to top-of-atmosphere transmittance, and  $R_{atmos}(\lambda)$  is the integrated atmospheric radiance that is transmitted to the top of the atmosphere. Equation [ A.1] can be re-written as

$$R_{clr}(\lambda) = \varepsilon_{sfc}(\lambda)B(\lambda, T_{sfc})t_{bc}(\lambda)t_{ac}(\lambda) + R_{bc}(\lambda)t_{ac}(\lambda) + R_{ac}(\lambda). \quad [A.2]$$

In Equation [ A.2] the total column upwelling atmospheric transmittance ( $t_{atmos}$ ) and radiance ( $R_{atmos}$ ) terms are simply decomposed into “below cloud (bc)” and “above cloud (ac)” layers, which will aid in the simplification of the cloudy infrared radiative transfer equation.

Assuming, a fully cloudy field of view, a non-scattering atmosphere (no molecular scattering), and a negligible contribution from downwelling cloud emission or molecular emission that is reflected by the surface and transmitted to the top of troposphere (Zhang and Menzel [2002] showed that this term is very small at infrared wavelengths), the upwelling all-sky radiative transfer equation for a given infrared channel or wavelength can be written as in Equation [ A.3].

$$R_{obs}(\lambda) = [1 - \varepsilon_{eff}(\lambda)][\varepsilon_{sfc}(\lambda)B(T_{sfc})t_{bc}(\lambda)t_{ac}(\lambda) + R_{bc}(\lambda)t_{ac}(\lambda)] + \varepsilon_{eff}(\lambda)B(\lambda, T_{eff})t_{ac}(\lambda) + R_{ac}(\lambda) \quad [A.3]$$

In Equation [ A.3],  $R_{\text{obs}}$  is the observed radiance,  $\varepsilon_{\text{eff}}(\lambda)$  is the effective cloud emissivity, and  $T_{\text{eff}}$  is the effective cloud temperature. All other terms were previously defined. Equation [ A.2] can be used to re-write Equation [ A.3] as follows.

$$R_{\text{obs}}(\lambda) = [1 - \varepsilon_{\text{eff}}(\lambda)][R_{\text{ctr}}(\lambda) - R_{\text{ac}}(\lambda)] + \varepsilon_{\text{eff}}(\lambda)B(\lambda, T_{\text{eff}})t_{\text{ac}}(\lambda) + R_{\text{ac}}(\lambda) \quad [ A.4]$$

Finally, Equation [ A.4] is algebraically manipulated as shown in Equation [ A.5] below.

$$R_{\text{obs}}(\lambda) = \varepsilon_{\text{eff}}(\lambda)R_{\text{ac}}(\lambda) + t_{\text{ac}}(\lambda)\varepsilon_{\text{eff}}(\lambda)B(\lambda, T_{\text{eff}}) + R_{\text{ctr}}(\lambda)(1 - \varepsilon_{\text{eff}}(\lambda)) \quad [ A.5]$$

Equation [ A.5] is the form of the all-sky form of the infrared radiative transfer equation used throughout this dissertation. This is the same form of the all-sky radiative transfer equation used in Heidinger and Pavolonis [2009].

### Appendix B: Derivation of analytical of Jacobians listed in Table 3.1

The infrared radiative transfer equation can be expressed as

$$R_{obs}(\lambda) = \varepsilon_{eff}(\lambda)R_{ac}(\lambda) + t_{ac}(\lambda)\varepsilon_{eff}(\lambda)B(\lambda, T_{eff}) + R_{clr}(\lambda)(1 - \varepsilon_{eff}(\lambda)). \quad [B.1]$$

In the above equation,  $\lambda$  is wavelength,  $R_{obs}(\lambda)$  is the observed radiance,  $R_{clr}(\lambda)$  is the clear sky radiance.  $R_{ac}(\lambda)$  and  $t_{ac}(\lambda)$  are the above cloud upwelling atmospheric radiance and transmittance, respectively.  $B$  is the Planck Function,  $T_{eff}$  is the effective cloud temperature, and  $\varepsilon$  is the cloud emissivity. In the infrared, the surface reflectance term is generally quite small so the clear sky radiance,  $R_{clr}(\lambda)$ , can be expressed as

$$R_{clr}(\lambda) = \varepsilon_{sfc}(\lambda)B(\lambda, T_{sfc})t_{atmos}(\lambda) + R_{atmos}(\lambda). \quad [B.2]$$

In Equation [ B.2],  $\varepsilon_{sfc}(\lambda)$  is the surface emissivity,  $T_{sfc}$  is the surface temperature,  $t_{atmos}(\lambda)$  is the surface to top-of-atmosphere transmittance, and  $R_{atmos}(\lambda)$  is the integrated atmospheric radiance that is transmitted to the top of the atmosphere which can be approximated by Equation [ B.3].

$$R_{atmos}(\lambda) \approx R_{atmos-1}(\lambda) + B(\lambda, T_{avg})[t_{atmos-1}(\lambda) - t_{atmos}(\lambda)] \quad [B.3]$$

In Equation [ B.3],  $R_{atmos-1}(\lambda)$  is the integrated atmospheric radiance that excludes the lowest (e.g. near the surface) atmospheric layer,  $B(\lambda, T_{avg})$  is the blackbody radiance based on the average temperature of the lowest atmospheric layer, and  $t_{atmos-1}$  is the transmittance of the atmosphere excluding the lowest layer. This expression is needed when evaluating radiometric sensitivity to atmospheric transmittance.

Equation [ B.1] can be re-arranged and solved for cloud emissivity, as shown below.

$$\varepsilon_{eff}(\lambda) = \frac{R_{obs}(\lambda) - R_{clr}(\lambda)}{R_{cld}(\lambda) - R_{clr}(\lambda)} \quad [B.4]$$

In [ B.4], a new variable,  $R_{cld}$  is defined for notational convenience.

$$R_{cld}(\lambda) = R_{ac}(\lambda) + B(\lambda, T_{eff})t_{ac}(\lambda) \quad [B.5]$$

In this sensitivity analysis, it is assumed that the effective cloud temperature,  $T_{eff}$ , is equal to the tropopause temperature ( $T_{tropo}$ ). As such, the effective absorption cloud optical depth ratio using the top of troposphere assumption,  $\beta_{tot}(\lambda_N, \lambda_D)$ , is defined by:

$$\beta_{tot}(\lambda_N, \lambda_D) = \frac{\ln[1 - \varepsilon_{tot}(\lambda_N)]}{\ln[1 - \varepsilon_{tot}(\lambda_D)]} \quad [B.6]$$

The cloud emissivity calculated assuming  $T_{eff} = T_{tropo}$  is given by  $\varepsilon_{tot}$ . In addition,  $\lambda_N$  and  $\lambda_D$  represent the wavelength used in the numerator and denominator of Equation B6, respectively. For the same given pair of wavelengths,  $\lambda_N$  and  $\lambda_D$ , a brightness temperature difference (BTD) can be defined such that

$$BTD(\lambda_N, \lambda_D) = BT(\lambda_D) - BT(\lambda_N) = B^{-1}[\lambda_D, R_{obs}(\lambda_D)] - B^{-1}[\lambda_N, R_{obs}(\lambda_N)] \quad [B.7]$$

In [ B.7], BT is the brightness temperature at a given wavelength, which is determined by applying the inverse of the Planck Function ( $B^{-1}$ ) to the radiance,  $R_{obs}$ .

The spectral variation in the total clear sky atmospheric transmittance ( $\beta_{atmos}(\lambda_N, \lambda_D)$ ) and surface emissivity ( $\beta_{sfc}(\lambda_N, \lambda_D)$ ) can be captured with expressions of the same form as the ratio of effective absorption cloud optical depth.

$$\beta_{atmos}(\lambda_N, \lambda_D) = \frac{\ln[t_{atmos}(\lambda_N)]}{\ln[t_{atmos}(\lambda_D)]} \quad [B.8]$$

$$\beta_{sfc}(\lambda_N, \lambda_D) = \frac{\ln[1 - \varepsilon_{sfc}(\lambda_N)]}{\ln[1 - \varepsilon_{sfc}(\lambda_D)]} \quad [B.9]$$

We now define some common partial derivatives using Equations [ B.1] – [ B.9]. All of the symbols used in the following equations have been previously defined, with the exception of  $\partial B(\lambda)/\partial T$ , which is simply the derivative of the Planck Function with respect to temperature.

$$\frac{\partial \beta_{tot}(\lambda_N, \lambda_D)}{\partial \varepsilon_{tot}(\lambda_N)} = \frac{-1}{\ln[1.0 - \varepsilon_{tot}(\lambda_D)][1 - \varepsilon_{tot}(\lambda_N)]} \quad [B.10]$$

$$\frac{\partial \beta_{tot}(\lambda_N, \lambda_D)}{\partial \varepsilon_{tot}(\lambda_D)} = \frac{\ln[1.0 - \varepsilon_{tot}(\lambda_N)]}{\ln[1.0 - \varepsilon_{tot}(\lambda_D)]^2 [1 - \varepsilon_{tot}(\lambda_D)]} \quad [B.11]$$

$$\frac{\partial \varepsilon_{tot}(\lambda_N)}{\partial R_{obs}(\lambda_N)} = \frac{\partial \varepsilon_{tot}(\lambda_D)}{\partial R_{obs}(\lambda_D)} = \frac{1}{R_{cld}(\lambda) - R_{clr}(\lambda)} \quad [B.12]$$

$$\frac{\partial \varepsilon_{tot}(\lambda_N)}{\partial R_{clr}(\lambda_N)} = \frac{\partial \varepsilon_{tot}(\lambda_D)}{\partial R_{clr}(\lambda_D)} = \frac{\varepsilon_{cld}(\lambda)[R_{cld}(\lambda) - R_{clr}(\lambda)]}{[R_{cld\_tot}(\lambda) - R_{clr}(\lambda)]^2} - \frac{\varepsilon_{cld}(\lambda)}{R_{cld\_tot}(\lambda) - R_{clr}(\lambda)} \quad [B.13]$$

In deriving Equation [ B.13], it is important to remember to include the dependence of  $R_{obs}(\lambda)$  on  $R_{clr}(\lambda)$  (see Equations [ B.1] and [ B.4]).

$$\frac{\partial R_{obs}(\lambda_N)}{\partial \beta(\lambda_N, \lambda_D)} = \ln[1 - \varepsilon_{cld}(\lambda_D)][1 - \varepsilon_{cld}(\lambda_D)]^{\beta(\lambda_N, \lambda_D)} [R_{clr}(\lambda_N) - R_{cld}(\lambda_N)] \quad [B.14]$$

$$\frac{\partial R_{obs}(\lambda_N)}{\partial \varepsilon_{cld}(\lambda_D)} = \beta(\lambda_N, \lambda_D) [1 - \varepsilon_{cld}(\lambda_D)]^{(\beta(\lambda_N, \lambda_D) - 1)} [R_{cld}(\lambda_N) - R_{clr}(\lambda_N)] \quad [B.15]$$

$$\frac{\partial R_{obs}(\lambda_D)}{\partial \varepsilon_{cld}(\lambda_D)} = R_{cld}(\lambda_D) - R_{clr}(\lambda_D) \quad [B.16]$$

$$\frac{\partial R_{obs}(\lambda_N)}{\partial R_{clr}(\lambda_N)} = \frac{\partial R_{obs}(\lambda_D)}{\partial R_{clr}(\lambda_D)} = 1 - \varepsilon_{cld}(\lambda) \quad [B.17]$$

$$\frac{\partial R_{clr}(\lambda_N)}{\partial T_{sfc}} = \frac{\partial R_{clr}(\lambda_D)}{\partial T_{sfc}} = \varepsilon_{sfc}(\lambda) t_{atmos}(\lambda) \left( \frac{\partial B(\lambda)}{\partial T_{sfc}} \right)^{-1} \quad [B.18]$$

$$\frac{\partial R_{obs}(\lambda_N)}{\partial T_{eff}} = \frac{\partial R_{obs}(\lambda_D)}{\partial T_{eff}} = \varepsilon_{cld}(\lambda) t_{ac}(\lambda) \left( \frac{\partial B(\lambda)}{\partial T_{eff}} \right)^{-1} \quad [B.19]$$

$$\frac{\partial R_{clr}(\lambda_N)}{\partial \varepsilon_{sfc}(\lambda_D)} = \beta_{sfc}(\lambda_N, \lambda_D) [1 - \varepsilon_{sfc}(\lambda_D)]^{(\beta_{sfc}(\lambda_N, \lambda_D) - 1)} t_{atmos}(\lambda_N) B(\lambda_N, T_{sfc}) \quad [B.20]$$

$$\frac{\partial R_{clr}(\lambda_D)}{\partial \varepsilon_{sfc}(\lambda_D)} = t_{atmos}(\lambda_D) B(\lambda_D, T_{sfc}) \quad [B.21]$$

$$\frac{\partial R_{clr}(\lambda_N)}{\partial \beta_{sfc}(\lambda_N, \lambda_D)} = -\ln[1 - \varepsilon_{sfc}(\lambda_D)][1 - \varepsilon_{sfc}(\lambda_D)]^{\beta_{sfc}(\lambda_N, \lambda_D)} t_{atmos}(\lambda_N) B(\lambda_N, T_{sfc}) \quad [B.22]$$

$$\frac{\partial R_{clr}(\lambda_N)}{\partial t_{atmos}(\lambda_D)} = \beta_{atmos}(\lambda_N, \lambda_D) [t_{atmos}(\lambda_D)]^{\beta_{atmos}(\lambda_N, \lambda_D) - 1} [\varepsilon_{sfc}(\lambda_N) B(\lambda_N, T_{sfc}) - B(\lambda_N, T_{avg})] \quad [B.23]$$

$$\frac{\partial R_{clr}(\lambda_D)}{\partial t_{atmos}(\lambda_D)} = \varepsilon_{sfc}(\lambda_D) B(\lambda_D, T_{sfc}) - B(\lambda_D, T_{avg}) \quad [B.24]$$

$$\frac{\partial R_{clr}(\lambda_N)}{\partial \beta_{atmos}(\lambda_N, \lambda_D)} = \ln[t_{atmos}(\lambda_D)] [t_{atmos}(\lambda_D)]^{\beta_{atmos}(\lambda_N, \lambda_D)} [B(\lambda_N, T_{sfc}) - B(\lambda_N, T_{avg})] \quad [B.25]$$

Equations [ B.10] – [ B.25] are used to derive analytical expressions for all of the partial derivatives listed in Table 3.1 via application of the Chain Rule of calculus. For clarity, these expressions include the equation number of each previously defined derivative used, but be aware that the wavelength dependence is not shown in tandem with the equation number.

### Derivatives with respect to cloud microphysics

$$\frac{\partial BTD(\lambda_N, \lambda_D)}{\partial \beta(\lambda_N, \lambda_D)} = -\frac{\partial R_{obs}(\lambda_N)}{\partial \beta(\lambda_N, \lambda_D)} \left( \frac{\partial B(\lambda_N)}{\partial T} \right)^{-1} \quad [B.26]$$

$$= -[B.14] \left( \frac{\partial B(\lambda_N)}{\partial T} \right)^{-1}$$

$$\frac{\partial \beta_{tot}(\lambda_N, \lambda_D)}{\partial \beta(\lambda_N, \lambda_D)} = \frac{\partial \beta_{tot}(\lambda_N, \lambda_D)}{\partial \varepsilon_{tot}(\lambda_N)} \frac{\partial \varepsilon_{tot}(\lambda_N)}{\partial R_{obs}(\lambda_N)} \frac{\partial R_{obs}(\lambda_N)}{\partial \beta(\lambda_N, \lambda_D)} \quad [B.27]$$

$$= [B.10][B.12][B.14]$$

### Derivatives with respect to the effective cloud temperature

$$\begin{aligned} \frac{\partial BTD(\lambda_N, \lambda_D)}{\partial T_{eff}} &= \frac{\partial R_{obs}(\lambda_D)}{\partial T_{eff}} \left( \frac{\partial B(\lambda_D)}{\partial T} \right)^{-1} - \frac{\partial R_{obs}(\lambda_N)}{\partial T_{eff}} \left( \frac{\partial B(\lambda_N)}{\partial T} \right)^{-1} & [B.28] \\ &= [B.19] \left( \frac{\partial B(\lambda_D)}{\partial T} \right)^{-1} - [B.19] \left( \frac{\partial B(\lambda_N)}{\partial T} \right)^{-1} \end{aligned}$$

$$\begin{aligned} \frac{\partial \beta_{tot}(\lambda_N, \lambda_D)}{\partial T_{eff}} &= \frac{\partial \beta_{tot}(\lambda_N, \lambda_D)}{\partial \varepsilon_{tot}(\lambda_N)} \frac{\partial \varepsilon_{tot}(\lambda_N)}{\partial R_{obs}(\lambda_N)} \frac{\partial R_{obs}(\lambda_N)}{\partial T_{eff}} + \frac{\partial \beta_{tot}(\lambda_N, \lambda_D)}{\partial \varepsilon_{tot}(\lambda_D)} \frac{\partial \varepsilon_{tot}(\lambda_D)}{\partial R_{obs}(\lambda_D)} \frac{\partial R_{obs}(\lambda_D)}{\partial T_{eff}} & [B.29] \\ &= [B.10][B.12][B.19] + [B.11][B.12][B.19] \end{aligned}$$

### Derivatives with respect to cloud emissivity

$$\begin{aligned} \frac{\partial BTD(\lambda_N, \lambda_D)}{\partial \varepsilon_{clD}(\lambda_D)} &= \frac{\partial R_{obs}(\lambda_D)}{\partial \varepsilon_{clD}(\lambda_D)} \left( \frac{\partial B(\lambda_D)}{\partial T} \right)^{-1} - \frac{\partial R_{obs}(\lambda_N)}{\partial \varepsilon_{clD}(\lambda_D)} \left( \frac{\partial B(\lambda_N)}{\partial T} \right)^{-1} & [B.30] \\ &= [B.16] \left( \frac{\partial B(\lambda_D)}{\partial T} \right)^{-1} - [B.15] \left( \frac{\partial B(\lambda_N)}{\partial T} \right)^{-1} \end{aligned}$$

$$\begin{aligned} \frac{\partial \beta_{tot}(\lambda_N, \lambda_D)}{\partial \varepsilon_{clD}(\lambda_D)} &= \frac{\partial \beta_{tot}(\lambda_N, \lambda_D)}{\partial \varepsilon_{tot}(\lambda_N)} \frac{\partial \varepsilon_{tot}(\lambda_N)}{\partial R_{obs}(\lambda_N)} \frac{\partial R_{obs}(\lambda_N)}{\partial \varepsilon_{clD}(\lambda_D)} + \frac{\partial \beta_{tot}(\lambda_N, \lambda_D)}{\partial \varepsilon_{tot}(\lambda_D)} \frac{\partial \varepsilon_{tot}(\lambda_D)}{\partial R_{obs}(\lambda_D)} \frac{\partial R_{obs}(\lambda_D)}{\partial \varepsilon_{clD}(\lambda_D)} & [B.31] \\ &= [B.10][B.12][B.15] + [B.11][B.12][B.16] \end{aligned}$$

### Derivatives with respect to surface temperature

$$\begin{aligned} \frac{\partial BTD(\lambda_N, \lambda_D)}{\partial T_{sfc}} &= \frac{\partial R_{obs}(\lambda_D)}{\partial R_{clr}(\lambda_D)} \frac{\partial R_{clr}(\lambda_D)}{\partial T_{sfc}} \left( \frac{\partial B(\lambda_D)}{\partial T} \right)^{-1} - \frac{\partial R_{obs}(\lambda_N)}{\partial R_{clr}(\lambda_N)} \frac{\partial R_{clr}(\lambda_N)}{\partial T_{sfc}} \left( \frac{\partial B(\lambda_N)}{\partial T} \right)^{-1} & [B.32] \\ &= [B.17][B.18] \left( \frac{\partial B(\lambda_D)}{\partial T} \right)^{-1} - [B.17][B.18] \left( \frac{\partial B(\lambda_N)}{\partial T} \right)^{-1} \end{aligned}$$

$$\begin{aligned} \frac{\partial \beta_{tot}(\lambda_N, \lambda_D)}{\partial T_{sfc}} &= \frac{\partial \beta_{tot}(\lambda_N, \lambda_D)}{\partial \varepsilon_{tot}(\lambda_N)} \frac{\partial \varepsilon_{tot}(\lambda_N)}{\partial R_{clr}(\lambda_N)} \frac{\partial R_{clr}(\lambda_N)}{\partial T_{sfc}} + \frac{\partial \beta_{tot}(\lambda_N, \lambda_D)}{\partial \varepsilon_{tot}(\lambda_D)} \frac{\partial \varepsilon_{tot}(\lambda_D)}{\partial R_{clr}(\lambda_D)} \frac{\partial R_{clr}(\lambda_D)}{\partial T_{sfc}} \quad [B.33] \\ &= [B.10][B.13][B.18] + [B.11][B.13][B.18] \end{aligned}$$

### Derivatives with respect to the denominator clear sky transmittance

$$\begin{aligned} \frac{\partial BTD(\lambda_N, \lambda_D)}{\partial t_{atmos}(\lambda_D)} &= \frac{\partial R_{obs}(\lambda_D)}{\partial R_{clr}(\lambda_D)} \frac{\partial R_{clr}(\lambda_D)}{\partial t_{atmos}(\lambda_D)} \left( \frac{\partial B(\lambda_D)}{\partial T} \right)^{-1} - \frac{\partial R_{obs}(\lambda_N)}{\partial R_{clr}(\lambda_N)} \frac{\partial R_{clr}(\lambda_N)}{\partial t_{atmos}(\lambda_D)} \left( \frac{\partial B(\lambda_N)}{\partial T} \right)^{-1} \quad [B.34] \\ &= [B.17][B.24] \left( \frac{\partial B(\lambda_D)}{\partial T} \right)^{-1} - [B.17][B.23] \left( \frac{\partial B(\lambda_N)}{\partial T} \right)^{-1} \end{aligned}$$

$$\begin{aligned} \frac{\partial \beta_{tot}(\lambda_N, \lambda_D)}{\partial t_{atmos}(\lambda_D)} &= \frac{\partial \beta_{tot}(\lambda_N, \lambda_D)}{\partial \varepsilon_{tot}(\lambda_N)} \frac{\partial \varepsilon_{tot}(\lambda_N)}{\partial R_{clr}(\lambda_N)} \frac{\partial R_{clr}(\lambda_N)}{\partial t_{atmos}(\lambda_D)} + \frac{\partial \beta_{tot}(\lambda_N, \lambda_D)}{\partial \varepsilon_{tot}(\lambda_D)} \frac{\partial \varepsilon_{tot}(\lambda_D)}{\partial R_{clr}(\lambda_D)} \frac{\partial R_{clr}(\lambda_D)}{\partial t_{atmos}(\lambda_D)} \quad [B.35] \\ &= [B.10][B.13][B.23] + [B.11][B.13][B.24] \end{aligned}$$

### Derivatives with respect to the spectral variation of clear sky transmittance

$$\begin{aligned} \frac{\partial BTD(\lambda_N, \lambda_D)}{\partial \beta_{atmos}(\lambda_N, \lambda_D)} &= - \frac{\partial R_{obs}(\lambda_N)}{\partial R_{clr}(\lambda_N)} \frac{\partial R_{clr}(\lambda_N)}{\partial \beta_{atmos}(\lambda_N, \lambda_D)} \left( \frac{\partial B(\lambda_N)}{\partial T} \right)^{-1} \quad [B.36] \\ &= -[B.17][B.25] \left( \frac{\partial B(\lambda_N)}{\partial T} \right)^{-1} \end{aligned}$$

$$\begin{aligned} \frac{\partial \beta_{tot}(\lambda_N, \lambda_D)}{\partial \beta_{atmos}(\lambda_N, \lambda_D)} &= \frac{\partial \beta_{tot}(\lambda_N, \lambda_D)}{\partial \varepsilon_{tot}(\lambda_N)} \frac{\partial \varepsilon_{tot}(\lambda_N)}{\partial R_{clr}(\lambda_N)} \frac{\partial R_{clr}(\lambda_N)}{\partial \beta_{atmos}(\lambda_N, \lambda_D)} \quad [B.37] \\ &= [B.10][B.13][B.25] \end{aligned}$$

### Derivatives with respect to the denominator surface emissivity

$$\frac{\partial BTD(\lambda_N, \lambda_D)}{\partial \varepsilon_{sfc}(\lambda_D)} = \frac{\partial R_{obs}(\lambda_D)}{\partial R_{clr}(\lambda_D)} \frac{\partial R_{clr}(\lambda_D)}{\partial \varepsilon_{sfc}(\lambda_D)} \left( \frac{\partial B(\lambda_D)}{\partial T} \right)^{-1} - \frac{\partial R_{obs}(\lambda_N)}{\partial R_{clr}(\lambda_N)} \frac{\partial R_{clr}(\lambda_N)}{\partial \varepsilon_{sfc}(\lambda_D)} \left( \frac{\partial B(\lambda_N)}{\partial T} \right)^{-1} \quad [B.38]$$

$$=[B.17][B.21]\left(\frac{\partial B(\lambda_D)}{\partial T}\right)^{-1} - [B.17][B.20]\left(\frac{\partial B(\lambda_N)}{\partial T}\right)^{-1}$$

$$\frac{\partial \beta_{tot}(\lambda_N, \lambda_D)}{\partial \varepsilon_{sfc}(\lambda_D)} = \frac{\partial \beta_{tot}(\lambda_N, \lambda_D)}{\partial \varepsilon_{tot}(\lambda_N)} \frac{\partial \varepsilon_{tot}(\lambda_N)}{\partial R_{clr}(\lambda_N)} \frac{\partial R_{clr}(\lambda_N)}{\partial \varepsilon_{sfc}(\lambda_D)} + \frac{\partial \beta_{tot}(\lambda_N, \lambda_D)}{\partial \varepsilon_{tot}(\lambda_D)} \frac{\partial \varepsilon_{tot}(\lambda_D)}{\partial R_{clr}(\lambda_D)} \frac{\partial R_{clr}(\lambda_D)}{\partial \varepsilon_{sfc}(\lambda_D)} \quad [B.39]$$

$$=[B.10][B.13][B.20] + [B.11][B.13][B.21]$$

### Derivatives with respect to the spectral variation of surface emissivity

$$\frac{\partial BTD(\lambda_N, \lambda_D)}{\partial \beta_{sfc}(\lambda_N, \lambda_D)} = - \frac{\partial R_{obs}(\lambda_N)}{\partial R_{clr}(\lambda_N)} \frac{\partial R_{clr}(\lambda_N)}{\partial \beta_{sfc}(\lambda_N, \lambda_D)} \left(\frac{\partial B(\lambda_N)}{\partial T}\right)^{-1} \quad [B.40]$$

$$= -[B.17][B.22]\left(\frac{\partial B(\lambda_N)}{\partial T}\right)^{-1}$$

$$\frac{\partial \beta_{tot}(\lambda_N, \lambda_D)}{\partial \beta_{sfc}(\lambda_N, \lambda_D)} = \frac{\partial \beta_{tot}(\lambda_N, \lambda_D)}{\partial \varepsilon_{tot}(\lambda_N)} \frac{\partial \varepsilon_{tot}(\lambda_N)}{\partial R_{clr}(\lambda_N)} \frac{\partial R_{clr}(\lambda_N)}{\partial \beta_{sfc}(\lambda_N, \lambda_D)} \quad [B.41]$$

$$=[B.10][B.13][B.22]$$

Finally, all of these partial derivatives are evaluated under various assumed conditions. The magnitude of each (after proper scaling, since the units differ) can be used to assess the sensitivity of  $\beta_{tot}(\lambda_N, \lambda_D)$  and  $BTD(\lambda_N, \lambda_D)$  to local changes in the various dependent variables.

### Appendix C: Description of Volcanic Ash and Dust Detection Training Data

Year	Month	Day	Time (UTC)	Satellite	Number of Pixels	Description
2012	12	23	1515	Terra	230	Tungurahua ash plume
2012	12	22	0350	Terra	27	Tungurahua ash plume
2012	12	18	0710	Aqua	302	Tungurahua ash plume
2012	12	18	0415	Terra	13	Tungurahua ash plume
2012	12	17	1850	Aqua	322	Tungurahua ash plume
2012	12	17	1555	Terra	370	Tungurahua ash plume
2012	12	16	1805	Aqua	447	Tungurahua ash plume
2012	11	24	0755	Aqua	70	Santa Maria ash plume
2012	08	24	1525	Terra	170	Tungurahua ash plume
2012	08	23	1620	Terra	35	Tungurahua ash plume
2012	08	21	1925	Aqua	1966	Tungurahua ash plume
2012	08	21	1630	Terra	1427	Tungurahua ash plume
2012	08	21	0705	Aqua	13927	Tungurahua ash plume
2012	08	21	0410	Terra	3628	Tungurahua ash plume
2012	08	20	1845	Aqua	2519	Tungurahua ash plume
2012	08	20	1550	Terra	1924	Tungurahua ash plume
2012	08	20	0625	Aqua	5025	Tungurahua ash plume
2012	08	20	0325	Terra	16787	Tungurahua ash plume
2012	08	19	1940	Aqua	482	Tungurahua ash plume
2012	08	19	1505	Terra	493	Tungurahua ash plume
2012	08	19	0720	Aqua	1699	Tungurahua ash plume
2012	08	19	0420	Terra	1779	Tungurahua ash plume
2012	08	18	1855	Aqua	2424	Tungurahua ash plume
2012	08	18	1600	Terra	10604	Tungurahua ash plume
2012	08	18	0635	Aqua	1055	Tungurahua ash plume
2012	08	18	0340	Terra	1590	Tungurahua ash plume
2012	08	17	1815	Aqua	81	Tungurahua ash plume
2012	08	17	1515	Terra	229	Tungurahua ash plume
2012	08	17	0730	Aqua	143	Tungurahua ash plume
2012	08	16	1910	Aqua	410	Tungurahua ash plume
2012	08	16	1610	Terra	1138	Tungurahua ash plume
2012	08	16	0645	Aqua	446	Tungurahua ash plume
2012	08	16	0350	Terra	262	Tungurahua ash plume
2012	08	15	0305	Terra	353	Tungurahua ash plume
2012	08	14	1920	Aqua	35	Tungurahua ash plume
2012	05	23	1555	Terra	255	Tungurahua ash plume
2012	05	02	1830	Aqua	24	Tungurahua ash plume
2012	05	02	1535	Terra	55	Tungurahua ash plume
2012	03	26	1815	Aqua	129	Tungurahua ash plume
2012	03	26	1515	Terra	248	Tungurahua ash plume
2012	02	24	0635	Aqua	77	Tungurahua ash plume
2012	02	24	0340	Terra	247	Tungurahua ash plume
2011	12	24	0325	Terra	14	Tungurahua ash plume
2011	12	22	1855	Aqua	1284	Tungurahua ash and so2 plume
2011	12	22	1600	Terra	1381	Tungurahua ash plume
2011	12	08	1845	Aqua	64	Tungurahua ash plume
2011	12	08	1550	Terra	42	Tungurahua ash plume
2011	12	08	1545	Terra	95	Tungurahua ash plume
2011	12	06	1855	Aqua	80	Tungurahua ash plume
2011	12	06	0635	Aqua	172	Tungurahua ash plume
2011	12	06	0340	Terra	34	Tungurahua ash plume
2011	12	05	1515	Terra	51	Tungurahua ash plume
2011	12	04	1910	Aqua	296	Tungurahua ash plume
2011	12	04	1610	Terra	1532	Tungurahua ash plume
2011	12	04	0645	Aqua	4849	Tungurahua ash plume
2011	12	04	0350	Terra	2199	Tungurahua ash plume
2011	12	03	1825	Aqua	1557	Tungurahua ash plume

Year	Month	Day	Time (UTC)	Satellite	Number of Pixels	Description
2011	12	03	1530	Terra	2659	Tungurahua ash plume
2011	12	01	1540	Terra	422	Tungurahua ash plume
2011	12	01	0320	Terra	26	Tungurahua ash plume
2011	11	29	1850	Aqua	72	Tungurahua ash plume
2011	11	28	1510	Terra	124	Tungurahua ash plume
2011	11	28	0430	Terra	34	Tungurahua ash plume
2011	08	03	0135	Aqua	1655	Shiveluch ash plume
2011	07	19	0220	Aqua	2347	Kizimen ash plume
2011	07	19	0030	Terra	2134	Kizimen ash plume
2011	05	24	0400	Terra	24	Tungurahua ash plume
2011	05	23	1835	Aqua	12	Tungurahua ash plume
2011	05	23	1540	Terra	25	Tungurahua ash plume
2011	05	23	1400	Aqua	21938	Grimsvotn ash cloud; explosive
2011	05	05	1850	Aqua	73	Tungurahua ash plume
2011	05	05	1555	Terra	54	Tungurahua ash plume
2011	05	05	0630	Aqua	81	Tungurahua ash plume
2011	05	03	0640	Aqua	1629	Tungurahua ash plume
2011	05	03	0345	Terra	343	Tungurahua ash plume
2011	05	02	1820	Aqua	139	Tungurahua ash plume
2011	05	02	1525	Terra	1010	Tungurahua ash plume
2011	05	01	1915	Aqua	2309	Tungurahua ash plume
2011	05	01	1620	Terra	1200	Tungurahua ash plume
2011	05	01	0655	Aqua	380	Tungurahua ash plume
2011	04	30	1830	Aqua	193	Tungurahua ash plume
2011	04	30	1535	Terra	502	Tungurahua ash and so2 plume
2011	04	30	0610	Aqua	331	Tungurahua ash and so2 plume
2011	04	30	0315	Terra	940	Tungurahua ash and so2 plume
2011	04	29	1925	Aqua	45	Tungurahua ash plume
2011	04	29	0705	Aqua	663	Tungurahua ash and so2 plume
2011	04	28	1845	Aqua	62	Tungurahua ash plume
2011	04	28	1550	Terra	224	Tungurahua ash plume
2011	04	28	0625	Aqua	84	Tungurahua ash plume
2011	04	28	0325	Terra	344	Tungurahua ash plume
2011	04	25	1815	Aqua	447	Tungurahua ash plume
2011	04	25	1515	Terra	607	Tungurahua ash plume
2011	04	24	1910	Aqua	1380	Tungurahua ash plume
2011	04	24	1610	Terra	1715	Tungurahua ash plume
2011	04	24	0645	Aqua	1384	Tungurahua ash plume
2011	04	24	0350	Terra	215	Tungurahua ash plume
2011	04	23	1825	Aqua	85	Tungurahua ash plume
2011	04	23	1530	Terra	488	Tungurahua ash plume
2011	04	22	0700	Aqua	59	Tungurahua ash plume
2011	04	22	0400	Terra	83	Tungurahua ash plume
2011	04	21	1840	Aqua	19	Tungurahua ash plume
2011	04	21	1540	Terra	276	Tungurahua ash plume
2011	04	21	0320	Terra	30	Tungurahua ash plume
2011	02	24	1100	Terra	4595	Kizimen ash plume
2011	02	24	0135	Aqua	6583	Kizimen ash and so2 plume
2011	02	10	0125	Aqua	253	Kizimen ash plume
2011	02	10	0110	Terra	226	Kizimen ash plume
2011	02	09	0030	Terra	666	Kizimen ash and so2 plume
2011	02	02	1540	Aqua	1408	Kizimen ash plume
2011	02	02	1135	Terra	1254	Kizimen ash and so2 plume
2011	02	02	0210	Aqua	7417	Kizimen ash and so2 plume
2011	02	02	0025	Terra	6576	Kizimen ash and so2 plume
2011	02	01	1500	Aqua	9289	Kizimen ash and so2 plume
2011	02	01	1055	Terra	5331	Kizimen ash and so2 plume
2011	02	01	0130	Aqua	6722	Kizimen ash and so2 plume
2011	01	31	2340	Terra	3241	Kizimen ash and so2 plume
2011	01	31	1555	Aqua	9118	Kizimen ash and so2 plume

Year	Month	Day	Time (UTC)	Satellite	Number of Pixels	Description
2011	01	31	1010	Terra	2776	Kizimen ash and so2 plume
2011	01	31	0225	Aqua	3349	Kizimen ash and so2 plume
2011	01	31	0035	Terra	5507	Kizimen ash and so2 plume
2011	01	27	1035	Terra	768	Kizimen ash and so2 plume
2011	01	27	0250	Aqua	1609	Kizimen ash and so2 plume
2011	01	27	0110	Aqua	1730	Kizimen ash and so2 plume
2011	01	27	0100	Terra	2574	Kizimen ash and so2 plume
2011	01	26	1535	Aqua	3463	Kizimen ash plume
2011	01	26	1130	Terra	2979	Kizimen ash plume
2011	01	25	0125	Aqua	1896	Kizimen ash plume
2011	01	25	0110	Terra	2345	Kizimen ash plume
2011	01	24	1550	Aqua	1907	Kizimen ash and so2 plume
2011	01	24	1005	Terra	2050	Kizimen ash and so2 plume
2011	01	24	0220	Aqua	5542	Kizimen ash and so2 plume
2011	01	24	0030	Terra	5105	Kizimen ash and so2 plume
2011	01	21	1640	Terra	2669	Fuego ash plume
2011	01	11	0110	Aqua	160	Kizimen ash plume
2011	01	11	0100	Terra	200	Kizimen ash plume
2011	01	09	1455	Aqua	1466	Kizimen ash and so2 plume
2011	01	09	1045	Terra	1090	Kizimen ash plume
2011	01	05	1520	Aqua	1332	Kizimen ash plume
2011	01	05	1515	Aqua	5505	Kizimen ash plume
2011	01	05	1110	Terra	11322	Kizimen ash and so2 plume
2011	01	05	0145	Aqua	2951	Kizimen ash and so2 cloud
2011	01	05	0000	Terra	1231	Kizimen ash and so2 plume
2011	01	01	1135	Terra	2678	Kizimen ash plume
2010	12	24	1825	Aqua	1864	Merapi ash plume; explosive
2010	12	24	0600	Aqua	758	Merapi ash plume; explosive
2010	12	24	0310	Terra	1169	Merapi ash cloud; explosive
2010	12	08	1915	Aqua	6019	Tungurahua ash plume
2010	12	08	1620	Terra	3029	Tungurahua ash plume
2010	12	06	1630	Terra	6898	Tungurahua ash plume
2010	12	06	0705	Aqua	1951	Tungurahua ash plume
2010	12	05	1845	Aqua	5842	Tungurahua ash plume
2010	12	05	1550	Terra	5482	Tungurahua ash plume
2010	12	05	0625	Aqua	139	Tungurahua ash plume
2010	11	11	0620	Aqua	5359	Merapi ash cloud; explosive
2010	11	08	0550	Aqua	389	Merapi ash plume; explosive
2010	11	06	1825	Aqua	559	Merapi ash and so2 plume; explosive
2010	11	03	0230	Aqua	207	Kliuchevskoi ash plume
2010	10	29	1540	Aqua	3116	Shiveluch ash and so2 cloud
2010	10	29	1135	Terra	645	Shiveluch ash and so2 cloud
2010	10	28	1500	Aqua	44067	Shiveluch ash and so2 cloud
2010	10	28	0915	Terra	6553	Shiveluch ash and so2 cloud
2010	10	28	0130	Aqua	8954	Shiveluch ash and so2 cloud
2010	10	27	2340	Terra	6438	Shiveluch ash and so2 cloud
2010	10	23	0250	Aqua	2829	Kliuchevskoi ash cloud
2010	09	11	0210	Aqua	2101	Kliuchevskoi ash plume
2010	06	01	1620	Aqua	1300	Bezymianny ash and so2 cloud
2010	06	01	1035	Terra	2786	Bezymianny ash and so2 cloud
2010	06	01	0250	Aqua	4056	Bezymianny ash and so2 cloud
2010	05	31	1535	Aqua	2063	Bezymianny ash and so2 cloud
2010	05	12	2235	Terra	27854	Eyjafjallajokull ash cloud; explosive
2010	05	12	1300	Terra	2919	Eyjafjallajokull ash cloud; explosive
2010	05	12	1255	Terra	5849	Eyjafjallajokull ash cloud; explosive
2010	05	12	0335	Aqua	21996	Eyjafjallajokull ash cloud; explosive
2010	05	11	2325	Terra	16056	Eyjafjallajokull ash cloud; explosive
2010	05	11	1405	Aqua	18771	Eyjafjallajokull ash cloud; explosive
2010	05	11	1215	Terra	20987	Eyjafjallajokull ash cloud; explosive
2010	05	11	0430	Aqua	5175	Eyjafjallajokull ash cloud; explosive

Year	Month	Day	Time (UTC)	Satellite	Number of Pixels	Description
2010	05	10	2245	Terra	8194	Eyjafjallajokull ash cloud; explosive
2010	05	10	1320	Aqua	4273	Eyjafjallajokull ash cloud; explosive
2010	05	10	1310	Terra	24877	Eyjafjallajokull ash cloud; explosive
2010	05	10	0350	Aqua	38768	Eyjafjallajokull ash cloud; explosive
2010	05	10	0345	Aqua	2152	Eyjafjallajokull ash cloud; explosive
2010	05	09	2205	Terra	4502	Eyjafjallajokull ash cloud; explosive
2010	05	09	1415	Aqua	33689	Eyjafjallajokull ash cloud; explosive
2010	05	09	1230	Terra	25994	Eyjafjallajokull ash cloud; explosive
2010	05	09	1225	Terra	64770	Eyjafjallajokull ash cloud; explosive
2010	05	09	0305	Aqua	69858	Eyjafjallajokull ash cloud; explosive
2010	05	08	2300	Terra	11110	Eyjafjallajokull ash cloud; explosive
2010	05	08	2255	Terra	59853	Eyjafjallajokull ash cloud; explosive
2010	05	08	1335	Aqua	65553	Eyjafjallajokull ash cloud; explosive
2010	05	08	1325	Terra	29261	Eyjafjallajokull ash cloud; explosive
2010	05	08	1320	Terra	15909	Eyjafjallajokull ash cloud; explosive
2010	05	08	0400	Aqua	88837	Eyjafjallajokull ash cloud; explosive
2010	05	07	2215	Terra	48393	Eyjafjallajokull ash cloud; explosive
2010	05	07	1430	Aqua	44382	Eyjafjallajokull ash cloud; explosive
2010	05	07	1425	Aqua	64872	Eyjafjallajokull ash cloud; explosive
2010	05	07	1240	Terra	28546	Eyjafjallajokull ash cloud; explosive
2010	05	07	0315	Aqua	87406	Eyjafjallajokull ash cloud; explosive
2010	05	06	2310	Terra	68957	Eyjafjallajokull ash cloud; explosive
2010	05	06	1350	Aqua	13491	Eyjafjallajokull ash cloud; explosive
2010	05	06	1345	Aqua	34968	Eyjafjallajokull ash cloud; explosive
2010	02	12	1800	Aqua	87005	Soufriere Hills ash cloud (small so2)
2010	02	12	0530	Aqua	244908	Soufriere Hills ash cloud (small so2)
2010	01	02	1810	Aqua	556	Soufriere Hills ash plume
2010	01	02	0535	Aqua	2018	Soufriere Hills ash plume
2009	12	30	1735	Aqua	9335	Soufriere Hills ash plume
2009	06	18	0230	Aqua	27898	Sarychev ash and so2 cloud; explosive
2009	06	17	1655	Aqua	103921	Sarychev ash and so2 cloud; explosive
2009	06	17	0325	Aqua	34003	Sarychev ash and so2 cloud; explosive
2009	06	17	0320	Aqua	260643	Sarychev ash and so2 cloud; explosive
2009	06	16	1615	Aqua	100575	Sarychev ash and so2 cloud; explosive
2009	06	16	1610	Aqua	138514	Sarychev ash and so2 cloud; explosive
2009	06	16	0240	Aqua	38598	Sarychev ash and so2 cloud; explosive
2009	06	16	0100	Aqua	7999	Sarychev ash and so2 cloud; explosive
2009	06	15	1710	Aqua	8785	Sarychev ash and so2 cloud; explosive
2009	06	15	1705	Aqua	20739	Sarychev ash and so2 cloud; explosive
2009	06	15	1530	Aqua	103888	Sarychev ash and so2 cloud; explosive
2009	06	15	0335	Aqua	68254	Sarychev ash and so2 cloud; explosive
2009	06	15	0155	Aqua	32417	Sarychev ash and so2 cloud; explosive
2009	06	14	1625	Aqua	103037	Sarychev ash and so2 cloud; explosive
2009	06	14	0250	Aqua	118930	Sarychev ash and so2 cloud; explosive
2009	06	13	0210	Aqua	20679	Sarychev ash and so2 cloud; explosive
2009	04	04	2235	Aqua	61595	Redoubt ash and so2 cloud
2009	04	02	1310	Aqua	283	Redoubt ash plume
2009	04	01	2345	Aqua	160	Redoubt ash plume
2009	04	01	2205	Aqua	638	Redoubt ash plume
2009	04	01	1230	Aqua	363	Redoubt ash plume
2009	03	27	2325	Aqua	914	Redoubt ash and so2 cloud
2009	03	27	1210	Aqua	10830	Redoubt ash and so2 cloud
2009	03	26	2240	Aqua	28619	Redoubt ash and so2 cloud
2009	03	24	2255	Aqua	22978	Redoubt ash and so2 cloud
2009	03	24	2115	Aqua	23368	Redoubt ash and so2 cloud
2009	03	24	1315	Aqua	18891	Redoubt ash and so2 cloud
2009	03	24	1140	Aqua	3645	Redoubt ash and so2 cloud
2009	03	23	2210	Aqua	23546	Redoubt ash and so2 cloud
2009	03	23	1235	Aqua	21040	Redoubt ash and so2 cloud
2008	08	16	1905	Aqua	2727	Okmok ash and so2 cloud; explosive

Year	Month	Day	Time (UTC)	Satellite	Number of Pixels	Description
2008	08	15	2005	Aqua	13416	Okmok ash and so2 cloud; explosive
2008	08	14	2100	Aqua	72431	Okmok ash and so2 cloud; explosive
2008	08	13	2155	Aqua	31413	Okmok ash and so2 cloud; explosive
2008	08	11	2205	Aqua	87392	Okmok ash and so2 cloud; explosive
2008	08	10	2300	Aqua	130684	Okmok ash and so2 cloud; explosive
2008	08	10	2255	Aqua	31471	Okmok ash and so2 cloud; explosive
2008	08	10	1330	Aqua	21885	Okmok ash and so2 cloud; explosive
2008	08	09	2355	Aqua	342388	Okmok ash and so2 cloud; explosive
2008	08	09	1245	Aqua	262509	Okmok ash and so2 cloud; explosive
2008	08	08	2315	Aqua	51614	Okmok ash and so2 cloud; explosive
2008	08	08	1340	Aqua	96015	Okmok ash and so2 cloud; explosive
2008	07	29	1425	Terra	10090	Soufriere Hills ash and so2 cloud
2008	07	29	0635	Aqua	1525	Soufriere Hills ash and so2 plume
2008	07	14	2320	Aqua	218571	Okmok ash and so2 cloud; explosive
2008	07	13	2235	Aqua	22108	Okmok ash and so2 cloud; explosive
2008	07	13	1305	Aqua	48560	Okmok ash and so2 cloud; explosive
2008	07	13	1300	Aqua	6936	Okmok ash and so2 cloud; explosive
2008	07	13	0855	Terra	47319	Okmok ash and so2 cloud; explosive
2008	07	12	2330	Aqua	420	Okmok ash cloud; explosive
2008	05	06	1915	Aqua	38988	Chaiten ash and so2 cloud; explosive
2008	05	06	1735	Aqua	14250	Chaiten ash and so2 cloud; explosive
2008	05	06	0540	Aqua	100295	Chaiten ash and so2 cloud; explosive
2008	05	06	0400	Aqua	39808	Chaiten ash and so2 cloud; explosive
2008	05	05	1830	Aqua	175343	Chaiten ash and so2 cloud; explosive
2008	05	05	0455	Aqua	32396	Chaiten ash and so2 cloud; explosive
2008	05	05	0315	Aqua	377022	Chaiten ash and so2 cloud; explosive
2008	05	04	1750	Aqua	61637	Chaiten ash and so2 cloud; explosive
2008	05	04	0550	Aqua	71127	Chaiten ash and so2 cloud; explosive
2008	05	04	0415	Aqua	158763	Chaiten ash and so2 cloud; explosive
2008	05	03	1845	Aqua	53610	Chaiten ash and so2 cloud; explosive
2008	05	03	0510	Aqua	78957	Chaiten ash and so2 cloud; explosive
2006	05	24	0000	Aqua	450	Cleveland ash and so2 plume
2006	01	29	2235	Aqua	7575	Augustine ash and so2 cloud
2006	01	29	2225	Terra	4196	Augustine ash and so2 cloud
2006	01	29	2045	Terra	12556	Augustine ash and so2 cloud
2006	01	29	1255	Aqua	1092	Augustine ash and so2 cloud
2006	01	29	0715	Terra	3374	Augustine ash and so2 cloud
2006	01	28	2330	Aqua	1210	Augustine ash and so2 cloud
2006	01	28	2140	Terra	1645	Augustine ash and so2 cloud
2006	01	28	1215	Aqua	3256	Augustine ash and so2 cloud
2006	01	28	0810	Terra	3727	Augustine ash and so2 cloud
2006	01	14	2130	Terra	10172	Augustine ash and so2 cloud
2006	01	14	1200	Aqua	21606	Augustine ash and so2 cloud
2006	01	14	0800	Terra	20355	Augustine ash and so2 cloud
2006	01	13	2235	Aqua	5874	Augustine ash and so2 cloud
2006	01	13	2225	Terra	3301	Augustine ash and so2 cloud
2006	01	13	2045	Terra	1977	Augustine ash and so2 cloud
2005	11	25	2225	Aqua	84077	Karthala ash cloud
2005	11	25	1925	Terra	74758	Karthala ash cloud
2005	11	25	1000	Aqua	3722	Karthala ash cloud
2005	11	25	0710	Terra	18570	Karthala ash cloud
2004	01	09	0435	Terra	1616	Fuego ash plume
2003	09	22	0830	Terra	15358	Katmai ash resuspension
2003	09	22	0655	Terra	11279	Katmai ash resuspension
2003	09	21	2305	Aqua	19473	Katmai ash resuspension
2003	09	21	2115	Terra	19045	Katmai ash resuspension
2003	09	21	1150	Aqua	8165	Katmai ash resuspension
2003	09	21	0750	Terra	7306	Katmai ash resuspension
2002	10	27	2100	Terra	36082	Etna ash plume
2002	10	27	1135	Aqua	12677	Etna ash plume

Year	Month	Day	Time (UTC)	Satellite	Number of Pixels	Description
2002	10	27	1000	Terra	21113	Etna ash plume
2002	09	26	1500	Terra	15866	Ruang ash and so2 cloud; explosive
2002	09	26	0530	Aqua	21960	Ruang ash and so2 cloud; explosive
2002	09	25	1710	Aqua	39819	Ruang ash and so2 cloud; explosive
2002	09	25	1415	Terra	46634	Ruang ash and so2 cloud; explosive
2002	09	25	0155	Terra	1107	Ruang ash and so2 cloud; explosive
2001	07	23	2140	Terra	31821	Etna ash plume
2001	07	23	1035	Terra	5557	Etna ash plume
<b>Total Number of Ash Pixels</b>					<b>6,505,254</b>	
2010	05	03	2125	Aqua	6687	North American dust
2009	09	24	1430	Aqua	43473	Australian dust
2009	09	24	1425	Aqua	40731	Australian dust
2009	09	24	0335	Aqua	101986	Australian dust
2009	09	24	0330	Aqua	71484	Australian dust
2009	09	22	0340	Aqua	9559	Australian dust
2009	07	04	0255	Aqua	31503	African dust
2009	07	03	1625	Aqua	46463	African dust
2009	07	02	1545	Aqua	11633	African dust
2009	07	02	1540	Aqua	150008	African dust
2009	07	02	1405	Aqua	14585	African dust
2009	07	02	0450	Aqua	93439	African dust
2009	07	02	0310	Aqua	69159	African dust
2009	07	01	1500	Aqua	60722	African dust
2009	07	01	1455	Aqua	128702	African dust
2009	07	01	0405	Aqua	34036	African dust
2009	07	01	0230	Aqua	31562	African dust
2009	07	01	0225	Aqua	42559	African dust
2008	05	03	1435	Terra	12131	Asian dust
2008	03	02	1745	Aqua	23528	Asian dust
2007	06	26	1810	Aqua	28613	African dust
2007	06	25	1730	Aqua	129038	African dust
2007	06	25	1725	Aqua	64059	African dust
2007	06	25	0500	Aqua	67841	African dust
2007	06	25	0455	Aqua	196900	African dust
2007	06	24	1645	Aqua	111679	African dust
2007	06	24	0415	Aqua	105774	African dust
2007	06	23	1600	Aqua	314085	African dust
2007	06	23	0510	Aqua	32590	African dust
2007	06	23	0335	Aqua	199801	African dust
2007	06	23	0330	Aqua	144372	African dust
2007	06	22	1515	Aqua	356340	African dust
2007	06	22	0425	Aqua	13447	African dust
2007	06	22	0250	Aqua	412780	African dust
2007	05	01	1050	Aqua	10535	African dust
2007	01	04	0255	Aqua	48481	African dust
2007	01	03	1440	Aqua	162013	African dust
2007	01	02	0305	Aqua	206049	African dust
2007	01	01	1455	Aqua	35570	African dust
<b>Total Number of Dust Pixels</b>					<b>3,663,917</b>	
<b>Total Number of Ash + Dust Pixels</b>					<b>10,169,171</b>	

## Appendix D: Cloud Property Retrieval Kernel Matrix

Given the choice of forward model, an analytical expression for each element of the kernel matrix,  $\mathbf{K}$ , can be derived from Equations ( 5.1) – ( 5.3), ( 5.6) - ( 5.10), and the Planck Function. The derivative of each of the forward model simulated observations with respect to  $T_{\text{eff}}$  is given by the following set of equations. In these equations,  $\partial B(\lambda)/\partial T_{\text{eff}}$  is the derivative of the Planck Function with respect to the effective cloud temperature,  $T_{\text{eff}}$ , and  $\partial B(\lambda)/\partial T$  is the derivative of the Planck Function with respect to the forward model derived brightness temperature. All other symbols were defined in Chapter 5.

$$\frac{\partial BT(11\mu\text{m})}{\partial T_{\text{eff}}} = \varepsilon(11\mu\text{m})t_{\text{oc}}(11\mu\text{m})\left(\frac{\partial B(11\mu\text{m})}{\partial T_{\text{eff}}}\right)\left(\frac{\partial B(11\mu\text{m})}{\partial T}\right)^{-1} \quad [D.1]$$

$$\frac{\partial BTD(11-12\mu\text{m})}{\partial T_{\text{eff}}} = \frac{\partial BT(11\mu\text{m})}{\partial T_{\text{eff}}} - \varepsilon(12\mu\text{m})t_{\text{oc}}(12\mu\text{m})\left(\frac{\partial B(12\mu\text{m})}{\partial T_{\text{eff}}}\right)\left(\frac{\partial B(12\mu\text{m})}{\partial T}\right)^{-1} \quad [D.2]$$

$$\frac{\partial BTD(11-13.3\mu\text{m})}{\partial T_{\text{eff}}} = \frac{\partial BT(11\mu\text{m})}{\partial T_{\text{eff}}} - \varepsilon(13.3\mu\text{m})t_{\text{oc}}(13.3\mu\text{m})\left(\frac{\partial B(13.3\mu\text{m})}{\partial T_{\text{eff}}}\right)\left(\frac{\partial B(13.3\mu\text{m})}{\partial T}\right)^{-1} \quad [D.3]$$

The following equations give the derivative of each forward model simulation with respect to  $\varepsilon(11\mu\text{m})$ .

$$\frac{\partial BT(11\mu\text{m})}{\partial \varepsilon(11\mu\text{m})} = [R_{\text{cl}d}(11\mu\text{m}) - R_{\text{cl}r}(11\mu\text{m})]\left(\frac{\partial B(11\mu\text{m})}{\partial T}\right)^{-1} \quad [D.4]$$

$$\frac{\partial BTD(11-12\mu m)}{\partial \varepsilon(11\mu m)} = \quad [D.5]$$

$$\frac{\partial BT(11\mu m)}{\partial \varepsilon(11\mu m)} - [R_{cld}(12\mu m) - R_{clr}(12\mu m)][\beta(12/11\mu m)(1 - \varepsilon(11\mu m))^{\beta(12/11\mu m)-1}] \left( \frac{\partial B(12\mu m)}{\partial T} \right)^{-1}$$

$$\frac{\partial BTD(11-13.3\mu m)}{\partial \varepsilon(11\mu m)} = \quad [D.6]$$

$$\frac{\partial BT(11\mu m)}{\partial \varepsilon(11\mu m)} - [R_{cld}(13.3\mu m) - R_{clr}(13.3\mu m)][\beta(13.3/11\mu m)(1 - \varepsilon(11\mu m))^{\beta(13.3/11\mu m)-1}] \left( \frac{\partial B(13.3\mu m)}{\partial T} \right)^{-1}$$

Finally, the derivative of each forward model simulation with respect to  $\beta(12/11\mu m)$  is given by the following equations. In Equation [ D.9],  $\partial\beta(13.3/11\mu m)/\partial\beta(12/11\mu m)$  is applied to Equation ( 5.11).

$$\frac{\partial BT(11\mu m)}{\partial \beta(12/11\mu m)} = 0.0 \quad [D.7]$$

$$\frac{\partial BTD(11-12\mu m)}{\partial \beta(12/11\mu m)} = [R_{cld}(12\mu m) - R_{clr}(12\mu m)] \ln[1 - \varepsilon(11\mu m)][1 - \varepsilon(12\mu m)] \left( \frac{\partial B(12\mu m)}{\partial T} \right)^{-1} \quad [D.8]$$

$$\frac{\partial BTD(11-13.3\mu m)}{\partial \beta(12/11\mu m)} = \quad [D.9]$$

$$[R_{cld}(13.3\mu m) - R_{clr}(13.3\mu m)] \ln[1 - \varepsilon(11\mu m)][1 - \varepsilon(13.3\mu m)] \left( \frac{\partial \beta(13.3/11\mu m)}{\partial \beta(12/11\mu m)} \right) \left( \frac{\partial B(13.3\mu m)}{\partial T} \right)^{-1}$$

## Appendix E: Cloud Object Membership Criteria

Cloud object membership is granted to a given satellite pixel if the ash/dust posterior probability  $[P(C_{yes}|\mathbf{F})]$  exceeds *any* of the five thresholds defined by Equation [ E.1], [ E.3], [ E.4], [ E.5], and [ E.6]. The first probability threshold ( $P_{thresh1}$ ) is determined through sequential evaluation of the conditions listed in Equation [ E.1] (the evaluation stops once a true condition on the right hand side is encountered). In Equation [ E.1],  $\epsilon_{tot}(11\mu m)$  is the 11  $\mu m$  top of troposphere emissivity (see Chapters 3 and 4),  $\epsilon_{err}(11\mu m)$  is the 11  $\mu m$  ash/dust cloud emissivity retrieval uncertainty divided by the first guess uncertainty (see Chapter 5), and  $BTD(11-12\mu m)$  is the 11 – 12  $\mu m$  brightness temperature difference.

$$P_{thresh1} = \begin{cases} 1\%, & \epsilon_{tot}(11\mu m) \geq 0.25 \text{ or } BTD(11-12\mu m) < -0.5K \\ 1\%, & \epsilon_{err}(11\mu m) \leq 0.40 \\ 5\%, & 0.40 < \epsilon_{err}(11\mu m) \leq 0.50 \\ 10\%, & 0.50 < \epsilon_{err}(11\mu m) \leq 0.70 \\ 90\%, & 0.70 < \epsilon_{err}(11\mu m) \leq 0.90 \\ 95\%, & \textit{otherwise} \end{cases} \quad [ E.1]$$

The second probability threshold ( $P_{thresh2}$ ) depends on the difference between the  $BTD(11-12\mu m)$  at the pixel of interest ( $BTD_o$ ) and the mean  $BTD(11-12\mu m)$  at locations within 25 km that have a  $P(C_{yes}|\mathbf{F})$  that is less than  $1.0e^{-6}\%$  ( $BTD_{region}$ ) and a  $\epsilon_{tot}(11\mu m)$  that differs by no more than 1/3 of the  $\epsilon_{tot}(11\mu m)$  value at the pixel of interest. Absolute  $[DBTD_{abs} = BTD_{region} - BTD_o]$  and relative  $[DBTD_{rel} = (BTD_{region} - BTD_o) / BTD_{region}]$  differences are computed and a decision tree equivalent to Equation [ E.2], evaluated in sequential order (the evaluation stops once a true condition on the right hand side is encountered), is executed.

$$\text{Condition2} = \begin{cases} \text{False, } BTD(11-12\mu\text{m}) > 2.0K \\ \text{False, } \varepsilon_{tot}(11\mu\text{m}) < 0.001 \text{ or } \varepsilon_{tot}(11\mu\text{m}) > 0.25 \\ \text{False, } \varepsilon(11\mu\text{m}) > 0.50 \\ \text{False, } BT_{sdev}(11\mu\text{m}) > 2.0K \\ \text{False, } N_{25km} < 5 \\ \text{False, } DBTD_{abs} < 0.25K \\ \text{True, } DBTD_{rel} < 0.25K \text{ and } \varepsilon_{err}(11\mu\text{m}) < 0.30 \\ \text{True, } DBTD_{rel} < 0.30K \text{ and } \varepsilon_{err}(11\mu\text{m}) < 0.35 \\ \text{True, } DBTD_{rel} < 0.35K \text{ and } \varepsilon_{err}(11\mu\text{m}) < 0.40 \\ \text{True, } DBTD_{rel} < 0.40K \text{ and } \varepsilon_{err}(11\mu\text{m}) < 0.45 \\ \text{True, } DBTD_{rel} < 0.45K \text{ and } \varepsilon_{err}(11\mu\text{m}) < 0.50 \\ \text{True, } DBTD_{rel} < 0.50K \text{ and } \varepsilon_{err}(11\mu\text{m}) < 0.55 \\ \text{True, } DBTD_{rel} < 0.55K \text{ and } \varepsilon_{err}(11\mu\text{m}) < 0.60 \\ \text{True, } DBTD_{rel} < 0.60K \text{ and } \varepsilon_{err}(11\mu\text{m}) < 0.65 \\ \text{True, } DBTD_{rel} < 0.65K \text{ and } \varepsilon_{err}(11\mu\text{m}) < 0.70 \\ \text{True, } DBTD_{rel} < 0.70K \text{ and } \varepsilon_{err}(11\mu\text{m}) < 0.75 \\ \text{True, } DBTD_{rel} < 0.75K \text{ and } \varepsilon_{err}(11\mu\text{m}) < 0.80 \\ \text{True, } DBTD_{rel} < 0.80K \text{ and } \varepsilon_{err}(11\mu\text{m}) < 0.85 \\ \text{True, } DBTD_{rel} < 0.85K \text{ and } \varepsilon_{err}(11\mu\text{m}) < 0.90 \\ \text{False, } \textit{Otherwise} \end{cases} \quad [ E.2]$$

In Equation [ E.2],  $\varepsilon(11\mu\text{m})$  is the retrieved ash/dust cloud emissivity at 11  $\mu\text{m}$ ,  $BT_{sdev}(11\mu\text{m})$  is the standard deviation of the 11  $\mu\text{m}$  brightness temperature in a 3x3 pixel window centered on the pixel of interest, and  $N_{25km}$  is the number of pixels used to compute  $DBTD_{abs}$  and  $DBTD_{rel}$ . The second cloud object membership ( $P_{thresh2}$ ) threshold is then determined using the relationship shown in Equation [ E.3].

$$P_{thresh2} = \begin{cases} 0.001\%, & \text{if Condition2 is true} \\ 100\%, & \textit{otherwise} \end{cases} \quad [ E.3]$$

The third probability threshold ( $P_{thresh3}$ ) is determined through sequential evaluation of Equation [ E.4] (the evaluation stops once a “true” condition on the right hand side is encountered).

$$P_{thresh3} = \begin{cases} 100\%, & \text{if } \varepsilon_{tot}(11\mu m) < 0.05 \\ 100\%, & \text{if } BTD(11-12\mu m) > -0.50 \\ 0.00\%, & \text{if } BTD\_BIAS > 1.50K \\ 0.00\%, & \text{if } BTD\_BIAS > 1.00K \text{ and } 0.30 \leq \varepsilon(11\mu m) \leq 0.70 \\ 0.0001\%, & \text{if } BTD\_BIAS > 1.00K \\ 100\%, & \text{otherwise} \end{cases} \quad [E.4]$$

The fourth probability threshold ( $P_{thresh4}$ ), given by Equation [ E.5], is designed to account for the presence of  $SO_2$ , which is common in volcanic eruptions. In Equation [ E.5],  $\beta_{tot}(8.5\mu m, 11\mu m)$ ,  $\beta_{opaque}(8.5\mu m, 11\mu m)$ , and  $\beta_{tot}(7.3\mu m, 11\mu m)$  are  $SO_2$  sensitive formulations of the  $\beta$ -ratio discussed in detail in Chapter 4.

$$P_{thresh4} = \begin{cases} 1.0e^{-8}\%, & \text{if } \beta_{tot}(8.5\mu m, 11\mu m) > 1.50 \text{ and} \\ & \beta_{opaque}(8.5\mu m, 11\mu m) > 2.50 \text{ and} \\ & \beta_{tot}(7.3\mu m, 11\mu m) > 1.0 \text{ and} \\ & \varepsilon_{tot}(11\mu m) > 0.01 \\ 100\%, & \text{otherwise} \end{cases} \quad [E.5]$$

The fifth and final probability threshold ( $P_{thresh5}$ ) simply depends on the retrieved ash/dust mass loading (ML) (see Equation [ E.6]).

$$P_{thresh5} = \begin{cases} 1.0e^{-13}\%, & \text{if } ML < 1g/m^2 \\ 100\%, & \text{otherwise} \end{cases} \quad [E.6]$$

## References

- Ansmann, A., et al. (2010), The 16 April 2010 major volcanic ash plume over central Europe: EARLINET lidar and AERONET photometer observations at Leipzig and Munich, Germany, *Geophysical Research Letters*, 37, doi:10.1029/2010gl043809.
- Arason, P., G. N. Petersen, and H. Bjornsson (2011), Observations of the altitude of the volcanic plume during the eruption of Eyjafjallajokull, April-May 2010, *Earth Syst. Sci. Data*, 3(1), 9-17, doi:10.5194/essd-3-9-2011.
- Baum, B. A., P. F. Soulen, K. I. Strabala, M. D. King, S. A. Ackerman, W. P. Menzel, and P. Yang (2000), Remote sensing of cloud properties using MODIS airborne simulator imagery during SUCCESS 2. Cloud thermodynamic phase, *Journal of Geophysical Research-Atmospheres*, 105(D9), 11781-11792, doi:10.1029/1999jd901090.
- Buchheit, R. M., and J. C. Ford (2008), Biological monitoring in the Aleutian Islands, Alaska in 2008: summary appendices, U.S. Fish and Wildlife Service Report <http://avo.alaska.edu/downloads/reference.php?citid=4483>
- Bukowiecki, N., et al. (2011), Ground-based and airborne in-situ measurements of the Eyjafjallajokull volcanic aerosol plume in Switzerland in spring 2010, *Atmospheric Chemistry and Physics*, 11(19), 10011-10030, doi:10.5194/acp-11-10011-2011.
- Bursik, M., et al. (2012), Estimation and propagation of volcanic source parameter uncertainty in an ash transport and dispersal model: application to the Eyjafjallajokull plume of 14-16 April 2010, *Bulletin of Volcanology*, 74(10), 2321-2338, doi:10.1007/s00445-012-0665-2.
- Burton, S. P., R. A. Ferrare, C. A. Hostetler, J. W. Hair, R. R. Rogers, M. D. Obland, C. F. Butler, A. L. Cook, D. B. Harper, and K. D. Froyd (2012), Aerosol classification using airborne High Spectral Resolution Lidar measurements - methodology and examples, *Atmospheric Measurement Techniques*, 5(1), 73-98, doi:10.5194/amt-5-73-2012.
- Campbell, J. R., E. J. Welton, N. A. Krotkov, K. Yang, S. A. Stewart, and M. D. Fromm (2012), Likely seeding of cirrus clouds by stratospheric Kasatochi volcanic aerosol particles near a mid-latitude tropopause fold, *Atmospheric Environment*, 46, 441-448, doi:10.1016/j.atmosenv.2011.09.027.
- CASADEVALL, T. (1994), THE 1989-1990 ERUPTION OF REDOUBT VOLCANO, ALASKA - IMPACTS ON AIRCRAFT OPERATIONS, *Journal of Volcanology and Geothermal Research*, 62(1-4), 301-316, doi:10.1016/0377-0273(94)90038-8.
- Cintineo, J., M. J. Pavolonis, J. Sieglaff, and D. Lindsey (2014), An Empirical Model for Assessing the Severe Weather Potential of Developing Convection. *Wea. Forecasting*, *Weather and Forecasting*, in press, doi:doi:10.1175/WAF-D-13-00113.1.

Cintineo, J. L., M. J. Pavolonis, J. M. Sieglaff, and A. K. Heidinger (2013), Evolution of Severe and Nonsevere Convection Inferred from GOES-Derived Cloud Properties, *Journal of Applied Meteorology and Climatology*, 52(9), 2009-2023, doi:10.1175/jamc-d-12-0330.1.

Clarisse, L., P. Coheur, F. Prata, J. Hadji-Lazaro, D. Hurtmans, and C. Clerbaux (2013), A unified approach to infrared aerosol remote sensing and type specification, *Atmospheric Chemistry and Physics*, 13(4), 2195-2221, doi:10.5194/acp-13-2195-2013.

Clarisse, L., D. Hurtmans, A. Prata, F. Karagulian, C. Clerbaux, M. De Maziere, and P. Coheur (2010a), Retrieving radius, concentration, optical depth, and mass of different types of aerosols from high-resolution infrared nadir spectra, *Applied Optics*, 49(19), 3713-3722.

Clarisse, L., F. Prata, J. Lacour, D. Hurtmans, C. Clerbaux, and P. Coheur (2010b), A correlation method for volcanic ash detection using hyperspectral infrared measurements, *Geophysical Research Letters*, 37, doi:10.1029/2010GL044828.

Clough, S. A. a. I. M. J. (1995), Line-by-line calculation of atmospheric fluxes and cooling rates: 2. Application to carbon dioxide, ozone, methane, nitrous oxide and the halocarbons, *Journal of Geophysical Research: Atmospheres*, 100(D8), 16519--16535, doi:10.1029/95JD01386.

Corradini, S., L. Merucci, A. Prata, and A. Piscini (2010), Volcanic ash and SO<sub>2</sub> in the 2008 Kasatochi eruption: Retrievals comparison from different IR satellite sensors, *Journal of Geophysical Research-Atmospheres*, 115, doi:10.1029/2009JD013634.

Corradini, S., C. Spinetti, E. Carboni, C. Tirelli, M. F. Buongiorno, S. Pugnaghi, and G. Gangale (2008), Mt. Etna tropospheric ash retrieval and sensitivity analysis using Moderate Resolution Imaging Spectroradiometer measurements, *Journal of Applied Remote Sensing*, 2, doi:10.1117/1.3046674.

Cox, S. K. (1976), OBSERVATIONS OF CLOUD INFRARED EFFECTIVE EMISSIVITY, *Journal of the Atmospheric Sciences*, 33(2), 287-289, doi:10.1175/1520-0469(1976)033<0287:oociee>2.0.co;2.

de Graaf, M., P. Stammes, O. Torres, and R. Koelemeijer (2005), Absorbing Aerosol Index: Sensitivity analysis, application to GOME and comparison with TOMS, *Journal of Geophysical Research-Atmospheres*, 110(D1), doi:10.1029/2004JD005178.

Denlinger, R., M. Pavolonis, and J. Sieglaff (2012), A robust method to forecast volcanic ash clouds, *Journal of Geophysical Research-Atmospheres*, 117, doi:10.1029/2012JD017732.

DeSouza-Machado, S., et al. (2010), Infrared retrievals of dust using AIRS: Comparisons of optical depths and heights derived for a North African dust storm to other collocated

EOS A-Train and surface observations, *Journal of Geophysical Research-Atmospheres*, 115, doi:10.1029/2009JD012842.

Domingos, P., and M. Pazzani (1997), On the optimality of the simple Bayesian classifier under zero-one loss, *Machine Learning*, 29(2-3), 103-130, doi:10.1023/a:1007413511361.

Downing, H. D., and D. Williams (1975), OPTICAL-CONSTANTS OF WATER IN INFRARED, *Journal of Geophysical Research*, 80(12), 1656-1661, doi:10.1029/JC080i012p01656.

Duggen, S., N. Olgun, P. Croot, L. Hoffmann, H. Dietze, P. Delmelle, and C. Teschner (2010), The role of airborne volcanic ash for the surface ocean biogeochemical iron-cycle: a review, *Biogeosciences*, 7(3), 827-844.

Dunion, J., and C. Velden (2004), The impact of the Saharan air layer on Atlantic tropical cyclone activity, *Bulletin of the American Meteorological Society*, 85(3), 353-+, doi:10.1175/BAMS-85-3-353.

Durant, A. J., R. A. Shaw, W. I. Rose, Y. Mi, and G. G. J. Ernst (2008), Ice nucleation and overseeding of ice in volcanic clouds, *Journal of Geophysical Research-Atmospheres*, 113(D9), doi:10.1029/2007jd009064.

Ed., P. B. (2012), Scientific and Technical Memorandum of the International Forum on Satellite EO and Geohazards, 21-23 May 2012, doi:10.5270/esa-geo-hzrd-2012.

Ellrod, G., B. Connell, and D. Hillger (2003), Improved detection of airborne volcanic ash using multispectral infrared satellite data, *Journal of Geophysical Research-Atmospheres*, 108(D12), doi:10.1029/2002JD002802.

Ellrod, G. P. (2004), Impact on volcanic ash detection caused by the loss of the 12.0  $\mu\text{m}$  "Split Window" band on GOES Imagers, *Journal of Volcanology and Geothermal Research*, 135(1-2), 91-103, doi:http://dx.doi.org/10.1016/j.jvolgeores.2003.12.009.

Eloranta, E. W. (2005), High spectral resolution lidar, in *Range-resolved optical remote sensing of the atmosphere*, edited by K. Weitkamp, pp. 143-163, Springer-Verlag.

Ernst, G. G. J., R. S. J. Sparks, S. N. Carey, and M. I. Bursik (1996), Sedimentation from turbulent jets and plumes, *Journal of Geophysical Research-Solid Earth*, 101(B3), 5575-5589, doi:10.1029/95jb01900.

Evan, A., G. Foltz, D. Zhang, and D. Vimont (2011), Influence of African dust on ocean-atmosphere variability in the tropical Atlantic, *Nature Geoscience*, 4(11), 762-765, doi:10.1038/NGEO1276.

Francis, P., M. Cooke, and R. Saunders (2012), Retrieval of physical properties of volcanic ash using Meteosat: A case study from the 2010 Eyjafjallajokull eruption, *Journal of Geophysical Research-Atmospheres*, 117, doi:10.1029/2011JD016788.

Gangale, G., A. Prata, and L. Clarisse (2010), The infrared spectral signature of volcanic ash determined from high-spectral resolution satellite measurements, *Remote Sensing of Environment*, 114(2), 414-425, doi:10.1016/j.rse.2009.09.007.

Garnier, A., J. Pelon, P. Dubuisson, M. Faivre, O. Chomette, N. Pascal, and D. P. Kratz (2012), Retrieval of Cloud Properties Using CALIPSO Imaging Infrared Radiometer. Part I: Effective Emissivity and Optical Depth, *Journal of Applied Meteorology and Climatology*, 51(7), 1407-1425, doi:10.1175/jamc-d-11-0220.1.

Gasteiger, J., S. Gross, V. Freudenthaler, and M. Wiegner (2011), Volcanic ash from Iceland over Munich: mass concentration retrieved from ground-based remote sensing measurements, *Atmospheric Chemistry and Physics*, 11(5), 2209-2223, doi:10.5194/acp-11-2209-2011.

Giraud, V., J. C. Buriez, Y. Fouquart, F. Parol, and G. Seze (1997), Large-scale analysis of cirrus clouds from AVHRR data: Assessment of both a microphysical index and the cloud-top temperature, *Journal of Applied Meteorology*, 36(6), 664-675, doi:10.1175/1520-0450-36.6.664.

Gu, Y., W. Rose, D. Schneider, G. Bluth, and I. Watson (2005), Advantageous GOES IR results for ash mapping at high latitudes: Cleveland eruptions 2001, *Geophysical Research Letters*, 32(2), doi:10.1029/2004GL021651.

Gu, Y. X., W. I. Rose, and G. J. S. Bluth (2003), Retrieval of mass and sizes of particles in sandstorms using two MODIS IR bands: A case study of April 7, 2001 sandstorm in China, *Geophysical Research Letters*, 30(15), doi:10.1029/2003gl017405.

Gudmundsson, M. T., R. Pedersen, K. Vogfjord, S. Thorbjarnardottir, S. Jakobsdottir, and M. J. Roberts (2010), Eruptions of Eyjafjallajokull Volcano, Iceland, *EOS*, 91, 190-191.

Guffanti, M., T. J. Casadevall, and K. Budding (2010a), Encounters of aircraft with volcanic ash cloud; A compilation of known incidents, 1953-2009, U.S. Geological Survey Data Series.

Guffanti, M., D. Schneider, K. Wallace, T. Hall, D. Bensimon, and L. Salinas (2010b), Aviation response to a widely dispersed volcanic ash and gas cloud from the August 2008 eruption of Kasatochi, Alaska, USA, *Journal of Geophysical Research-Atmospheres*, 115, doi:10.1029/2010JD013868.

Hadley, D., G. L. Hufford, and J. J. Simpson (2004), Resuspension of relic volcanic ash and dust from Katmai: Still an aviation hazard, *Weather and Forecasting*, 19(5), 829-840, doi:10.1175/1520-0434(2004)019<0829:rorvaa>2.0.co;2.

Hamill, T. M., J. S. Whitaker, and S. L. Mullen (2006), Reforecasts - An important dataset for improving weather predictions, *Bulletin of the American Meteorological Society*, 87(1), 33-+, doi:10.1175/bams-87-1-33.

Hand, D. J., and K. M. Yu (2001), Idiot's Bayes - Not so stupid after all?, *International Statistical Review*, 69(3), 385-398, doi:10.2307/1403452.

Hannon, S., L. L. Strow, and W. W. McMillan (1996), Atmospheric infrared fast transmittance models: A comparison of two approaches, paper presented at Conference on Optical Spectroscopic Techniques and Instrumentation for Atmospheric and Space Research II, SPIE - INT SOC OPTICAL ENGINEERING, Denver, CO.

Hansen, J. E., and L. D. Travis (1974), LIGHT-SCATTERING IN PLANETARY ATMOSPHERES, *Space Science Reviews*, 16(4), 527-610, doi:10.1007/bf00168069.

Hanstrum, B. N., and A. S. Watson (1983), A case study of two eruptions of Mount Galunggung and an investigation of volcanic eruption cloud characteristics using remote sensing techniques, *Aust Meteorol Mag*, 131-177.

Harris, D. M., and W. I. Rose (1983), ESTIMATING PARTICLE SIZES, CONCENTRATIONS, AND TOTAL MASS OF ASH IN VOLCANIC CLOUDS USING WEATHER RADAR, *Journal of Geophysical Research-Oceans and Atmospheres*, 88(NC15), 969-983, doi:10.1029/JC088iC15p10969.

Heidinger, A., and M. Pavolonis (2009), Gazing at Cirrus Clouds for 25 Years through a Split Window. Part I: Methodology, *Journal of Applied Meteorology and Climatology*, 48(6), 1100-1116, doi:10.1175/2008JAMC1882.1.

Heidinger, A., M. Pavolonis, R. Holz, B. Baum, and S. Berthier (2010), Using CALIPSO to explore the sensitivity to cirrus height in the infrared observations from NPOESS/VIIRS and GOES-R/ABI, *Journal of Geophysical Research-Atmospheres*, 115, doi:10.1029/2009JD012152.

Heidinger, A. K., A. T. Evan, M. J. Foster, and A. Walther (2012), A Naive Bayesian Cloud-Detection Scheme Derived from CALIPSO and Applied within PATMOS-x, *Journal of Applied Meteorology and Climatology*, 51(6), 1129-1144, doi:10.1175/jamc-d-11-02.1.

Hillger, D., and J. Clark (2002a), Principal component image analysis of MODIS for volcanic ash. Part I: Most important bands and implications for future GOES Imagers, *Journal of Applied Meteorology*, 41(10), 985-1001.

Hillger, D., and J. Clark (2002b), Principal component image analysis of MODIS for volcanic ash. Part II: Simulation of current GOES and GOES-M Imagers, *Journal of Applied Meteorology*, 41(10), 1003-1010, doi:10.1175/1520-0450(2002)041<1003:PCIAOM>2.0.CO;2.

Hobbs, P. V., L. F. Radke, J. H. Lyons, R. J. Ferek, D. J. Coffman, and T. J. Casadevall (1991), AIRBORNE MEASUREMENTS OF PARTICLE AND GAS EMISSIONS FROM THE 1990 VOLCANIC-ERUPTIONS OF MOUNT REDOUBT, *Journal of Geophysical Research-Atmospheres*, 96(D10), 18735-18752, doi:10.1029/91jd01635.

Hobbs, P. V., J. P. Tuell, D. A. Hegg, L. F. Radke, and M. W. Eltgroth (1982), PARTICLES AND GASES IN THE EMISSIONS FROM THE 1980-1981 VOLCANIC-ERUPTIONS OF MT ST-HELENS, *Journal of Geophysical Research-Oceans and Atmospheres*, 87(NC13), 1062-1086, doi:10.1029/JC087iC13p11062.

Huang, H. L., W. L. Smith, J. Li, P. Antonelli, X. Q. Wu, R. O. Knuteson, B. M. Huang, and B. J. Osborne (2004), Minimum local emissivity variance retrieval of cloud altitude and effective spectral emissivity - Simulation and initial verification, *Journal of Applied Meteorology*, 43(5), 795-809, doi:10.1175/2090.1.

Hunt, W., D. Winker, M. Vaughan, K. Powell, P. Lucker, and C. Weimer (2009), CALIPSO Lidar Description and Performance Assessment, *Journal of Atmospheric and Oceanic Technology*, 26(7), 1214-1228, doi:10.1175/2009JTECHA1223.1.

ICAO (2007), Manual on Volcanic Ash, Radioactive Material, and Toxic Chemical Clouds, 500 pp, <http://www.paris.icao.int/news/pdf/9691.pdf>.

Inoue, T. (1985), ON THE TEMPERATURE AND EFFECTIVE EMISSIVITY DETERMINATION OF SEMI-TRANSPARENT CIRRUS CLOUDS BY BI-SPECTRAL MEASUREMENTS IN THE 10 MU-M WINDOW REGION, *Journal of the Meteorological Society of Japan*, 63(1), 88-99.

Inoue, T. (1987), A CLOUD TYPE CLASSIFICATION WITH NOAA 7 SPLIT-WINDOW MEASUREMENTS, *Journal of Geophysical Research-Atmospheres*, 92(D4), 3991-4000, doi:10.1029/JD092iD04p03991.

Jickells, T., et al. (2005), Global iron connections between desert dust, ocean biogeochemistry, and climate, *Science*, 308(5718), 67-71, doi:10.1126/science.1105959.

Johnson, B., et al. (2012), In situ observations of volcanic ash clouds from the FAAM aircraft during the eruption of Eyjafjallajokull in 2010, *Journal of Geophysical Research-Atmospheres*, 117, doi:10.1029/2011jd016760.

Karagulian, F., L. Clarisse, C. Clerbaux, A. Prata, D. Hurtmans, and P. Coheur (2010), Detection of volcanic SO<sub>2</sub>, ash, and H<sub>2</sub>SO<sub>4</sub> using the Infrared Atmospheric Sounding

Interferometer (IASI), *Journal of Geophysical Research-Atmospheres*, 115, doi:10.1029/2009JD012786.

Kossin, J. P., and M. Sitkowski (2009), An Objective Model for Identifying Secondary Eyewall Formation in Hurricanes, *Monthly Weather Review*, 137(3), 876-892, doi:10.1175/2008mwr2701.1.

Krotkov, N. A., M. R. Schoeberl, G. A. Morris, S. Carn, and K. Yang (2010), Dispersion and lifetime of the SO<sub>2</sub> cloud from the August 2008 Kasatochi eruption, *Journal of Geophysical Research-Atmospheres*, 115, doi:10.1029/2010jd013984.

Lacasse, C., S. Karlsdottir, G. Larsen, H. Soosalu, W. I. Rose, and G. G. J. Ernst (2004), Weather radar observations of the Hekla 2000 eruption cloud, Iceland, *Bulletin of Volcanology*, 66(5), 457-473, doi:10.1007/s00445-003-0329-3.

Langmann, B., K. Zaksek, and M. Hort (2010), Atmospheric distribution and removal of volcanic ash after the eruption of Kasatochi volcano: A regional model study, *Journal of Geophysical Research-Atmospheres*, 115, doi:10.1029/2009jd013298.

Legrand, M., A. Plana-Fattori, and C. N'doume (2001), Satellite detection of dust using the IR imagery of Meteosat 1. Infrared difference dust index, *Journal of Geophysical Research-Atmospheres*, 106(D16), 18251-18274, doi:10.1029/2000JD900749.

Lensky, I., and D. Rosenfeld (2008), Clouds-Aerosols-Precipitation Satellite Analysis Tool (CAPSAT), *Atmospheric Chemistry and Physics*, 8(22), 6739-6753.

Liu, D., Z. Wang, Z. Liu, D. Winker, and C. Trepte (2008), A height resolved global view of dust aerosols from the first year CALIPSO lidar measurements, *Journal of Geophysical Research-Atmospheres*, 113(D16), doi:10.1029/2007JD009776.

Mackie, S., and M. Watson (2014), Probabilistic detection of volcanic ash using a Bayesian approach, edited, *J. Geophys. Res. Atmos.*, doi:10.1002/2013JD021077.

Malingreau, J. P., and Kaswanda (1986), MONITORING VOLCANIC-ERUPTIONS IN INDONESIA USING WEATHER-SATELLITE DATA - THE COLO ERUPTION OF JULY 28, 1983, *Journal of Volcanology and Geothermal Research*, 27(1-2), 179-194, doi:10.1016/0377-0273(86)90085-5.

Marenco, F., B. Johnson, K. Turnbull, S. Newman, J. Haywood, H. Webster, and H. Ricketts (2011), Airborne lidar observations of the 2010 Eyjafjallajokull volcanic ash plume, *Journal of Geophysical Research-Atmospheres*, 116, doi:10.1029/2011jd016396.

Marzano, F. S., S. Barbieri, G. Vulpiani, and W. I. Rose (2006a), Volcanic ash cloud retrieval by ground-based microwave weather radar, *Ieee Transactions on Geoscience and Remote Sensing*, 44(11), 3235-3246, doi:10.1109/tgrs.2006.879116.

- Marzano, F. S., S. Marchiotto, C. Textor, and D. J. Schneider (2010), Model-Based Weather Radar Remote Sensing of Explosive Volcanic Ash Eruption, *Ieee Transactions on Geoscience and Remote Sensing*, 48(10), 3591-3607, doi:10.1109/tgrs.2010.2047862.
- Marzano, F. S., G. Vulpiani, and W. I. Rose (2006b), Microphysical characterization of microwave radar reflectivity due to volcanic ash clouds, *Ieee Transactions on Geoscience and Remote Sensing*, 44(2), 313-327, doi:10.1109/tgrs.2005.861010.
- Mastin, L., et al. (2009), A multidisciplinary effort to assign realistic source parameters to models of volcanic ash-cloud transport and dispersion during eruptions, *Journal of Volcanology and Geothermal Research*, 186(1-2), 10-21, doi:10.1016/j.jvolgeores.2009.01.008.
- McGimsey, R. G., C. A. Neal, and O. Girina (2004), 2001 Volcanic Activity in Alaska and Kamchatka: Summary of events and response of the Alaska Volcano Observatory, Report., 53 pp, U.S. Geological Survey.
- McKeen, S. A., S. C. Liu, and C. S. Kiang (1984), ON THE CHEMISTRY OF STRATOSPHERIC SO<sub>2</sub> FROM VOLCANIC-ERUPTIONS, *Journal of Geophysical Research-Atmospheres*, 89(ND3), 4873-4881, doi:10.1029/JD089iD03p04873.
- Menzel, W. P., R. A. Frey, H. Zhang, D. P. Wylie, C. C. Moeller, R. E. Holz, B. Maddux, B. A. Baum, K. I. Strabala, and L. E. Gumley (2008), MODIS global cloud-top pressure and amount estimation: Algorithm description and results, *Journal of Applied Meteorology and Climatology*, 47(4), 1175-1198, doi:10.1175/2007jamc1705.1.
- Merchant, C. J., A. R. Harris, E. Maturi, and S. MacCallum (2005), Probabilistic physically based cloud screening of satellite infrared imagery for operational sea surface temperature retrieval, *Quarterly Journal of the Royal Meteorological Society*, 131(611), 2735-2755, doi:10.1256/qj.05.15.
- Miller, S. (2003), A consolidated technique for enhancing desert dust storms with MODIS, *Geophysical Research Letters*, 30(20), doi:10.1029/2003GL018279.
- Miller, T. P., and T. J. Casadevall (2000), Volcanic ash hazards to aviation, in *Encyclopedia of Volcanoes*, edited by H. Sigurdsson, pp. 915-930, Academic, San Diego.
- Millington, S., R. Saunders, P. Francis, and H. Webster (2012), Simulated volcanic ash imagery: A method to compare NAME ash concentration forecasts with SEVIRI imagery for the Eyjafjallajokull eruption in 2010, *Journal of Geophysical Research-Atmospheres*, 117, doi:10.1029/2011JD016770.
- Mitchell, D. L. (2000), Parameterization of the Mie extinction and absorption coefficients for water clouds, *Journal of the Atmospheric Sciences*, 57(9), 1311-1326, doi:10.1175/1520-0469(2000)057<1311:potmea>2.0.co;2.

- Miyabuchi, Y., D. Hanada, H. Niimi, and T. Kobayashi (2013), Stratigraphy, grain-size and component characteristics of the 2011 Shinmoedake eruption deposits, Kirishima Volcano, Japan, *Journal of Volcanology and Geothermal Research*, 258, 31-46, doi:10.1016/j.jvolgeores.2013.03.027.
- Neal, C. A., R. G. McGimsey, C. A. Gardnew, M. L. Harbin, and C. J. Nye (1994), Tephra-fall deposits from 1992 eruptions of Crater Peak Mount Spurr Volcano, AK: A preliminary report of stratigraphy, and composition. The 1992 eruptions of Crater Peak vent, Mount Spurr volcano Alaska, U.S. Geological Survey Bulletin, 2139, 65-79.
- Newhall, C. G., and S. Self (1982), THE VOLCANIC EXPLOSIVITY INDEX (VEI) - AN ESTIMATE OF EXPLOSIVE MAGNITUDE FOR HISTORICAL VOLCANISM, *Journal of Geophysical Research-Oceans and Atmospheres*, 87(NC2), 1231-1238, doi:10.1029/JC087iC02p01231.
- Newman, S. M., L. Clarisse, D. Hurtmans, F. Marenco, B. Johnson, K. Turnbull, S. Havemann, A. J. Baran, D. O'Sullivan, and J. Haywood (2012), A case study of observations of volcanic ash from the Eyjafjallajokull eruption: 2. Airborne and satellite radiative measurements, *Journal of Geophysical Research-Atmospheres*, 117, doi:10.1029/2011jd016780.
- Nolin, A. W., R. Armstrong, and J. Maslanik (1998), Near-Real-Time SSM/I-SSMIS EASE-Grid Daily Global Ice Concentration and Snow Extent, National Snow and Ice Data Center, Boulder, Colorado USA.
- Onodera, S., and K. Kamo (1994), Aviation safety measures for ash clouds in Japan and the system of Japan Air Lines for monitoring eruptions at Sakurajima Volcano, U.S. Geological Survey Bulletin, 2047, 213-219.
- Oxford Economics (2010), The Economic Impacts of Air Travel Restrictions Due to Volcanic Ash, <http://www.oxfordeconomics.com/my-oxford/projects/129051>.
- Pappalardo, G., A. Amodeo, L. Mona, M. Pandolfi, N. Pergola, and V. Cuomo (2004), Raman lidar observations of aerosol emitted during the 2002 Etna eruption, *Geophysical Research Letters*, 31(5), doi:10.1029/2003gl019073.
- Parol, F., J. C. Buriez, G. Brogniez, and Y. Fouquart (1991), INFORMATION-CONTENT OF AVHRR CHANNELS 4 AND 5 WITH RESPECT TO THE EFFECTIVE RADIUS OF CIRRUS CLOUD PARTICLES, *Journal of Applied Meteorology*, 30(7), 973-984, doi:10.1175/1520-0450-30.7.973.
- Pavolonis, M. (2010), Advances in Extracting Cloud Composition Information from Spaceborne Infrared Radiances-A Robust Alternative to Brightness Temperatures. Part I: Theory, *Journal of Applied Meteorology and Climatology*, 49(9), 1992-2012, doi:10.1175/2010JAMC2433.1.

Pavolonis, M., W. Feltz, A. Heidinger, and G. Gallina (2006), A daytime complement to the reverse absorption technique for improved automated detection of volcanic ash, *Journal of Atmospheric and Oceanic Technology*, 23(11), 1422-1444, doi:10.1175/JTECH1926.1.

Pavolonis, M., and A. Heidinger (2004), Daytime cloud overlap detection from AVHRR and VIIRS, *Journal of Applied Meteorology*, 43(5), 762-778, doi:10.1175/2099.1.

Pavolonis, M., A. Heidinger, and J. Sieglaff (2013), Automated retrievals of volcanic ash and dust cloud properties from upwelling infrared measurements, *Journal of Geophysical Research-Atmospheres*, 118(3), 1436-1458, doi:10.1002/jgrd.50173.

Pavolonis, M., A. Heidinger, and T. Uttal (2005), Daytime global cloud typing from AVHRR and VIIRS: Algorithm description, validation, and comparisons, *Journal of Applied Meteorology*, 44(6), 804-826, doi:10.1175/JAM2236.1.

Pavolonis, M. J., and J. Sieglaff (2010), GOES-R Advanced Baseline Imager (ABI) Algorithm Theoretical Basis Document for Volcanic Ash (Detection and Height), 84 pp, NOAA.

Pergola, N., V. Tramutoli, F. Marchese, I. Scaffidi, and T. Lacava (2004), Improving volcanic ash cloud detection by a robust satellite technique, *Remote Sensing of Environment*, 90(1), 1-22, doi:10.1016/j.rse.2003.11.014.

Peyridieu, S., A. Chedin, D. Tanre, V. Capelle, C. Pierangelo, N. Lamquin, and R. Armante (2010), Saharan dust infrared optical depth and altitude retrieved from AIRS: a focus over North Atlantic - comparison to MODIS and CALIPSO, *Atmospheric Chemistry and Physics*, 10(4), 1953-1967.

Piovano, E. L., D. Ariztegui, and S. D. Moreira (2002), Recent environmental changes in Laguna Mar Chiquita (central Argentina): a sedimentary model for a highly variable saline lake, *Sedimentology*, 49(6), 1371-1384, doi:10.1046/j.1365-3091.2002.00503.x.

Pollack, J. B., O. B. Toon, and B. N. Khare (1973), OPTICAL PROPERTIES OF SOME TERRESTRIAL ROCKS AND GLASSES, *Icarus*, 19(3), 372-389, doi:10.1016/0019-1035(73)90115-2.

Pouget, S., M. Bursik, P. Webley, J. Dehn, and M. Pavolonis (2013), Estimation of eruption source parameters from umbrella cloud or downwind plume growth rate, *Journal of Volcanology and Geothermal Research*, 258, 100-112, doi:10.1016/j.jvolgeores.2013.04.002.

PRATA, A. (1989a), INFRARED RADIATIVE-TRANSFER CALCULATIONS FOR VOLCANIC ASH CLOUDS, *Geophysical Research Letters*, 16(11), 1293-1296, doi:10.1029/GL016i011p01293.

PRATA, A. (1989b), OBSERVATIONS OF VOLCANIC ASH CLOUDS IN THE 10-12-MU-M WINDOW USING AVHRR/2 DATA, *International Journal of Remote Sensing*, 10(4-5), 751-761.

Prata, A., and C. Bernardo (2009), Retrieval of volcanic ash particle size, mass and optical depth from a ground-based thermal infrared camera, *Journal of Volcanology and Geothermal Research*, 186(1-2), 91-107, doi:10.1016/j.jvolgeores.2009.02.007.

Prata, A., and I. Grant (2001), Retrieval of microphysical and morphological properties of volcanic ash plumes from satellite data: Application to Mt Ruapehu, New Zealand, *Quarterly Journal of the Royal Meteorological Society*, 127(576), 2153-2179, doi:10.1256/smsqj.57614.

Prata, A., and A. Prata (2012), Eyjafjallajokull volcanic ash concentrations determined using Spin Enhanced Visible and Infrared Imager measurements, *Journal of Geophysical Research-Atmospheres*, 117, doi:10.1029/2011JD016800.

Prata, A. J. (2009), Satellite detection of hazardous volcanic clouds and the risk to global air traffic, *Natural Hazards*, 51(2), 303-324, doi:10.1007/s11069-008-9273-z.

Prata, A. J., G. Gangale, L. Clarisse, and F. Karagulian (2010), Ash and sulfur dioxide in the 2008 eruptions of Okmok and Kasatochi: Insights from high spectral resolution satellite measurements, *Journal of Geophysical Research-Atmospheres*, 115, doi:10.1029/2009jd013556.

Prata, F., G. Bluth, B. Rose, D. Schneider, and A. Tupper (2001), Failures in detecting volcanic ash from a satellite-based technique - Comments, *Remote Sensing of Environment*, 78(3), 341-346, doi:10.1016/S0034-4257(01)00231-0.

Prospero, J., and P. Lamb (2003), African droughts and dust transport to the Caribbean: Climate change implications, *Science*, 302(5647), 1024-1027, doi:10.1126/science.1089915.

Ramsay, B. H. (1998), The interactive multisensor snow and ice mapping system, *Hydrological Processes*, 12(10-11), 1537-1546, doi:10.1002/(sici)1099-1085(199808/09)12:10/11<1537::aid-hyp679>3.0.co;2-a.

Ramsperger, B., L. Herrmann, and K. Stahr (1998a), Dust characteristics and source-sink relations in eastern west Africa (SW-Niger and Benin) and South America (Argentinean pampas), *Zeitschrift Fur Pflanzenernahrung Und Bodenkunde*, 161(4), 357-363.

Ramsperger, B., N. Peinemann, and K. Stahr (1998b), Deposition rates and characteristics of aeolian dust in the semi-arid and sub-humid regions of the Argentinean Pampa, *Journal of Arid Environments*, 39(3), 467-476, doi:10.1006/jare.1997.0366.

Robock, A. (2000), Volcanic eruptions and climate, *Reviews of Geophysics*, 38(2), 191-219, doi:10.1029/1998rg000054.

Rodgers, C. D. (1976), RETRIEVAL OF ATMOSPHERIC-TEMPERATURE AND COMPOSITION FROM REMOTE MEASUREMENTS OF THERMAL-RADIATION, *Reviews of Geophysics*, 14(4), 609-624, doi:10.1029/RG014i004p00609.

Rose, W. I. (1993), COMMENT ON ANOTHER LOOK AT THE CALCULATION OF FALLOUT TEPHRA VOLUMES, *Bulletin of Volcanology*, 55(5), 372-374, doi:10.1007/bf00301148.

Rose, W. I., G. J. S. Bluth, and G. G. J. Ernst (2000), Integrating retrievals of volcanic cloud characteristics from satellite remote sensors: a summary, *Philosophical Transactions of the Royal Society of London Series a-Mathematical Physical and Engineering Sciences*, 358(1770), 1585-1606.

Rose, W. I., and A. J. Durant (2011), Fate of volcanic ash: Aggregation and fallout, *Geology*, 39(9), 895-896, doi:10.1130/focus092011.1.

Roush, T., J. Pollack, and J. Orenberg (1991), DERIVATION OF MIDINFRARED (5-25 MU-M) OPTICAL-CONSTANTS OF SOME SILICATES AND PALAGONITE, *Icarus*, 94(1), 191-208, doi:10.1016/0019-1035(91)90150-r.

Sawada, Y. (1987), Study on analysis of volcanic eruptions based in eruption cloud image data obtained by the Geostationary Meteorological Satellite (GMS), Technical report of the Meteorological Institute, 335 pp.

Scaillet, B. a. L. J. F. a. C. M. R. (2013), Petrological and Volcanological Constraints on Volcanic Sulfur Emissions to the Atmosphere, 11--40, doi:10.1029/139GM02.

Schmehl, K., S. Haupt, and M. Pavolonis (2012), A Genetic Algorithm Variational Approach to Data Assimilation and Application to Volcanic Emissions, *Pure and Applied Geophysics*, 169(3), 519-537, doi:10.1007/s00024-011-0385-0.

Schmit, T. J., M. M. Gunshor, W. P. Menzel, J. J. Gurka, J. Li, and A. S. Bachmeier (2005), Introducing the next-generation Advanced Baseline Imager on goes-R, *Bulletin of the American Meteorological Society*, 86(8), 1079-+, doi:10.1175/bams-86-8-1079.

Schmit, T. J., E. M. Prins, A. J. Schreiner, and J. J. Gurka (2001), Introducing the GOES-M Imager, *Natl. Wea. Dig.*, 25(34), 28-37.

Schneider, D. J., and R. P. Hoblitt (2013), Doppler weather radar observations of the 2009 eruption of Redoubt Volcano, Alaska, *Journal of Volcanology and Geothermal Research*, 259(0), 133-144, doi:http://dx.doi.org/10.1016/j.jvolgeores.2012.11.004.

Schumann, U., et al. (2011), Airborne observations of the Eyjafjalla volcano ash cloud over Europe during air space closure in April and May 2010, *Atmospheric Chemistry and Physics*, 11(5), 2245-2279, doi:10.5194/acp-11-2245-2011.

Scollo, S., R. Kahn, D. Nelson, M. Coltelli, D. Diner, M. Garay, and V. Realmuto (2012), MISR observations of Etna volcanic plumes, *Journal of Geophysical Research-Atmospheres*, 117, doi:10.1029/2011JD016625.

Seemann, S. W., E. E. Borbas, R. O. Knuteson, G. R. Stephenson, and H.-L. Huang (2008), Development of a global infrared land surface emissivity database for application to clear sky sounding retrievals from multispectral satellite radiance measurements, *Journal of Applied Meteorology and Climatology*, 47(1), 108-123, doi:10.1175/2007jamc1590.1.

Simkin, T., and L. Siebert (1994), *Volcanoes of the World*, 2<sup>nd</sup> edition.

Simpson, J. J., G. L. Hufford, D. Pieri, and J. S. Berg (2001), Failures in detecting volcanic ash from a satellite-based technique - Response, *Remote Sensing of Environment*, 78(3), 347-357, doi:10.1016/s0034-4257(01)00230-9.

Stamnes, K., S. C. Tsay, W. Wiscombe, and K. Jayaweera (1988), NUMERICALLY STABLE ALGORITHM FOR DISCRETE-ORDINATE-METHOD RADIATIVE-TRANSFER IN MULTIPLE-SCATTERING AND EMITTING LAYERED MEDIA, *Applied Optics*, 27(12), 2502-2509.

Stohl, A., et al. (2011), Determination of time- and height-resolved volcanic ash emissions and their use for quantitative ash dispersion modeling: the 2010 Eyjafjallajökull eruption, *Atmospheric Chemistry and Physics*, 11(9), 4333-4351, doi:10.5194/acp-11-4333-2011.

Strabala, K. I., S. A. Ackerman, and W. P. Menzel (1994), CLOUD PROPERTIES INFERRED FROM 8-12-MU-M DATA, *Journal of Applied Meteorology*, 33(2), 212-229, doi:10.1175/1520-0450(1994)033<0212:cpifd>2.0.co;2.

Strow, L. L., S. E. Hannon, S. De Souza-Machado, H. E. Motteler, and D. Tobin (2003), An overview of the AIRS radiative transfer model, *Ieee Transactions on Geoscience and Remote Sensing*, 41(2), 303-313, doi:10.1109/tgrs.2002.808244.

Tupper, A., S. Carn, J. Davey, Y. Kamada, R. Potts, F. Prata, and M. Tokuno (2004), An evaluation of volcanic cloud detection techniques during recent significant eruptions in the western 'Ring of Fire', *Remote Sensing of Environment*, 91(1), 27-46, doi:10.1016/j.rse.2004.02.004.

Tupper, A., J. S. Oswalt, and D. Rosenfeld (2005), Satellite and radar analysis of the volcanic-cumulonimbi at Mount Pinatubo, Philippines, 1991, *Journal of Geophysical Research-Atmospheres*, 110(D9), doi:10.1029/2004jd005499.

Turnbull, K., B. Johnson, F. Marengo, J. Haywood, A. Minikin, B. Weinzierl, H. Schlager, U. Schumann, S. Leadbetter, and A. Woolley (2012), A case study of observations of volcanic ash from the Eyjafjallajokull eruption: 1. In situ airborne observations, *Journal of Geophysical Research-Atmospheres*, 117, doi:10.1029/2011jd016688.

Turner, D. D. (2005), Arctic mixed-phase cloud properties from AERI lidar observations: Algorithm and results from SHEBA, *Journal of Applied Meteorology*, 44(4), 427-444, doi:10.1175/jam2208.1.

Turner, D. D. (2008), Ground-based infrared retrievals of optical depth, effective radius, and composition of airborne mineral dust above the Sahel, *Journal of Geophysical Research-Atmospheres*, 113, doi:10.1029/2008jd010054.

Uddstrom, M. J., W. R. Gray, R. Murphy, N. A. Oien, and T. Murray (1999), A Bayesian cloud mask for sea surface temperature retrieval, *Journal of Atmospheric and Oceanic Technology*, 16(1), 117-132, doi:10.1175/1520-0426(1999)016<0117:abcmfs>2.0.co;2.

Van de Hulst, H. C. (1980), *Multiple Light Scattering: Tables, Formulas, and Applications*, Academic Press, New York, USA.

Varandas da Silva, L. S., E. L. Piovano, D. d. A. Azevedo, and F. R. de Aquino Neto (2008), Quantitative evaluation of sedimentary organic matter from Laguna Mar Chiquita, Argentina, *Organic Geochemistry*, 39(4), 450-464, doi:10.1016/j.orggeochem.2008.01.002.

Vaughan, M., K. Powell, R. Kuehn, S. Young, D. Winker, C. Hostetler, W. Hunt, Z. Liu, M. McGill, and B. Getzewich (2009), Fully Automated Detection of Cloud and Aerosol Layers in the CALIPSO Lidar Measurements, *Journal of Atmospheric and Oceanic Technology*, 26(10), 2034-2050, doi:10.1175/2009JTECHA1228.1.

Wang, C., S. Dong, A. Evan, G. Foltz, and S. Lee (2012), Multidecadal Covariability of North Atlantic Sea Surface Temperature, African Dust, Sahel Rainfall, and Atlantic Hurricanes, *Journal of Climate*, 25(15), 5404-5415, doi:10.1175/JCLI-D-11-00413.1.

Warren, S. G., and R. E. Brandt (2008), Optical constants of ice from the ultraviolet to the microwave: A revised compilation, *Journal of Geophysical Research-Atmospheres*, 113(D14), doi:10.1029/2007jd009744.

Watson, I. M., V. J. Realmuto, W. I. Rose, A. J. Prata, G. J. S. Bluth, Y. Gu, C. E. Bader, and T. Yu (2004), Thermal infrared remote sensing of volcanic emissions using the moderate resolution imaging spectroradiometer, *Journal of Volcanology and Geothermal Research*, 135(1-2), 75-89, doi:10.1016/j.jvolgeores.2003.12.017.

Waythomas, C. F., W. E. Scott, S. G. Prejean, D. J. Schneider, P. Izbekov, and C. J. Nye (2010), The 7-8 August 2008 eruption of Kasatochi Volcano, central Aleutian Islands, Alaska, *Journal of Geophysical Research-Solid Earth*, 115, doi:10.1029/2010jb007437.

Webley, P., T. Steensen, M. Stuefer, G. Grell, S. Freitas, and M. Pavolonis (2012), Analyzing the Eyjafjallajokull 2010 eruption using satellite remote sensing, lidar and WRF-Chem dispersion and tracking model, *Journal of Geophysical Research-Atmospheres*, 117, doi:10.1029/2011JD016817.

Wen, S., and W. I. Rose (1994), Retrieval of sizes and total masses of particles in volcanic clouds using AVHRR bands 4 and 5, *J. Geophys. Res.*, 99(- D3), 5421-5431, doi:- 10.1029/93jd03340.

Wielicki, B. A., and R. M. Welch (1986), CUMULUS CLOUD PROPERTIES DERIVED USING LANDSAT SATELLITE DATA, *Journal of Climate and Applied Meteorology*, 25(3), 261-276, doi:10.1175/1520-0450(1986)025<0261:ccpdul>2.0.co;2.

Winker, D., Z. Liu, A. Omar, J. Tackett, and D. Fairlie (2012), CALIOP observations of the transport of ash from the Eyjafjallajokull volcano in April 2010, *Journal of Geophysical Research-Atmospheres*, 117, doi:10.1029/2011JD016499.

Winker, D., et al. (2010), THE CALIPSO MISSION A Global 3D View of Aerosols and Clouds, *Bulletin of the American Meteorological Society*, 91(9), 1211-1229, doi:10.1175/2010BAMS3009.1.

Yang, P., H. L. Wei, H. L. Huang, B. A. Baum, Y. X. Hu, G. W. Kattawar, M. I. Mishchenko, and Q. Fu (2005), Scattering and absorption property database for nonspherical ice particles in the near- through far-infrared spectral region, *Applied Optics*, 44(26), 5512-5523, doi:10.1364/ao.44.005512.

Zhang, H., and W. P. Menzel (2002), Improvement in thin cirrus retrievals using an emissivity-adjusted CO<sub>2</sub> slicing algorithm, *Journal of Geophysical Research-Atmospheres*, 107(D17), doi:10.1029/2001jd001037.

Zhang, P., N.-m. Lu, X.-q. Hu, and C.-h. Dong (2006), Identification and physical retrieval of dust storm using three MODIS thermal IR channels, *Global and Planetary Change*, 52(1-4), 197-206, doi:10.1016/j.gloplacha.2006.02.014.